

AD-A074 702

DAVID W TAYLOR NAVAL SHIP RESEARCH AND DEVELOPMENT CE--ETC F/G 13/10  
ACCURACY OF HYDROFOIL LOADING PREDICTIONS OBTAINED FROM A LIFTI--ETC(U)  
SEP 79 P K BESCH, E P ROOD

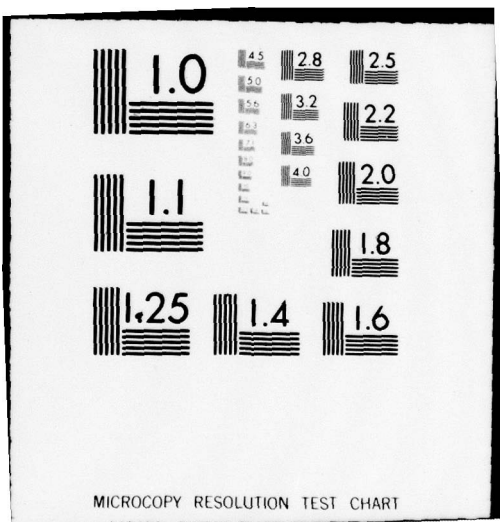
UNCLASSIFIED

DTNSRDC-79/039

NL

OF 3  
ADA  
074702





**DDC FILE COPY**  
ACCURACY OF HYDROFOIL LOADING PREDICTIONS OBTAINED FROM A LIFTING-SURFACE  
COMPUTER PROGRAM

DTNSRDC-79/039

**LEVEL** *(initials)*  
**DAVID W. TAYLOR NAVAL SHIP**  
**RESEARCH AND DEVELOPMENT CENTER**

Bethesda, Maryland 20084

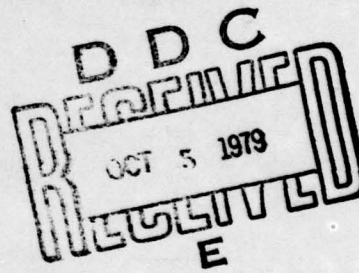


**AD A074702**

**ACCURACY OF HYDROFOIL LOADING PREDICTIONS OBTAINED  
FROM A LIFTING-SURFACE COMPUTER PROGRAM**

by

Peter K. Besch  
Edwin P. Rood, Jr.



**APPROVED FOR PUBLIC RELEASE: DISTRIBUTION UNLIMITED**

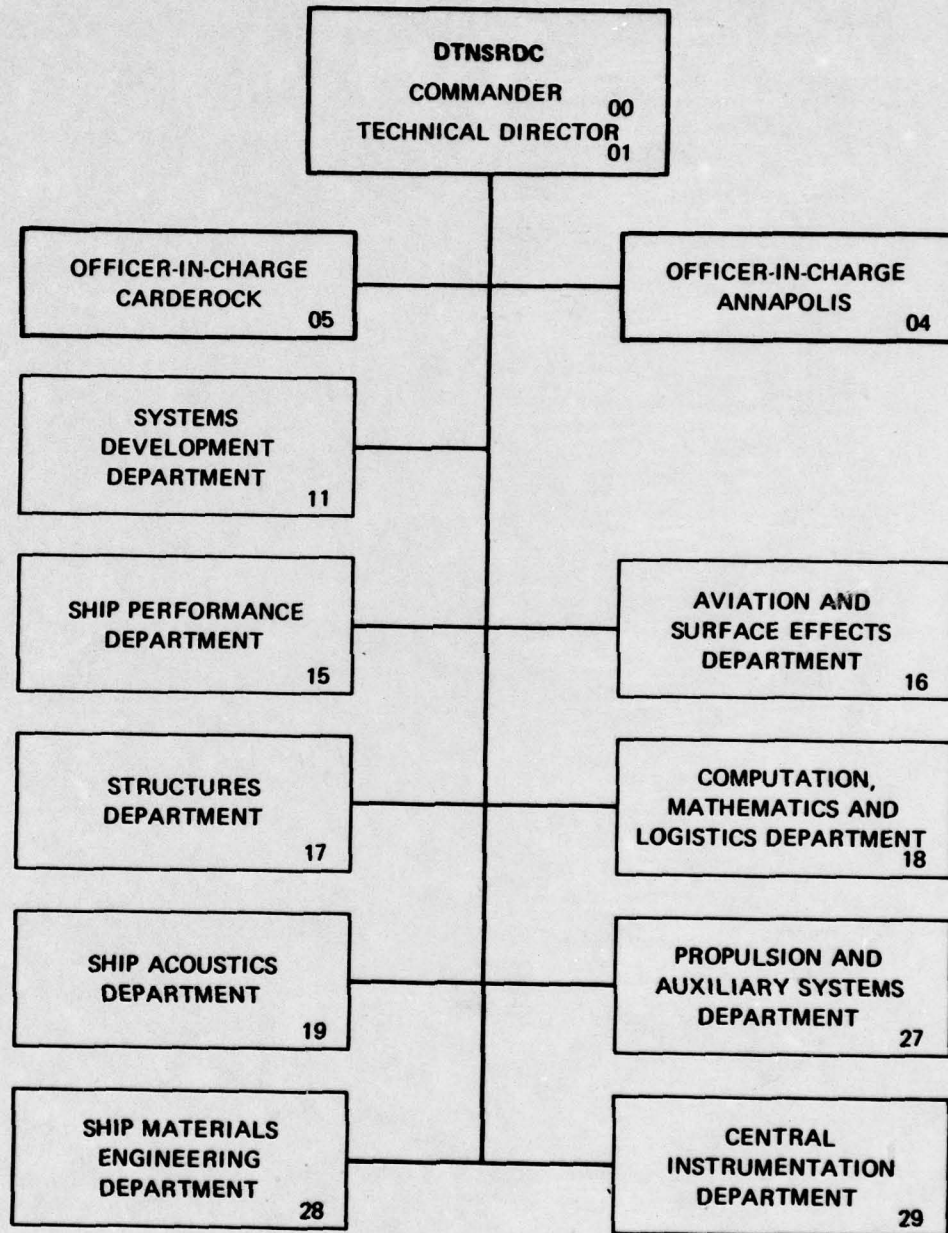
**SHIP PERFORMANCE DEPARTMENT  
RESEARCH AND DEVELOPMENT REPORT**

September 1979

DTNSRDC-79/039

79 10 04 022

## MAJOR DTNSRDC ORGANIZATIONAL COMPONENTS



**UNCLASSIFIED**

---

SECURITY CLASSIFICATION OF THIS PAGE (When Data Entered)

REPORT DOCUMENTATION PAGE		READ INSTRUCTIONS BEFORE COMPLETING FORM.
1. REPORT NUMBER <b>DTNSRDC-79/039</b>	2. GOVT ACCESSION NO.	3. RECIPIENT'S CATALOG NUMBER
4. TITLE (and Subtitle) <b>ACCURACY OF HYDROFOIL LOADING PREDICTIONS OBTAINED FROM A LIFTING-SURFACE COMPUTER PROGRAM</b>		5. TYPE OF REPORT & PERIOD COVERED <b>Final</b>
7. AUTHOR(s) <b>Peter K. Besch and Edwin P. Rood, Jr.</b>		8. CONTRACT OR GRANT NUMBER(s)
9. PERFORMING ORGANIZATION NAME AND ADDRESS <b>David W. Taylor Naval Ship Research and Development Center Bethesda, Maryland 20084</b>		10. PROGRAM ELEMENT, PROJECT, TASK AREA & WORK UNIT NUMBERS <b>Program Element 62543N Task Area ZF-43-421-01 Work Unit 1500-102</b>
11. CONTROLLING OFFICE NAME AND ADDRESS <b>Naval Material Command NAVMAT 087 Washington, D.C. 20360</b>		12. REPORT DATE <b>Sep 1979</b>
14. MONITORING AGENCY NAME & ADDRESS (if different from Controlling Office) <b>F43421</b>		13. NUMBER OF PAGES <b>203</b>
16. DISTRIBUTION STATEMENT (of this Report)  <b>APPROVED FOR PUBLIC RELEASE: DISTRIBUTION UNLIMITED</b>		15. SECURITY CLASS. (of this report) <b>UNCLASSIFIED</b>
17. DISTRIBUTION STATEMENT (of the abstract entered in Block 20, if different from Report)		
18. SUPPLEMENTARY NOTES		
19. KEY WORDS (Continue on reverse side if necessary and identify by block number) <b>Hydrofoil Subcavitating Hydrodynamic Loading Theoretical, Experimental Airfoil Theoretical, Experimental Lifting-Surface Theory Aerodynamic Loading Computer Program Numerical Approximation</b>		
20. ABSTRACT (Continue on reverse side if necessary and identify by block number)  <b>To provide guidance for hydrofoil designers, an extensive operational evaluation was made of a computer-based lifting-surface theory for calculating hydrodynamic loading on hydrofoils in steady and unsteady motion in inviscid, subcavitating flow at finite depth. Both the numerical stability and the accuracy in comparison with model data were estimated. By use of an empirical correction, lift predictions can be made with an accuracy of about 15 to 20 percent, while pitching moment predictions are substantially less</b> <b>(Continued on reverse side)</b>		

CONT

**UNCLASSIFIED**

**SECURITY CLASSIFICATION OF THIS PAGE (When Data Entered)**

(Block 20 continued)

*cont'* → accurate. Determination of the accuracy was hindered by insufficient or imprecise data. Documentation for the computer program is given.

Accession For	
NTIS GRA&I	<input checked="" type="checkbox"/>
DDC TAB	<input type="checkbox"/>
Unannounced	<input type="checkbox"/>
Justification	
By _____	
Distribution/	
Availability Codes	
Dist.	Avail and/or special
A	

**UNCLASSIFIED**

**SECURITY CLASSIFICATION OF THIS PAGE(When Data Entered)**

## TABLE OF CONTENTS

	Page
LIST OF FIGURES . . . . .	iv
LIST OF TABLES. . . . .	ix
NOTATION. . . . .	xi
ABSTRACT. . . . .	1
ADMINISTRATIVE INFORMATION. . . . .	1
INTRODUCTION. . . . .	1
SUMMARY OF THE LIFTING-SURFACE THEORY . . . . .	3
NUMERICAL STABILITY OF THE CALCULATION. . . . .	7
NUMERICAL STABILITY OF THE STEADY LOADING CALCULATION. . . . .	8
Number of Chordwise Pressure Modes, NOLT. . . . .	8
Number of Chordwise Integration Stations, NCP and MP. . . . .	20
Number of Collocation Points, NOCP. . . . .	23
Number of Spanwise Pressure Modes, NOST . . . . .	25
Number of Spanwise Integration Stations, NI . . . . .	25
Effect of Foil Aspect Ratio . . . . .	25
Effect of Finite Depth. . . . .	30
Effects of Sweep and Taper. . . . .	30
NUMERICAL STABILITY OF THE UNSTEADY LOADING CALCULATION. . . . .	38
SUMMARY OF RESIDUAL INSTABILITY. . . . .	38
COMPUTATIONAL PRECISION. . . . .	43
COMPARISON WITH EXPERIMENT. . . . .	44
STEADY LOADING--THEORY AND EXPERIMENT . . . . .	45
ERROR DUE TO STRUT-POD INTERFERENCE. . . . .	64
ERROR DUE TO CAMBER VARIATION. . . . .	64
ERROR DUE TO VISCOUS EFFECTS . . . . .	65
ERROR DUE TO UNREPORTED EXPERIMENTAL UNCERTAINTY . . . . .	65
STATISTICAL ANALYSIS OF DATA . . . . .	66
COMPARISON WITH THE BANDLER PROGRAM. . . . .	68
UNSTEADY LOADING--THEORY AND EXPERIMENT . . . . .	69
OSCILLATING FOILS. . . . .	69

	Page
NACA 66-209(S) Hydrofoil . . . . .	69
NACA 0010 Hydrofoil and Airfoil . . . . .	103
AGEH-1 One-Twelfth-Scale Hydrofoil . . . . .	103
NACA 65A010 Airfoil . . . . .	104
WAVE-INDUCED LOADING . . . . .	105
AGEH-1 One-Twelfth-Scale Hydrofoil . . . . .	105
NACA 66-209(S) Hydrofoil . . . . .	106
NACA 16-509 Hydrofoil . . . . .	106
SUMMARY OF UNSTEADY LOADING PREDICTIONS . . . . .	106
DISCUSSION . . . . .	107
CONCLUSIONS . . . . .	108
RECOMMENDATIONS . . . . .	109
APPENDIX A - DESCRIPTION OF EXPERIMENTAL MODELS . . . . .	111
APPENDIX B - COMPUTER PROGRAM USER'S MANUAL . . . . .	119
APPENDIX C - PROGRAM LISTINGS AND INPUT FOR SAMPLE CALCULATIONS . . . . .	145
APPENDIX D - PROGRAM 1 OUTPUT FOR SAMPLE CALCULATION . . . . .	171
APPENDIX E - PROGRAM 2 OUTPUT FOR SAMPLE CALCULATION . . . . .	177
APPENDIX F - PROGRAM 3 OUTPUT FOR SAMPLE CALCULATION . . . . .	181
REFERENCES . . . . .	183

#### LIST OF FIGURES

1 - Configuration of a Nonplanar Lifting Surface . . . . .	4
2 - The Steady Lift Coefficient $C_L(\alpha = 0)$ as a Function of the Number of Chordwise Modes NOLT for a Planar Rectangular AR = 10 Hydrofoil at Infinite Depth . . . . .	9
3 - The Effect of the Number of Chordwise Integration Steps NCP and MP on the Steady Lift Coefficient $C_L(\alpha = 0)$ for a Planar Rectangular AR = 10 Hydrofoil at Infinite Depth . . . . .	10

Page

4 - The Effect of the Number of Integration Steps NCP, MP, and NI and Control Points NOCP on the Steady Lift Coefficient $C_L(\alpha = 0)$ for a Planar Rectangular AR = 10 Hydrofoil at Infinite Depth. . . . .	11
5 - The Steady Moment Coefficient $C_M(\alpha = 0)$ as a Function of the Number of Chordwise Modes NOLT for a Planar Rectangular AR = 10 Hydrofoil at Infinite Depth. . . . .	12
6 - The Effect of the Number of Chordwise Integration Steps NCP and MP on the Steady Moment Coefficient $C_M(\alpha = 0)$ for a Planar Rectangular AR = 10 Hydrofoil at Infinite Depth. . . . .	13
7 - The Effect of the Number of Integration Steps NCP, MP, and NI and Control Points NOCP on the Steady Moment Coefficient $C_M(\alpha = 0)$ for a Planar Rectangular AR = 10 Hydrofoil at Infinite Depth. . . . .	14
8 - The Steady Lift Coefficient Slope $C_{L\alpha}$ as a Function of the Number of Chordwise Modes NOLT for a Planar Rectangular AR = 10 Hydrofoil at Infinite Depth. . . . .	15
9 - The Effect of the Number of Chordwise Integration Steps NCP and MP on the Steady Lift Coefficient Slope $C_{L\alpha}$ for a Planar Rectangular AR = 10 Hydrofoil at Infinite Depth . . . . .	16
10 - The Effect of the Number of Integration Steps NCP, MP, and NI and Control Points NOCP on the Steady Lift Coefficient Slope $C_{L\alpha}$ for a Planar Rectangular AR = 10 Hydrofoil at Infinite Depth. . . . .	17
11 - The Steady Moment Coefficient Slope $C_{M\alpha}$ as a Function of the Number of Chordwise Modes NOLT for a Planar Rectangular AR = 10 Hydrofoil at Infinite Depth. . . . .	18
12 - The Effect of the Number of Chordwise Integration Steps NCP and MP on the Steady Moment Coefficient Slope $C_{M\alpha}$ for a Planar Rectangular AR = 10 Hydrofoil at Infinite Depth . . . . .	18
13 - The Effect of the Number of Integration Steps NCP, MP, and NI and Control Points NOCP on the Steady Moment Coeffi- cient Slope $C_{M\alpha}$ for a Planar Rectangular AR = 10 Hydrofoil at Infinite Depth. . . . .	19

	Page
14 - Numerical Instability of the Chordwise Distribution of Lift at the Midspan of an AR = 10 Rectangular Hydrofoil at Infinite Depth . . . . .	21
15 - The Effect of the Number of Chordwise Control Points $j$ and Spanwise Control Points $k$ on the Steady Lift Coefficient $C_L(\alpha = 0)$ for a Planar Rectangular AR = 10 Hydrofoil at Infinite Depth. . . . .	26
16 - The Effect of the Number of Chordwise Control Points $j$ and Spanwise Control Points $k$ on the Steady Moment Coefficient $C_M(\alpha = 0)$ for a Planar Rectangular AR = 10 Hydrofoil at Infinite Depth. . . . .	26
17 - The Effect of the Number of Chordwise Control Points $j$ and Spanwise Control Points $k$ on the Steady Lift Coefficient Slope $C_{L\alpha}$ for a Planar Rectangular AR = 10 Hydrofoil at Infinite Depth. . . . .	27
18 - The Effect of the Number of Chordwise Control Points $j$ and Spanwise Control Points $k$ on the Steady Moment Coefficient Slope $C_{M\alpha}$ for a Planar Rectangular AR = 10 Hydrofoil at Infinite Depth. . . . .	27
19 - The Steady Lift Coefficient $C_L(\alpha = 0)$ as a Function of the Number of Spanwise Modes NOST for a Planar Rectangular AR = 10 Hydrofoil at Infinite Depth. . . . .	28
20 - The Steady Moment Coefficient $C_M(\alpha = 0)$ as a Function of the Number of Spanwise Modes NOST for a Planar Rectangular AR = 10 Hydrofoil at Infinite Depth. . . . .	28
21 - The Steady Lift Coefficient Slope $C_{L\alpha}$ as a Function of the Number of Spanwise Modes NOST for a Planar Rectangular AR = 10 Hydrofoil at Infinite Depth . . . . .	29
22 - The Steady Moment Coefficient Slope $C_{M\alpha}$ as a Function of the Number of Spanwise Modes NOST for a Planar Rectangular AR = 10 Hydrofoil at Infinite Depth . . . . .	29
23 - The Effect of Aspect Ratio on the Chordwise Distribution of Lift at the Midspan of a Rectangular Hydrofoil at Infinite Depth . . . . .	31

Page

24 - The Steady Lift Coefficient $C_L(\alpha = 0)$ as a Function of the Number of Chordwise Modes NOLT for a Rectangular AR = 6 Hydrofoil at Infinite Depth. . . . .	33
25 - The Steady Moment Coefficient $C_M(\alpha = 0)$ as a Function of the Number of Chordwise Modes NOLT for a Rectangular AR = 6 Hydrofoil at Infinite Depth. . . . .	33
26 - The Steady Lift Coefficient Slope $C_{L\alpha}$ as a Function of the Number of Chordwise Modes NOLT for a Rectangular AR = 6 Hydrofoil at Infinite Depth . . . . .	34
27 - The Steady Moment Coefficient Slope $C_{M\alpha}$ as a Function of the Number of Chordwise Modes NOLT for a Rectangular AR = 6 Hydrofoil at Infinite Depth. . . . .	34
28 - The Steady Lift Coefficient $C_L(\alpha = 0)$ as a Function of the Number of Chordwise Modes NOLT for a Rectangular AR = 1 Hydrofoil at Infinite Depth. . . . .	35
29 - The Steady Moment Coefficient $C_M(\alpha = 0)$ as a Function of the Number of Chordwise Modes NOLT for a Rectangular AR = 1 Hydrofoil at Infinite Depth. . . . .	35
30 - The Steady Lift Coefficient Slope $C_{L\alpha}$ as a Function of the Number of Chordwise Modes NOLT for a Rectangular AR = 1 Hydrofoil at Infinite Depth . . . . .	36
31 - The Steady Moment Coefficient Slope $C_{M\alpha}$ as a Function of the Number of Chordwise Modes NOLT for a Rectangular AR = 1 Hydrofoil at Infinite Depth . . . . .	36
32 - The Effect of the Number of Spanwise Control Points k on the Lift Coefficient Magnitude $ C_{L\alpha} $ and Phase $\phi_L$ and Moment Coefficient Magnitude $ C_{M\alpha} $ and Phase $\phi_M$ for Bending and Torsion Oscillations for a Rectangular AR = 10 Hydrofoil at Infinite Depth with k = 1.97 (Number of Chordwise Control Points = 15; NOCP = 15 * k) . . . . .	40
33 - The Effect of the Number of Chordwise Modes NOLT on the Unsteady Loading due to Bending and Torsional Oscillations of a Rectangular AR = 10 Hydrofoil at Infinite Depth with k = 1.97 (NOCP = 60; 15 Chordwise, 4 Spanwise) . . . . .	41

Page

34 - Total Steady Lift Coefficient as a Function of Submergence for Various Hydrofoils with Rectangular Planforms ( $\Lambda = 0$ ; $\tau = 1.0$ ) . . . . .	46
35 - Total Steady Lift Slope Coefficient as a Function of Sub- mergence for Various Hydrofoils with Rectangular Planforms ( $\Lambda = 0$ ; $\tau = 1.0$ ) . . . . .	51
36 - Spanwise Distribution of Steady Lift Coefficient for the NACA 0010 Hydrofoil ( $\Lambda = 0$ ; $\tau = 1.0$ ; AR = 5) . . . . .	55
37 - Total Steady Lift and Lift Slope Coefficients as Functions of Submergence for the One-Eighth-Scale PCH-1 Hydrofoil Model ( $\Lambda = 15$ Degrees; $\tau = 0.25$ ; AR = 6.1) . . . . .	56
38 - Total Steady Loading as a Function of Submergence for the One-Twelfth-Scale AGEH-1 Hydrofoil Model ( $\Lambda = 35$ Degrees; $\tau = 0.3$ ; AR = 3) . . . . .	57
39 - Comparison of Total Lift Coefficients on a Hydrofoil and an Airfoil in Two-Dimensional Flow . . . . .	60
40 - Total Lift Coefficient on a Hydrofoil in Two-Dimensional Flow at Finite Depth . . . . .	61
41 - Prediction Accuracy of the Widnall Program as a Function of Aspect Ratio for Steady Lift at Deep Submergence. . . . .	63
42 - Total Unsteady Lift Coefficient due to Heave Oscillation as a Function of Reduced Frequency for the NACA 66-209(S) Hydrofoil ( $\Lambda = 0$ ; $\tau = 1.0$ ; AR = 5) . . . . .	70
43 - Spanwise Distributions of Unsteady Loading due to Bending and Torsional Oscillations for the NACA 0010 Airfoil ( $\Lambda = 0$ ; $\tau = 1$ ; AR = 5) . . . . .	71
44 - Spanwise Distributions of Unsteady Loading due to Bending and Torsional Oscillations for the NACA 0010 Hydrofoil ( $\Lambda = 0$ ; $\tau = 1$ ; AR = 5) . . . . .	79
45 - Total Unsteady Loading due to Pitching Oscillation as a Function of Reduced Frequency for the One-Twelfth- Scale AGEH-1 Hydrofoil Model ( $\Lambda = 35$ Degrees; $\tau = 0.3$ ; AR = 3) . . . . .	84
46 - Total Unsteady Loading due to Pitching and Flapping Oscillations as a Function of Reduced Frequency for the NACA 65A010 Airfoil ( $\Lambda = 0$ ; $\tau = 1$ ; AR = 2) . . . . .	89

	Page
47 - Total Unsteady Loading in a Head Sea as a Function of Wave-length for the One-Twelfth-Scale AGEH-1 Hydrofoil Model ( $\Lambda = 35$ Degrees; $\tau = 0.3$ ; AR = 3) . . . . .	94
48 - Magnitude and Phase Angle of the Total Unsteady Lift in a Head Sea as a Function of Reduced Frequency for the NACA 66-209(S) Hydrofoil ( $\Lambda = 0$ ; $\tau = 1.0$ ; AR = 5) . . . . .	101
49 - Magnitude and Phase Angle of the Total Unsteady Lift in Head and Following Seas as a Function of Wavelength for the NACA 16-509 Hydrofoil ( $\Lambda = 0$ ; $\tau = 1$ ; AR = 6) . . . . .	102
B.1 - Relationship among Programs YKWS, YKWU, and YKWA . . . . .	120
B.2 - Integration Regions for a Typical Control Point. . . . .	126
B.3 - View of Nonplanar Foil Looking Upstream. . . . .	126
B.4 - Foil Configuration for Steady Loading Test Case. . . . .	140
B.5 - Foil Configuration for Unsteady Loading Test Case. . . . .	142

#### LIST OF TABLES

1 - Numerical Stability of Calculated Load Coefficients for a Planar Rectangular Hydrofoil at Infinite Depth . . . . .	23
2 - Input Parameter Baseline Values Required for Approximate Numerical Stability of the Steady Loading Calculation. . . . .	24
3 - Effect of Control Point Arrangement and Number of Pressure Modes on the Numerical Stability of Steady Lift Coefficient $C_L$ ( $\alpha = 0$ ) . . . . .	24
4 - Effect of Foil Submergence on the Numerical Stability of the Steady Loading Calculation . . . . .	37
5 - Effect of Sweep and Taper on the Numerical Stability of the Steady Loading Calculation. . . . .	37
6 - Input Parameter Baseline Values Required for Approximate Numerical Stability of the Unsteady Loading Calculation. . . . .	39
7 - Numerical Stability of the Unsteady Loading Calculation. . . . .	39
8 - Approximate Numerical Instabilities for Steady and Unsteady Loading Coefficients. . . . .	44

	Page
B.1 - Composition of Deck for Program 1 (YKWS) . . . . .	121
B.2 - Composition of Deck for Program 2 (YKWU) . . . . .	121
B.3 - Composition of Deck for Program 3 (YKWA) . . . . .	122
B.4 - FORTRAN Input Notation . . . . .	123
B.5 - Data Card Input. . . . .	130
B.6 - Output Load Coefficients . . . . .	137

## NOTATION

A	Integration surface equivalent to foil surface
AR	Aspect ratio; $b^2/S$
a	Refers to an airfoil or hydrofoil mean line producing a uniform load distribution forward of a and a distribution decreasing linearly to zero aft of a; a is given in fraction of chord
$a_{nm}$	Coefficient of series representing pressure jump $\Delta p$
b	Span of submerged foil section, measured perpendicular to free stream
$b'$	Fractional distance along submerged foil section, measured perpendicular to free stream
$C_L$	Lift coefficient; increases with increasing angle of attack; lift/qS
$C_{L\alpha}, C_{L\delta}$	Rate of change of $C_L$ or $C_\ell$ with respect to angle of attack $\alpha$ or $\delta$ , respectively, in units of radians $^{-1}$ unless otherwise noted
$C_\ell, C_1$	Local lift coefficient; (lift per unit span)/qC
$C_M$	Pitching moment coefficient; positive tending to increase angle of attack; (pitching moment)/qSc'
$C_{M\alpha}, C_{M\delta}$	Rate of change of $C_M$ with respect to angle of attack $\alpha$ or $\delta$ , respectively, in units of radians $^{-1}$
$C_m$	Local pitching moment coefficient; (pitching moment per unit span)/qSc'
$C_R$	Roll moment coefficient; (roll moment)/qSc'
c	Chord length of lifting surface, measured in streamwise direction
$c'$	Mean geometric chord; S/b
$c_o$	Root chord of section (chord at $b' = 0$ )
f	Location of foil surface

$f_i$	$i^{\text{th}}$ spanwise pressure mode
$h$	Depth beneath undisturbed free surface
$j$	Number of chordwise control points
$K$	Kernel function
$k$	Reduced frequency, $\omega c'/2U$ ; also, number of spanwise control points
$M$	Mach number
$q$	Stagnation pressure; $\rho U^2/2$
$S$	Submerged foil area
$t$	Time
$U$	Free stream velocity
$U'$	Magnitude of orbital velocity due to waves
$v_n$	Downwash, or perturbation velocity induced normal to the undisturbed flow by the foil, positive in direction opposite to direction of positive lift
$x$	Frame of reference coordinate parallel to flow and positive in the same direction as the free stream velocity
$x_{cp}$	Unsteady center of pressure; ratio of magnitude of unsteady moment in phase with lift to the unsteady lift magnitude, expressed as percent of chord aft of the foil leading edge
$y$	Spanwise position or frame of reference coordinate
$z$	Frame of reference coordinate
$\alpha$	Angle of attack relative to flow
$\beta$	Angular position in flapping motion
$\delta$	Unsteady linear displacement of lifting surface from its mean position, normal to surface at zero angle of attack; also, angle of attack of hydrofoil relative to pod
$\zeta$	Dummy integration coordinate used for integration over $z$
$\zeta_w$	Wave height from trough to crest
$\eta$	Dummy integration coordinate used for integration over $y$

$\theta$	Dummy integration coordinate used for chordwise integration
$\Lambda$	Sweep angle of quarter-chord line
$\lambda$	Wavelength
$\xi$	Dummy integration coordinate used for integration over x
$\rho$	Fluid mass density
$\tau$	Taper ratio; ratio of tip chord to root chord
$\phi$	Phase angle of loading relative to displacement
$\omega$	Circular frequency of oscillation in rad/sec
$\omega'$	Circular frequency of wave in fixed coordinate system in rad/sec

#### Subscripts

$o$	Single amplitude of subscripted quantity
$T$	Single amplitude at tip of foil
$w$	Single amplitude of effective unsteady angle of attack due to waves
91.7	Single amplitude at 91.7 percent of foil semispan

#### Superscript

( $\bar{}$ )	Mean value with respect to time
--------------	---------------------------------

## ABSTRACT

To provide guidance for hydrofoil designers, an extensive operational evaluation was made of a computer-based lifting-surface theory for calculating hydrodynamic loading on hydrofoils in steady and unsteady motion in inviscid, subcavitating flow at finite depth. Both the numerical stability and the accuracy in comparison with model data were estimated. By use of an empirical correction, lift predictions can be made with an accuracy of about 15 to 20 percent, while pitching moment predictions are substantially less accurate. Determination of the accuracy was hindered by insufficient or imprecise data. Documentation for the computer program is given.

## ADMINISTRATIVE INFORMATION

This work was authorized and partially funded under the Hydrofoil Development Program of the Naval Sea Systems Command, Subproject S4606, Task 1703, and performed under Work Unit 1153-003. The work was subsequently expanded under the authority of the Naval Material Command (NAVMAT 087), Program Element 62543N, Task Area ZF-43-421-01, and administered by the Ship Performance Department High Performance Vehicles Program (1507) under Work Unit 1500-102.

## INTRODUCTION

This report is an evaluation of one version of a commonly-used general approach (lifting-surface theory) to calculating fluid-dynamic loading on airfoils and hydrofoils. This particular treatment was developed by Ashley et al.<sup>1\*</sup> and Widnall<sup>2</sup> and programmed for computer use by Widnall. The program will be referred to as the Widnall program after its author. The theory is capable of calculating both steady and unsteady loading on non-planar hydrofoil systems at finite depth. It extends the theory developed by Watkins et al.<sup>3</sup> to include nonplanar surfaces, finite depth effects, and cavitation.

The Navy's interest in this type of calculation arises from possible design applications for hydrofoil craft and ship appendages. These applications include certain hydrodynamic performance characteristics (lift and

---

\*A complete listing of references is given on page 183.

side force, for example, but not drag) and, in combination with appropriate structural analyses, predictions of hydroelastic stability of lifting-surface structures.

To establish the usefulness of a calculation for design work, the accuracy of the method must be known. Although the Widnall program has been available for some time, a detailed analysis of its accuracy had not been performed. Therefore, the present study was undertaken. The approach consisted of comparing the program predictions with a large body of available model loading data from both fully-submerged hydrofoils and airfoils. As a part of the effort, the numerical behavior of the calculation was explored to find the most favorable range of numerical parameter values for program operation.

Some relatively limited evaluations of the theory have previously been made. In the initial development,<sup>1</sup> a two-dimensional version was found to agree with analytical results at infinite depth. Subsequently, Pattison<sup>4</sup> compared the two-dimensional calculation with experimental measurements. Significant differences were found, but some of the discrepancy may have been due to the experimental configuration and measurement uncertainty.

In an evaluation of three-dimensional loading predictions, Langan and Wang<sup>5</sup> compared results from the Widnall program with experimental loading on several airfoils. Their work was particularly valuable in that it studied fourteen other computer-based calculations as well. Some aspects of both numerical behavior and calculation accuracy relative to experiment were compared. None of the fifteen calculations was numerically stable to three significant figures. Accuracies were usually within 5 percent of airfoil loading data, but the Widnall prediction of lift due to camber was somewhat less accurate (within 9 percent). These latter calculations corresponded to conditions of optimum numerical stability as determined by the present study, part of which preceded that of Langan and Wang.

These results suggest that a program that is more accurate than the Widnall program can be chosen from the above study. However, the capabilities of treating free-surface effects, including surface-piercing configurations, and unsteady loading, not generally available in the other

programs, make the Widnall program potentially more useful in designing hydrofoils. Therefore, the present study is made available to provide a more comprehensive evaluation of the Widnall program by relating its predictions to available hydrofoil and airfoil data.

Both a description of the numerical characteristics, and comparisons between predicted loading and experimental results for the Widnall three-dimensional calculation, are presented in this report. Comparisons are made for both steady and unsteady loading on planar, fully-wetted foils. A description of the program as used, and instructions for program use, are given in the appendices.

The results contained in this report were obtained from a computer program which was a modification of the original version received by the Center. Changes in coding were made by the authors to modify input and output, to increase the number of chordwise integration modes, and to adapt the program to various computers. Results generated by the present program agree with previously published results<sup>1</sup> for equivalent inputs. It is, therefore, believed that the present results are the same as would have been obtained from the original version.

#### SUMMARY OF THE LIFTING-SURFACE THEORY

The computer programs described in this report are used to compute hydrodynamic loading on three-dimensional hydrofoils in inviscid, subcavitating flow<sup>2</sup> according to the lifting-surface theory presented by Ashley et al.<sup>1</sup> Calculations for hydrofoils in supercavitating flow are not included. A brief summary of the theory will be given in order to facilitate description of program characteristics.

The lifting surface under consideration consists of a foil or combination of foils which may be nonplanar. The surface is assumed to be of zero thickness and to make small angles with the direction of flow. An example of a single nonplanar foil is shown in Figure 1 along with a possible coordinate system. The choice of a coordinate system is limited only by the requirements that flow be in the positive x-direction and that a free surface, when present, coincide with the plane z = 0.

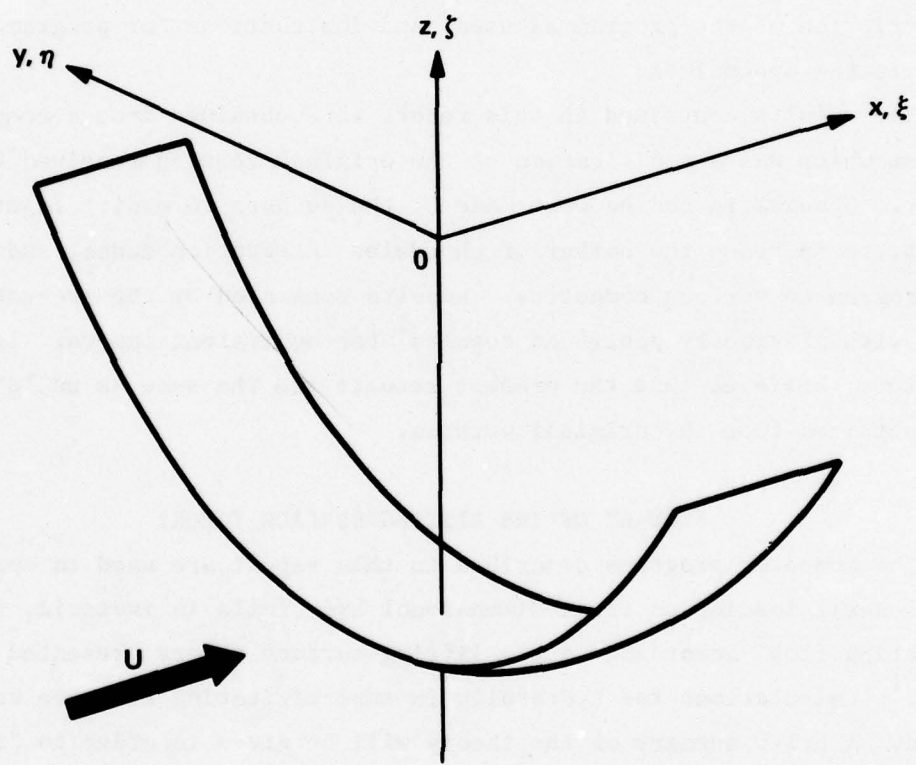


Figure 1 - Configuration of a Nonplanar Lifting Surface

The foil is represented theoretically by a distribution of pressure doublets over the surface of the foil. The downwash, or velocity perturbation normal to the undisturbed flow, is a known quantity determined by flow tangency on the foil and is given by

$$v_n(x, y, z, t) = \iint_A \Delta p(\xi, \eta, \zeta) K(x-\xi, y-\eta, z-\zeta, t) dA \quad (1)$$

The kernel function  $K$  is a geometrically determined pressure influence function relating the pressure jump at  $(\xi, \eta, \zeta)$  to the velocity induced at  $(x, y, z)$ . Time dependence is included as simple harmonic variation in the magnitudes of  $K$  and  $v_n$ , using complex number notation. Therefore, unsteady loading may be calculated only for sinusoidally varying flow conditions or foil motions. Superposition of Fourier components may be used to treat nonsinusoidal time dependence. The kernel function contains a term for the foil being treated and a term for an image foil equidistant from the free surface when a free surface is present. This representation of a free surface corresponds to assuming that gravity waves created by the foil are unimportant, i.e., infinite Froude number.

The pressure jump distribution,  $\Delta p$ , is found by inverting Equation (1) to give  $\Delta p$  as a function of known quantities. First,  $\Delta p$  is written in the form of a series of chordwise and spanwise pressure modes with unknown coefficients as follows:

$$\begin{aligned} \Delta p(\theta, s') = & 8\pi\rho U^2 \frac{b}{c(b')} \left[ \sum_{m=0}^{m'} a_{0m} f_m(b') \cot \frac{\theta}{2} \right. \\ & \left. + \sum_{n=1}^{n'} \sum_{m=0}^{m'} \frac{4}{2^n} a_{nm} f_m(b') \sin n\theta \right] \end{aligned} \quad (2)$$

The chordwise modes (the trigonometric functions of  $\theta$ ) used in this expansion were taken from two-dimensional airfoil theory, while the spanwise

modes  $f_m$  are left to be specified by the program user according to boundary conditions as described in Appendix B.

The integration indicated in Equation (1) is performed numerically in terms of the unknown pressure mode coefficients  $a_{nm}$ . A set of linear equations is obtained relating the pressure mode coefficients to the downwash at a number of locations on the foil. The set of equations is inverted to give the pressure mode coefficients in terms of the downwash values. Finally, the pressure jump distribution and, therefore, any foil loading coefficient may be determined by inserting the foil's downwash values into the inverted equations.

Downwash values are chosen to correspond to flow conditions on the foil. In order to achieve flow tangency, the steady downwash is chosen to be proportional to the local angle of attack. The unsteady downwash consists of flow components needed to maintain the flow in contact with, and tangent to, the foil surface. Calculation of the downwash is described in Appendix B.

For numerical reasons, the downwash must be specified at a minimum number of points on the foil corresponding to the product of the numbers of spanwise and chordwise modes. However, the downwash may be specified at additional points to obtain presumably more accurate results by means of a least square fit inversion technique. Over-specification of downwash values is, in fact, essential to obtaining numerical stability, as described in the following section dealing with numerical behavior.

Final specification of the pressure jump distribution on the foil in terms of the pressure mode coefficients  $a_{nm}$  is obtained by combining the downwash input with the coefficient matrix obtained by integration and inversion of Equation (1). Real and imaginary parts of the calculation are treated separately in order to obtain the phase relationship between pressure distribution and displacement.

Load coefficients over various regions of the foil are calculated by expressing the desired coefficient in terms of the pressure jump  $\Delta p$  and integrating over the region. Real and imaginary parts of the integration are treated identically. The present form of the computer program calculates spanwise lift, pitch moment, and roll moment coefficients, chordwise

pressure coefficient distribution for steady loading, total lift, pitch moment and roll moment coefficients, and centers of pressure. Unsteady load coefficients are given in the form of magnitude and phase angle by which the load coefficient leads the unsteady displacement vector. Other load coefficients may be programmed as desired.

The numerical solution procedure just described is controlled by the program user, who specifies the number of collocation stations at which downwash is input, the number of integration intervals, and the number of modes used in the pressure representation. Instructions for generating the program input data are given in Appendix B.

#### NUMERICAL STABILITY OF THE CALCULATION

In order to discuss the numerical behavior of the program, the computer code names of the numerical variables with their numerical significance will be introduced at this time. A more complete description of the variables is given in Table B.5.

NOLT -- Number of chordwise pressure modes (n in Equation (2))

NOST -- Number of spanwise pressure modes (m in Equation (2))

NOCP -- Number of collocation stations

NCP, MP -- Numbers of chordwise integration steps

NI -- Number of spanwise integration steps

The Widnall program was exercised with a wide range of values for the above quantities. The object was to find a combination of parameter values which produced a numerically stable calculation. The term numerical stability is used to indicate a condition in which several significant figures in the calculated quantities do not change when the input quantities are varied by a small amount.

Four hydrofoil configurations were used as test cases for the numerical studies. Rectangular hydrofoils of AR = 1, 6, and 10 provided most of the stability information. An AR = 6.1 foil with a sweep angle  $\Lambda$  of 15

deg and a taper ratio  $\tau$  of 0.25 represented the effects of sweep and taper. The foils were given a NACA  $a = 1.0$  mean line to study camber loading predictions. This choice of camber was based on the presence of the NACA  $a = 1.0$  camber line on most of the hydrofoil models for which data are available.

To summarize the results, the degree of numerical stability that could be achieved was quite limited, being more than one but less than three significant figures. More precisely, the calculations for the AR = 10 hydrofoil had a residual instability of 0.4 to 9 percent, depending on the load coefficient considered. Most coefficients became more stable at lower aspect ratio; at AR = 1 the instability was about 1 percent for all coefficients. Results for the swept, tapered planform were similar, except for the pitching moment slope which had an instability of 27 percent. Specific effects of the numerical parameters and model configurations will be discussed in the following sections.

#### NUMERICAL STABILITY OF THE STEADY LOADING CALCULATION

A large number of calculations were performed for hydrofoils under steady flow conditions. Camber-induced loading was investigated separately from loading due to angle of attack. Camber loading is expressed in terms of the coefficients  $C_L(\alpha = 0)$  and  $C_M(\alpha = 0)$ . Angle of attack loading is presented as the coefficient slopes  $C_{L\alpha}(\alpha = 0)$  and  $C_{M\alpha}(\alpha = 0)$ .

#### Number of Chordwise Pressure Modes, NOLT

The stability of the steady loading calculation was extremely sensitive to the number of chordwise pressure modes used. The calculated coefficients are shown in Figures 2 through 13.

As the number of pressure modes was initially increased, most values of lift and pitching moment began to approach a stable condition in an almost monotonic manner, as shown in Figures 2 through 7 and 11 through 13. A somewhat different pattern was followed by the lift slope, which oscillated with decreasing amplitude as it approached an apparently stable value;

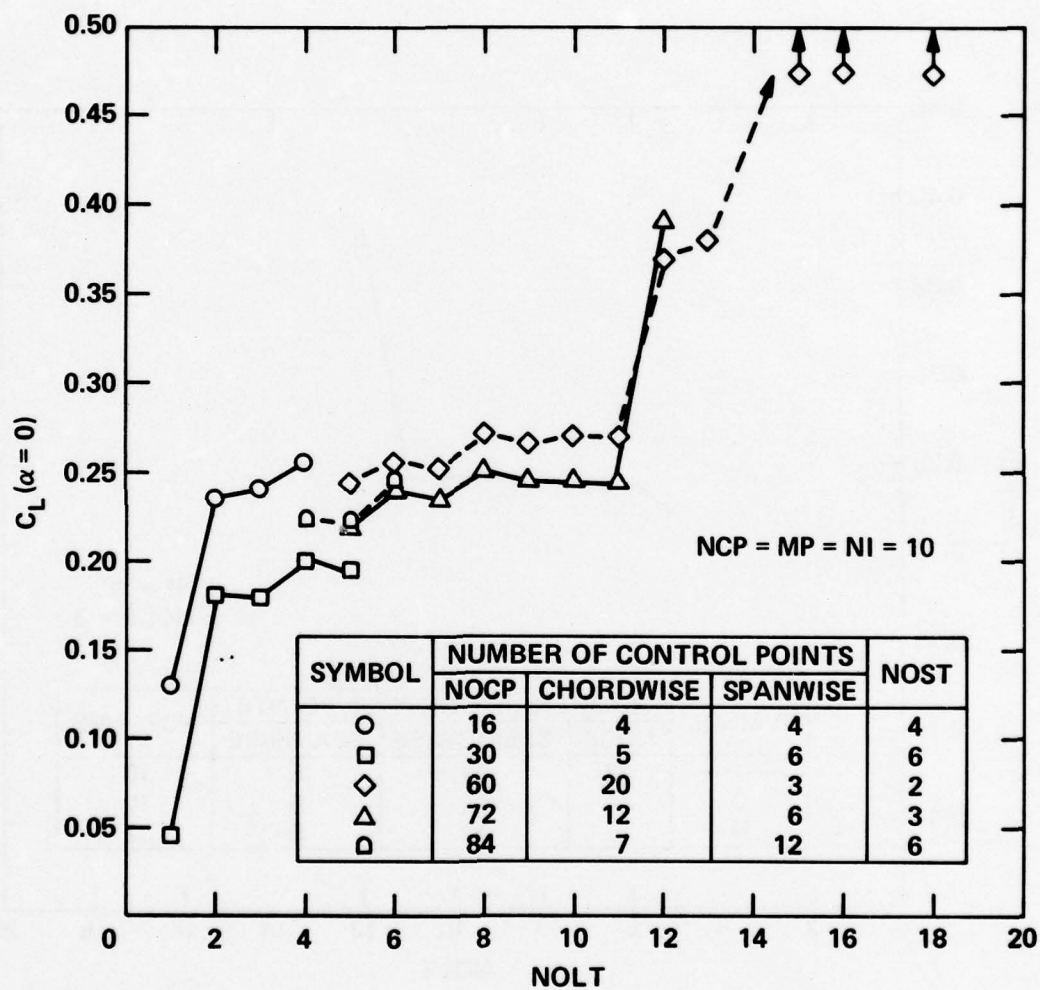


Figure 2 - The Steady Lift Coefficient  $C_L(\alpha = 0)$  as a Function of the Number of Chordwise Modes  $NOLT$  for a Planar Rectangular  $AR = 10$  Hydrofoil at Infinite Depth

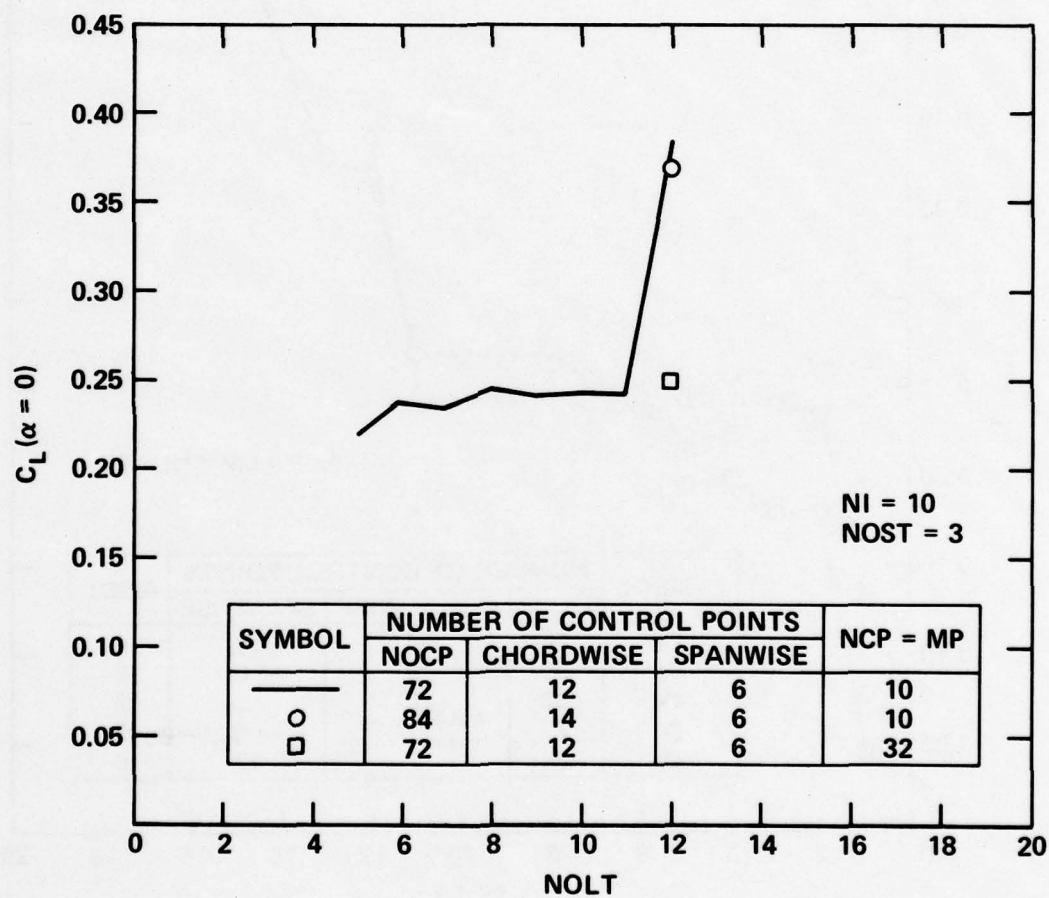


Figure 3 - The Effect of the Number of Chordwise Integration Steps NCP and MP on the Steady Lift Coefficient  $C_L(\alpha = 0)$  for a Planar Rectangular AR = 10 Hydrofoil at Infinite Depth

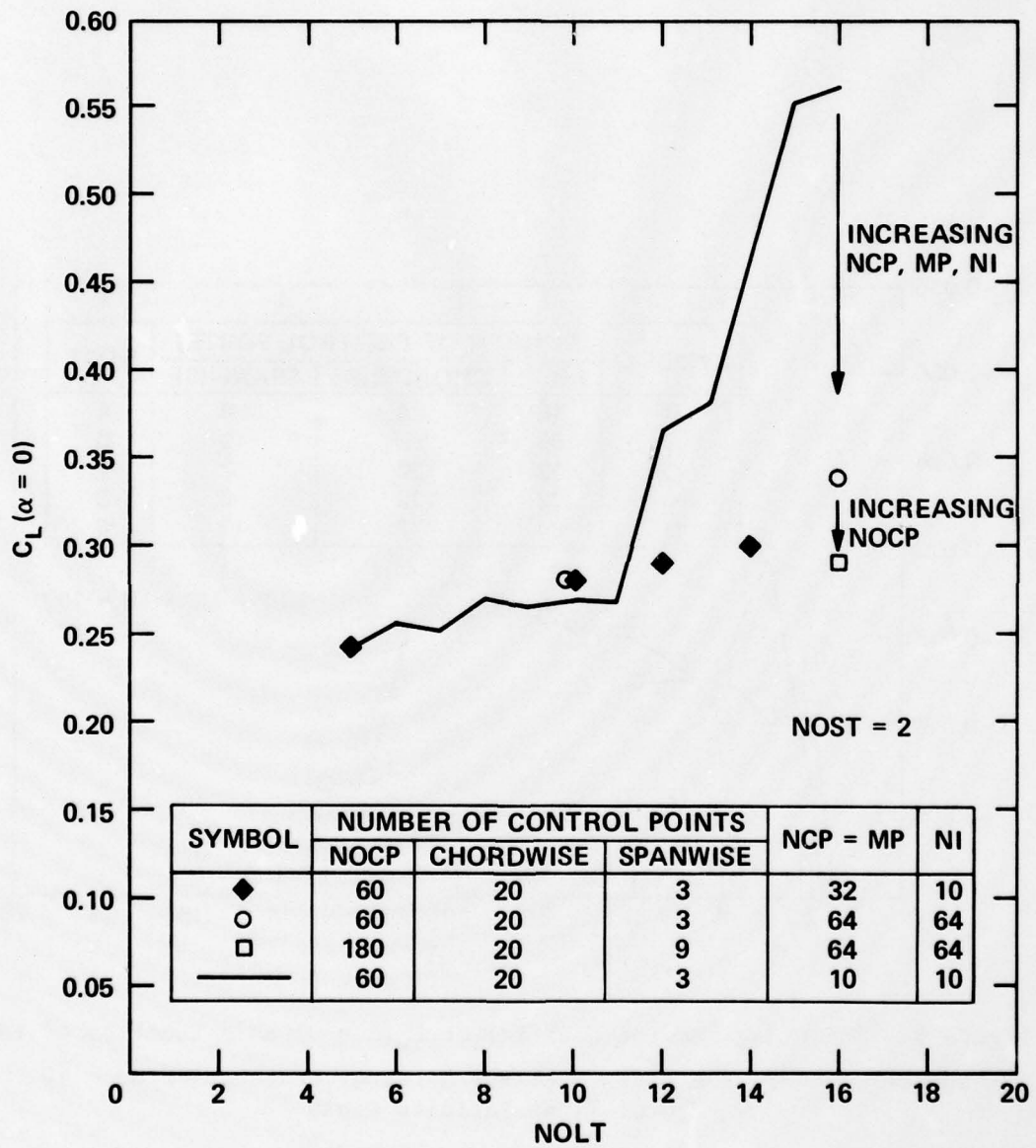


Figure 4 – The Effect of the Number of Integration Steps NCP, MP, and NI and Control Points NOCP on the Steady Lift Coefficient  $C_L(\alpha = 0)$  for a Planar Rectangular AR = 10 Hydrofoil at Infinite Depth

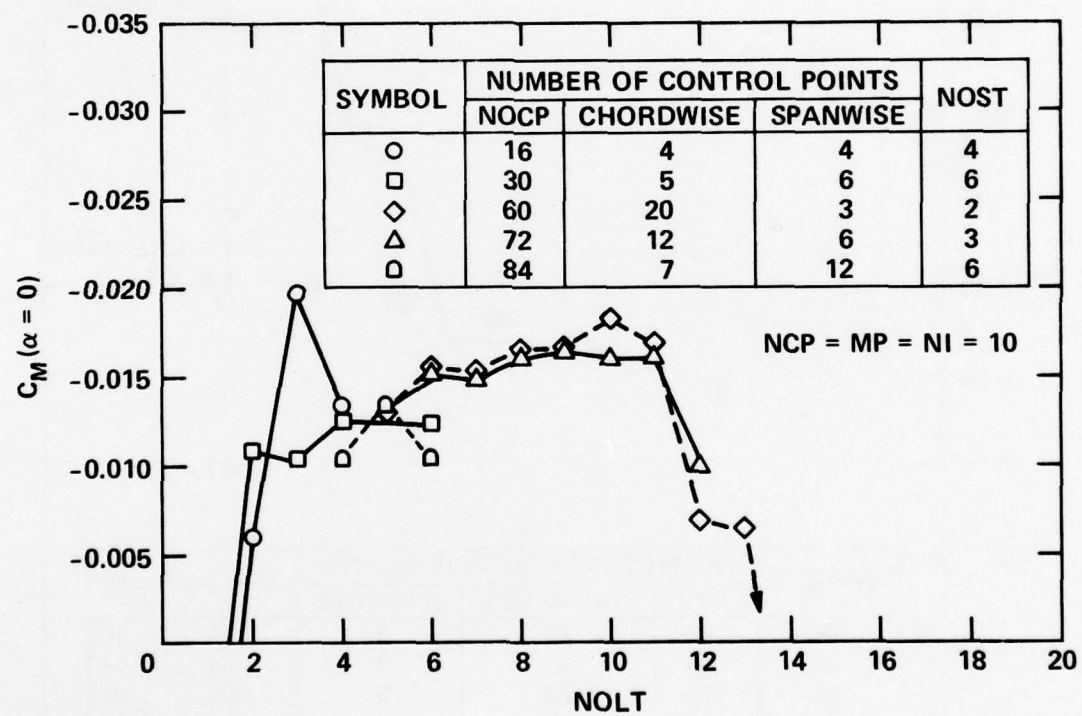


Figure 5 - The Steady Moment Coefficient  $C_M(\alpha = 0)$  as a Function of the Number of Chordwise Modes NOLT for a Planar Rectangular AR = 10 Hydrofoil at Infinite Depth

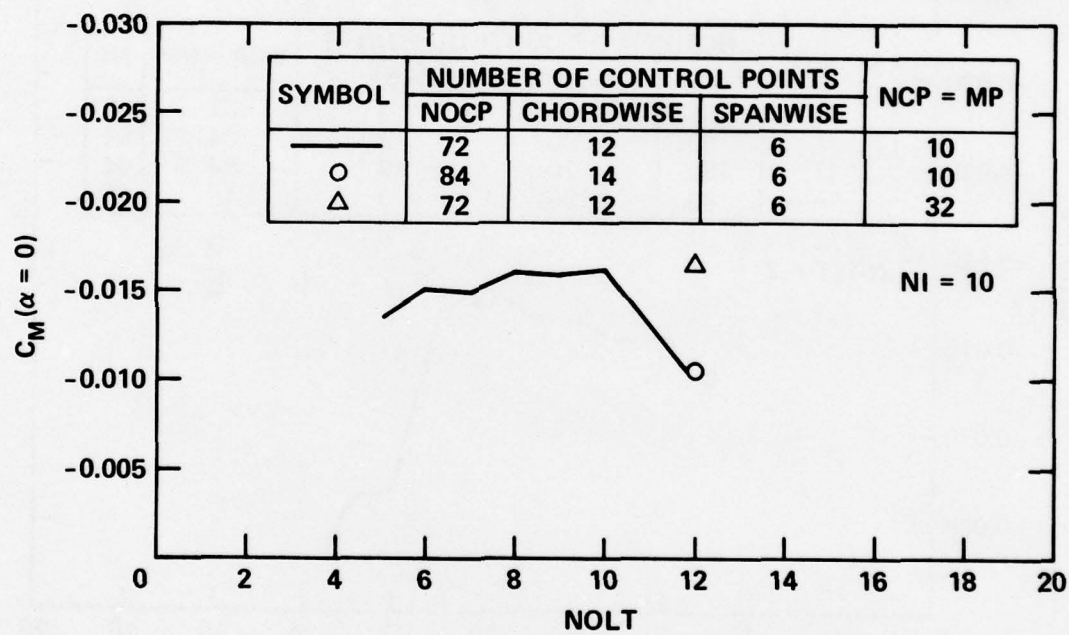


Figure 6 - The Effect of the Number of Chordwise Integration Steps NCP and MP on the Steady Moment Coefficient  $C_M(\alpha = 0)$  for a Planar Rectangular AR = 10 Hydrofoil at Infinite Depth

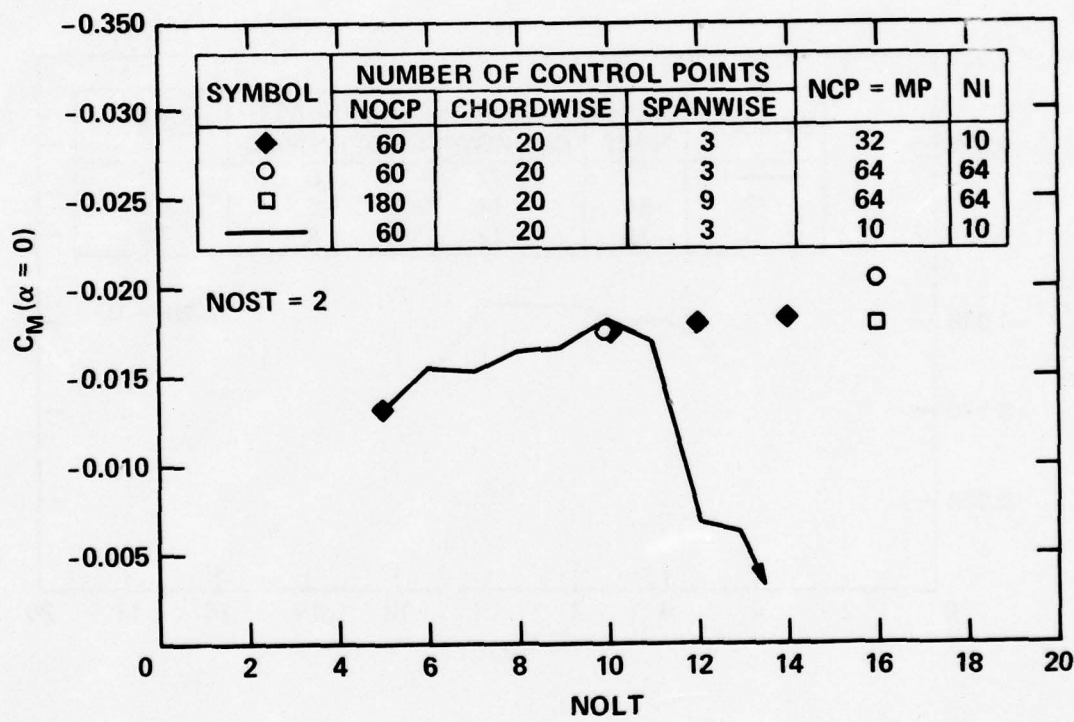


Figure 7 - The Effect of the Number of Integration Steps NCP, MP, and NI and Control Points NOCP on the Steady Moment Coefficient  $C_M(\alpha = 0)$  for a Planar Rectangular AR = 10 Hydrofoil at Infinite Depth

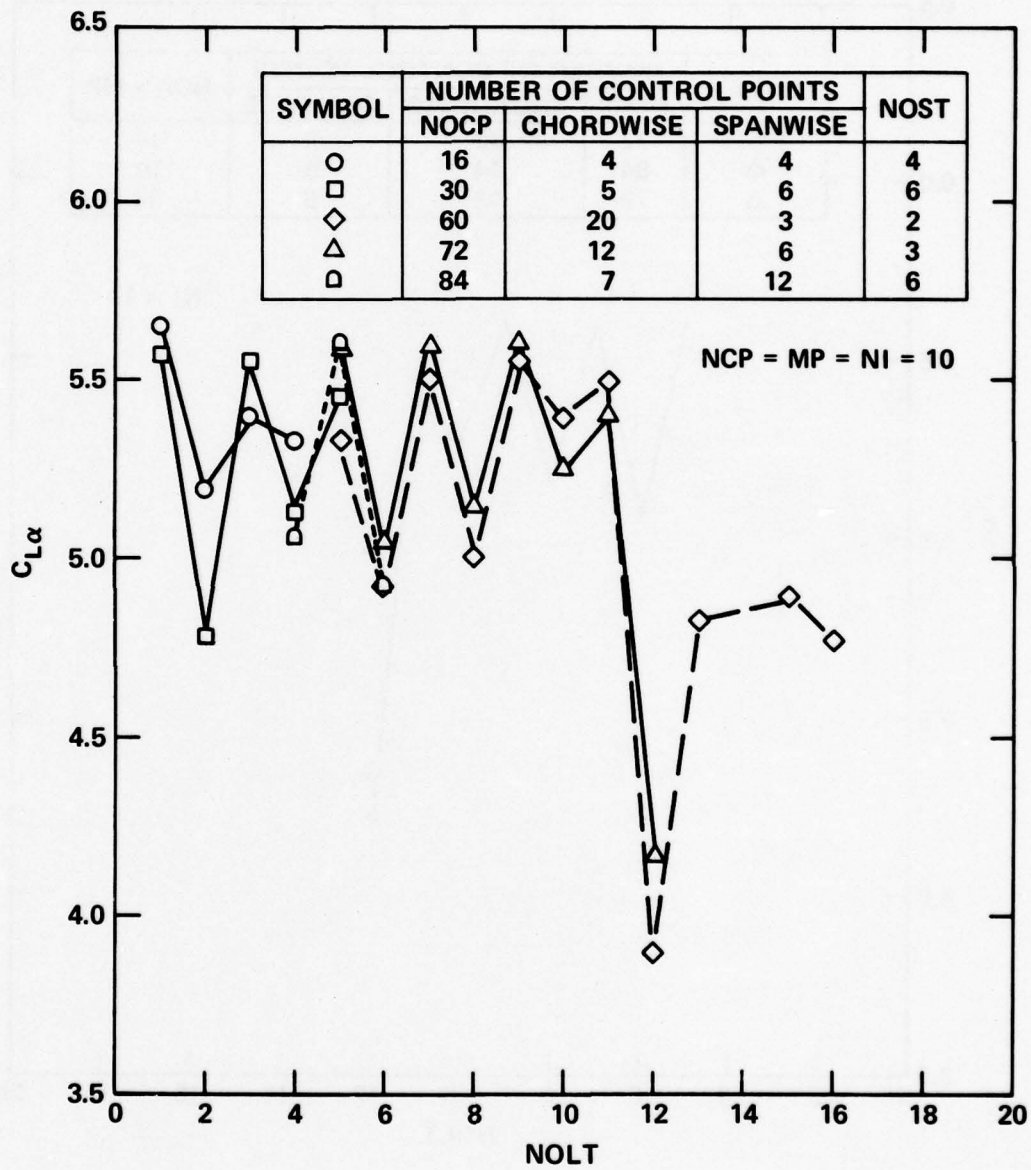


Figure 8 - The Steady Lift Coefficient Slope  $C_{L\alpha}$  as a Function of the Number of Chordwise Modes NOLT for a Planar Rectangular AR = 10 Hydrofoil at Infinite Depth

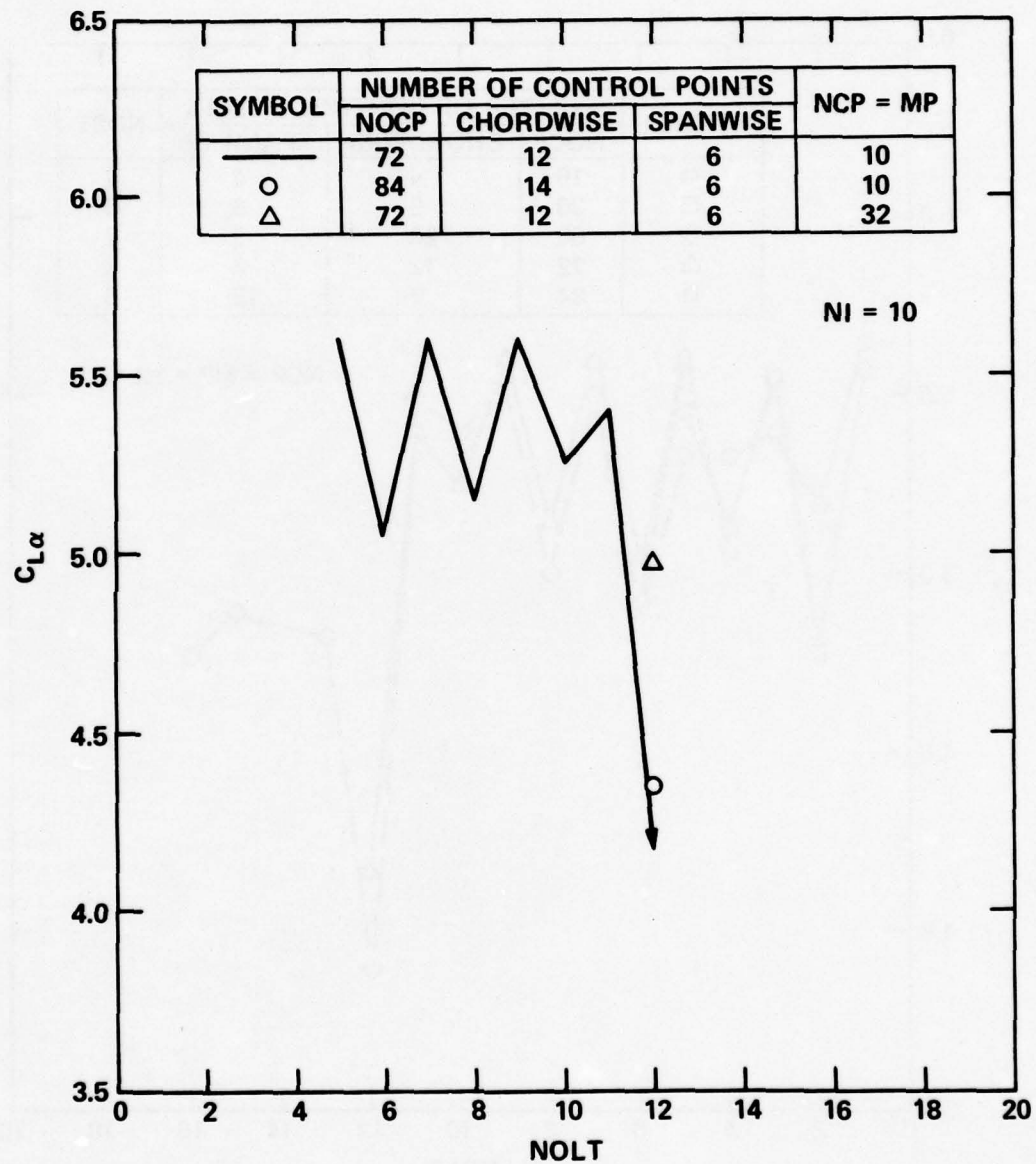


Figure 9 - The Effect of the Number of Chordwise Integration Steps NCP and MP on the Steady Lift Coefficient Slope  $C_{L\alpha}$  for a Planar Rectangular AR = 10 Hydrofoil at Infinite Depth

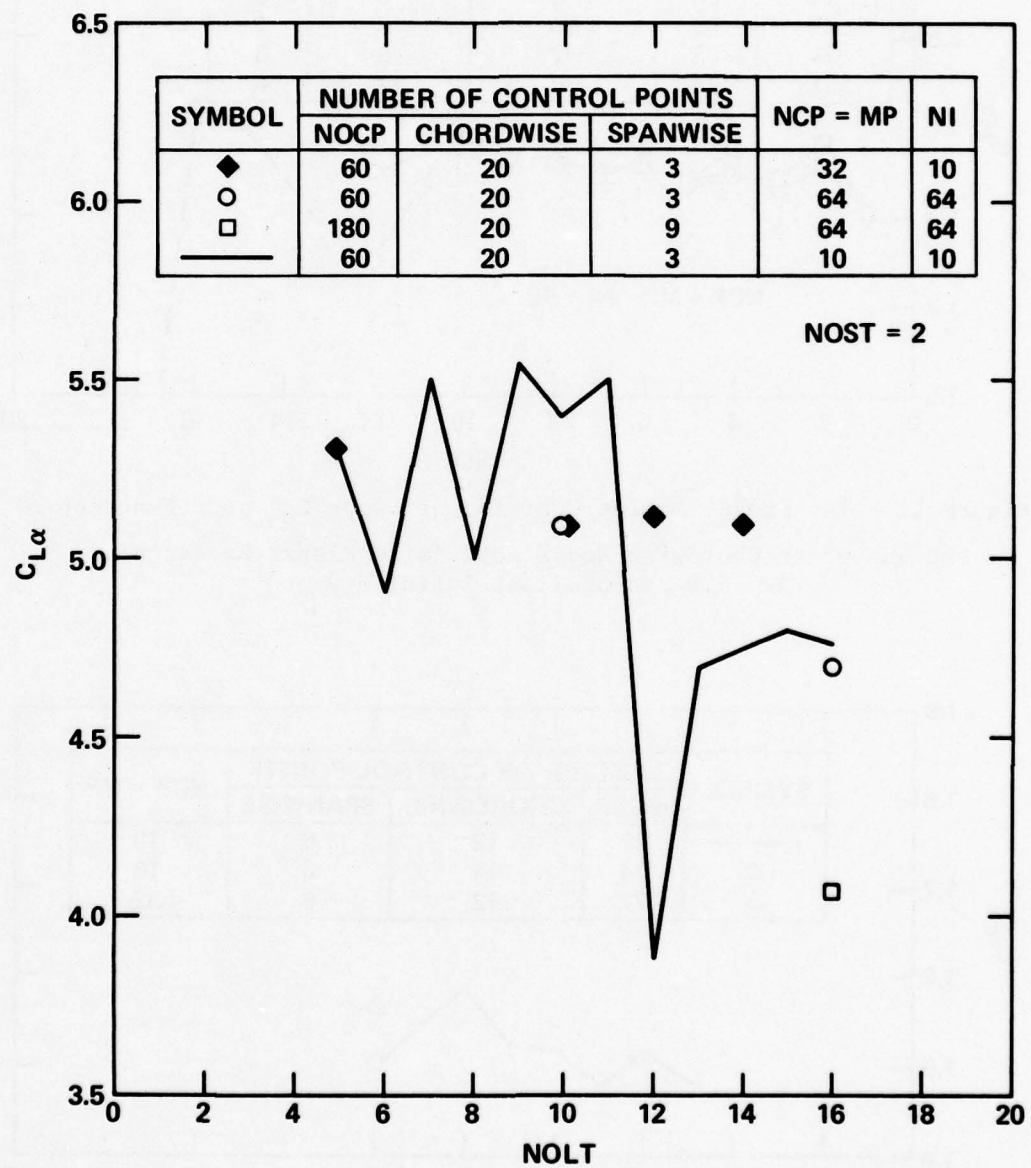


Figure 10 - The Effect of the Number of Integration Steps NCP, MP, and NI and Control Points NOCP on the Steady Lift Coefficient Slope  $C_{L\alpha}$  for a Planar Rectangular AR = 10 Hydrofoil at Infinite Depth

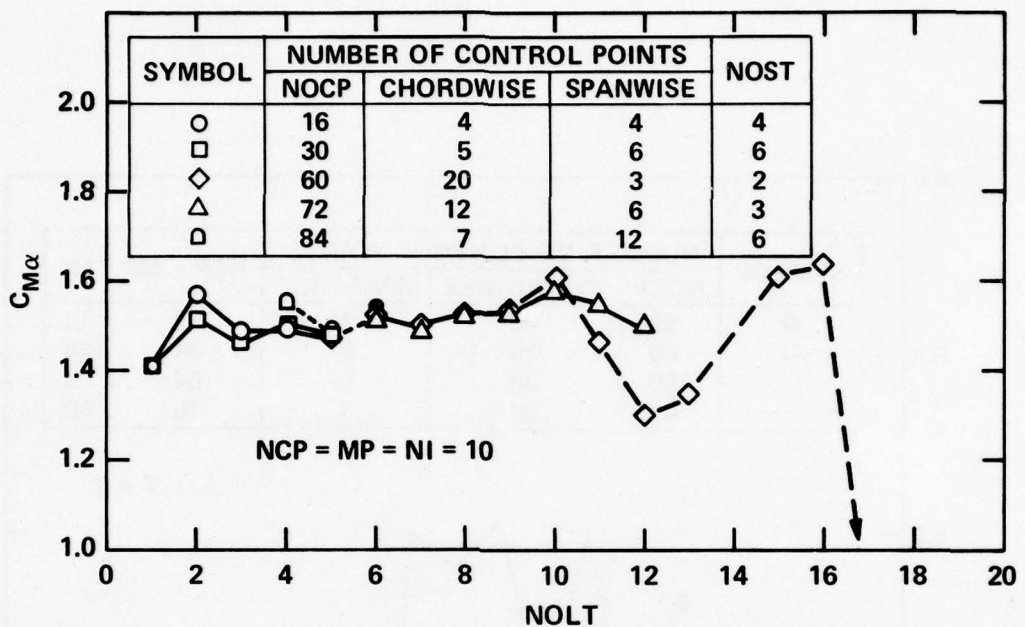


Figure 11 - The Steady Moment Coefficient Slope  $C_{M\alpha}$  as a Function of the Number of Chordwise Modes NOLT for a Planar Rectangular AR = 10 Hydrofoil at Infinite Depth

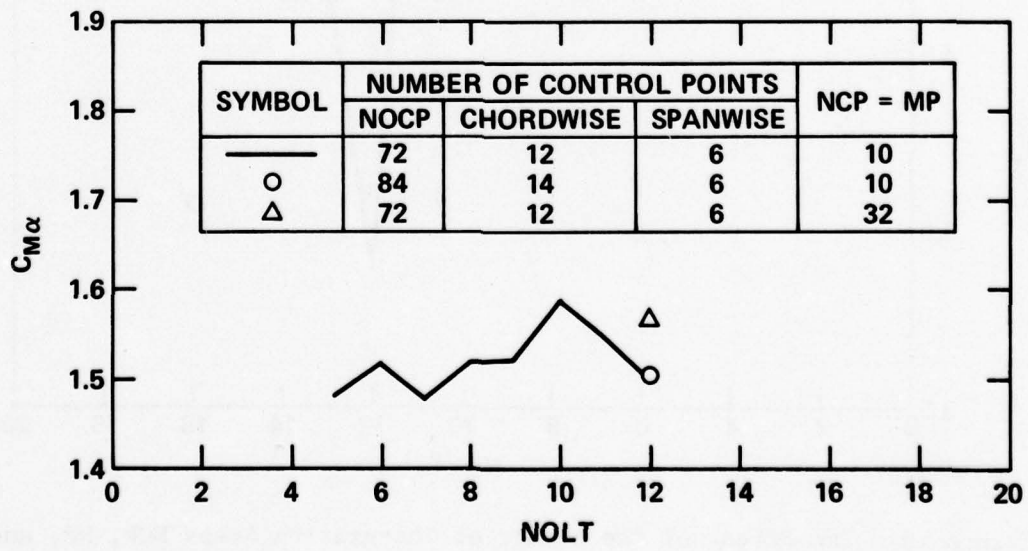


Figure 12 - The Effect of the Number of Chordwise Integration Steps NCP and MP on the Steady Moment Coefficient Slope  $C_{M\alpha}$  for a Planar Rectangular AR = 10 Hydrofoil at Infinite Depth

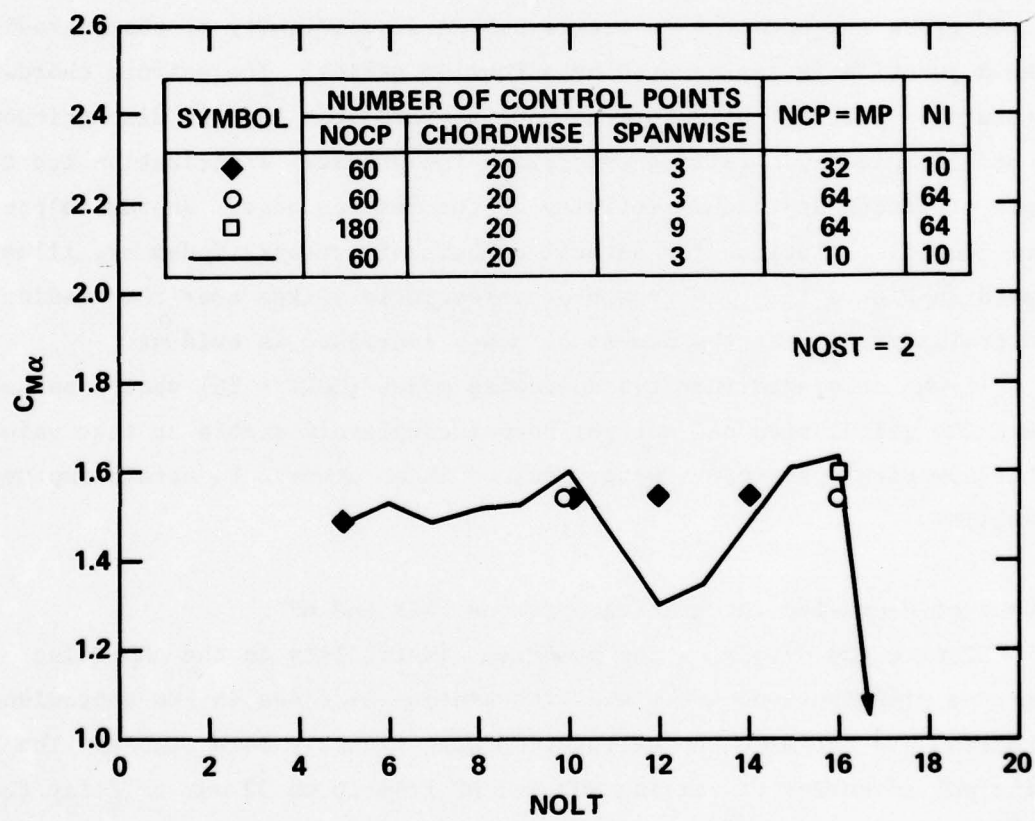


Figure 13 - The Effect of the Number of Integration Steps NCP, MP, and NI and Control Points NOCP on the Steady Moment Coefficient Slope  $C_{M\alpha}$  for a Planar Rectangular AR = 10 Hydrofoil at Infinite Depth

see Figures 8 through 10. These differences are attributed to the different combination of pressure modes required to represent the chordwise pressure distribution arising from the two types of downwash.

Before the calculation had become completely stable, however, the coefficients abruptly shifted away from the approaching stable values and, thereafter, exhibited gross instability. This latter instability was discovered upon examination of the calculated chordwise pressure distribution to be an occurrence of the Gibbs phenomenon. The Gibbs phenomenon refers to the gross inaccuracy that occurs near a discontinuity or sharp gradient when a function is represented by a Fourier series. The uniform chordwise pressure jump distribution of the NACA  $a = 1.0$  mean line is discontinuous at both leading and trailing edges, and the pressure distribution due to angle of attack approaches infinity at the leading edge. Chordwise pressure jump distributions for several numbers of pressure modes are illustrated in Figure 14. The growth of unrealistic spikes near the leading and trailing edges as the number of modes increases is evident.

It was concluded that ten chordwise modes ( $NOLT = 10$ ) should be used. Since the calculation had not yet become completely stable at that value, other numerical parameters were examined in an attempt to attain improved stability.

#### Number of Chordwise Integration Stations, NCP and MP

Despite the origin of the numerical instability in the chordwise pressure distribution, additional integration stations in the chordwise direction did not make the calculation significantly more stable. The principal advantage of raising NCP and MP from 10 to 32 was to delay the complete breakdown in the convergence process; this effect can be seen most clearly in Figures 4, 7, 10, and 13. The calculation continued to be unstable at  $NCP = MP = 32$ , however, as is apparent in the figures and Table 1. A further increase in NCP and MP to 64 appeared to have a stabilizing effect on the camber-induced loading (Figures 4 and 7) but a destabilizing effect on the loading slopes (Figures 10 and 13). These unsuccessful results with larger numbers of chordwise integration stations led to the selection of  $NCP = MP = 10$  as baseline values.

Figure 14 - Numerical Instability of the Chordwise Distribution of Lift at the Midspan of an AR = 10 Rectangular Hydrofoil at Infinite Depth

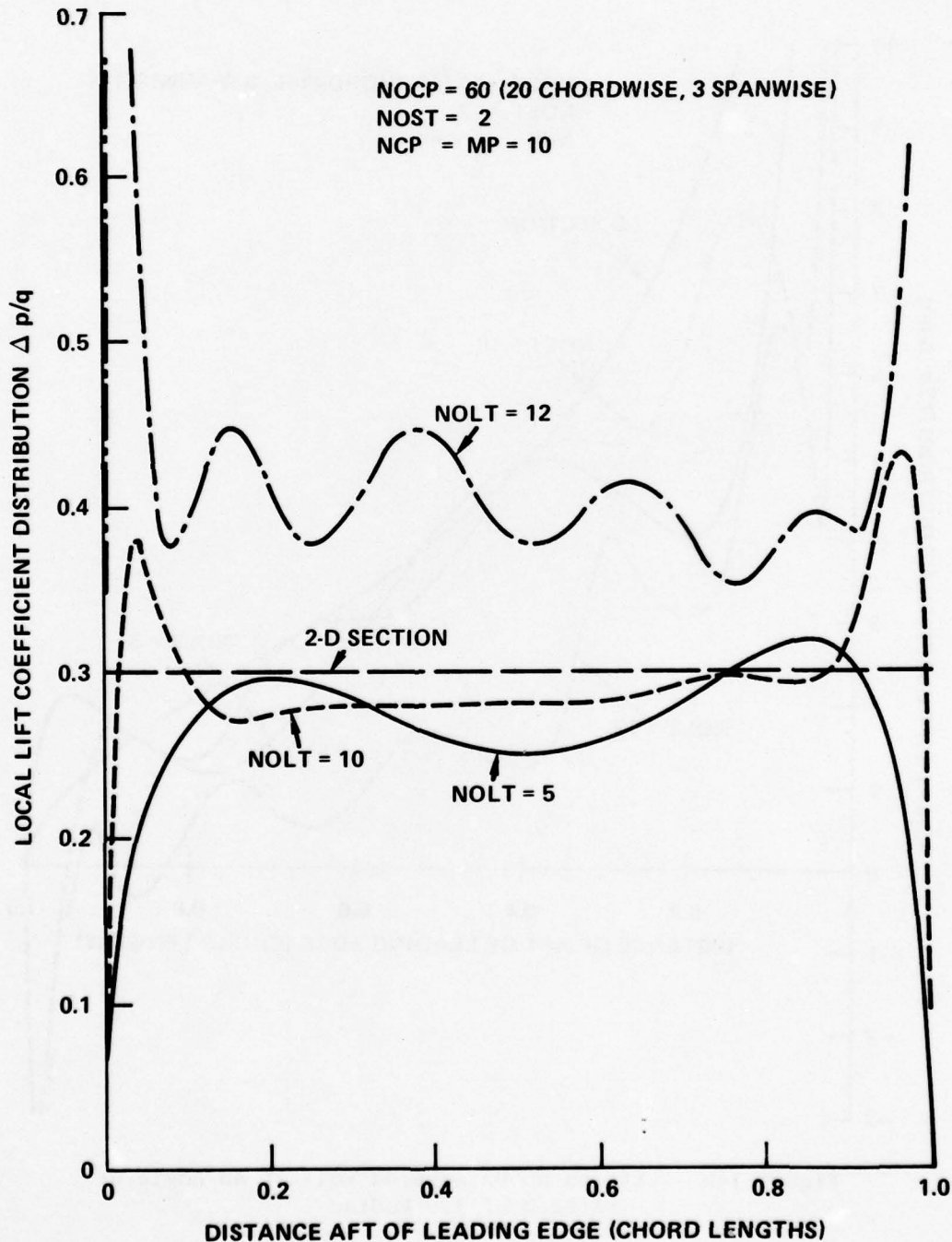


Figure 14a - Lift due to a NACA  $a = 1.0$  ( $C_l = 0.3$ ) Camber Line

Figure 14 (Continued)

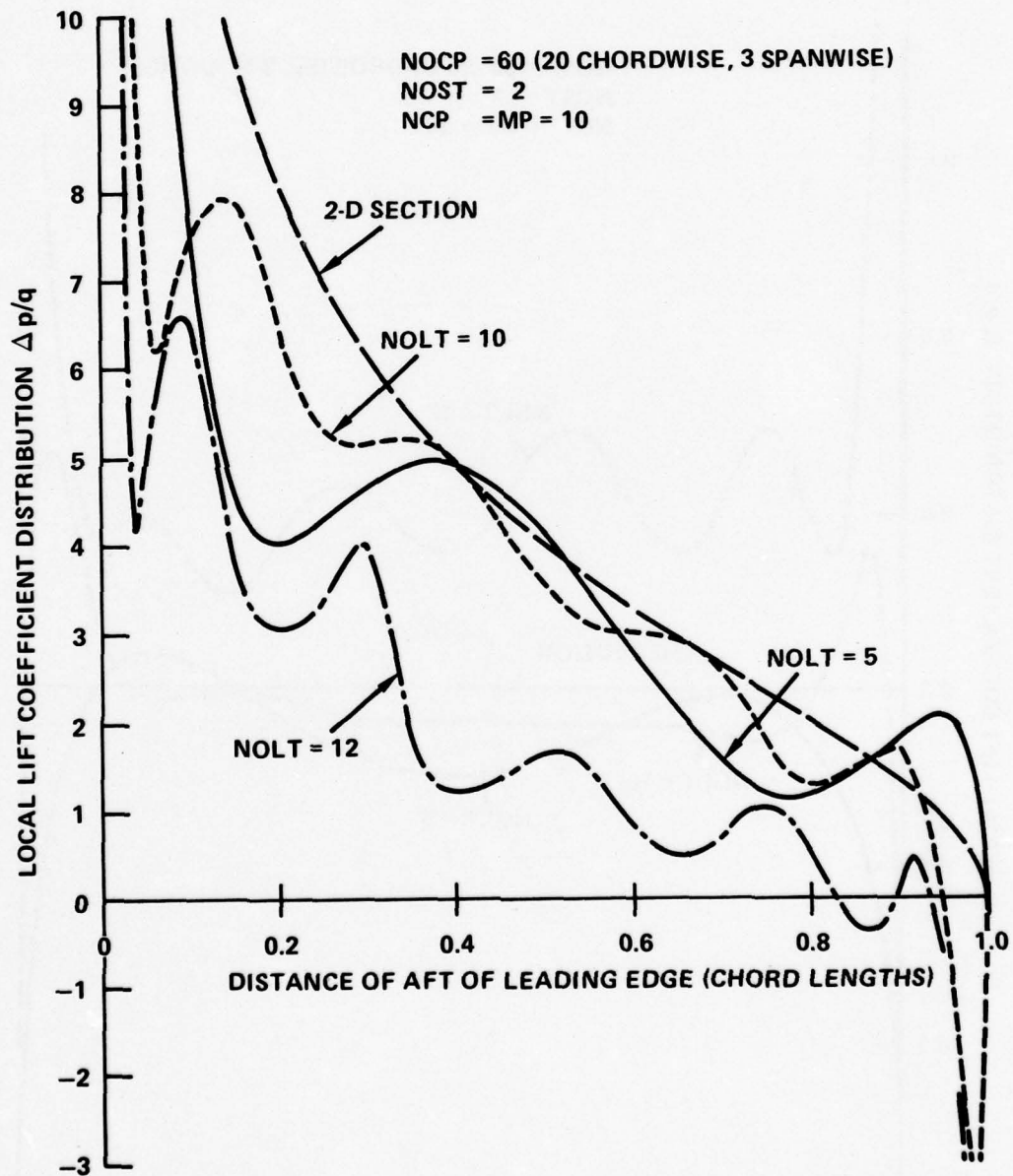


Figure 14b - Lift on an Uncambered Foil at an Angle of Attack of 1.0 Radian

TABLE 1 - NUMERICAL STABILITY OF CALCULATED LOAD COEFFICIENTS FOR A PLANAR RECTANGULAR HYDROFOIL AT INFINITE DEPTH

AR	NCP, MP	NOLT	$C_L(\alpha=0)$	$C_M(\alpha=0)$	$C_{L\alpha}(\text{rad}^{-1})$	$C_{M\alpha}(\text{rad}^{-1})$	Percent Change			
							$\Delta C_L$	$\Delta C_M$	$\Delta C_{L\alpha}$	$\Delta C_{M\alpha}$
10	10	5	0.2423	-0.01312	5.331	1.471	-	-	-	-
		6	0.2566	-0.01552	4.929	1.534	+5.9	-18.3	-7.5	+4.3
		7	0.2526	-0.01517	5.497	1.490	-1.6	+2.3	+11.5	-2.9
		8	0.2700	-0.01654	5.013	1.526	+6.9	-9.0	-8.8	+2.4
		9	0.2656	-0.01660	5.541	1.539	-1.6	-0.4	+10.5	+0.9
		10	0.2693	-0.01835	5.394	1.607	+1.4	-10.5	-2.7	+4.4
		11	0.2681	-0.01679	5.498	1.465	-0.4	+8.5	+1.9	-8.9
		12	0.3670	-0.00692	3.876	1.297	+36.9	+58.8	-29.5	-11.5
		32	10	0.2797	-0.01746	5.082	1.543	-	-	-
			11	0.2764	-0.01721	5.487	1.516	-1.2	+1.4	+8.0
			12	0.2895	-0.01805	5.112	1.537	+4.7	-4.9	-6.8
			13	0.2884	-0.01795	5.368	1.525	-0.4	+0.6	+5.0
6	10	8	9	0.2995	-0.01861	5.087	1.539	+3.8	-3.7	+5.2
			10	0.2139	-0.01904	4.234	1.250	-	-	-
			11	0.2094	-0.01885	4.581	1.238	-2.1	+1.0	+8.2
			10	0.2184	-0.02024	4.338	1.274	+4.3	-7.4	-5.3
		11	0.2150	-0.01947	4.566	1.223	-1.6	+3.8	+5.3	-4.0
1	10	8	0.08276	-0.02435	1.454	0.4944	-	-	-	-
		9	0.08196	-0.02416	1.471	0.4904	-1.0	+0.8	+1.2	-0.8
		10	0.08420	-0.02486	1.456	0.4953	+2.7	-2.9	-1.0	+1.0
		11	0.08354	-0.02462	1.470	0.4901	-0.8	+1.0	+1.0	-1.0
<p>NOTE:</p> <p>The above results were obtained with 60 control points (NOCP=60) arranged as in Table 2. Also, NOST=2 and NI=10.</p>										

#### Number of Collocation Points, NOCP

In general, a large number of collocation or control points are required in the chordwise direction, while relatively few suffice in the spanwise direction. Exploratory calculations were made using a basic array of 20 chordwise and 3 spanwise rows of control points (NOCP = 60) located as given in Table 2. Evenly distributed chordwise rows of points were removed or spanwise rows added as required.

TABLE 2 - INPUT PARAMETER BASELINE VALUES REQUIRED  
FOR APPROXIMATE NUMERICAL STABILITY OF THE  
STEADY LOADING CALCULATION

Program Variable	Input Value
NOCP	60
NOLT	10
NOST	2
NCP	10
MP	10
NI	10
XOC	0.025, 0.05, 0.1, 0.15, 0.2, 0.25, 0.3, 0.35, 0.4, 0.45, 0.55, 0.6, 0.65, 0.7, 0.75, 0.8, 0.85, 0.9, 0.95, 0.975
SOS	0.35, 0.65, 0.9

Two minimum conditions were found necessary to avoid marked instabilities in the calculation: the number of rows of control points in both chordwise and spanwise directions had to exceed the number of pressure modes in the respective directions. This result is indicated in Table 3. The effects of additional control points beyond this minimum number are shown

TABLE 3 - EFFECT OF CONTROL POINT ARRANGEMENT AND NUMBER OF PRESSURE MODES  
ON THE NUMERICAL STABILITY OF STEADY LIFT COEFFICIENT  $C_L$  ( $\alpha=0$ )  
(AR=10 rectangular foil; NACA 16-300 ( $a=1.0$ ) profile;  $h/c = \infty$ ; NCP=  
MP=32; NI=10)

Number of Control Points (NOCP)	Number of Chordwise Rows of Control Points	Number of Chordwise Pressure Modes (NOLT)	Number of Spanwise Rows of Control Points	Number of Spanwise Pressure Modes (NOST)	Lift Coefficient $C_L$
60	20	8	3	4	Unstable
60	20	8	3	2	Stable
84	7	13	12	4	Unstable
84	7	10	12	4	Unstable
84	7	7	12	4	Stable
84	7	4	12	4	Stable

in Figures 15 through 18. Adding rows of control points in the chordwise direction improved the stability of the calculation, while increasing the number of spanwise rows of control points beyond the minimum had no effect. The calculations showed that 20 chordwise and 3 spanwise rows were sufficient to eliminate the more severe instabilities in the load coefficients.

#### Number of Spanwise Pressure Modes, NOST

Two spanwise pressure modes ( $NOST = 2$ ) were sufficient for good numerical stability, as shown in Figures 19 through 22. This result occurred because the spanwise foil loading closely resembled the first, elliptically-shaped pressure mode. (The modes used for this test case were the same as those in Subroutine FUNCTN in Programs 2 and 3, Appendix C.) Note that other spanwise loading conditions may require additional spanwise pressure modes for accurate representation.

#### Number of Spanwise Integration Stations, NI

This variable was not extensively evaluated, in view of the relative insensitivity of the calculated coefficients to the number of spanwise pressure modes. Only two calculations were made with a value of NI other than 10. In these calculations, shown in Figures 4, 7, 10, and 13, NI was increased from 10 to 64 while NCP and MP were simultaneously increased from 32 to 64. Since the results did not change noticeably, it was concluded that 10 spanwise integration stations ( $NI = 10$ ) are adequate.

#### Effect of Foil Aspect Ratio

The stability of the calculation improved as aspect ratio decreased. As derived from Table 1, calculations made at aspect ratios of 10, 6, and 1 had the following ranges of variation when the value of NOLT was increased from 10 to 11.

Aspect Ratio	Range of Change in Load Coefficients (percent)
10	0.4 to 8.9
6	1.6 to 5.3
1	0.8 to 1.0

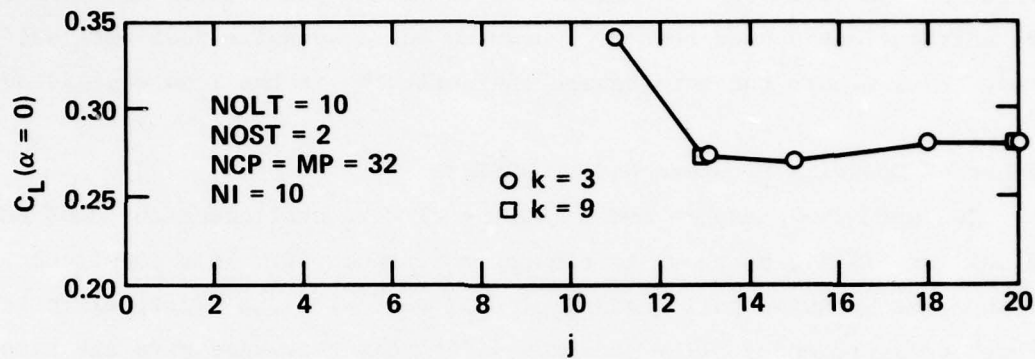


Figure 15 - The Effect of the Number of Chordwise Control Points  $j$  and Spanwise Control Points  $k$  on the Steady Lift Coefficient  $C_L(\alpha = 0)$  for a Planar Rectangular AR = 10 Hydrofoil at Infinite Depth

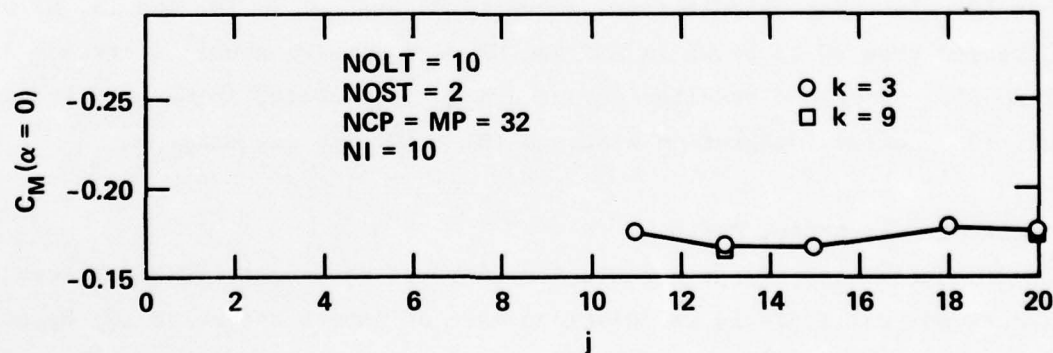


Figure 16 - The Effect of the Number of Chordwise Control Points  $j$  and Spanwise Control Points  $k$  on the Steady Moment Coefficient  $C_M(\alpha = 0)$  for a Planar Rectangular AR = 10 Hydrofoil at Infinite Depth

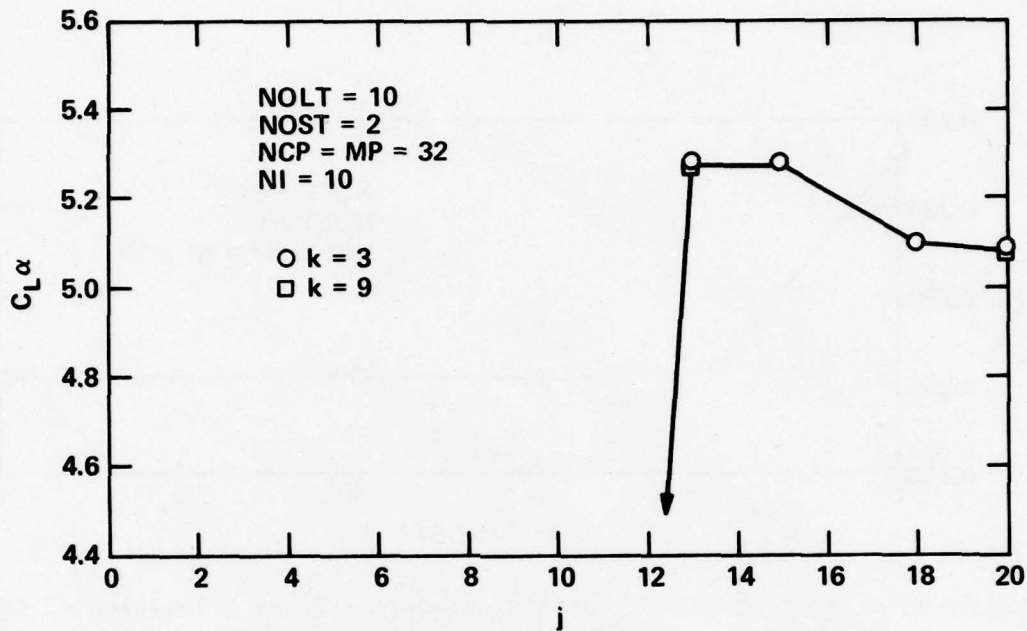


Figure 17 - The Effect of the Number of Chordwise Control Points  $j$  and Spanwise Control Points  $k$  on the Steady Lift Coefficient Slope  $C_{L\alpha}$  for a Planar Rectangular AR = 10 Hydrofoil at Infinite Depth

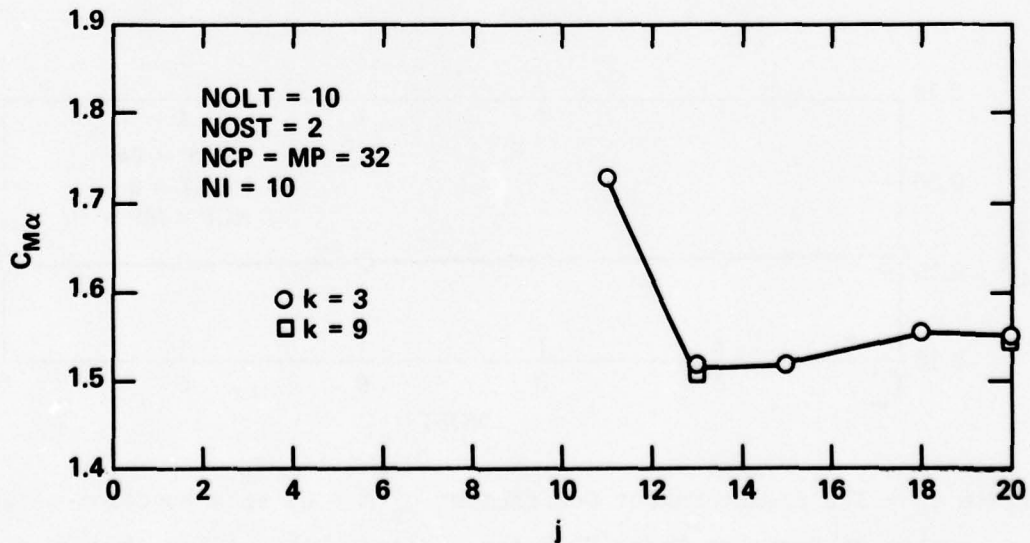


Figure 18 - The Effect of the Number of Chordwise Control Points  $j$  and Spanwise Control Points  $k$  on the Steady Moment Coefficient Slope  $C_{M\alpha}$  for a Planar Rectangular AR = 10 Hydrofoil at Infinite Depth

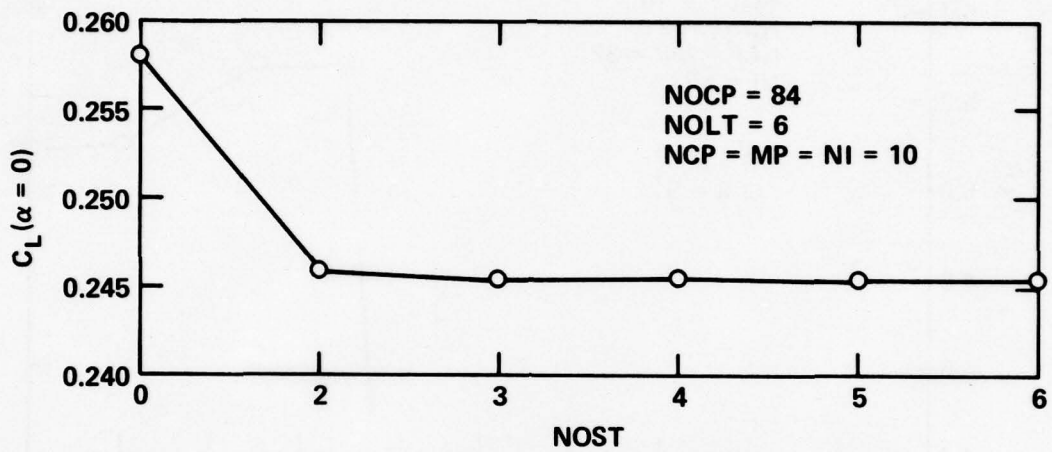


Figure 19 - The Steady Lift Coefficient  $C_L(\alpha = 0)$  as a Function of the Number of Spanwise Modes  $NOST$  for a Planar Rectangular  $AR = 10$  Hydrofoil at Infinite Depth

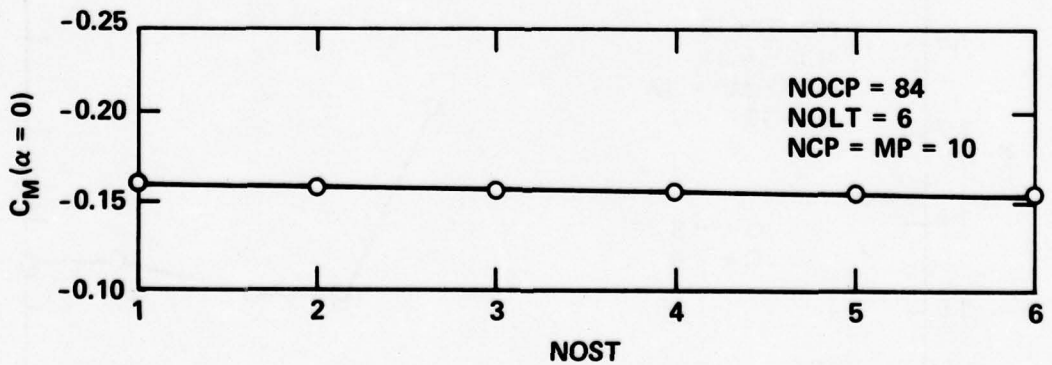


Figure 20 - The Steady Moment Coefficient  $C_M(\alpha = 0)$  as a Function of the Number of Spanwise Modes  $NOST$  for a Planar Rectangular  $AR = 10$  Hydrofoil at Infinite Depth

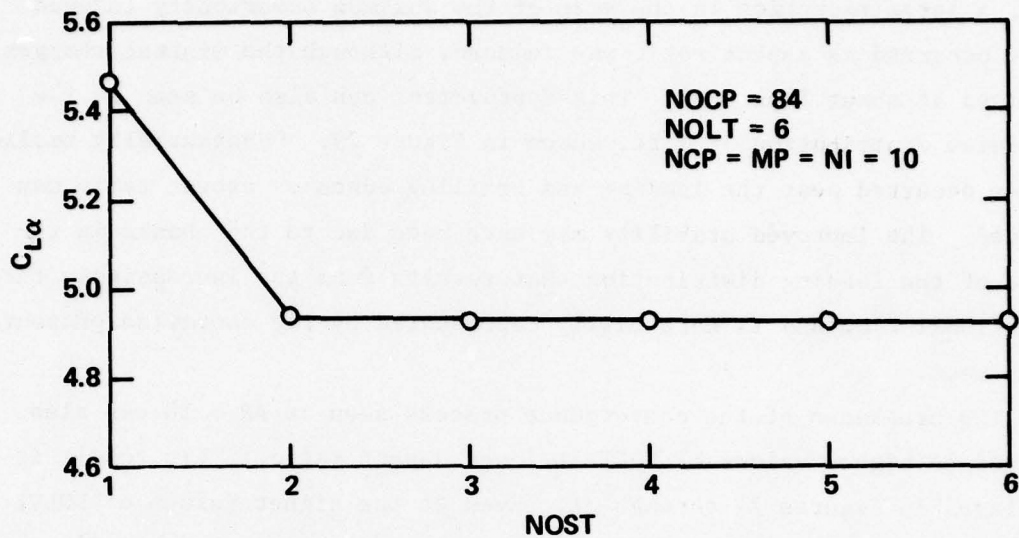


Figure 21 - The Steady Lift Coefficient Slope  $C_{L\alpha}$  as a Function of the Number of Spanwise Modes NOST for a Planar Rectangular AR = 10 Hydrofoil at Infinite Depth

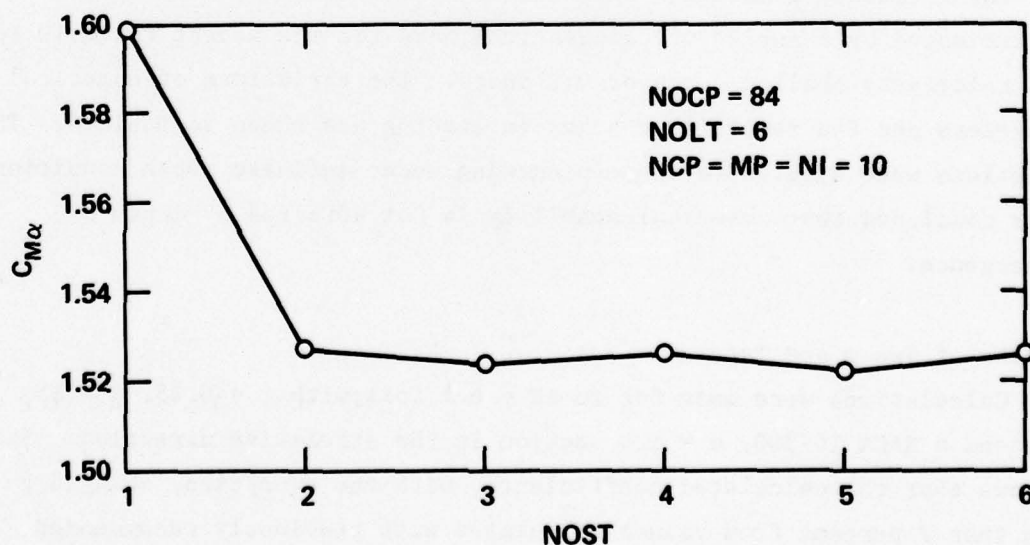


Figure 22 - The Steady Moment Coefficient Slope  $C_{M\alpha}$  as a Function of the Number of Spanwise Modes NOST for a Planar Rectangular AR = 10 Hydrofoil at Infinite Depth

Thus, a large reduction in the size of the maximum numerically induced shift occurred as aspect ratio was reduced, although the minimum changes remained at about 1 percent. This improvement can also be seen in the chordwise distribution of lift, shown in Figure 23. Substantially smaller spikes occurred near the leading and trailing edges as aspect ratio was reduced. The improved stability may have been due to the change in the shape of the loading distribution that results from the increasingly three-dimensional flow and is more easily represented by the chordwise pressure modes used.

The breakdown of the convergence process seen at AR = 10 was also delayed to higher values of NOLT at lower aspect ratio. This result is displayed in Figures 24 through 31. Even at the higher values of NOLT, however, the calculated coefficients continued to vary substantially rather than become stable. Since the sensitivity to numerical parameters decreased with decreasing aspect ratio, it was concluded that the previously selected parameter values were adequate for aspect ratios of less than 10.

#### Effect of Finite Depth

The influence of shallow submergence on the numerical representation was estimated by a series of calculations made for the aspect ratio 10 foil at a relatively shallow depth of 0.2 chord. The variations of numerical parameters and the resulting changes in loading are shown in Table 4. The variations were similar to those occurring under infinite depth conditions. It is concluded that numerical stability is not affected by depth of submergence.

#### Effects of Sweep and Taper

Calculations were made for an AR = 6.1 foil with  $\tau = 0.25$ ,  $\Lambda = 15$  deg, and a NACA 16-300,  $a = 1.0$  section in the streamwise direction. Table 5 shows that the calculated coefficients, with one exception, changed by less than 7 percent from values calculated with previously recommended parameter values, as the numerical parameters varied. However, the exception,  $C_{M\alpha}$ , oscillated by up to 27 percent as NOLT varied. This large

Figure 23 - The Effect of Aspect Ratio on the Chordwise Distribution of Lift at the Midspan of a Rectangular Hydrofoil at Infinite Depth

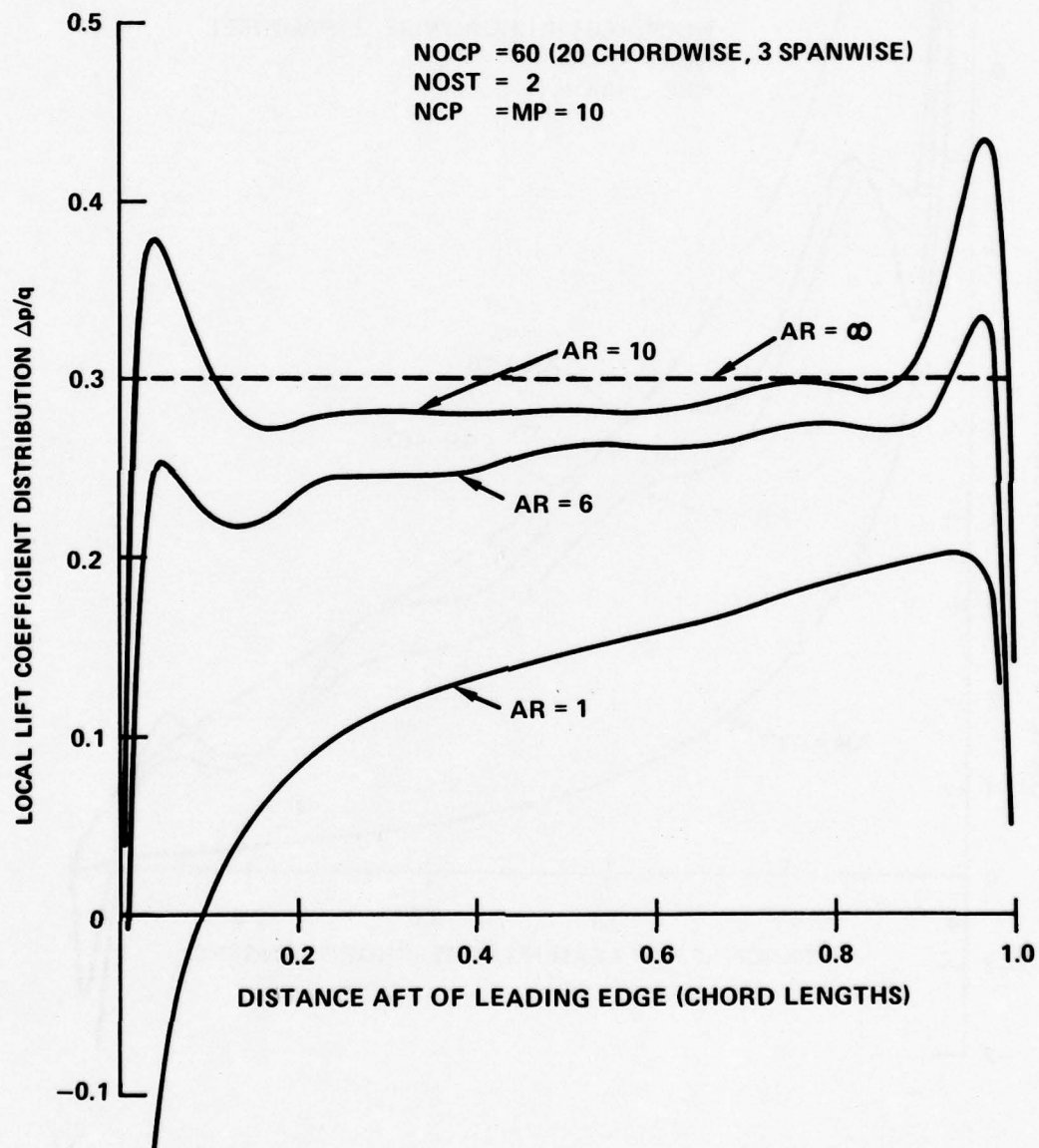


Figure 23a - Lift due to a NACA  $a = 1.0$  ( $C_l = 0.3$ ) Camber Line

Figure 23 (Continued)

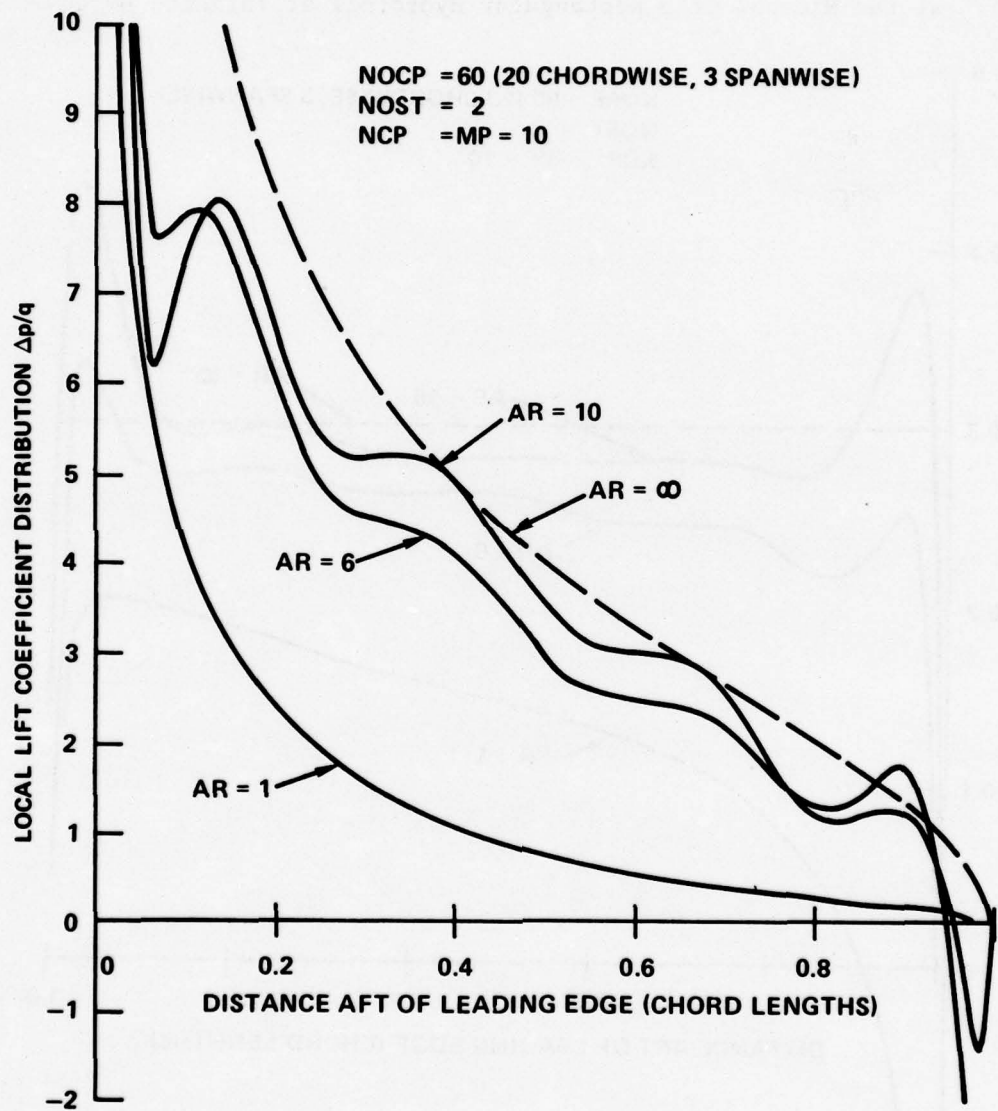


Figure 23b - Lift on an Uncambered Foil at an Angle of Attack of 1.0 Radian

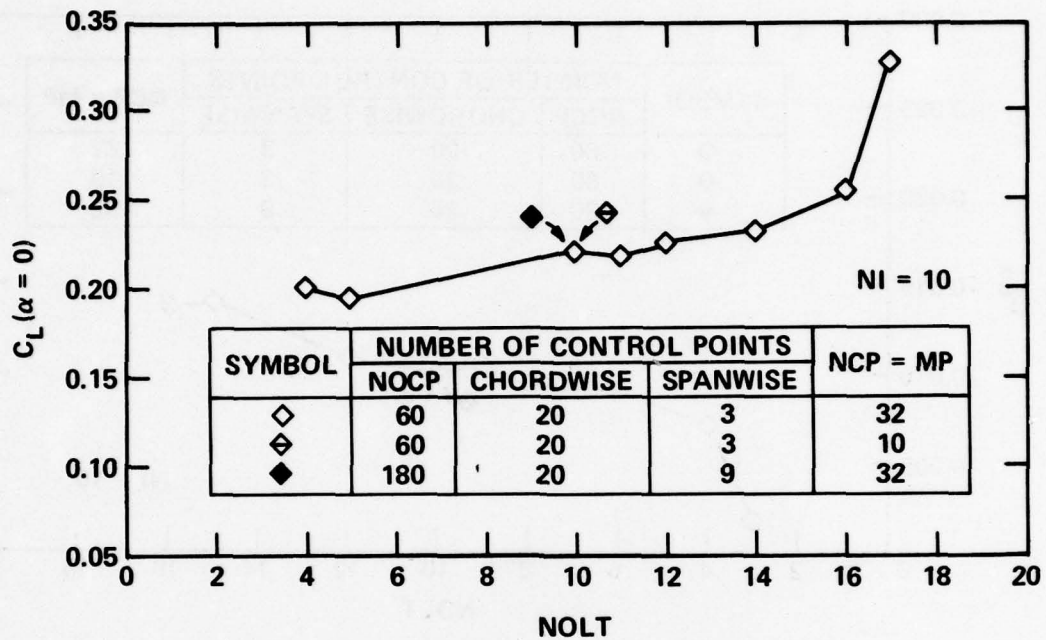


Figure 24 - The Steady Lift Coefficient  $C_L(\alpha = 0)$  as a Function of the Number of Chordwise Modes  $NOLT$  for a Rectangular  $AR = 6$  Hydrofoil at Infinite Depth

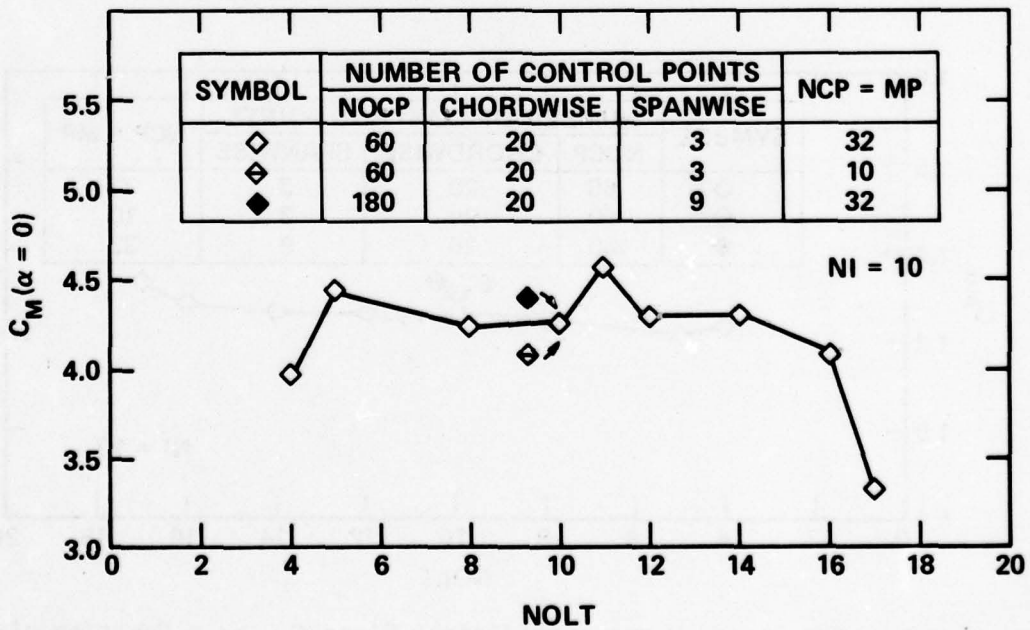


Figure 25 - The Steady Moment Coefficient  $C_M(\alpha = 0)$  as a Function of the Number of Chordwise Modes  $NOLT$  for a Rectangular  $AR = 6$  Hydrofoil at Infinite Depth

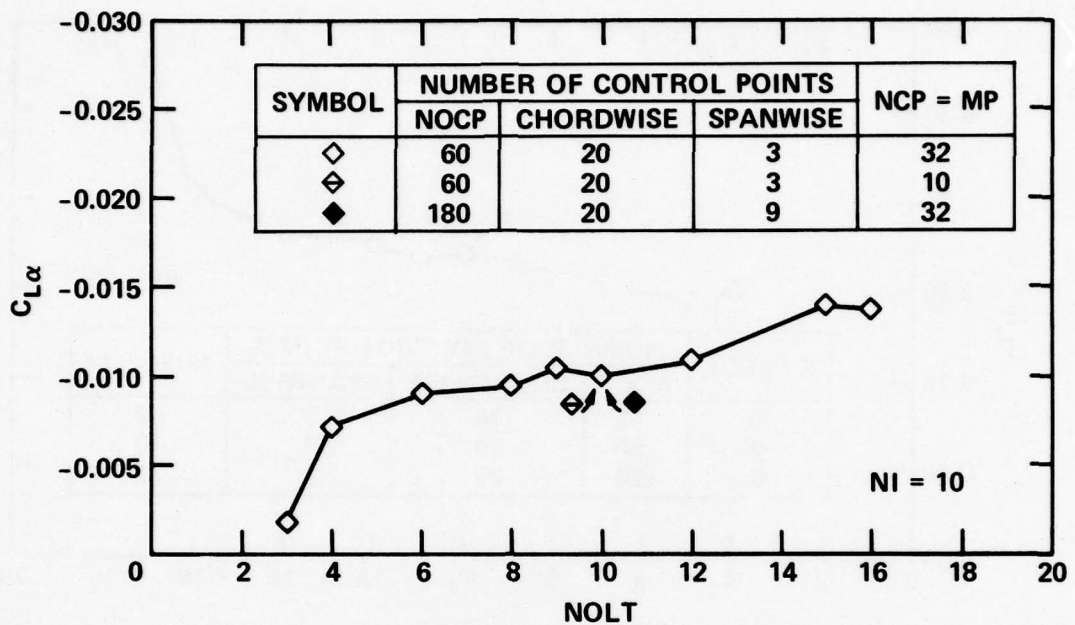


Figure 26 - The Steady Lift Coefficient Slope  $C_{L\alpha}$  as a Function of the Number of Chordwise Modes  $NOLT$  for a Rectangular AR = 6 Hydrofoil at Infinite Depth

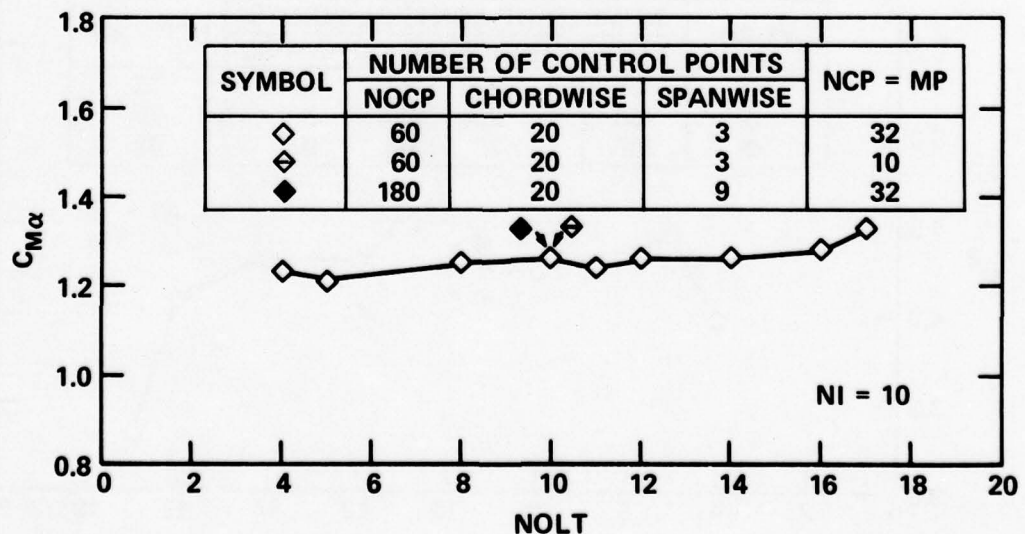


Figure 27 - The Steady Moment Coefficient Slope  $C_{M\alpha}$  as a Function of the Number of Chordwise Modes  $NOLT$  for a Rectangular AR = 6 Hydrofoil at Infinite Depth

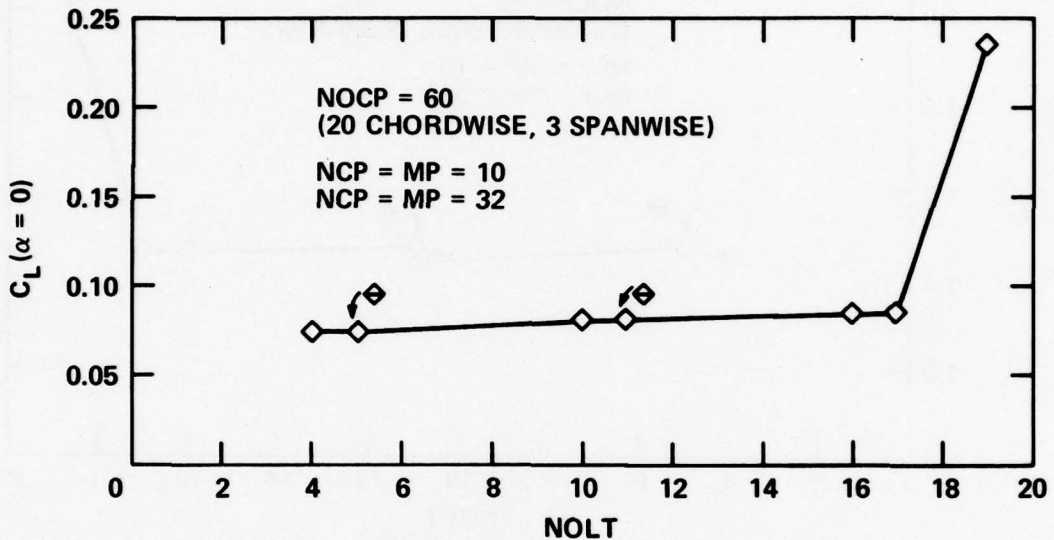


Figure 28 - The Steady Lift Coefficient  $C_L(\alpha = 0)$  as a Function of the Number of Chordwise Modes  $NOLT$  for a Rectangular  $AR = 1$  Hydrofoil at Infinite Depth

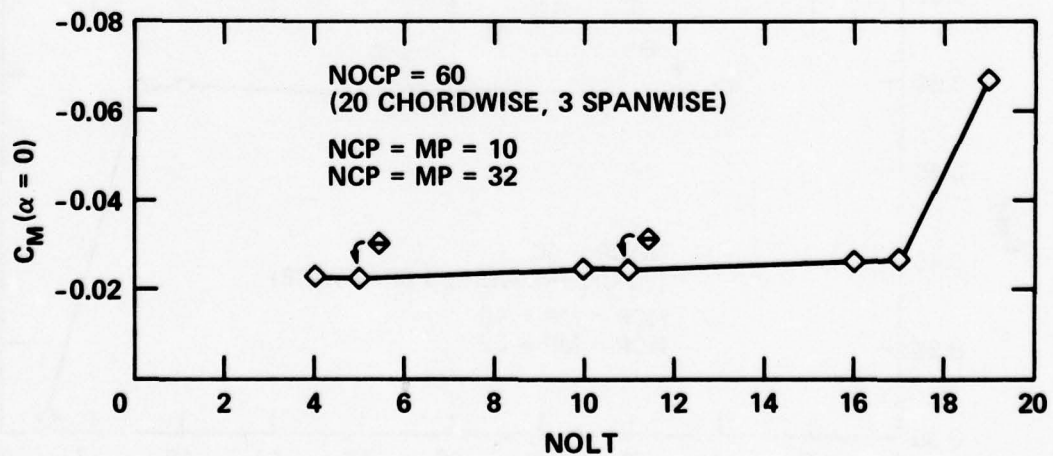


Figure 29 - The Steady Moment Coefficient  $C_M(\alpha = 0)$  as a Function of the Number of Chordwise Modes  $NOLT$  for a Rectangular  $AR = 1$  Hydrofoil at Infinite Depth

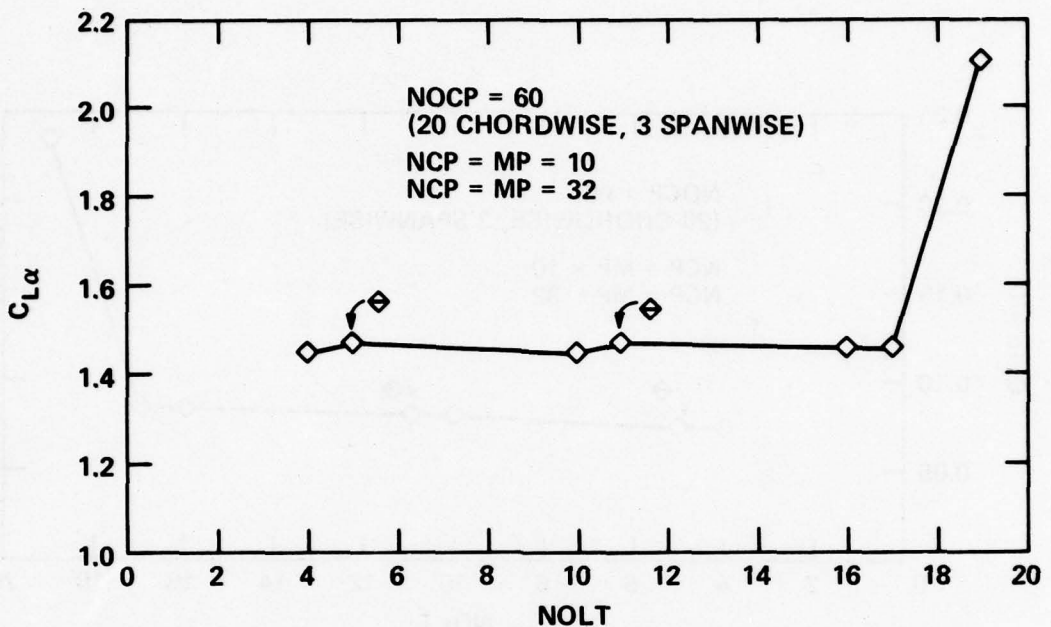


Figure 30 - The Steady Lift Coefficient Slope  $C_{L\alpha}$  as a Function of the Number of Chordwise Modes  $N_{OLT}$  for a Rectangular AR = 1 Hydrofoil at Infinite Depth

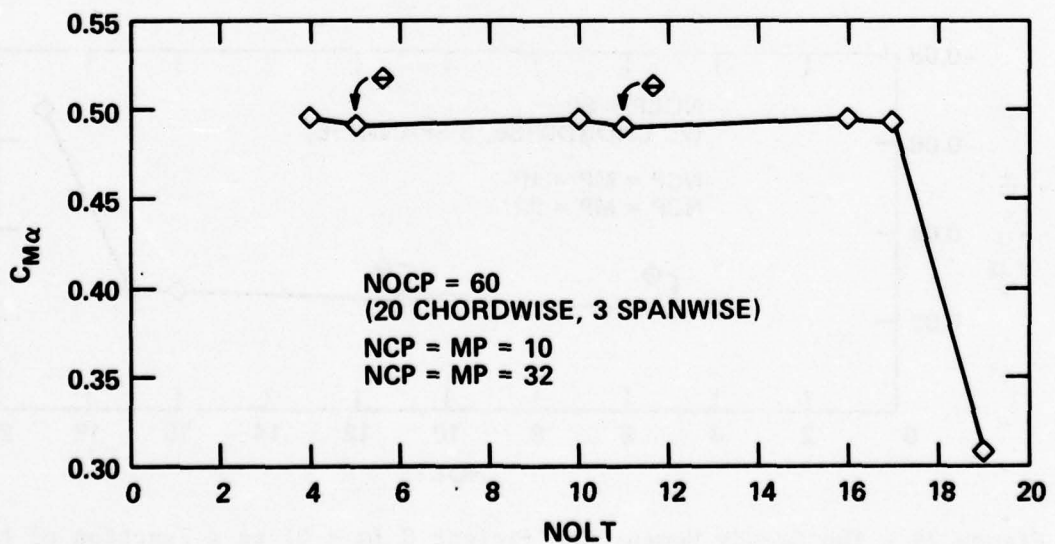


Figure 31 - The Steady Moment Coefficient Slope  $C_{M\alpha}$  as a Function of the Number of Chordwise Modes  $N_{OLT}$  for a Rectangular AR = 1 Hydrofoil at Infinite Depth

TABLE 4 - EFFECT OF FOIL SUBMERGENCE ON THE NUMERICAL  
STABILITY OF THE STEADY LOADING CALCULATION

(AR=10 rectangular foil; NACA 16-300 ( $a=1.0$ ) profile;  $h/c = 0.2$ )

Parameter	Baseline Value	New Value	Change in Load Coefficient (Percent)			
			$C_L(\alpha=0)$	$C_{L\alpha}$	$C_M(\alpha=0)$	$C_{M\alpha}$
NOCP	60	80	+3.3	+5.3	-6.7	+2.5
NOLT	10	11	-1.0	+3.4	+6.1	-6.7
NOST	2*	3*	-1.3	-1.7	-1.1	0.0
NCP=MP	10	32	+3.2	-4.8	+4.3	-3.3
	10	64	+3.2	-4.8	+4.3	-3.3
NI	10	32	0.0	0.0	0.0	0.0

\*NOCP=80, with four spanwise rows of control points.

TABLE 5 - EFFECT OF SWEEP AND TAPER ON THE NUMERICAL  
STABILITY OF THE STEADY LOADING CALCULATION

(AR=6.1;  $\tau = 0.25$ ;  $\Lambda = 15$  deg; NACA 16-300 ( $a=1.0$ ) streamwise profile;  $h/c' = \infty$ )

Parameter	Baseline Value	New Value	Change in Load Coefficient (Percent)			
			$C_L(\alpha=0)$	$C_{L\alpha}$	$C_M(\alpha=0)$	$C_{M\alpha}$
NOCP	60	80	+2.9	+3.3	-5.8	+6.7
NOLT	10	11	-1.9	-6.9	+2.9	-27
NOST	2*	3*	0.0	-1.4	+1.0	+5.7
NCP-MP	10	32	0.0	-1.1	+1.0	+4.7

\*NOCP=80, with four spanwise rows of control points.

variation indicated that the  $C_{M\alpha}$  calculation was not stable, and that considerable computer run time would be required to achieve stability. It is concluded that stability of the load coefficients  $C_L(\alpha = 0)$ ,  $C_{L\alpha}$ , and  $C_M(\alpha = 0)$  is not affected by sweep and taper, but that the stability of  $C_{M\alpha}$  is greatly reduced.

## NUMERICAL STABILITY OF THE UNSTEADY LOADING CALCULATION

In an abbreviated numerical survey, it was found that the unsteady calculation was more sensitive than the steady calculation to the number of spanwise pressure modes used. In other respects, the calculation was similar to the steady loading calculation.

The sensitivity to spanwise pressure modes may have resulted from the choice of the model. An AR = 10 rectangular foil was used, with unsteady loading produced by foil oscillation simulating bending and torsional motion. The oscillation amplitudes were symmetrical about the midspan and varied linearly from 0 at the midspan to a maximum at the foil tips. This type of motion produced greater spanwise variation in loading than the constant camber and angle of attack used for the steady loading study. A relatively high reduced frequency of 1.97 was used to accentuate the unsteady aspects of the calculation.

Since preliminary calculations showed a sensitivity to the number of spanwise pressure modes, a baseline array of 15 chordwise and 4 spanwise rows of control points, located as given in Table 6, was used. The magnitudes and phase angles of  $C_L$  and  $C_M$  were examined for stability; camber lift produces no unsteady component.

As shown in Table 7, the calculated unsteady loading showed good stability when numerical parameters were varied from the baseline values. The requirement for 4 spanwise rows of control points is evident in Figure 32. Stability breakdown again occurred at high values of NOLT, as shown in Figure 33. Except for the rearrangement in control point location and the addition of a pressure mode in the spanwise direction, the numerical parameter values selected for the unsteady calculation were the same as for the steady calculation. The values chosen are given in Table 6.

## SUMMARY OF RESIDUAL INSTABILITY

Both steady and unsteady loading calculations failed to achieve a value which was stable to several significant figures. Estimating residual instability with a high degree of confidence is not possible, because most

TABLE 6 - INPUT PARAMETER BASELINE VALUES REQUIRED  
FOR APPROXIMATE NUMERICAL STABILITY OF  
THE UNSTEADY LOADING CALCULATION

Program Variable	Input Value
NOCP	60
NOLT	10
NOST	3
NCP	10
MP	10
NI	10
XOC	0.025, 0.05, 0.1, 0.15, 0.25, 0.3, 0.4, 0.45, 0.55, 0.6, 0.7, 0.75, 0.85, 0.95, 0.975
SOS	0.1, 0.35, 0.65, 0.9

TABLE 7 - NUMERICAL STABILITY OF THE UNSTEADY LOADING CALCULATION  
(AR=10 rectangular foil; uncambered profile;  $h/c = \infty$ ; bending and  
torsional oscillation)

Parameter	Baseline Value	New Value	Oscillation Mode	Change in Load Coefficient			
				$C_L$ (percent)	$\phi$ (deg)	$C_M$ (percent)	$\phi$ (deg)
NOCP	60	80	Bending	0	0	0	0
	60	80	Torsion	0	+1	-1	0
NOST	3*	4*	Bending	0	0	+1	0
NCP=MP	10	32	Bending	+1	+1	+4	0
	10	32	Torsion	0	+1	+1	+1
NI	10	32	Bending	0	0	0	0
	10	32	Torsion	0	0	0	0

\*NOCP=75, with 5 spanwise rows of control points.

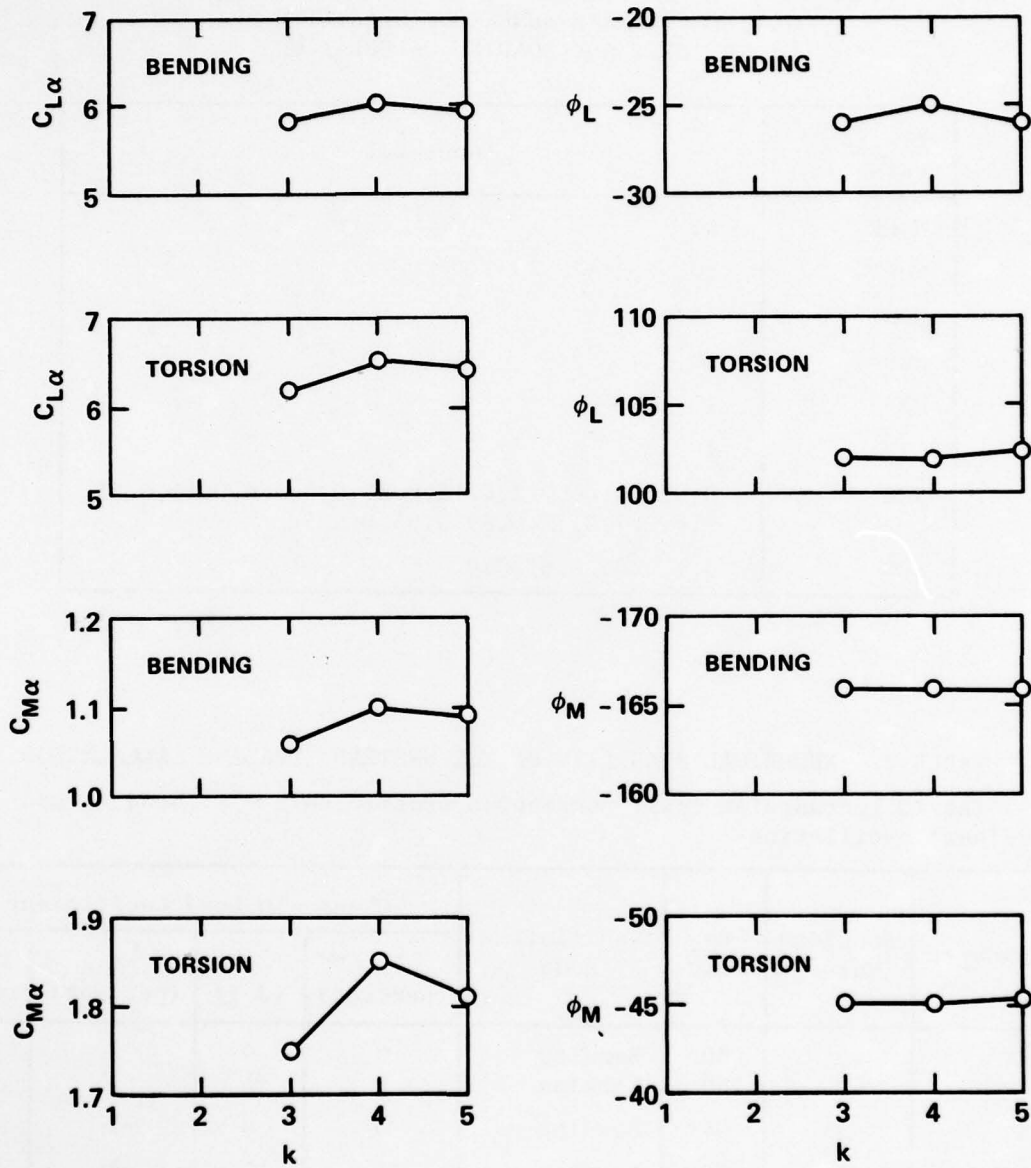


Figure 32 - The Effect of the Number of Spanwise Control Points  $k$  on the Lift Coefficient Magnitude  $|C_{L\alpha}|$  and Phase  $\phi_L$  and Moment Coefficient Magnitude  $|C_{M\alpha}|$  and Phase  $\phi_M$  for Bending and Torsion Oscillations for a Rectangular AR = 10 Hydrofoil at Infinite Depth with  $k = 1.97$  (Number of Chordwise Control Points = 15; NOCP = 15 \*  $k$ )

Figure 33 - The Effect of the Number of Chordwise Modes NOLT on the Unsteady Loading due to Bending and Torsional Oscillations of a Rectangular AR = 10 Hydrofoil at Infinite Depth with  $k = 1.97$   
 (NOCP = 60; 15 Chordwise, 4 Spanwise)

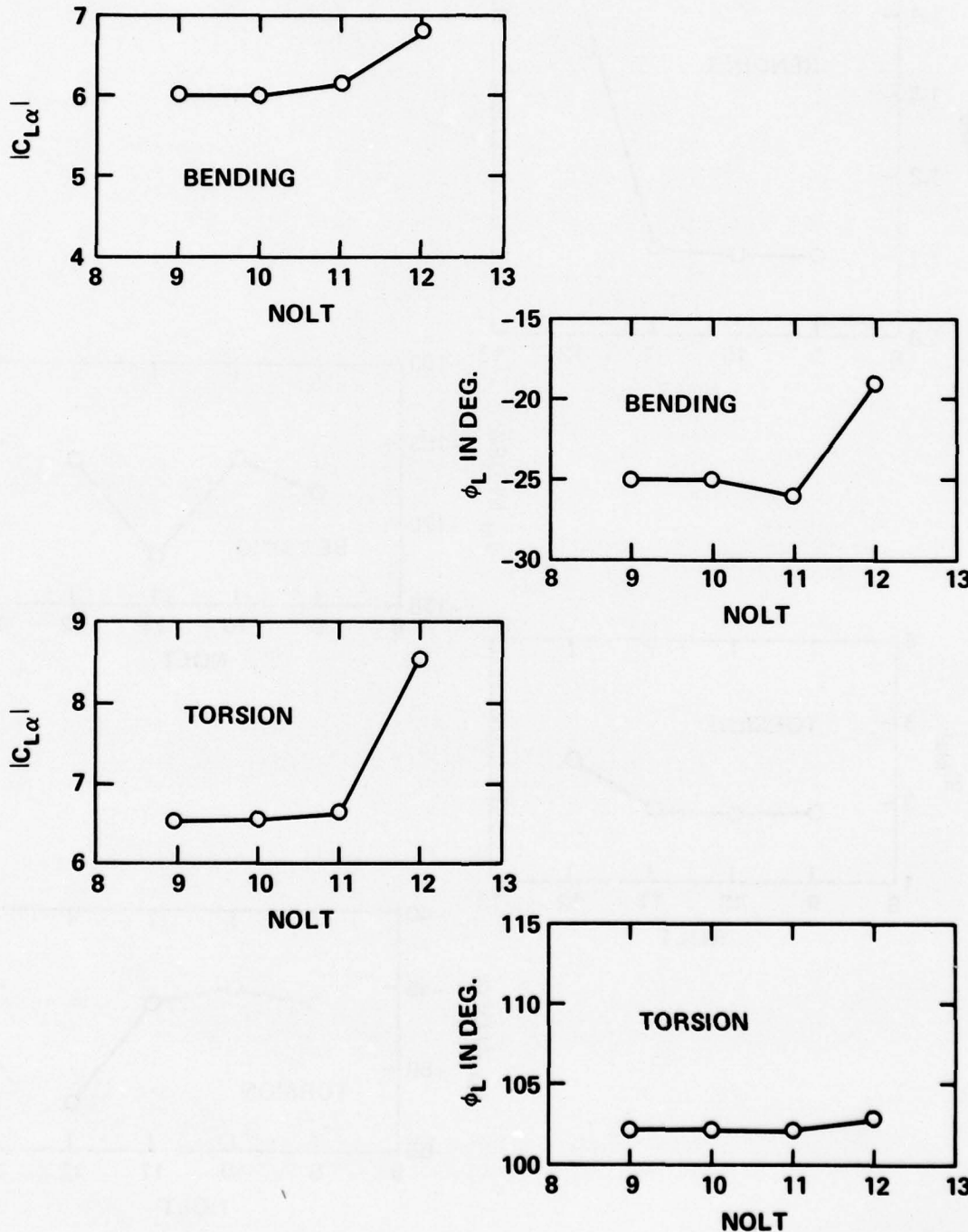


Figure 33a - Lift Coefficient Magnitude  $|C_{L\alpha}|$  and Phase Angle  $\phi_L$

Figure 33 (Continued)

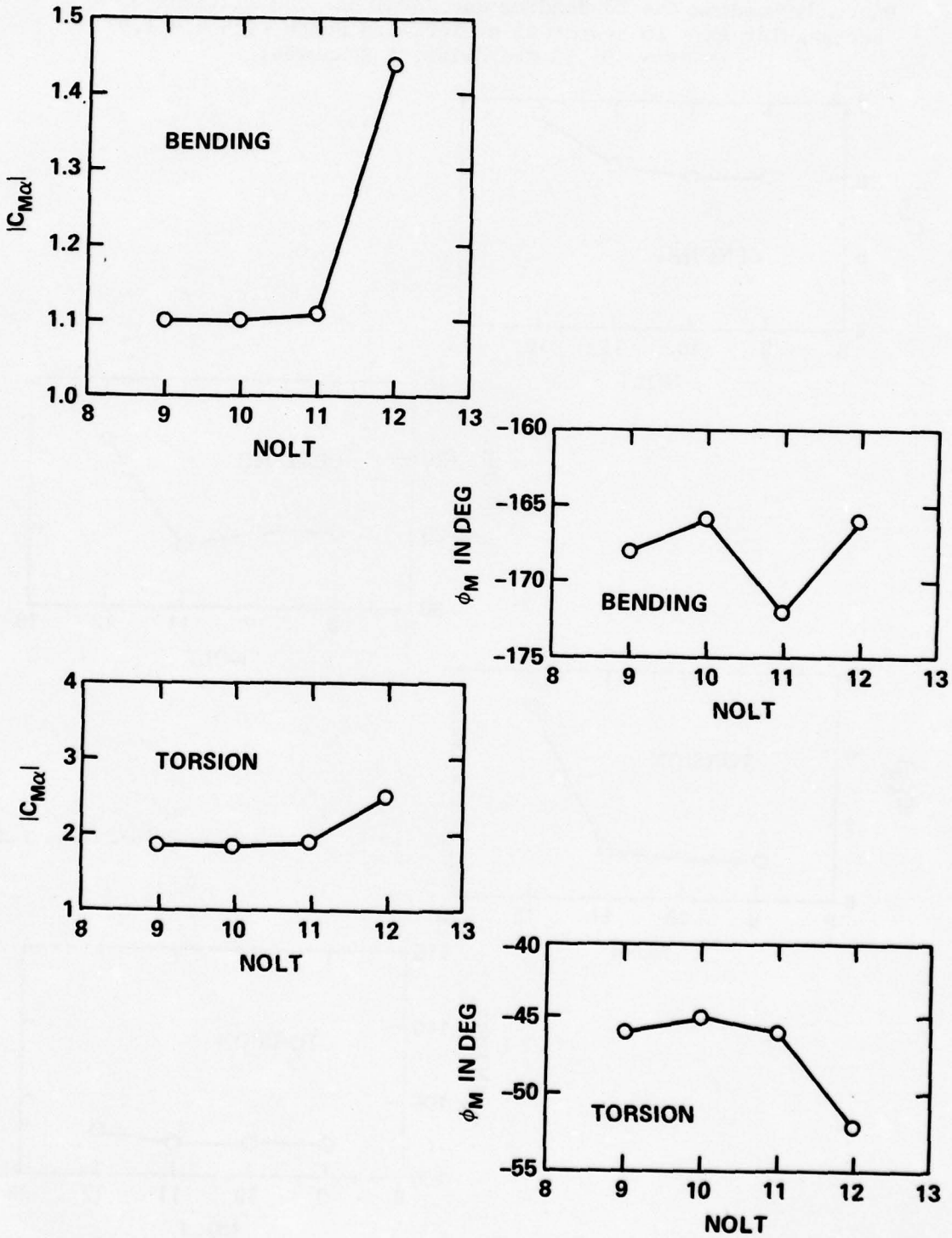


Figure 33b - Moment Coefficient Magnitude  $|C_{M\alpha}|$  and Phase Angle  $\phi_M$

calculated results oscillated around a changing local average, rather than oscillating around or asymptotically approaching a constant limiting value. Attaining stability may require much smaller numerical intervals, which were not attempted for cost reasons, or may be limited to chordwise loading distributions which are easily represented by trigonometric modes.

To provide a rough approximation of the residual instability, the incremental change in load coefficient, due to an increase in the number of chordwise pressure modes (NOLT) from 10 to 11, was used. The instabilities thus determined are given in Table 8.

#### COMPUTATIONAL PRECISION

The Widnall program was used on three different computers: the IBM 7090 and CDC 6700 computers at the Center, and an IBM 360 computer at the Johns Hopkins University Applied Physics Laboratory (APL). It was surprising to discover that initially the program yielded substantially different results on the different computers although it was written in the same language (FORTRAN IV). These preliminary calculations were done in single precision (approximately eight significant figures) except for the matrix inversion which was done in double precision. Line-by-line comparisons of intermediate program steps revealed the following reason for the discrepancies. The computations of the matrix elements relating the pressure coefficients to the downwash involve differences of terms of similar magnitude. In some cases, the differences were formed from meaningless, computer-generated digits carried at the low end of the terms being subtracted. It was found that these imprecise quantities were associated with high order chordwise pressure modes, which are insignificant in comparison with modes of low order. Unfortunately, however, these erroneous numbers tended to cluster in rows and columns of the calculated matrix. Consequently, the determinant of the matrix was erroneous, and so was the calculated pressure distribution.

As an example of the effect of computer system characteristics in such circumstances, the APL IBM 360 used two different system control tapes which gave differing values for corresponding matrix elements for the

TABLE 8 - APPROXIMATE NUMERICAL INSTABILITIES FOR STEADY  
AND UNSTEADY LOADING COEFFICIENTS

Type of Loading	Foil Configuration	Instability (Percent)			
		$C_L(\alpha=0)$	$C_{L\alpha}$	$C_M(\alpha=0)$	$C_{M\alpha}$
Steady	AR=10, rectangular	1	8	9	9
	AR=6, rectangular	2	4	5	4
	AR=1, rectangular	1	1	1	1
	AR=6.1, swept and tapered	2	7	3	27
Unsteady	AR=10, rectangular, bending and torsion	-	3	-	3

single precision version of the program. With the use of double precision values (12 precise digits) for all of the program variables and constants, the two systems gave identical results. In fact, the results also agreed with those from the IBM 7090 computer using double precision (16 precise digits) and with those from the CDC 6700 (15 precise digits).

No effort was made to determine the relationships between the number of chordwise modes and the required number of precise digits. However, all of the steady and unsteady calculations presented in this report were performed using 15 precise digits and the Center's CDC 6700.

The discovery that the pressure distribution calculated by the computer program might have been imprecise caused concern for the validity of the constants used in the program. An examination of the unsteady program, which contained more constants than did the steady program, revealed no more than a 1-percent change in the calculated lift and moment coefficients when the least significant figure in each of the constants was randomly changed by one unit. Therefore, it was concluded that the program constants were valid and did not need more significant figures.

#### COMPARISON WITH EXPERIMENT

To determine the accuracy of the Widnall calculation in predicting hydrofoil loading, loading values were calculated for a large number of

small-scale hydrofoil models for which experimental data were available. Both steady and unsteady loading conditions were represented in these test cases. In addition, because only a small amount of data was available for unsteady loading on hydrofoils, the unsteady hydrofoil data were supplemented by a limited amount of unsteady data obtained from airfoil models. With regard to the theory, additional perspective was provided by parallel calculations made with other theoretical approaches. In the case of a lifting-surface theory, programmed by Bandler<sup>6</sup> from an original development by Richardson,<sup>7</sup> these calculations were made by the authors. Other calculated theoretical values were reproduced from previous publications.

Only very simple types of hydrofoil and airfoil configurations were examined to minimize demands on the theories. All hydrofoils consisted of a planar lifting surface traveling in a horizontal orientation at varying depths beneath a free surface, or extended perpendicularly to a large end plate. The airfoils were similarly extended from a large wall. The foils were either actually or effectively bilaterally symmetrical. Both rectangular and swept, tapered planforms were included. Most models had supporting struts, and one had a fairing (pod) at the strut-foil junction. In such cases, the foil was considered, in the theoretical representation, to include the area within the strut and pod formed by extending the leading and trailing edges of the foil. No corrections were made for effects of the strut and pod on the predicted foil loading.

#### STEADY LOADING--THEORY AND EXPERIMENT

Calculated hydrodynamic loading due to steady motion was compared with data from twenty-one different hydrofoil model configurations and one airfoil model. The models<sup>8-21</sup> are described in Appendix A. Two models corresponded to foil systems on U.S. Navy hydrofoil craft; the others covered a wide range of characteristics. Both measured and predicted loading values are shown in Figures 34 through 40. Ranges of experimental uncertainty are given when available from the data source. The large uncertainties in lift at zero incidence will be commented on shortly. In this study, experimental uncertainty refers to the estimated maximum range of error between the measured value and the actual value.

Figure 34 - Total Steady Lift Coefficient as a Function of Submergence  
for Various Hydrofoils with Rectangular Planforms ( $\Lambda = 0$ ;  $\tau = 1.0$ )

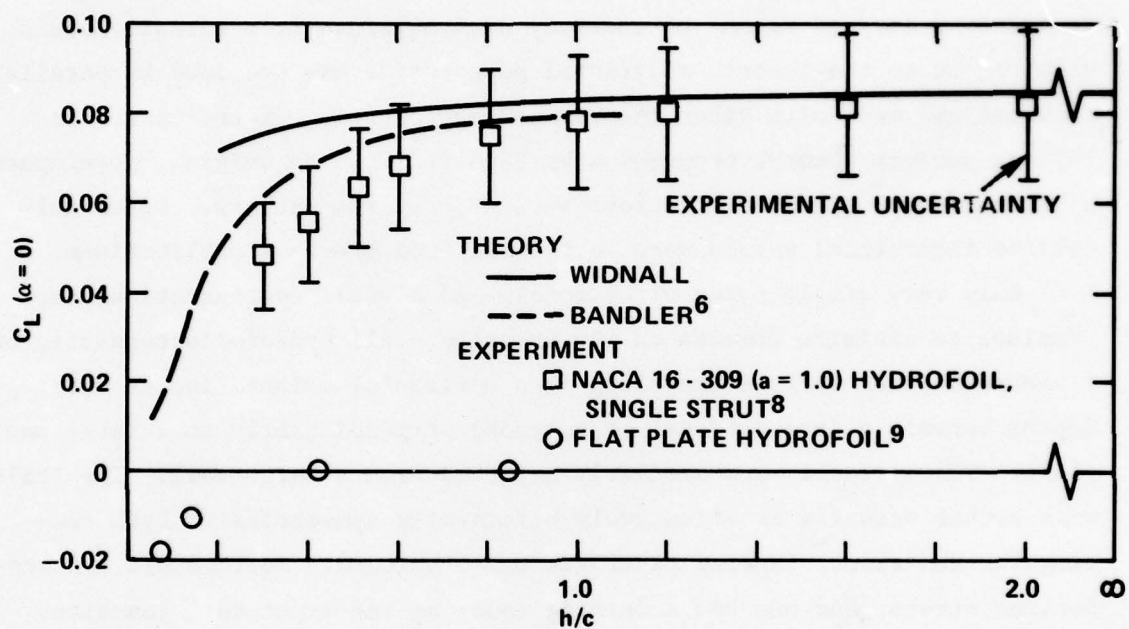


Figure 34a - AR = 1

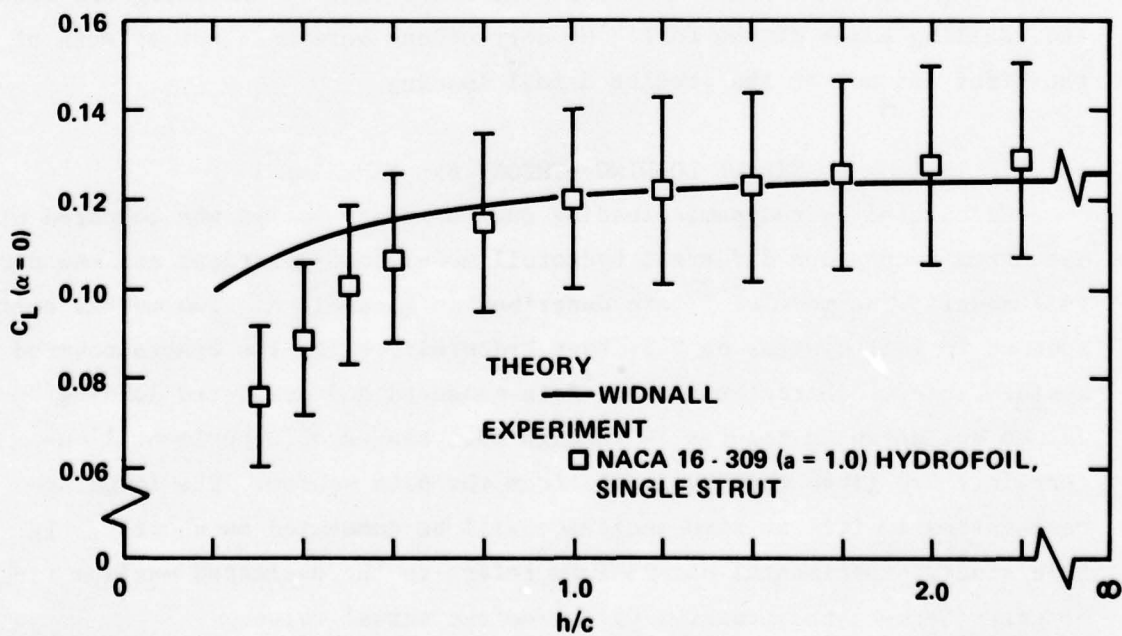


Figure 34b - AR = 2

Figure 34 (Continued)

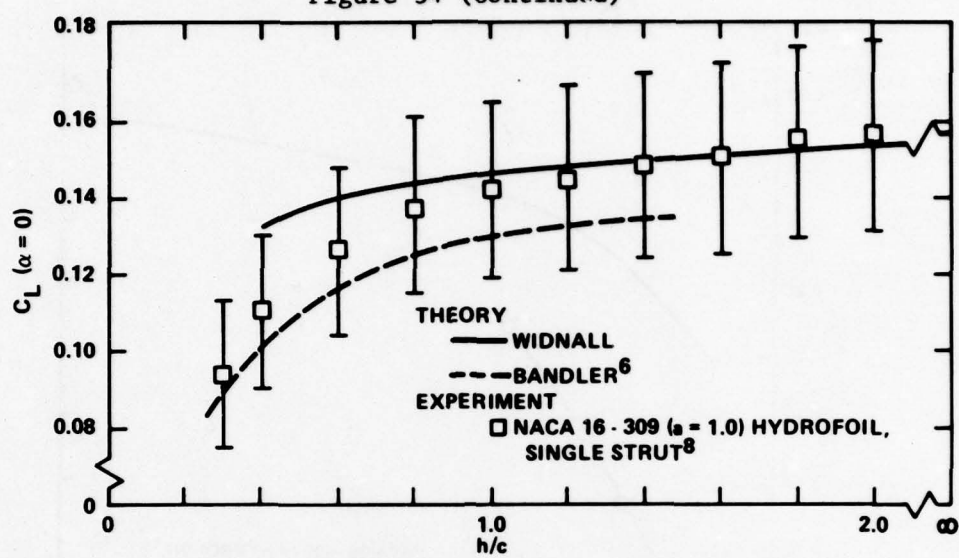


Figure 34c - AR = 3

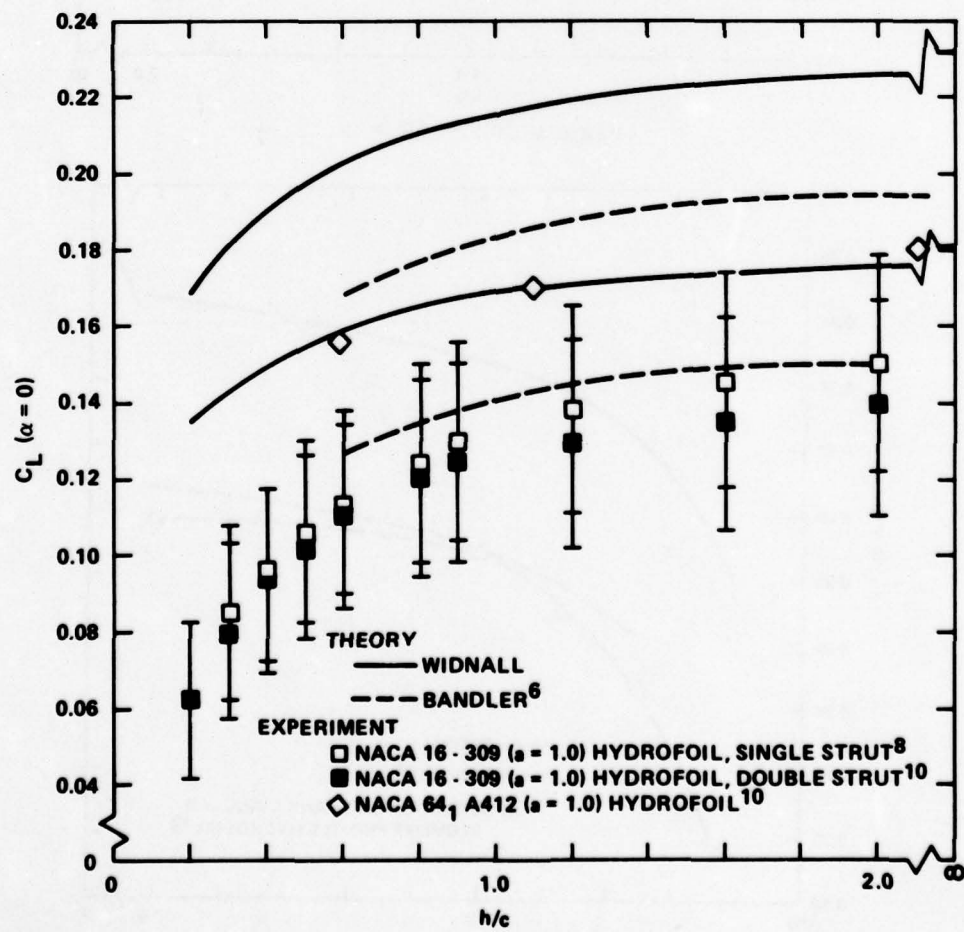


Figure 34d - AR = 4

Figure 34 (Continued)

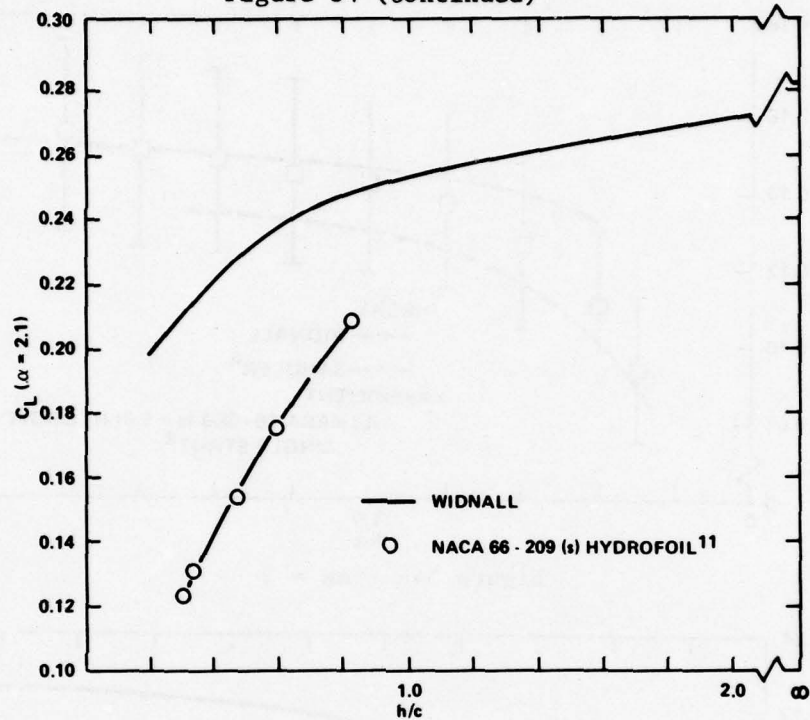


Figure 34e -  $AR = 5$

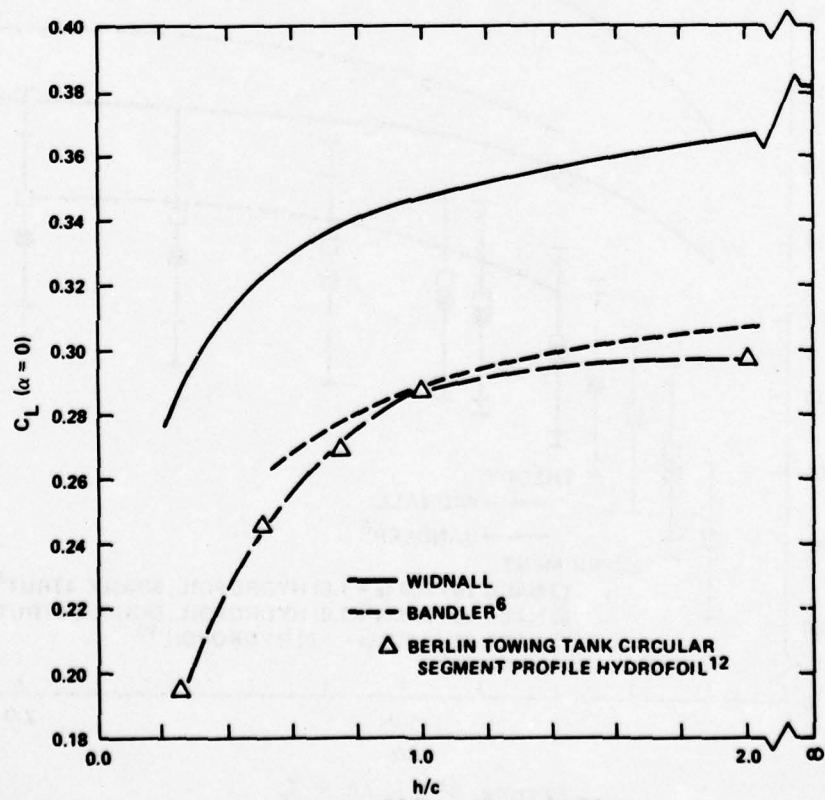


Figure 34f -  $AR = 5.84$

Figure 34 (Continued)

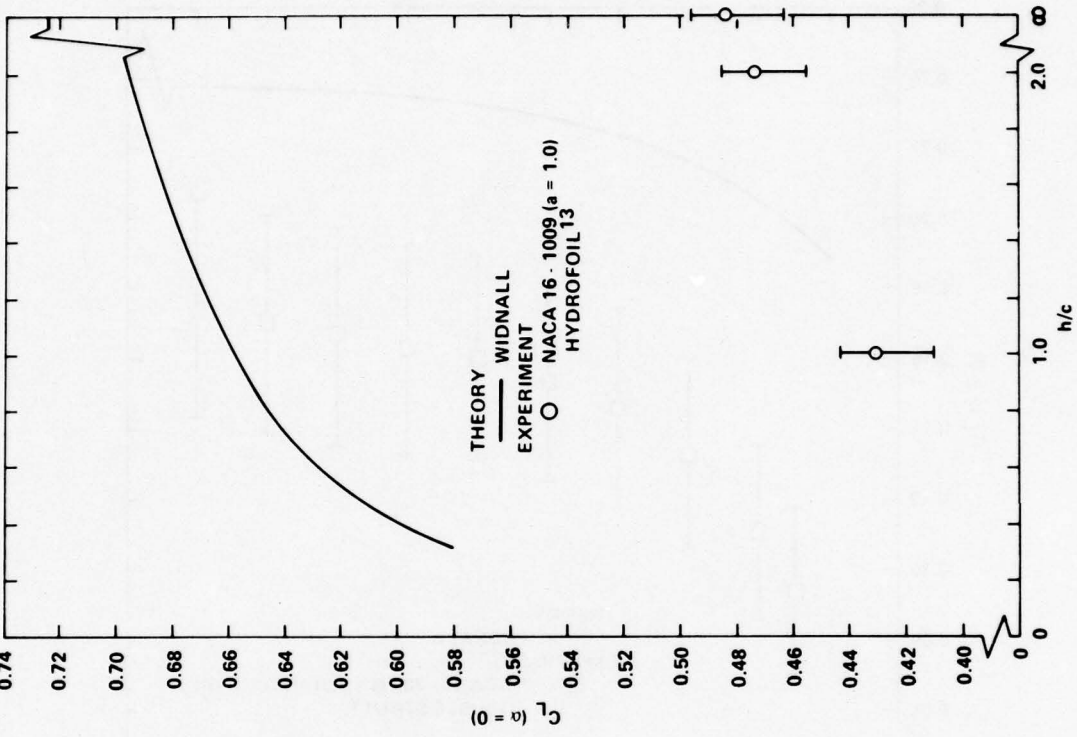
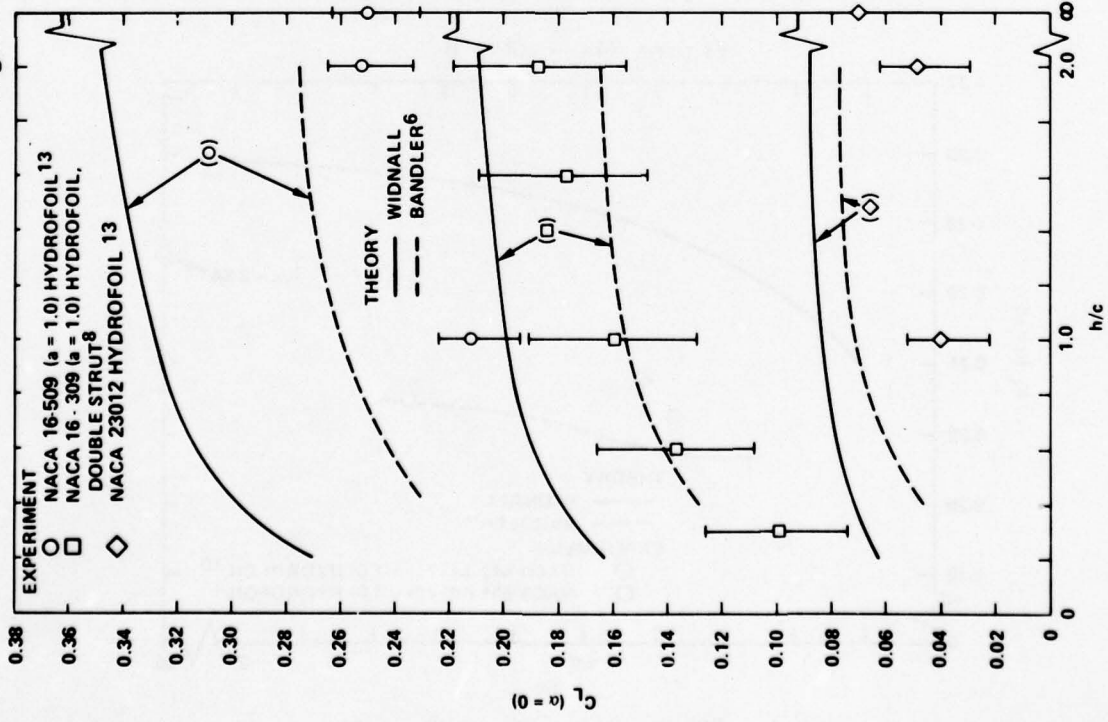


Figure 34g - AR = 6

Figure 34 (Continued)

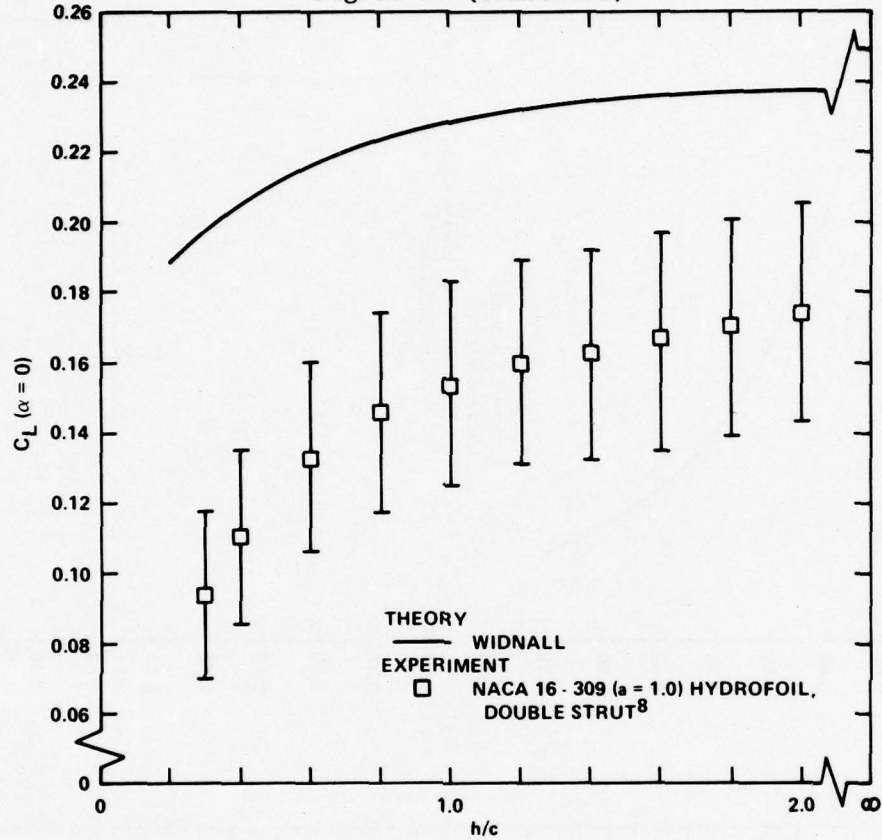


Figure 34h - AR = 8

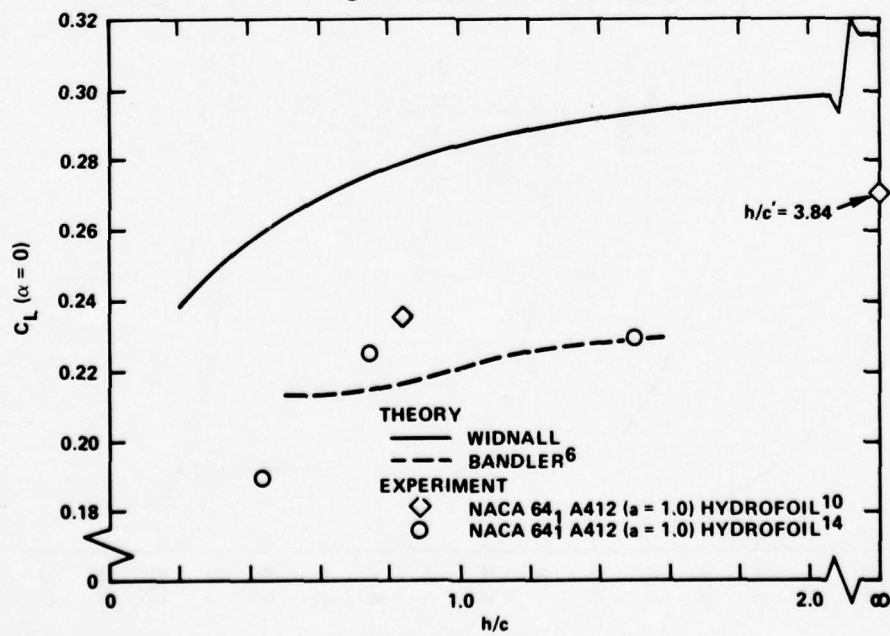


Figure 34i - AR = 10

Figure 35 - Total Steady Lift Slope Coefficient as a Function of Submergence for Various Hydrofoils with Rectangular Planforms  
 $(\Lambda = 0; \tau = 1.0)$

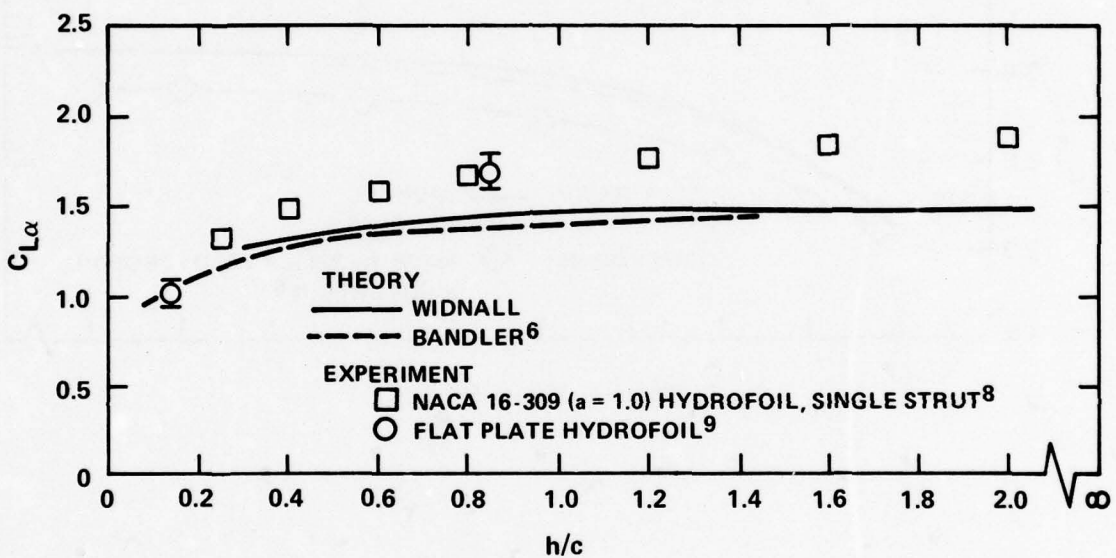


Figure 35a - AR = 1

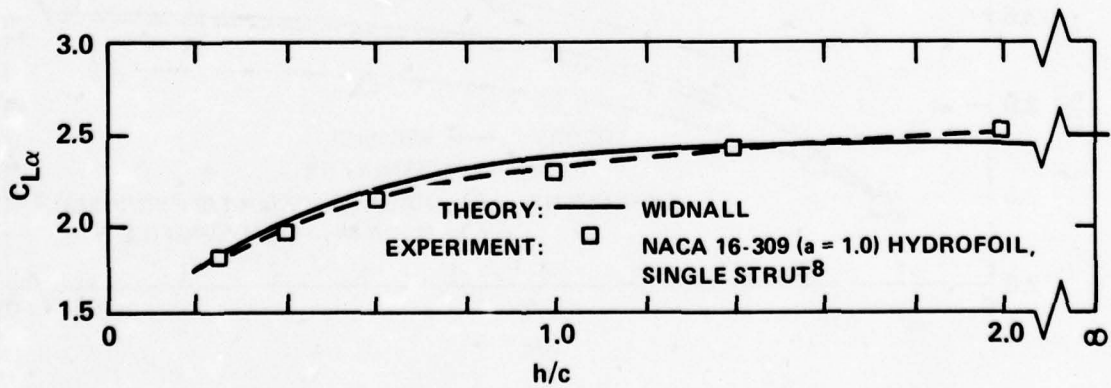


Figure 35b - AR = 2

Figure 35 (Continued)

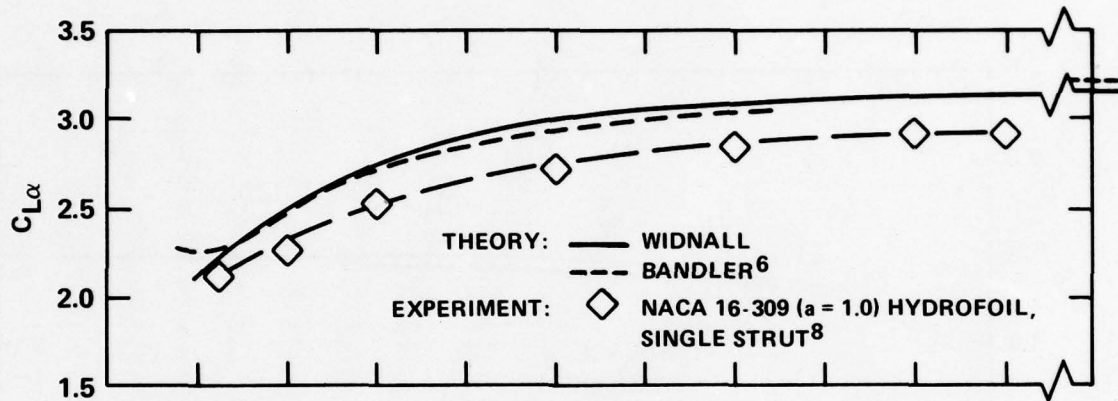


Figure 35c -  $AR = 3$

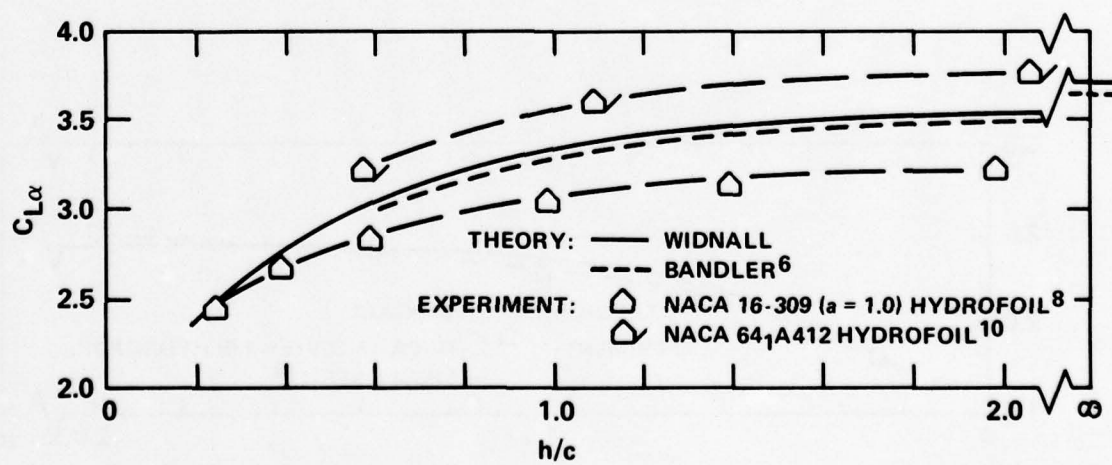


Figure 35d -  $AR = 4$

Figure 35 (Continued)

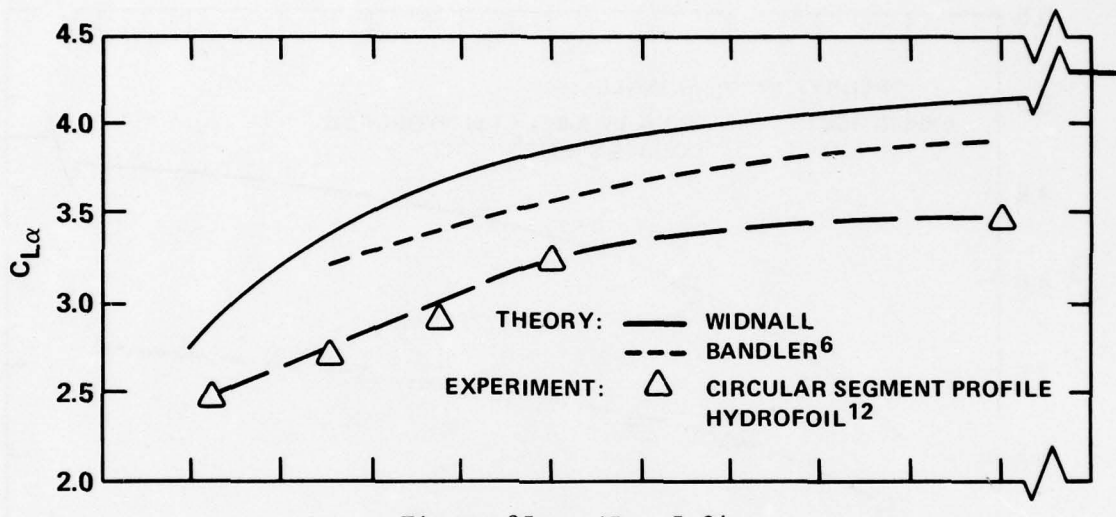


Figure 35e - AR = 5.84

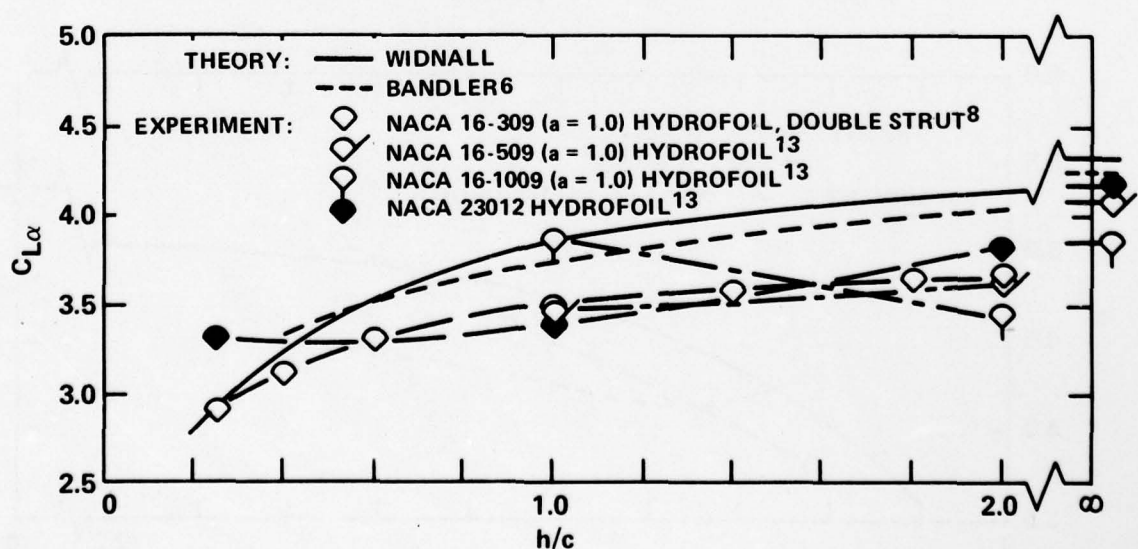


Figure 35f - AR = 6

Figure 35 (Continued)

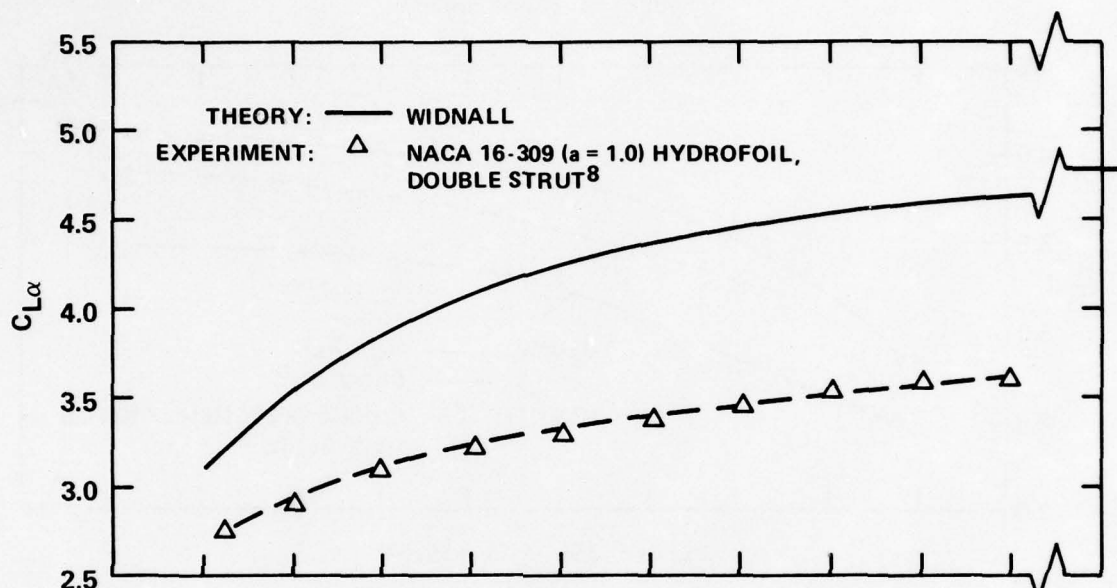


Figure 35g - AR = 8

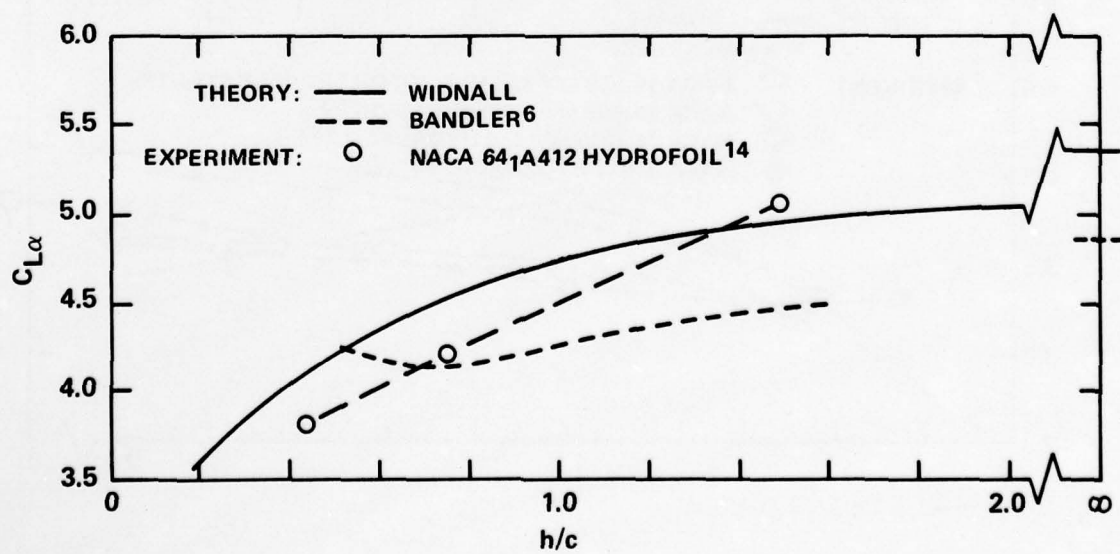


Figure 35h - AR = 10

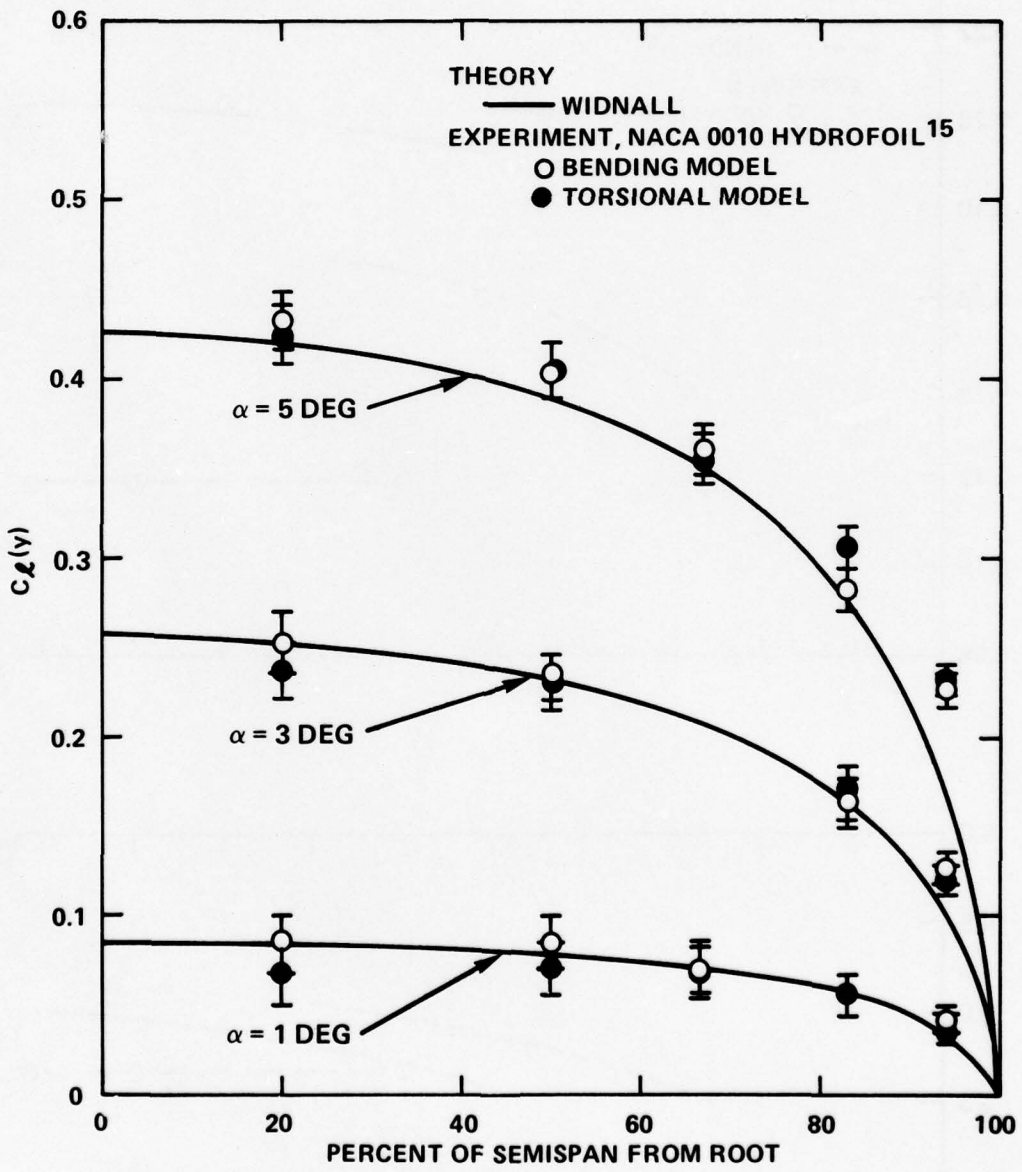


Figure 36 - Spanwise Distribution of Steady Lift Coefficient for the NACA 0010 Hydrofoil ( $\Lambda = 0$ ;  $\tau = 1.0$ ;  $AR = 5$ )

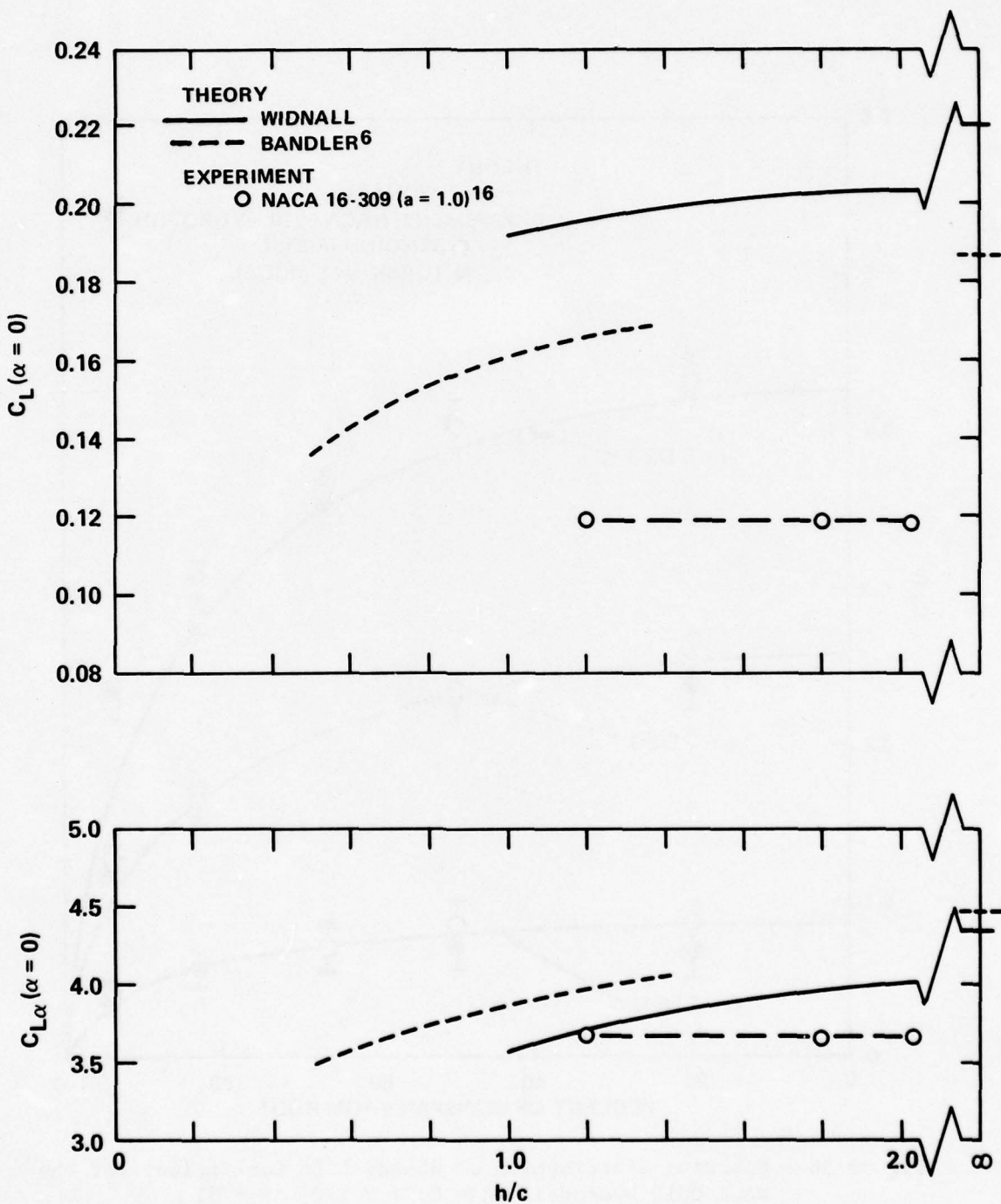


Figure 37 - Total Steady Lift and Lift Slope Coefficients as Functions of Submergence for the One-Eighth-Scale PCH-1 Hydrofoil Model  
 $(\Lambda = 15 \text{ Degrees}; \tau = 0.25; AR = 6.1)$

Figure 38 - Total Steady Loading as a Function of Submergence for the One-Twelfth-Scale AGEH-1 Hydrofoil Model  
 $(\Lambda = 35$  Degrees;  $\tau = 0.3$ ;  $AR = 3)$

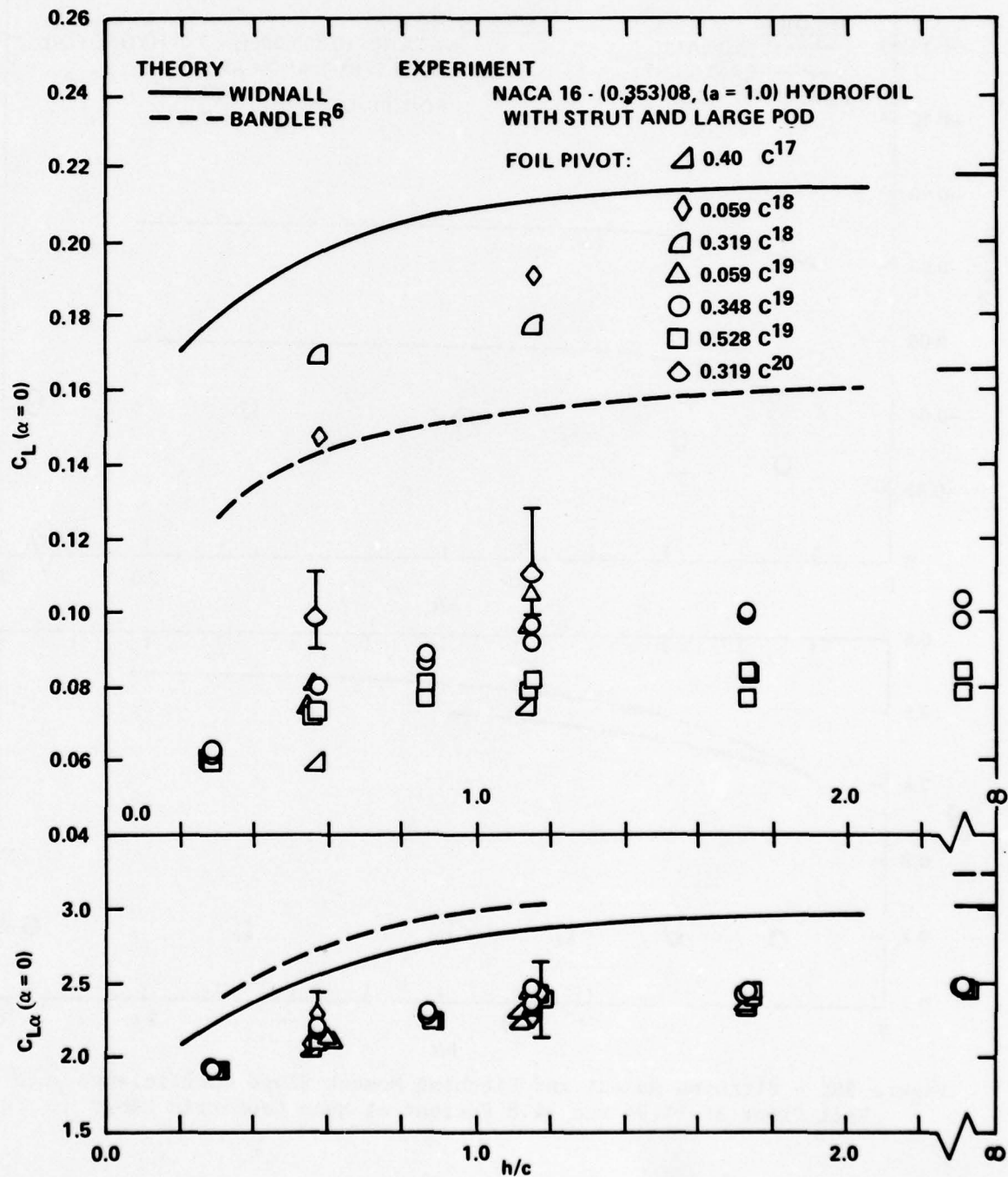


Figure 38a - Lift and Lift Slope Coefficients

Figure 38 (Continued)

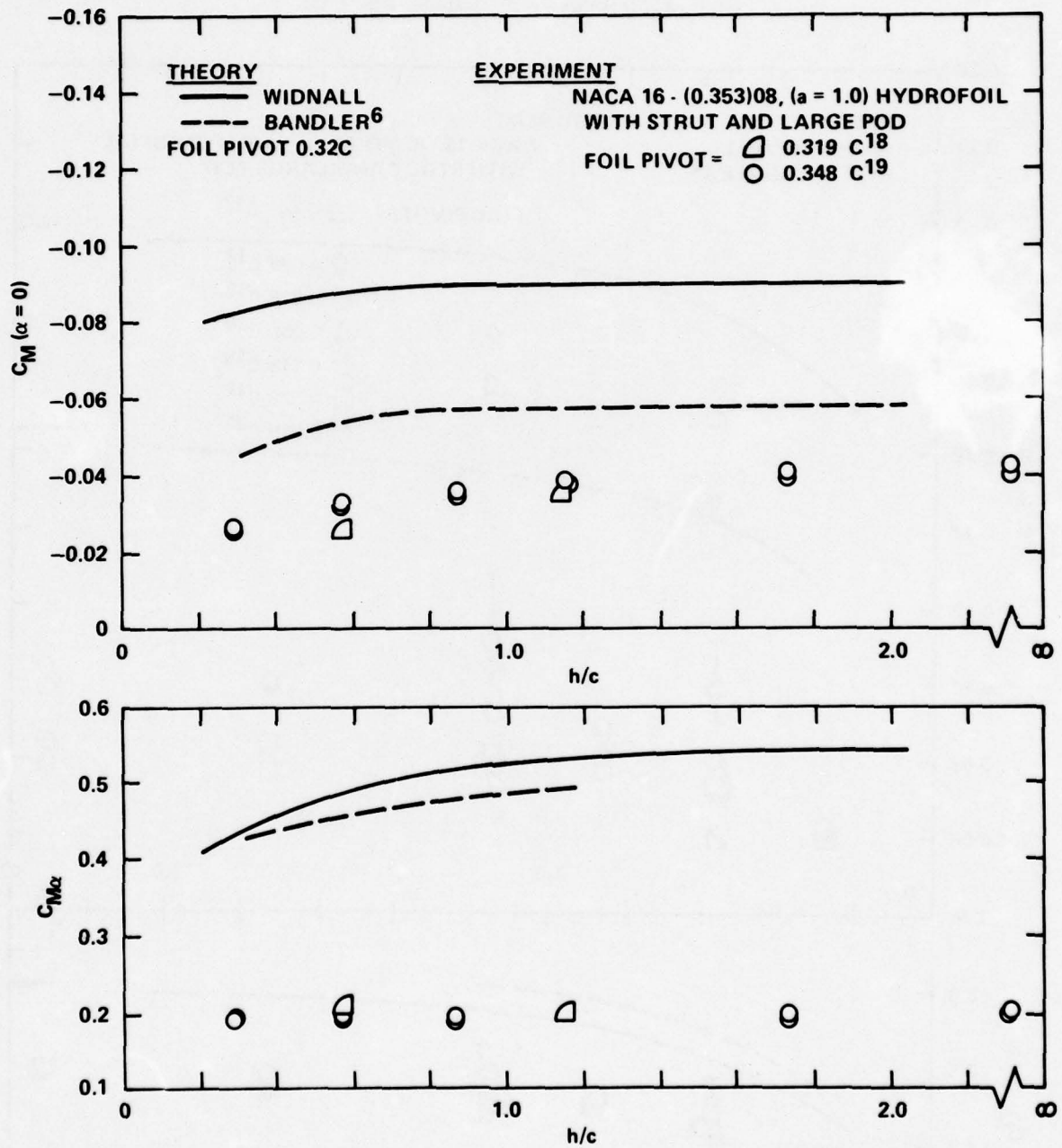


Figure 38b - Pitching Moment and Pitching Moment Slope Coefficients with Foil Pivot at 31.94 and 34.8 Percent of Mean Geometric Chord

Figure 38 (Continued)

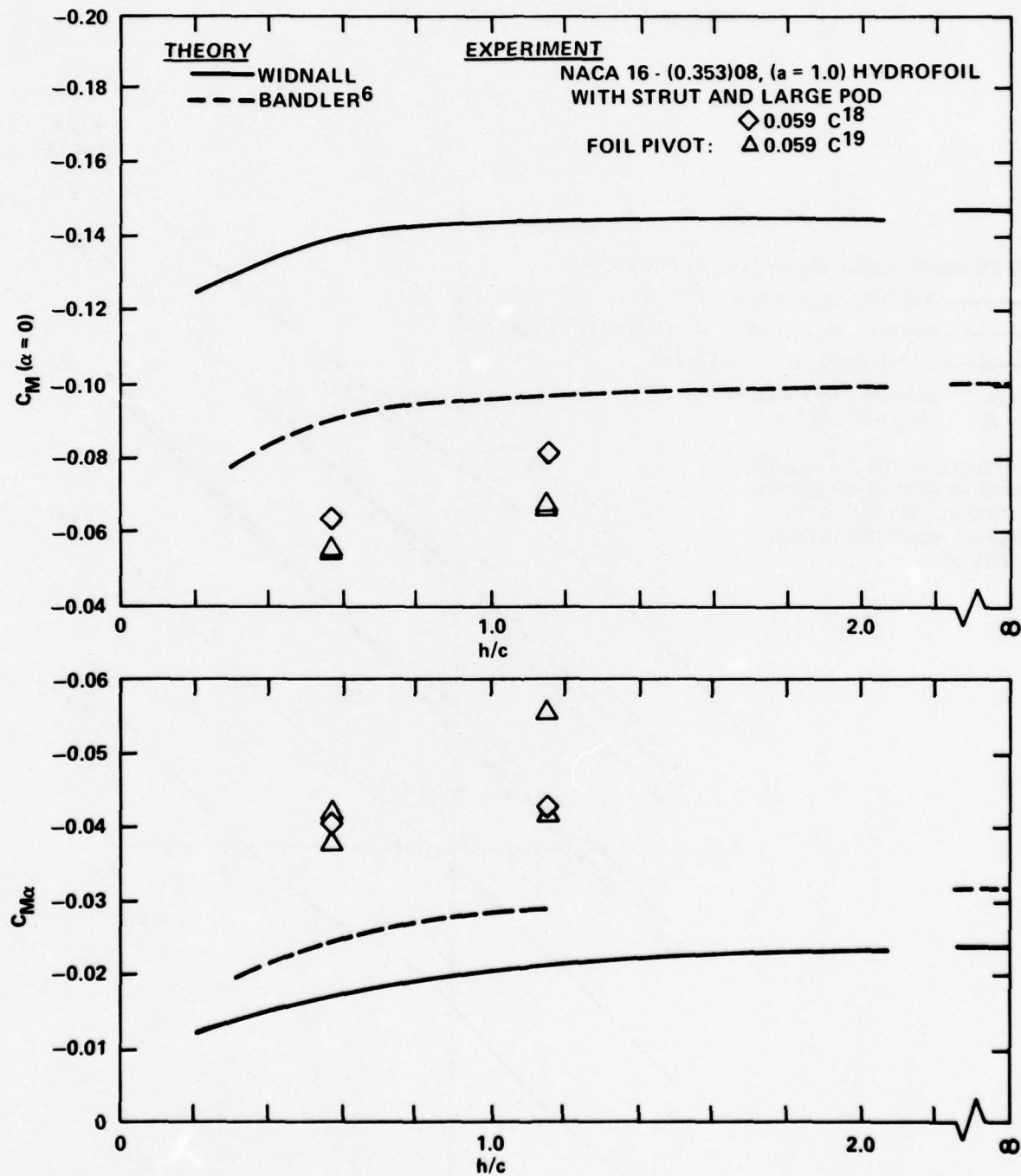


Figure 38c - Pitching Moment and Pitching Moment Slope Coefficients with Foil Pivot at 5.9 Percent of Mean Geometric Chord

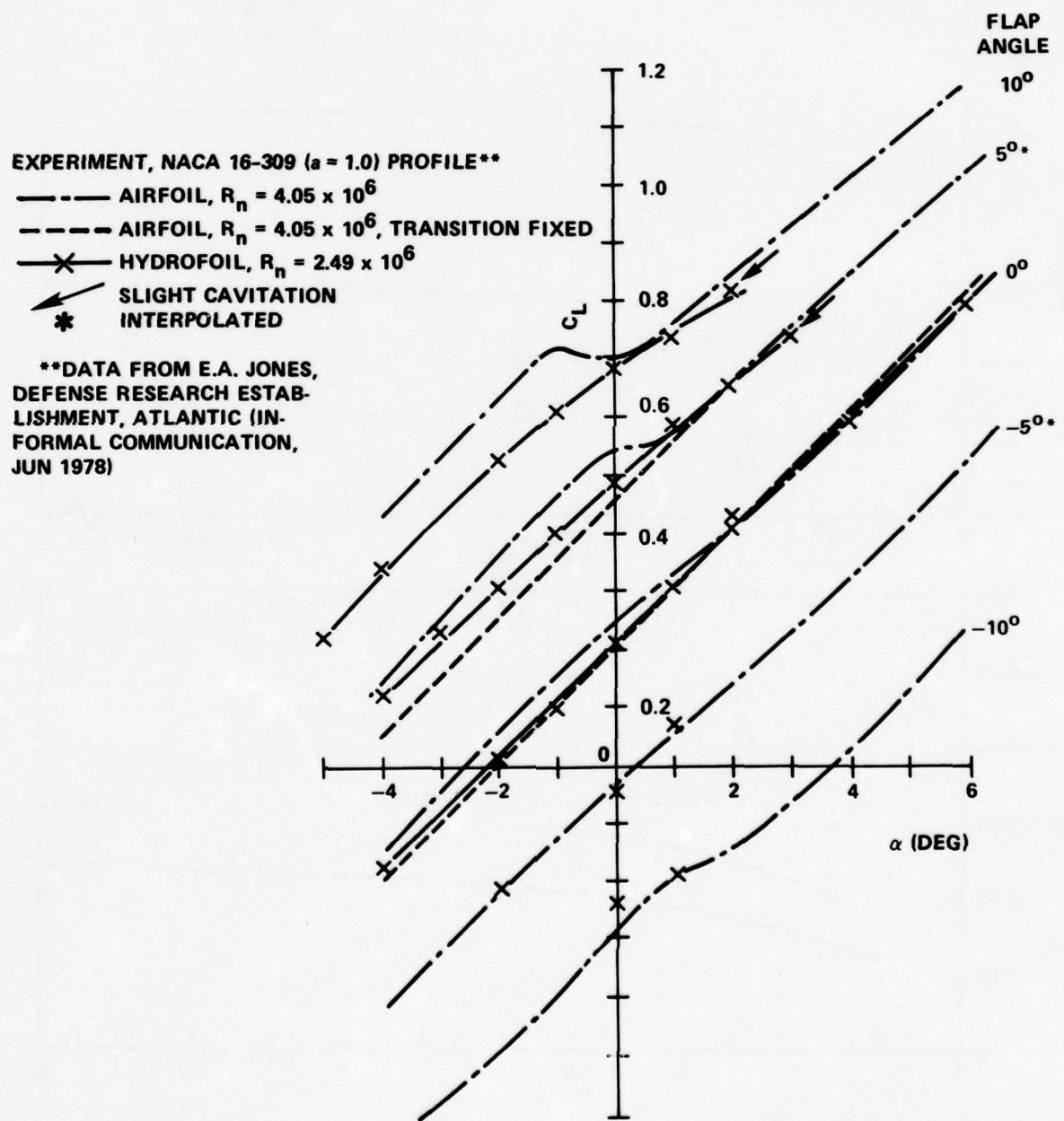


Figure 39 - Comparison of Total Lift Coefficients on a Hydrofoil and an Airfoil in Two-Dimensional Flow

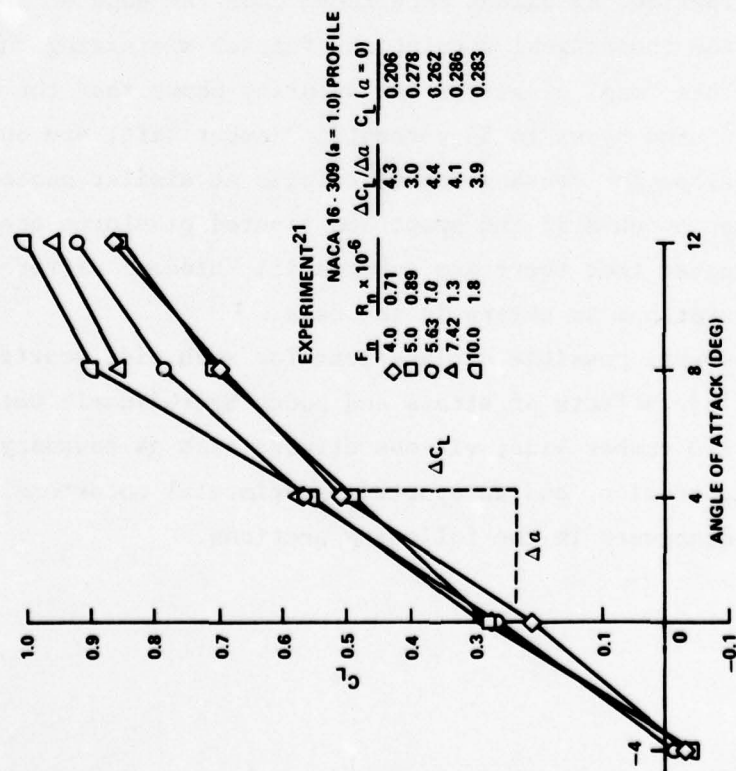


Figure 40a -  $h/c = 2$

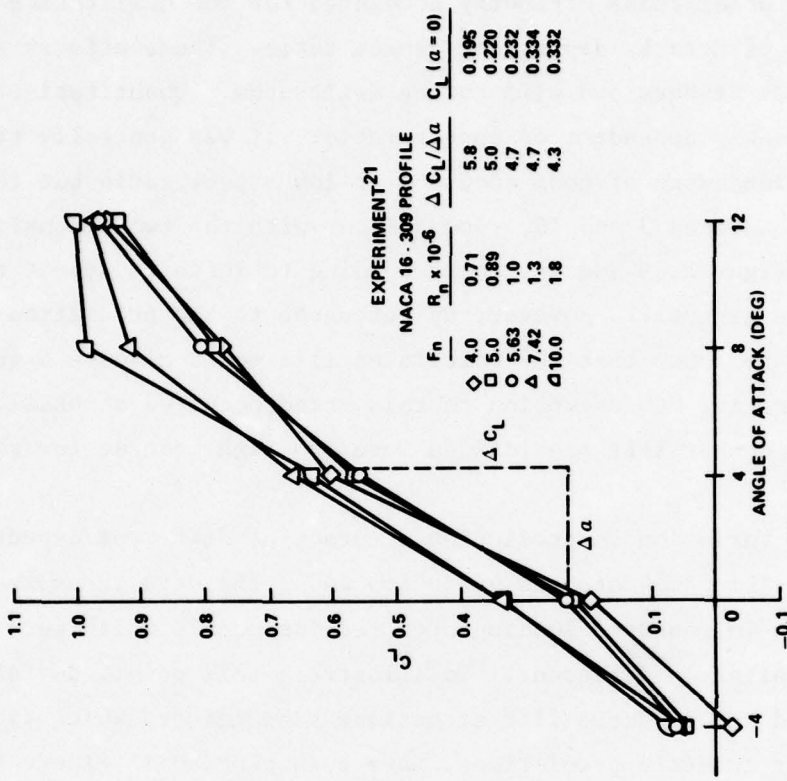


Figure 40b -  $h/c = 3$

Figure 40 - Total Lift Coefficient on a Hydrofoil in Two-Dimensional Flow at Finite Depth

The loading predictions correctly accounted for the qualitative effects of camber, angle of attack, depth, and aspect ratio. These effects are well known to most readers and will not be dwelt upon. Quantitatively, the accuracy was strongly dependent on aspect ratio: it was generally true that the predictions were of good accuracy at low aspect ratio but too high at aspect ratios between 3 and 10. Comparisons with the two-dimensional loading data in Figures 39 and 40, corresponding to infinite aspect ratio, could not be made directly. However, by reference to the prediction at AR = 10, it will be shown that the calculated lift would also be high at infinite aspect ratio. An exception to this trend occurred at shallow submergences, where camber lift predictions were too high even at low values of aspect ratio.

Besides the variation in prediction accuracy at different aspect ratios, it is striking to note the variation among the data themselves. Large differences in measured loading occurred for models which were either similar or only slightly different. To illustrate this point, deviations between predicted and measured lift at maximum submergence, which usually produced the most accurate predictions, have been plotted in Figure 41. When possible, experimental values were taken from the edge of the error band closest to the theoretical prediction, further minimizing the resulting deviation. This "map" of prediction accuracy shows that the experimental values differed by up to 50 percent in camber lift, and up to 29 percent in lift slope for rectangular hydrofoils at similar aspect ratios, and by even larger amounts if the swept and tapered planforms are included. These results suggest that there are substantial "hidden" differences in the model configurations or errors in the data.

There are several possible explanations for such wide scatter in the data. These include effects of struts and pods, hydrodynamic peculiarity of the NACA  $a = 1.0$  camber line, viscous effects such as boundary layer transition and separation, and unreported experimental uncertainty. These effects will be discussed in the following sections.

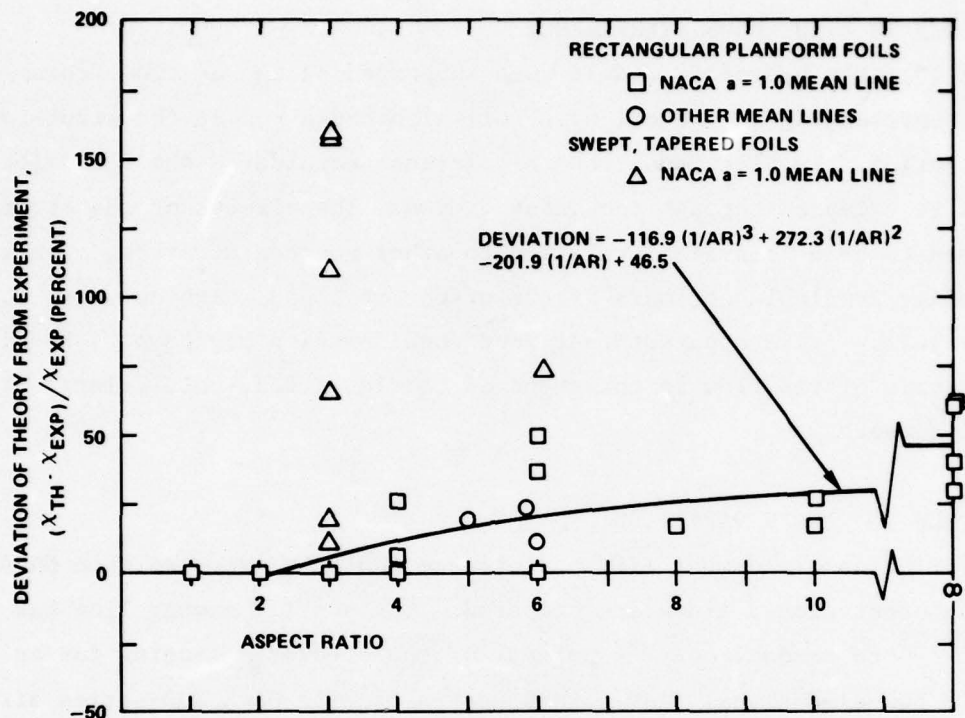


Figure 41a -  $C_L (\alpha = 0)$

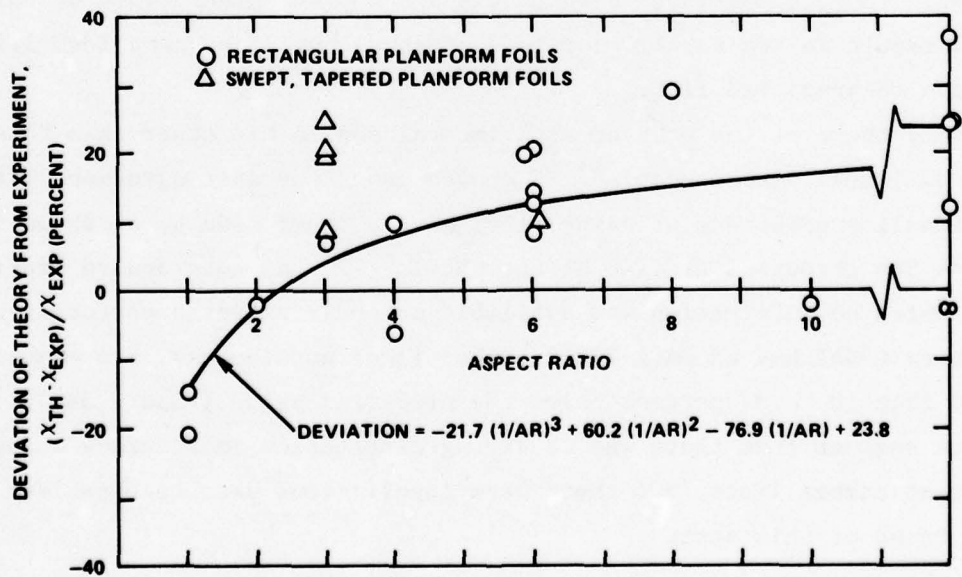


Figure 41b -  $C_{L\alpha}$

Figure 41 - Prediction Accuracy of the Widnall Program as a Function of Aspect Ratio for Steady Lift at Deep Submergence

#### ERROR DUE TO STRUT-POD INTERFERENCE

All of the hydrofoil models were supported by one or two struts. The model representing the AGEH-1 main foil also had a pod at the strut-foil intersection. In all cases, the calculations considered the foil alone as though it extended through the strut or pod. The effects of the strut are believed to have been small relative to other sources of error. There is no readily available estimate of the effect of a pod which does not rotate with a foil. It is apparent that more consideration may have to be given to an analysis of the flow in this type of configuration, particularly at zero incidence.

#### ERROR DUE TO CAMBER VARIATION

Variations in camber lift performance would be expected when NACA  $a = 1.0$  and other camber lines are compared. The  $a = 1.0$  camber line has been found<sup>22,23</sup> to produce only 74 percent of the predicted loading for an airfoil in two-dimensional flow. This contrasts with NACA 230-series airfoil sections, which produced 108 percent of the predicted loading, and NACA four-digit airfoil sections, which produced 93 percent of the predicted loading. Thus, comparisons between the  $a = 1.0$  and other types of camber should result in the  $a = 1.0$  sections having about 25 percent less lift, relative to predicted lift.

Only three of the present experimental models had other than NACA  $a = 1.0$  mean lines. Those models<sup>11-13</sup> showed about the same agreement with the Widnall predictions of camber lift as the other models, as shown in Figures 34e through 34g. Two of the models<sup>11,12</sup> had nonstandard profiles about which no information was available on their expected performance. The third model had an NACA 23012 camber line; nonetheless, its camber lift ranged from 10 to 37 percent below the predicted value (Figure 34g). These results suggest that there was no strong distinction in accuracy among different camber lines, but there were insufficient data to establish a clear trend of this sort.

#### ERROR DUE TO VISCOUS EFFECTS

The accuracy of the loading predictions was not systematically affected by viscous behavior of the fluid medium (water or air). Experimental values of Reynolds number  $R_n$  ranged from  $2.7 \times 10^5$  to  $4.4 \times 10^6$ . These values encompassed the region in which boundary layer transition would be expected. No correlation was found between prediction accuracy and  $R_n$ .

A recent investigation by Jones\* has uncovered one type of viscous effect which can influence model loading measurements. Wind tunnel measurements, shown in Figure 39, displayed a nonlinearity in lift at low angles of attack. Flow visualization observations showed that the shift was caused by movement of transition from midchord to near the leading edge on the suction side of the airfoil, as the angle of attack increased. The shift was eliminated when turbulence-stimulating strips were attached near the leading edge. Full-scale systems operating at much higher  $R_n$  would correspond to the forward transition location.

Jones' observations are important because they define a mechanism by which the camber lift can differ by as much as 22 percent between apparently similar foil models. Small imperfections in models, randomly distributed, would trigger transition at the forward location in some instances and not in others. It does not appear that the lift slope would be affected significantly, because the nonlinearity was confined to a small range of angle of attack.

#### ERROR DUE TO UNREPORTED EXPERIMENTAL UNCERTAINTY

Most of the data scatter appears to be caused by relatively large experimental uncertainty in the data. Two model parameters are especially suspect: angle of attack and profile geometry. Angle of attack is not easy to determine, and, in most cases, the lift due to an angle of attack of one or two degrees is equal to the entire lift due to camber. Lift slope values also would be affected if changes in angle could not be measured much more accurately than the angle itself.

---

\*Informal communication (Jun 1978) with E.A. Jones of the Canadian Defence Research Establishment Atlantic.

Experimental uncertainty in angle of attack was rarely mentioned in the reported data. In one case, a minimum uncertainty of  $\pm 0.5$  deg could be inferred from the Feldman data.<sup>8</sup> This uncertainty led to relatively wide error bands which could explain the decrease in camber lift as aspect ratio increased from 6 to 8; see Figures 34g and 34h. The tendency for camber lift data to have greater scatter than lift slope data also suggests angle of attack uncertainty, because slope would be unaffected by systematic errors in angle. These observations indicate the need for improvement in the quality of angle of attack measurements. It would also be helpful for values of experimental uncertainty to be reported in all experiments.

Errors in model profile, originating in manufacturing defects or accumulations of dirt during testing, would affect camber lift rather than lift slope. Either the mean line itself, or the transition behavior, could be affected.

Jones\* described a tendency for manufacturing errors to remain constant in absolute size, and thus to become more important as model size decreases. The smaller hydrofoil models, which had chords as small as 0.10 m (3.9 in.), would seem to have been susceptible to profile errors. Offset discrepancies of 10 percent were reported by Coder,<sup>19</sup> although these were not definitely ascribed to manufacturing error, on a foil with  $c' = 0.220$  m (8.65 in.). Again, it is not common practice to report profile accuracy of models, and such information could be significant.

#### STATISTICAL ANALYSIS OF DATA

Despite the amount of data scatter, the assembled body of data has value as a collection of multisample<sup>24</sup> data. Such data, taken by independent investigators, are not likely to have been affected by systematic errors. Given enough points, the data will form a normal distribution for which the mean is the most probable value.

Unfortunately, there are not enough values to perform such an analysis at any one aspect ratio with the present data. Only two foil configurations have had several independent measurements made of loading characteristics. The AR = 6 rectangular hydrofoil has had four measurements

---

\*E. A. Jones, informal communication.

made of lift slope; the measurements for the AR = 5.84 hydrofoil could be considered a fifth value. These measurements are too few in number to form a normal distribution. It may be useful, however, to know that the average of the five values for  $C_{L\alpha}$  is 3.6 at  $h/c = 2.0$ . The predicted value is 4.15, or 15 percent high. Closer agreement is obtained for the three values corresponding to deeper submergence.

A second example is the AGEH-1 model, for which four measurements of lift and moment have been made.<sup>14,16-18</sup> Camber lift and lift slope predictions at  $h/c = 1.156$  were 130 and 23 percent, respectively, above the average of the data other than the camber lift data of Reference 18. The preponderance of the data, independent except that the same model was used (except for the addition of a sealed flap to the foil in Reference 19), strongly implies that the higher camber lift value of Reference 1<sup>o</sup> was erroneous. These results, incidentally, reemphasize the less accurate character of the camber lift prediction.

A similar analysis can be made of the two-dimensional data, for which four independent values of lift and lift slope are available:

2-D Data Source	Average $C_L$ ( $\alpha=0$ )	Average $C_{L\alpha}$
Lindsey (airfoil) <sup>25</sup>	0.24	6.0
Jones (hydrofoil)*	0.21	5.4
Jones (airfoil)*	0.21	5.4
Robins (hydrofoil, $h/c = 3$ ) <sup>21</sup>	0.26	4.9
Data Average	0.23	5.4

In this comparison, the Jones airfoil data corresponded to fixed transition. The Robins data are more questionable than the others because it was not certain that a completely two-dimensional flow condition was achieved. It can be seen from expressions presented by Abramson et al.<sup>26</sup> that results at AR = 10 are about 80 percent of the two-dimensional values.

---

\*E. A. Jones, informal communication.

This correction was used to extrapolate the Widnall predictions from AR = 10 (see Table 1) to infinite aspect ratio. The predictions of lift and lift slope were then 46 and 25 percent high, respectively. These deviations were included in Figure 41.

To provide an estimate of the accuracy of the Widnall calculation over the complete range of aspect ratio, a third-order polynomial curve fit has been made to the deviations between theory and experiment as a function of the reciprocal of the aspect ratio. Only rectangular foils were included, using data from the maximum submergences. The resulting curve, replotted in Figure 41 in terms of aspect ratio, indicates that the deviation of the calculation ranges from 0 to +47 percent for camber lift and from -15 to +24 percent for lift slope, for aspect ratios of 1 and above. By applying a correction equal to the value of the fitted curve to the Widnall prediction at any aspect ratio, the resulting accuracy is expected to be within  $\pm 15$  percent of the value measured in a series of independent experiments. It appears that a higher degree of accuracy could be ascribed to the corrected predictions if more data were available to define the correction in a statistically more rigorous manner.

In view of the large amount of data showing the effect of varying submergence, a further correction could be determined which would extend the Widnall predictions to shallow submergences with little probable loss of accuracy. This correction was not determined in the present study.

#### COMPARISON WITH THE BANDLER PROGRAM

The Bandler loading calculation,<sup>6</sup> included in Figures 34, 35, 37, and 38, provided what appears to be much more accurate predictions than the Widnall calculation. In particular, the Bandler program predicted substantially lower values of camber lift than the Widnall program. However, in view of the probable influence of viscous effects in lowering camber lift for NACA  $a = 1.0$  mean line sections, the Bandler program (which also did not consider viscosity) is thought to have underpredicted camber lift. A further deficiency of the calculation involved numerical instability. Unpublished calculations showed that the numerical stability of the program

was limited to one or two significant figures. A severe limitation in the number of control points, and hence pressure modes (only sixteen collocation points were allowed) prevented proper exploration of this aspect. It is concluded that the Bandler calculation is not suitable for loading prediction in its present form, but should be reformulated to ensure numerical stability. This effort would be particularly desirable because the analysis permits inclusion of foil thickness and, in an unusual feature among existing theories, predicts the effects of gravity wave generation (finite Froude number) on foil loading.

#### UNSTEADY LOADING--THEORY AND EXPERIMENT

The unsteady loading predictions of the Widnall program were compared with data from four hydrofoil and two airfoil model configurations.<sup>15,18,27-32</sup> The models are described in Appendix A. Comparisons were also made with other theoretical results, namely, the Woolston et al. lifting-surface program,<sup>31</sup> a quasi-steady calculation,<sup>32</sup> and a two-dimensional version of the Widnall calculation.<sup>18</sup> The results are shown in Figures 42 through 49. In each case, the calculated results are shown in the form presented by the experimental investigator. Predictions for each of the models will be described in the following sections.

#### OSCILLATING FOILS

Results for loading produced by forced oscillation of foils are shown in Figures 42 through 46. Individual model results are discussed in the following sections.

##### NACA 66-209(S) Hydrofoil

The lift due to heave oscillation of an aspect ratio 5 rectangular hydrofoil<sup>27</sup> is shown in Figure 42. At the intermediate depth used in the calculation, the predicted lift was always larger than the experimental lift, with the error increasing at larger reduced frequency. The maximum error was approximately 40 percent. The phase angle was predicted well except at shallow depths where the calculated value led the experimental value by up to 20 deg.

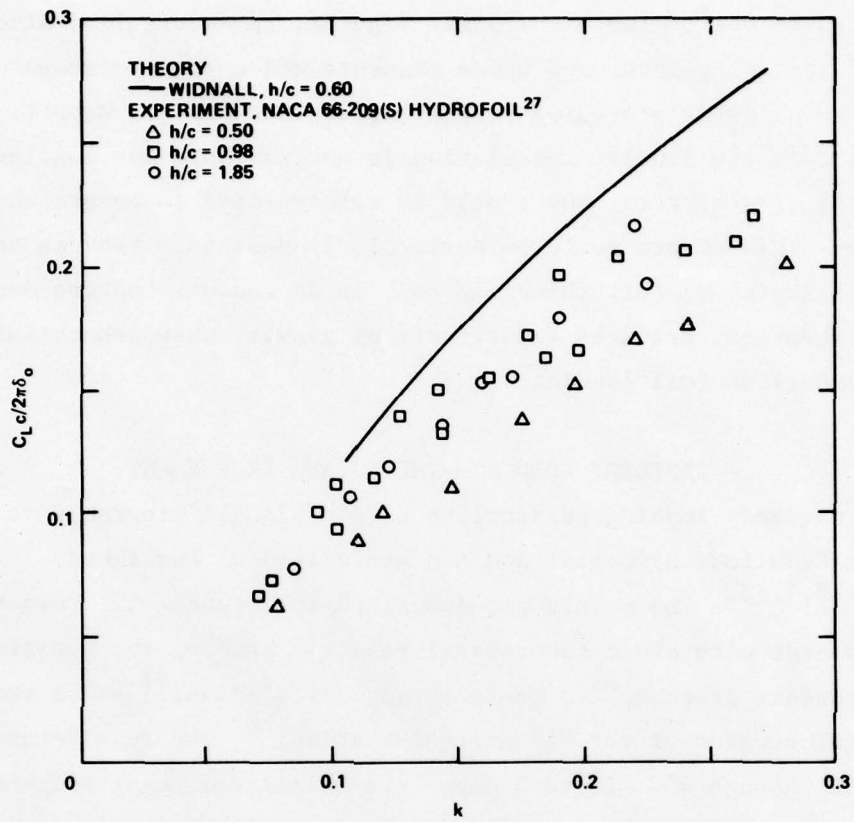


Figure 42a - Magnitude of Lift Coefficient

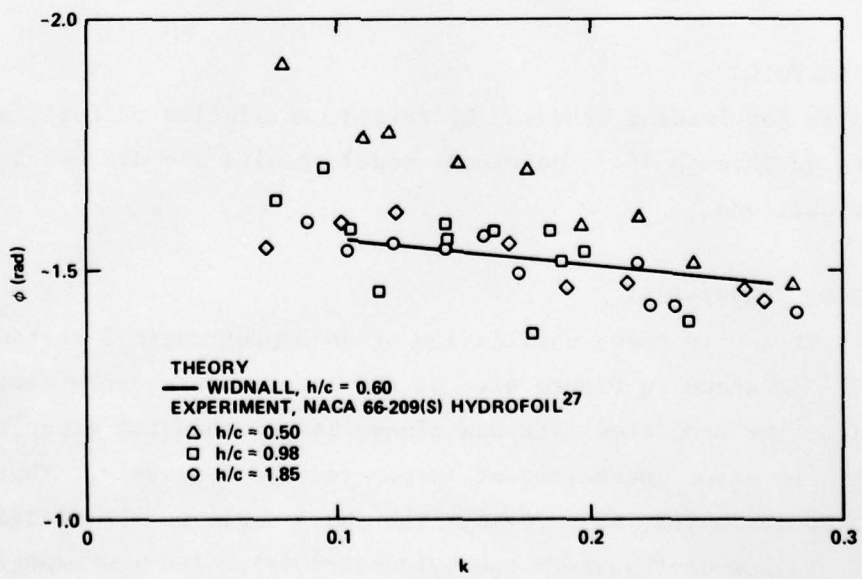
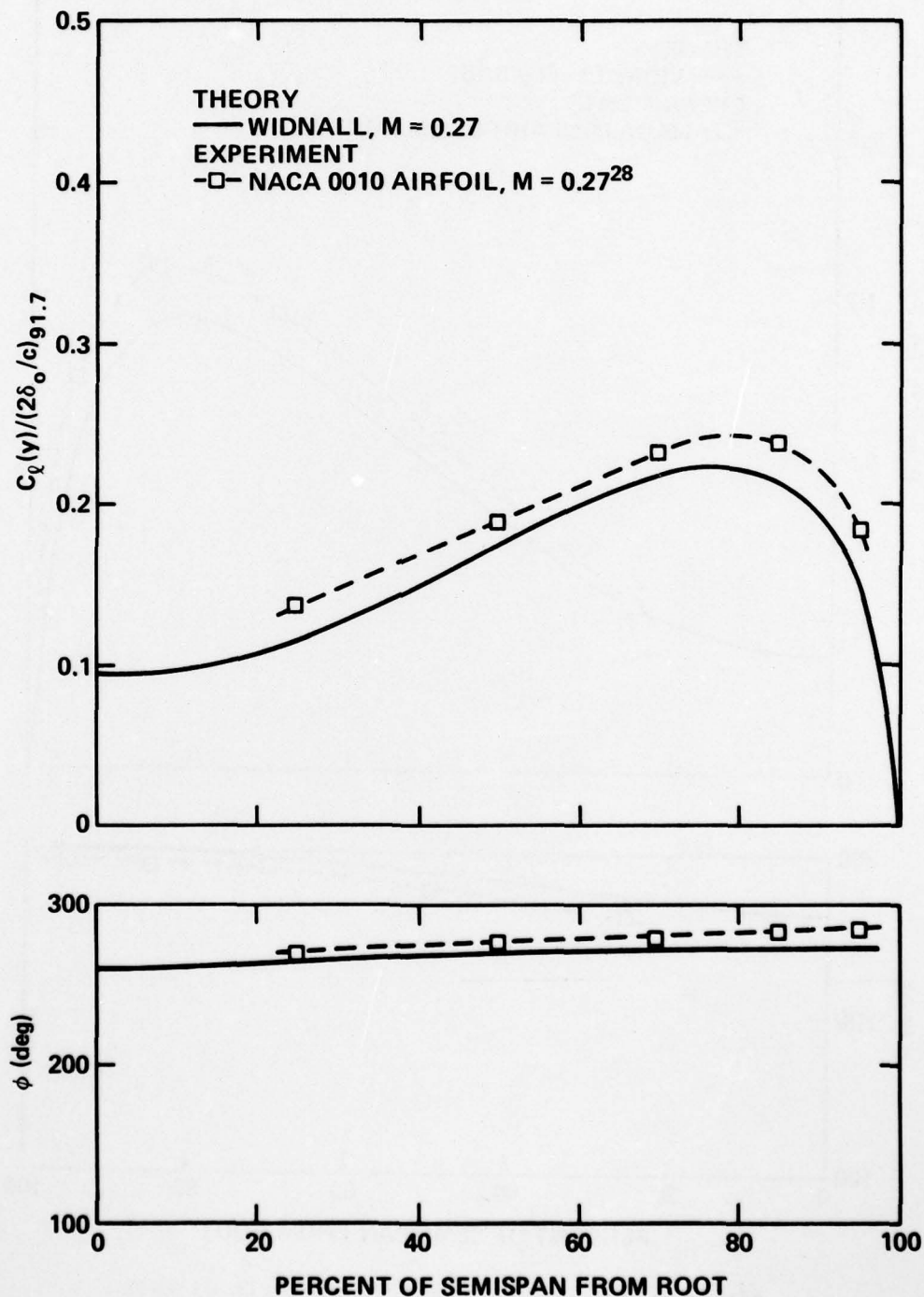


Figure 42b - Phase Angle of Lift Coefficient

Figure 42 - Total Unsteady Lift Coefficient due to Heave Oscillation as a Function of Reduced Frequency for the NACA 66-209(S) Hydrofoil ( $\Lambda = 0$ ;  $\tau = 1.0$ ;  $AR = 5$ )

**Figure 43 - Spanwise Distributions of Unsteady Loading due to Bending and Torsional Oscillations for the NACA 0010 Airfoil**  
 $(\Lambda = 0; \tau = 1; AR = 5)$



**Figure 43a - Magnitude and Phase Angle of Lift Coefficient due to Bending at  $k = 0.1$**

Figure 43 (Continued)

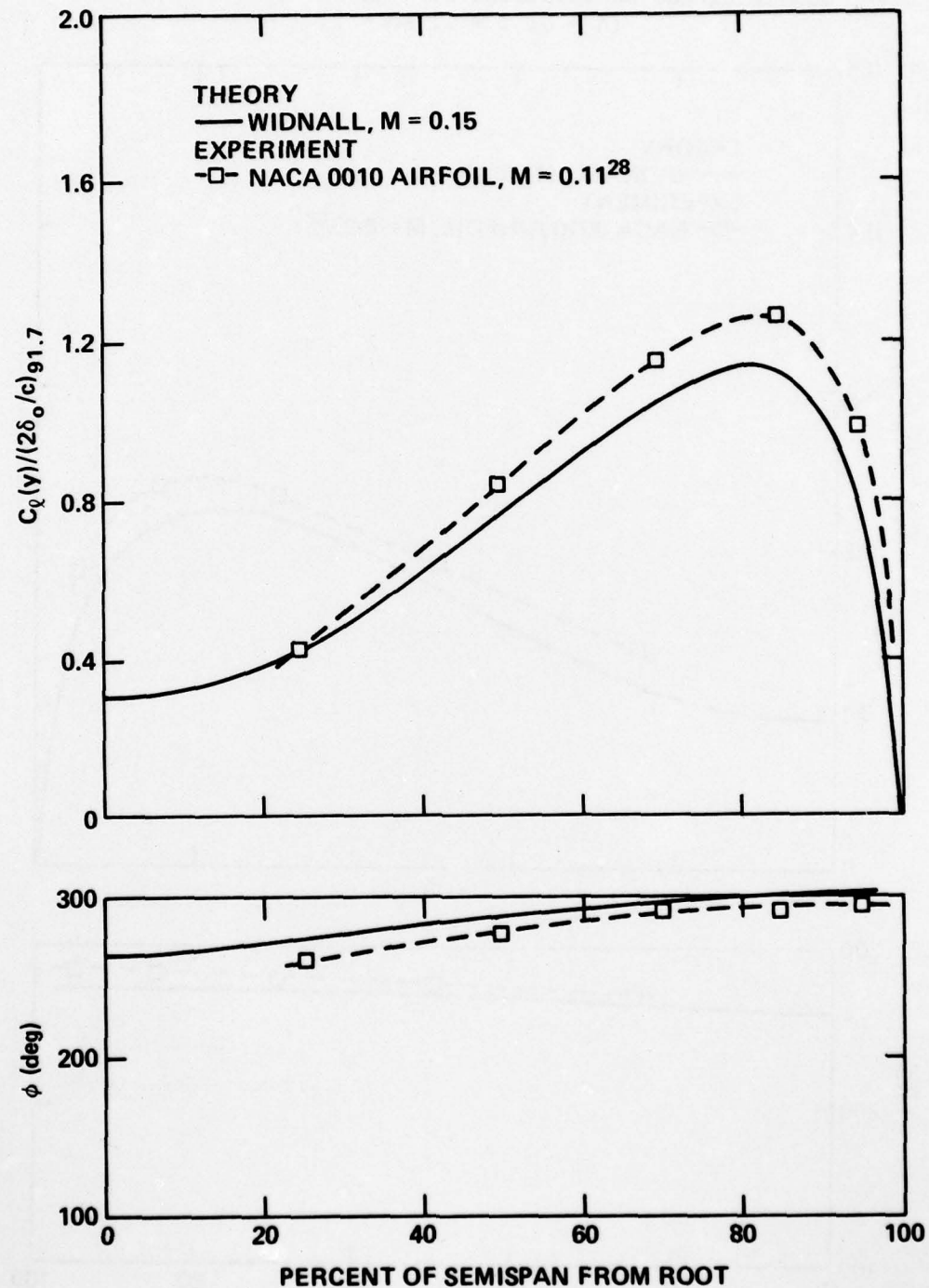


Figure 43b - Magnitude and Phase Angle of Lift Coefficient due to Bending at  $k = 0.5$

Figure 43 (Continued)

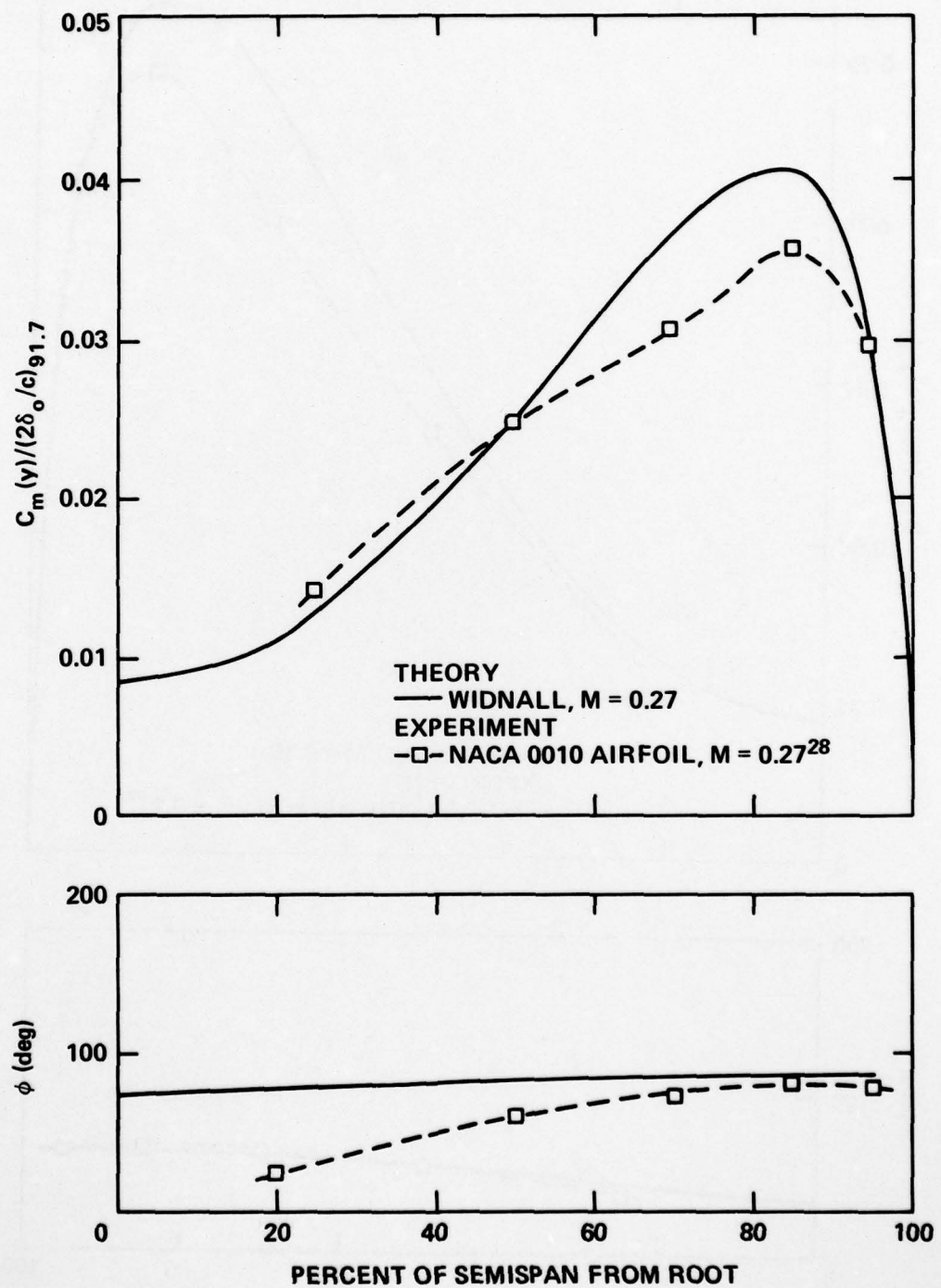


Figure 43c - Magnitude and Phase Angle of Pitching Moment Coefficient due to Bending at  $k = 0.1$

Figure 43 (Continued)

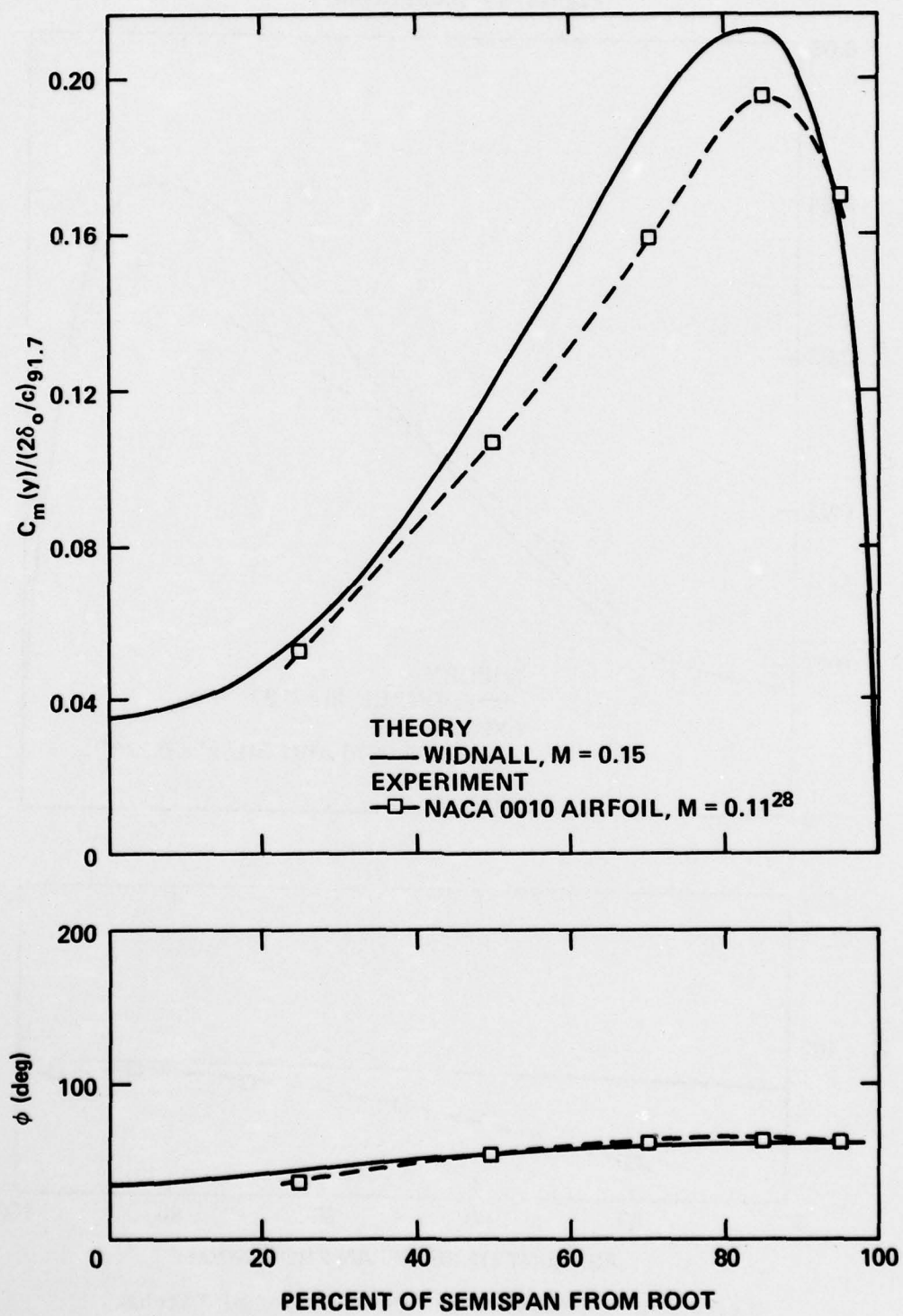


Figure 43d - Magnitude and Phase Angle of Pitching Moment Coefficient due to Bending at  $k = 0.5$

Figure 43 (Continued)

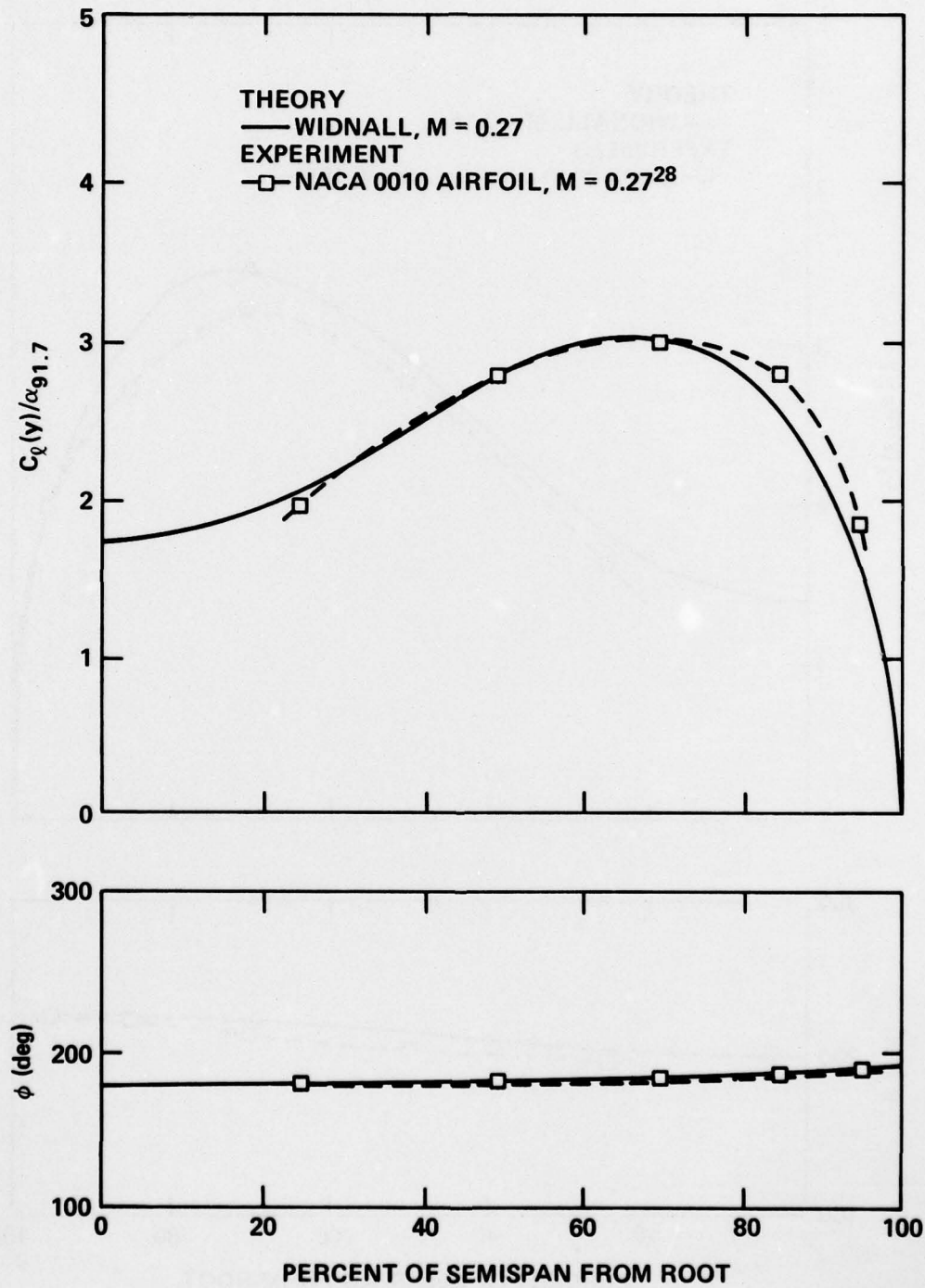


Figure 43e - Magnitude and Phase Angle of Lift Coefficient due to Torsion at  $k = 0.1$

Figure 43 (Continued)

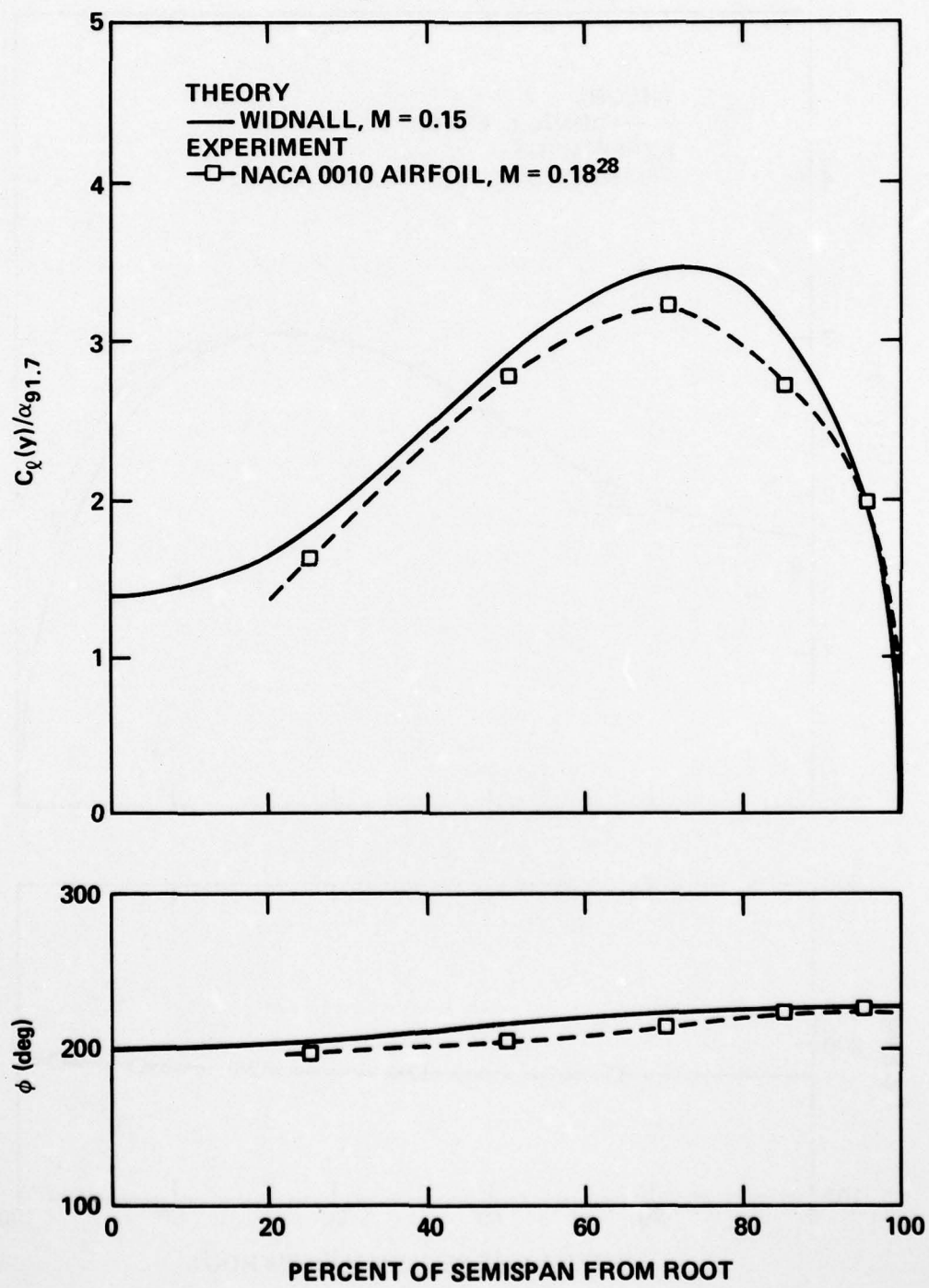


Figure 43f - Magnitude and Phase Angle of Lift Coefficient due to Torsion at  $k = 0.5$

Figure 43 (Continued)

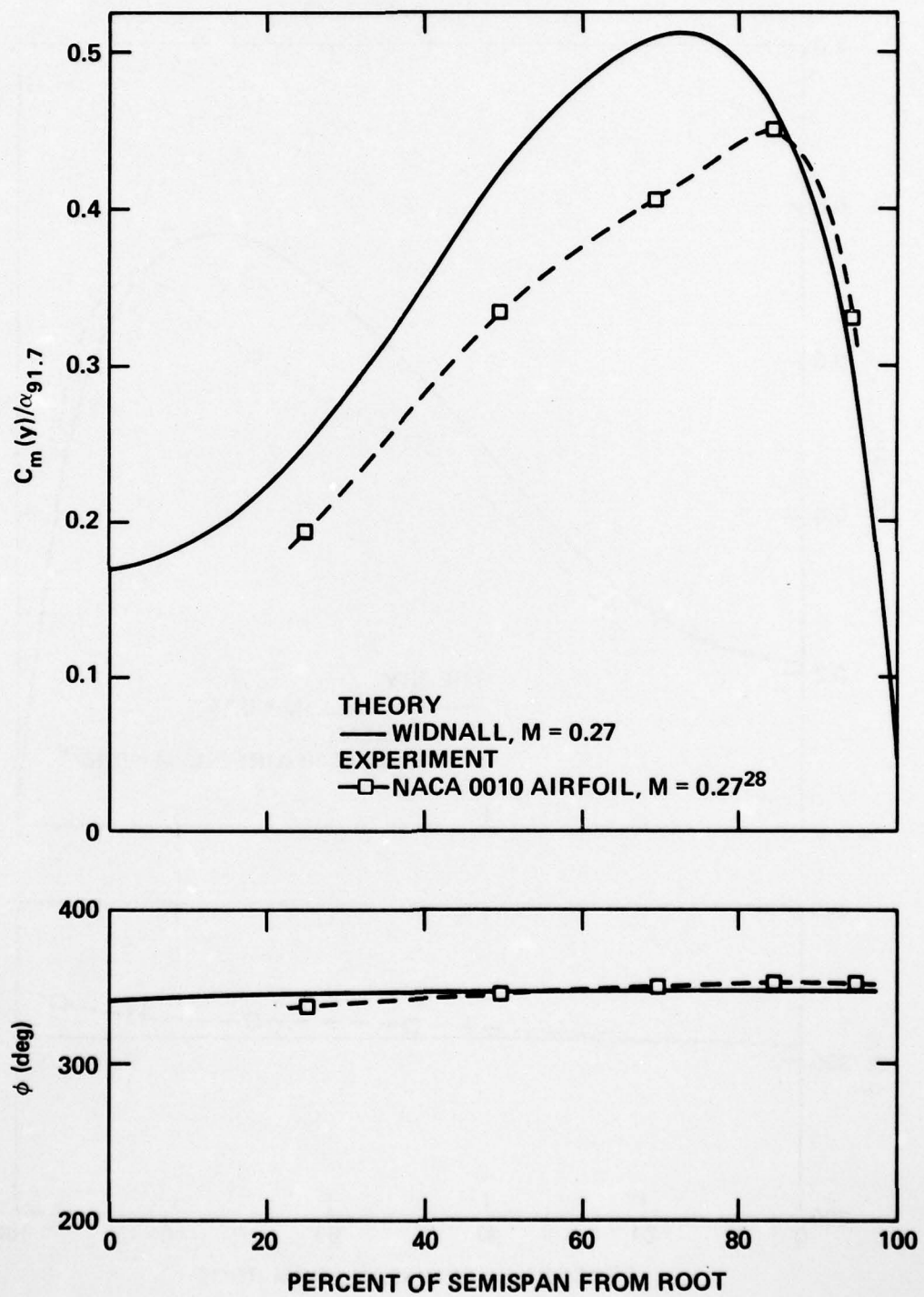


Figure 43g - Magnitude and Phase Angle of Pitching Moment Coefficient due to Torsion at  $k = 0.1$

Figure 43 (Continued)

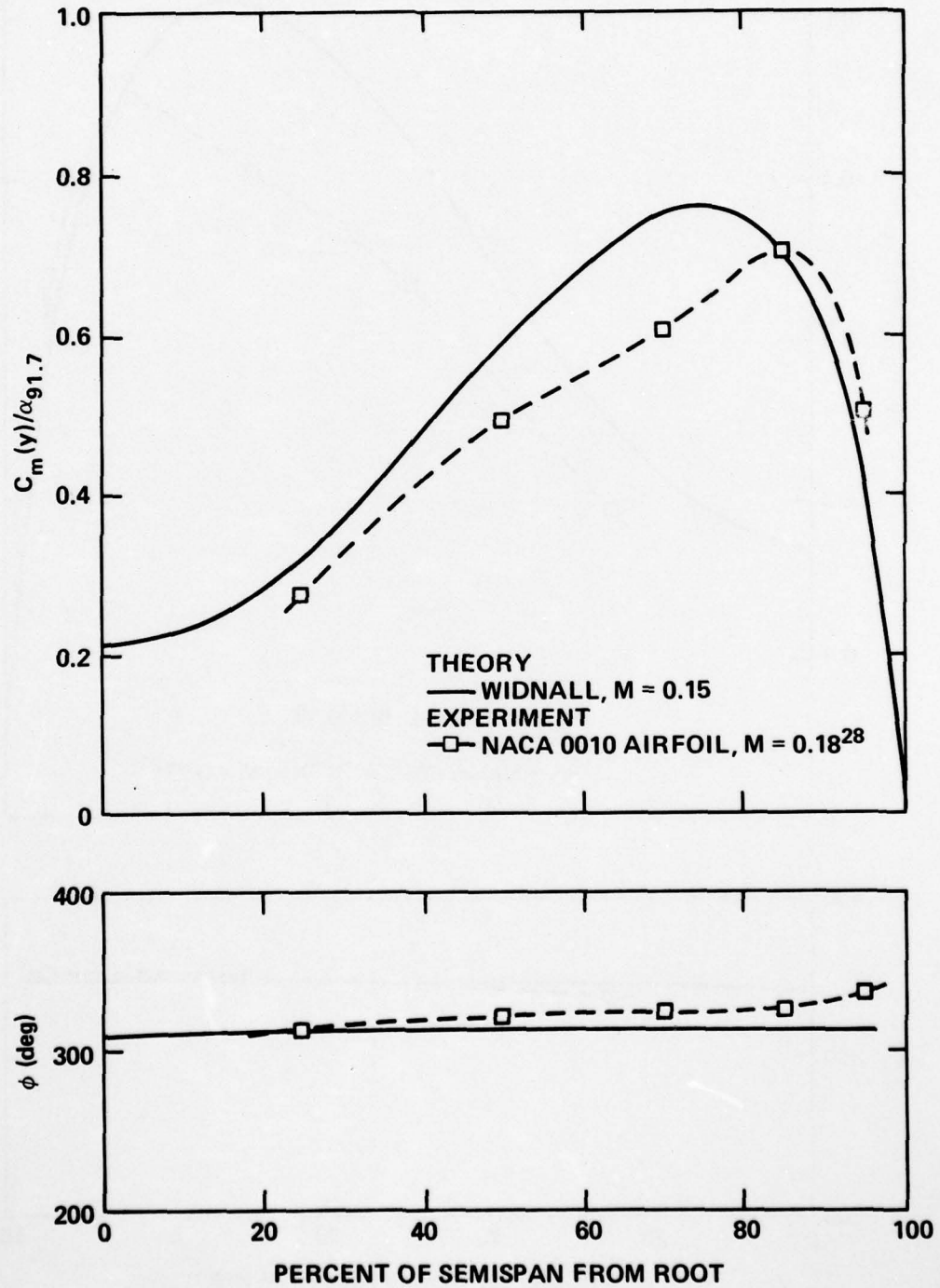


Figure 43h - Magnitude and Phase Angle of Pitching Moment Coefficient due to Torsion at  $k = 0.5$

Figure 44 - Spanwise Distributions of Unsteady Loading due to Bending and Torsional Oscillations for the NACA 0010 Hydrofoil  
 $(\Lambda = 0; \tau = 1; AR = 5)$

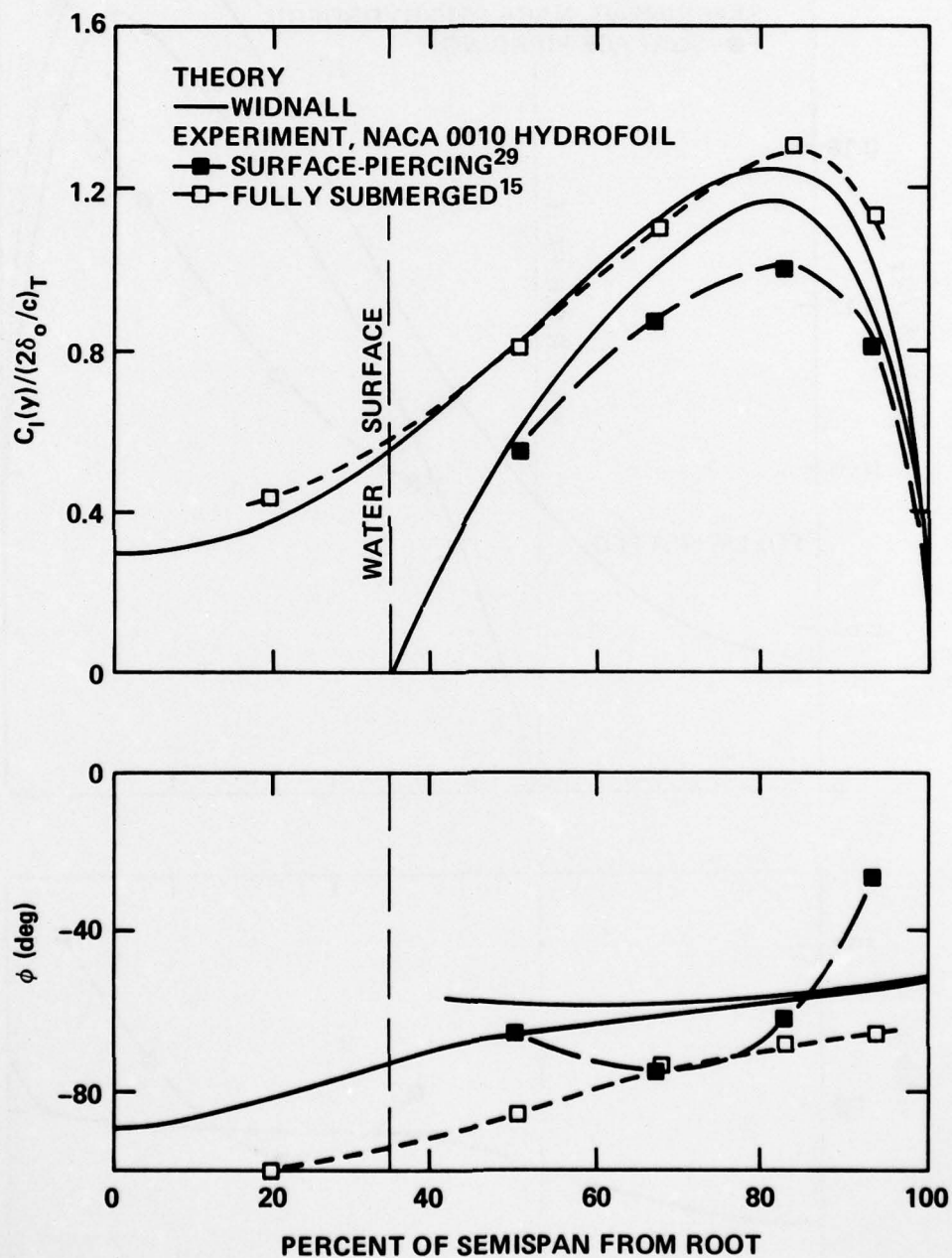


Figure 44a - Magnitude and Phase Angle of Lift Coefficient due to Bending at  $k = 0.6$

Figure 44 (Continued)

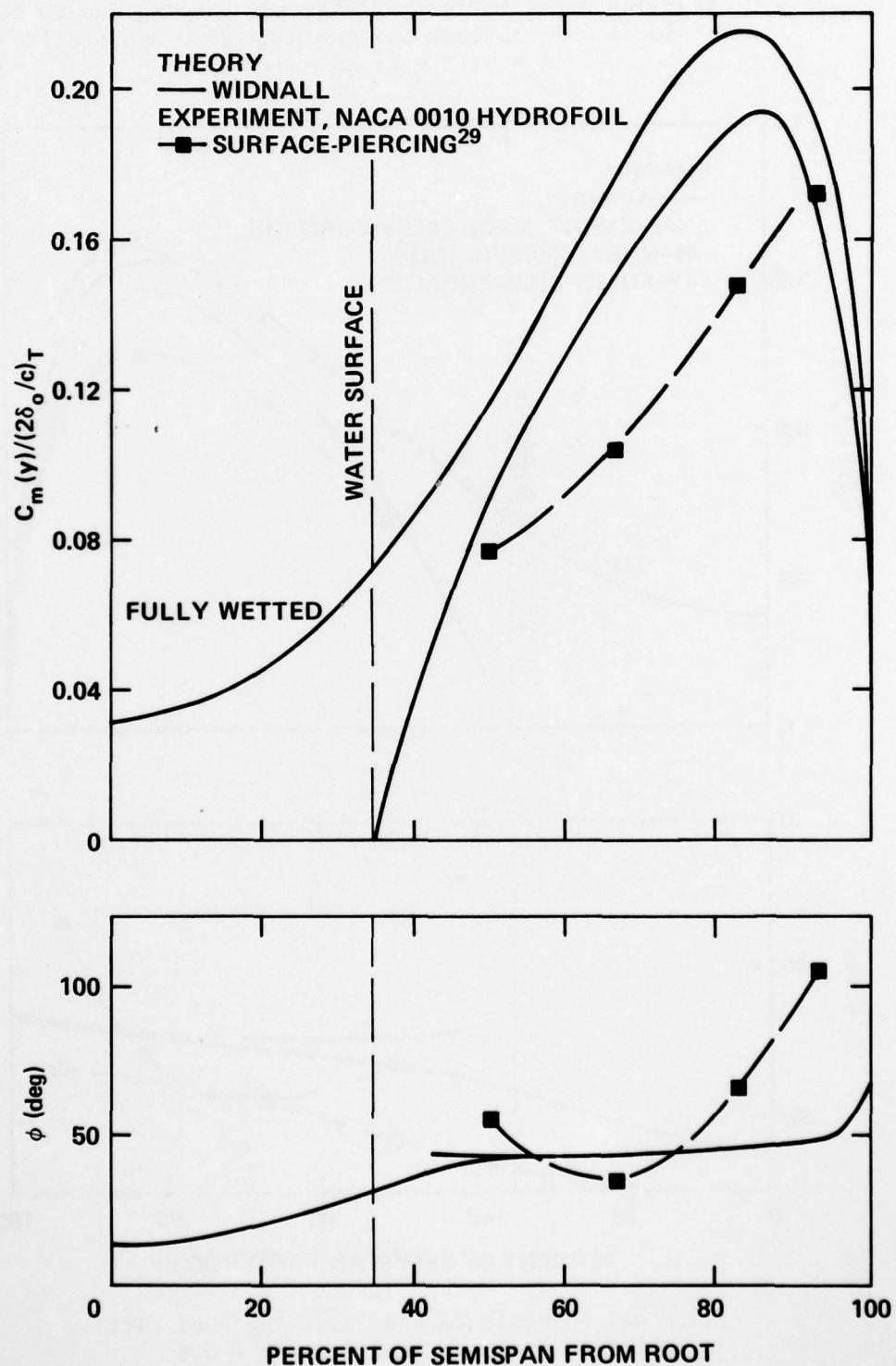


Figure 44b - Magnitude and Phase Angle of Pitching Moment Coefficient due to Bending at  $k = 0.6$

Figure 44 (Continued)

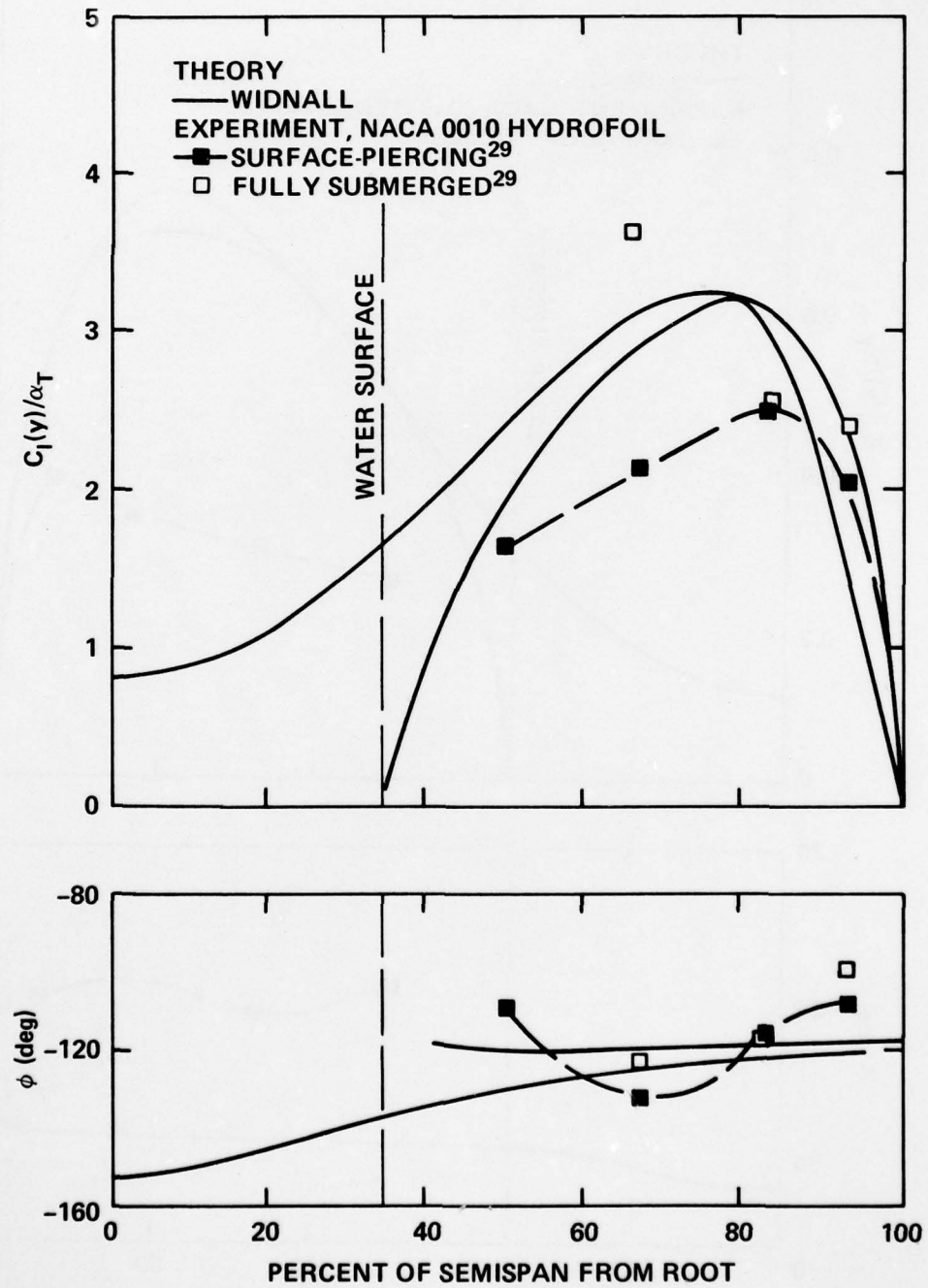


Figure 44c - Magnitude and Phase Angle of Lift Coefficient due to Torsion at  $k = 0.6$

AD-A074 702

DAVID W TAYLOR NAVAL SHIP RESEARCH AND DEVELOPMENT CE--ETC F/G 13/10  
ACCURACY OF HYDROFOIL LOADING PREDICTIONS OBTAINED FROM A LIFTI--ETC(U)  
SEP 79 P K BESCH, E P ROOD

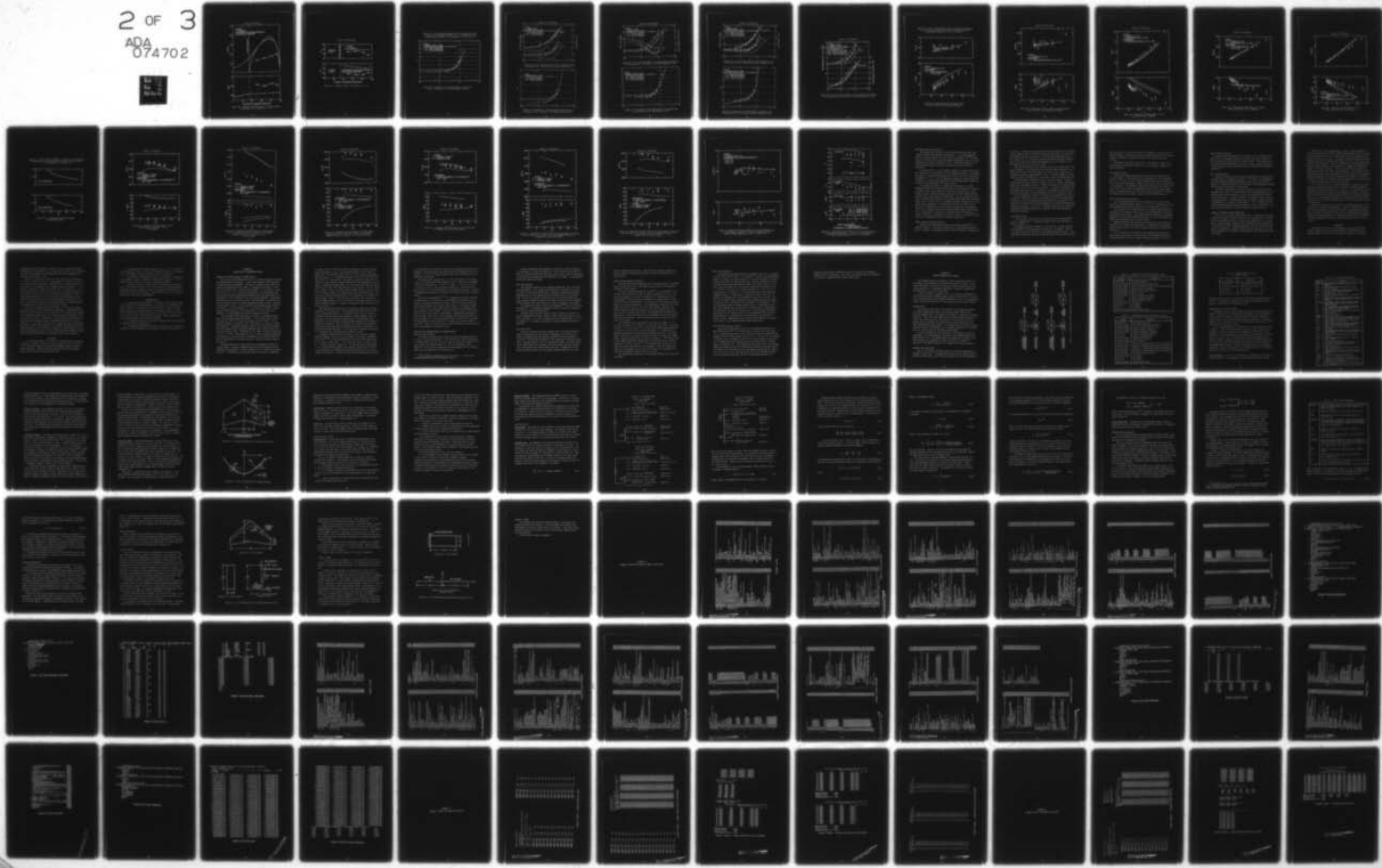
UNCLASSIFIED

DTNSRDC-79/039

NL

2 OF 3  
ADA  
074702

SEE  
BACK



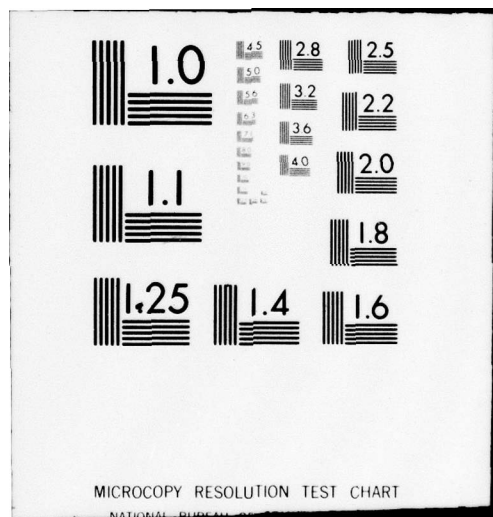


Figure 44 (Continued)

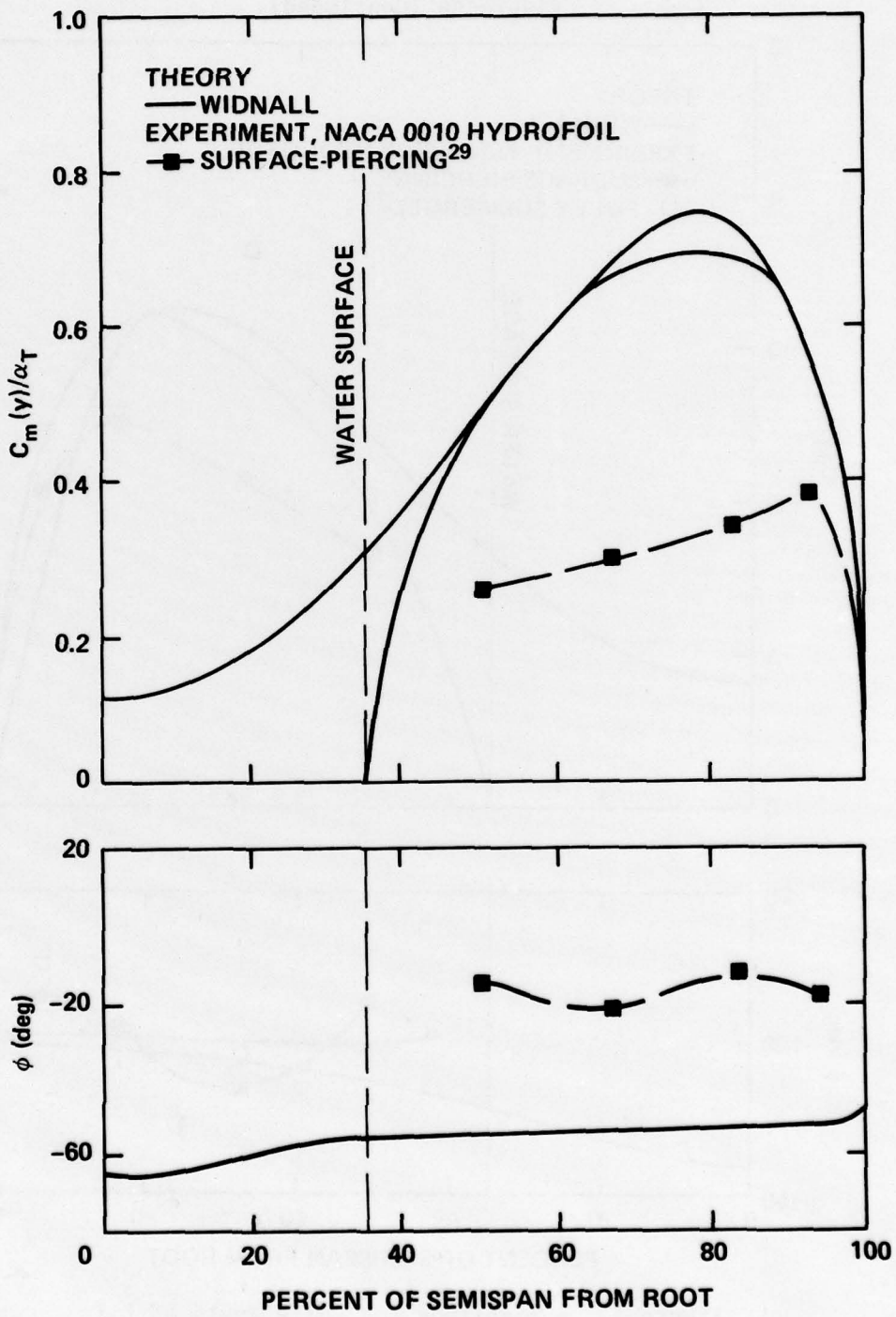


Figure 44d - Magnitude and Phase Angle of Pitching Moment Coefficient due to Torsion at  $k = 0.6$

Figure 44 (Continued)

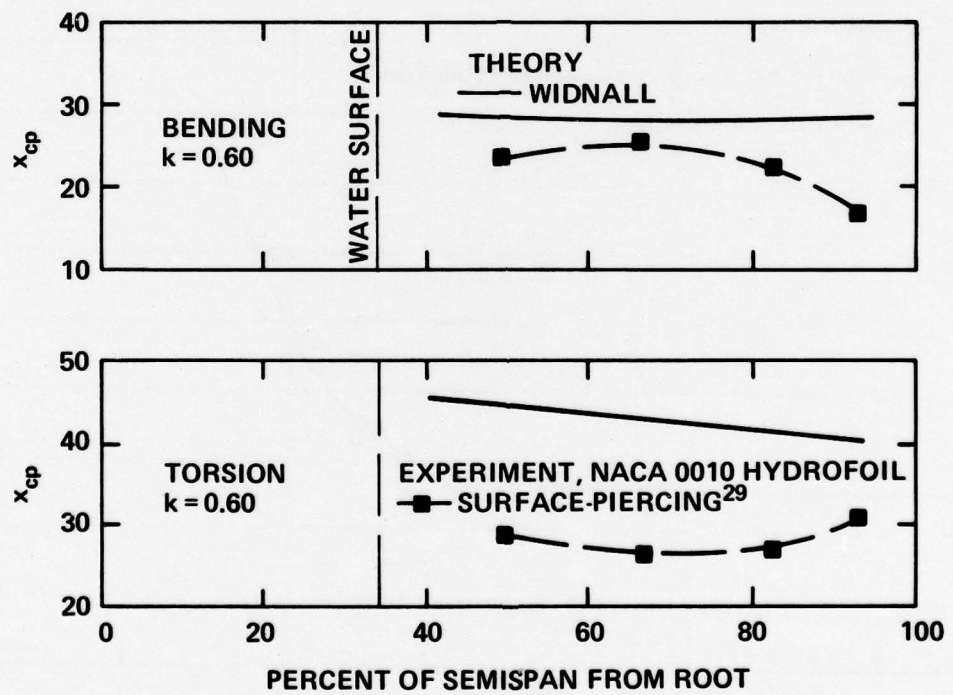


Figure 44e - Unsteady Center of Pressure at  $k = 0.6$

Figure 45 - Total Unsteady Loading due to Pitching Oscillation  
as a Function of Reduced Frequency for the One-Twelfth-Scale  
AGEH-1 Hydrofoil Model ( $\Lambda = 35$  Degrees;  $\tau = 0.3$ ; AR = 3)

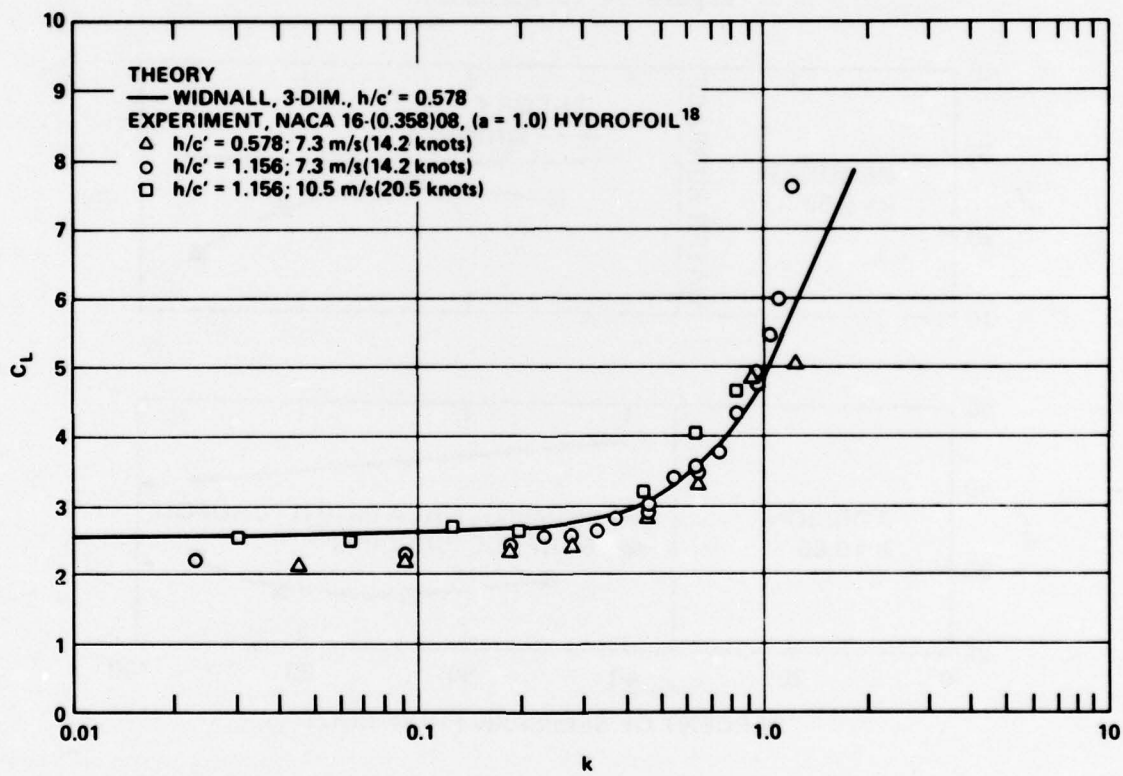


Figure 45a - Magnitude of Lift Coefficient, for Pitching  
Axis at 32 Percent of the Mean Geometric Chord

Figure 45 (Continued)

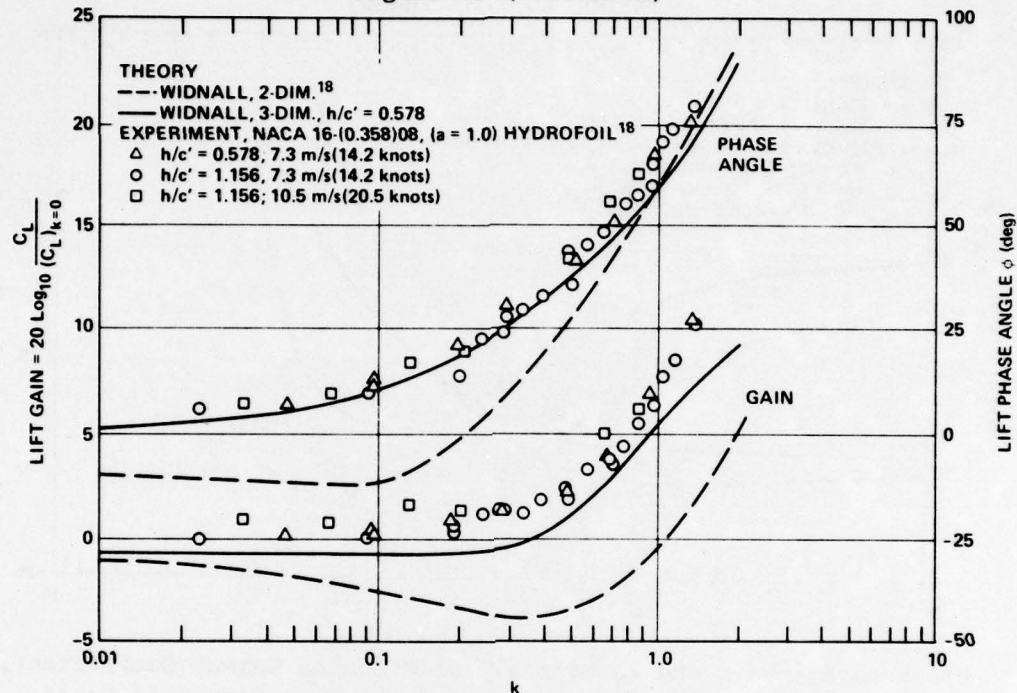


Figure 45b - Gain and Phase Angle of Lift Coefficient, for Pitching Axis at 32 Percent of the Mean Geometric Chord

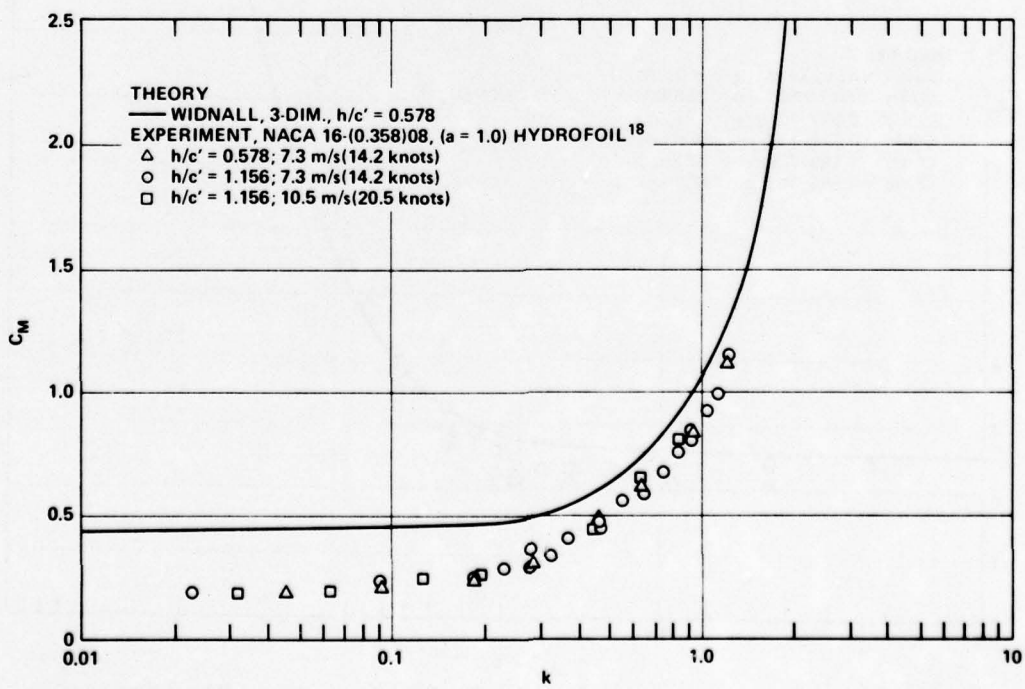


Figure 45c - Magnitude of Pitching Moment Coefficient, for Pitching Axis at 32 Percent of the Mean Geometric Chord

Figure 45 (Continued)

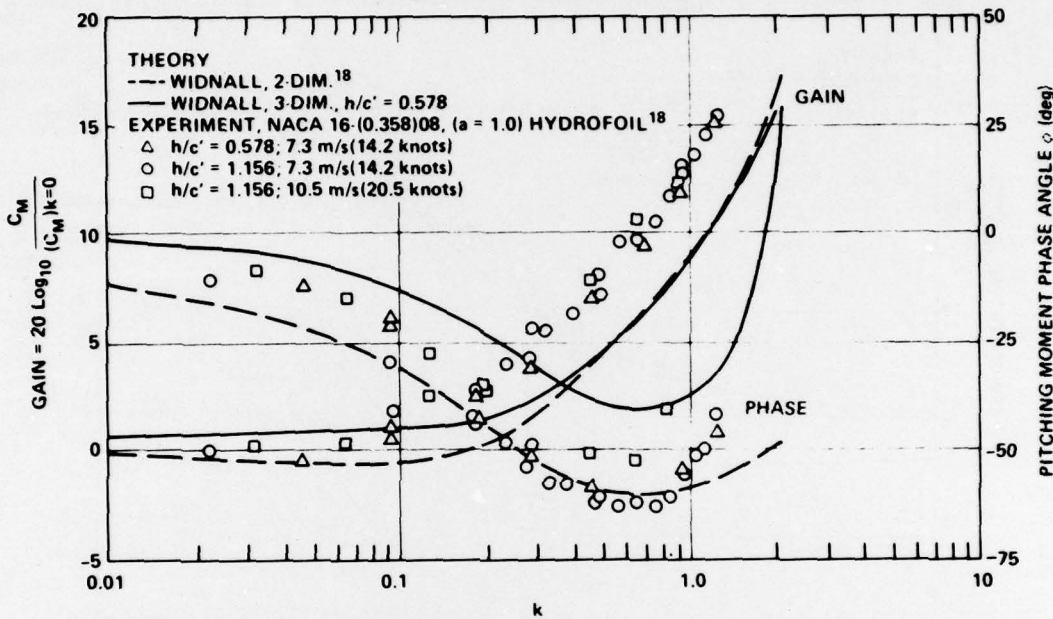


Figure 45d - Gain and Phase Angle of Pitching Moment Coefficient, for Pitching Axis at 32 Percent of the Mean Geometric Chord

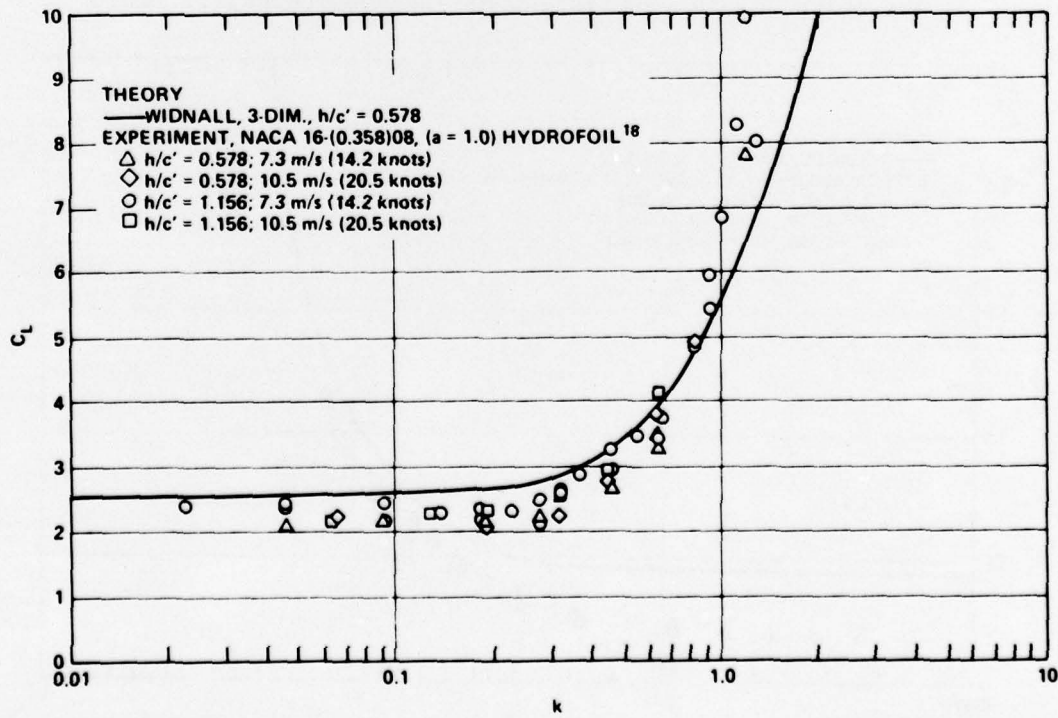


Figure 45e - Magnitude of Lift Coefficient, for Pitching Axis at 6.2 Percent of the Mean Geometric Chord

Figure 45 (Continued)

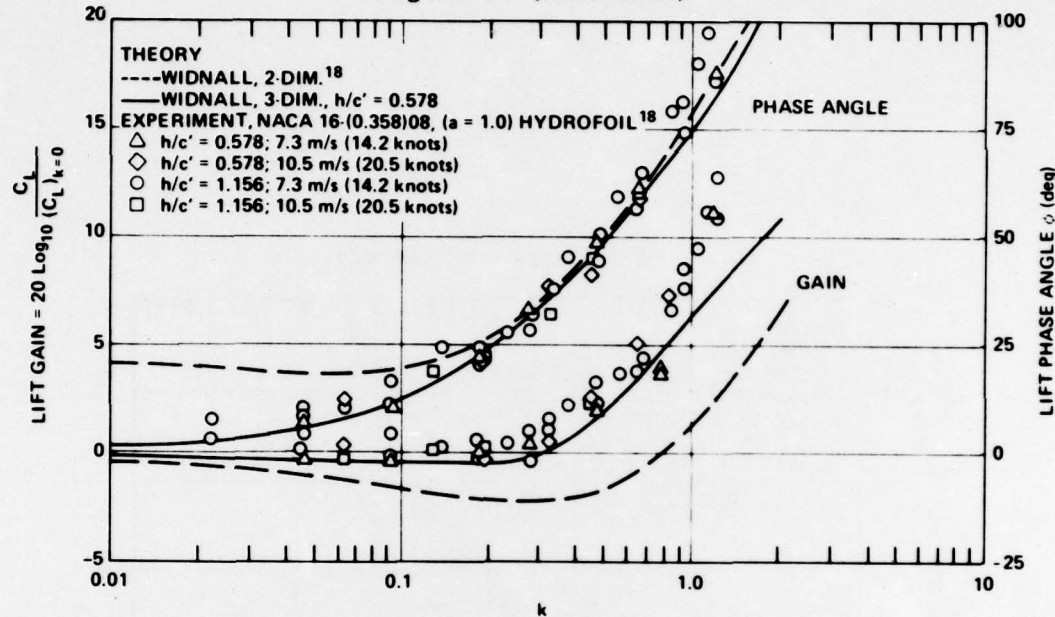


Figure 45f - Gain and Phase Angle of Lift Coefficient, for Pitching Axis at 6.2 Percent of the Mean Geometric Chord

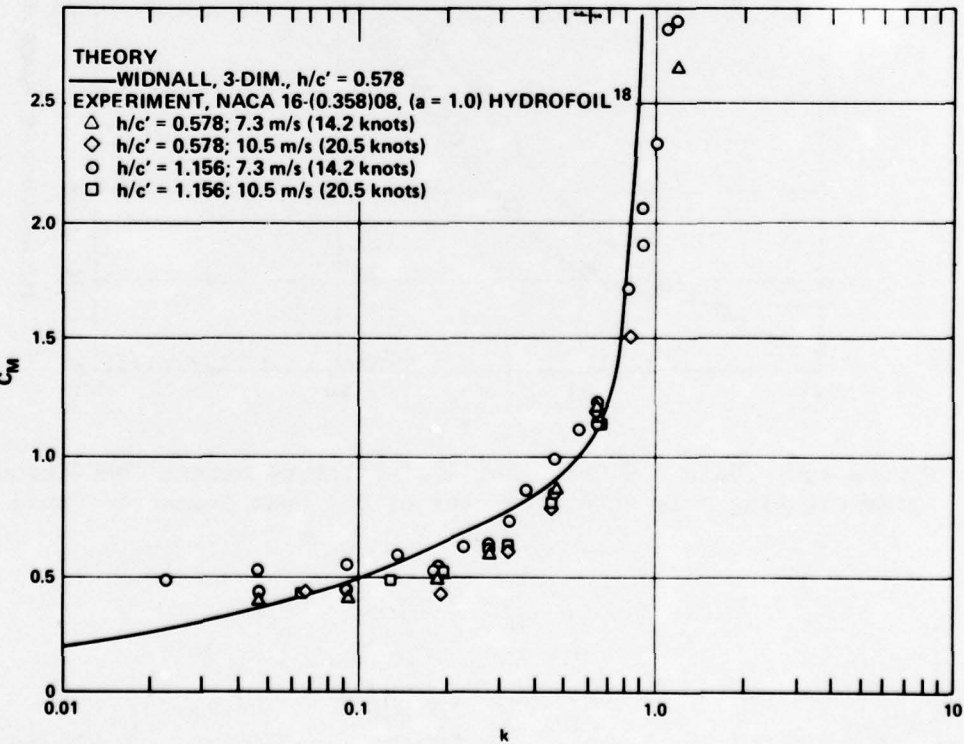


Figure 45g - Magnitude of Pitching Moment Coefficient, for Pitching Axis at 6.2 Percent of the Mean Geometric Chord

Figure 45 (Continued)

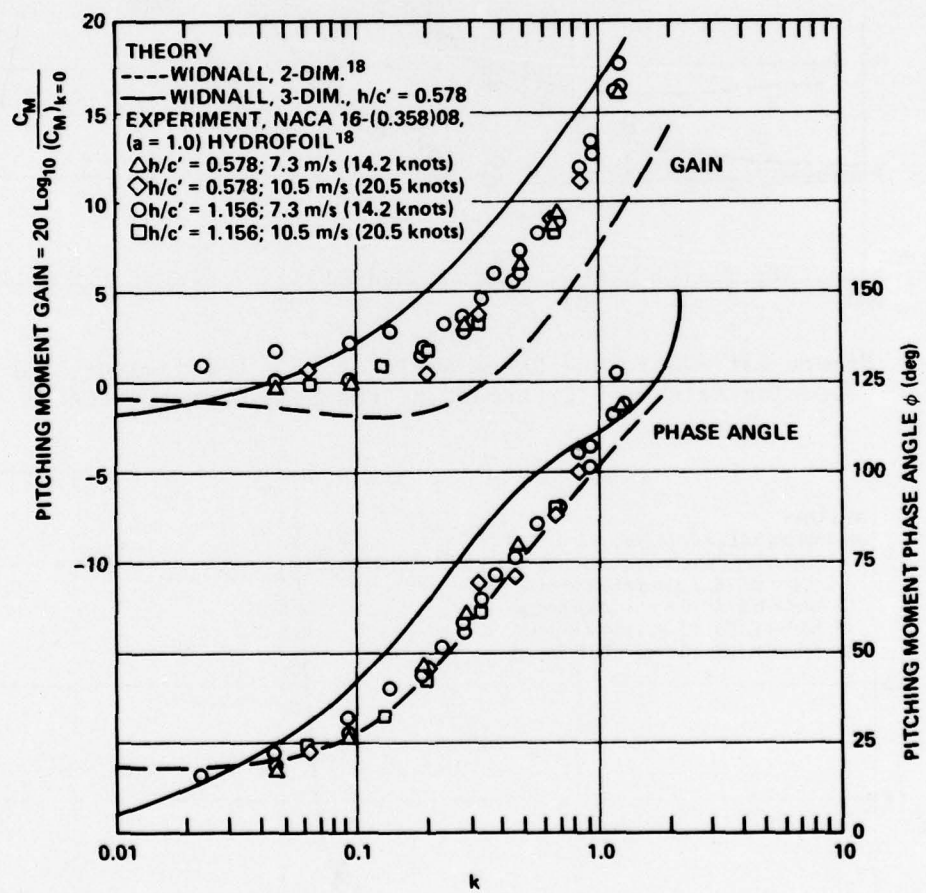


Figure 45h - Gain and Phase Angle of Pitching Moment Coefficient,  
for Pitching Axis at 6.2 Percent of the Mean Geometric Chord

Figure 46 - Total Unsteady Loading due to Pitching and Flapping Oscillations as a Function of Reduced Frequency for the NACA 65A010 Airfoil ( $\Lambda = 0$ ;  $\tau = 1$ ; AR = 2)

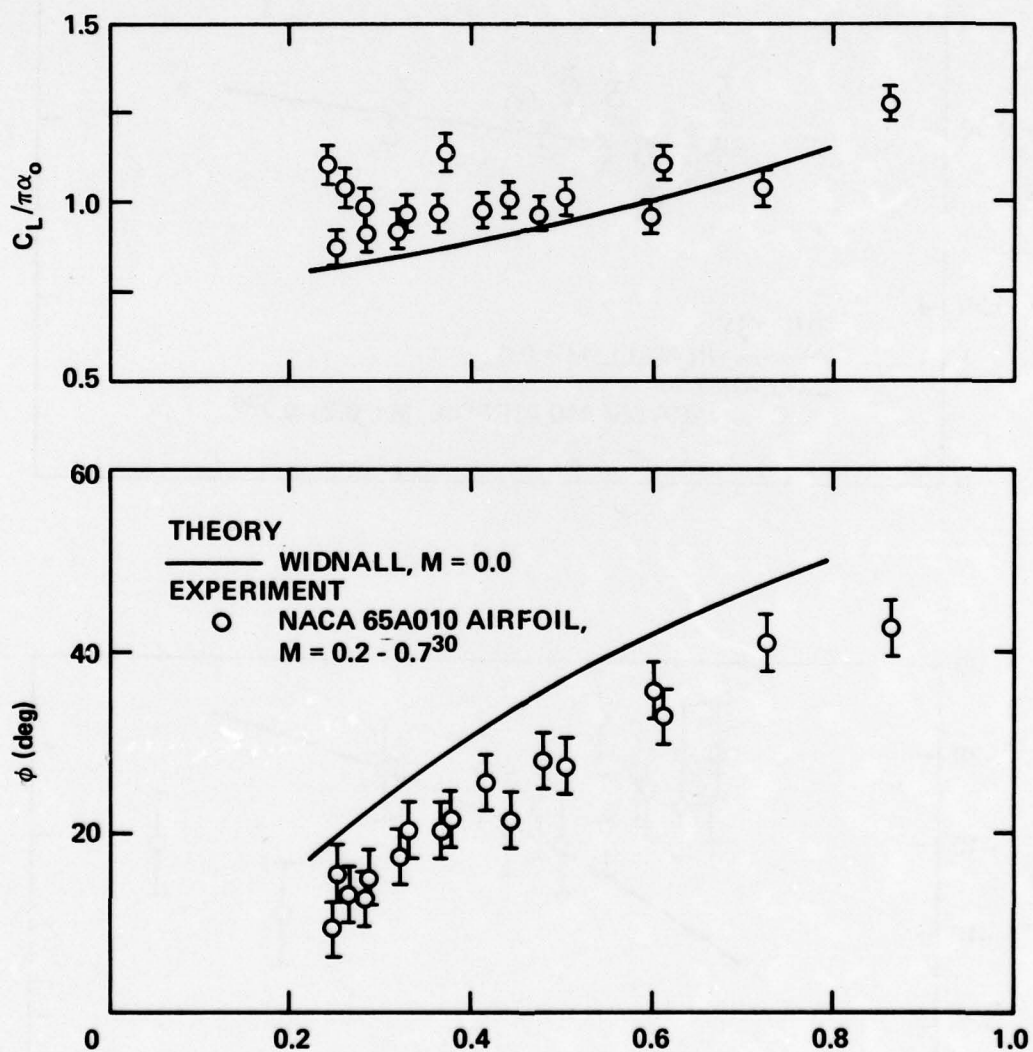


Figure 46a - Magnitude and Phase Angle of Lift Coefficient due to Pitching about Midchord

Figure 46 (Continued)

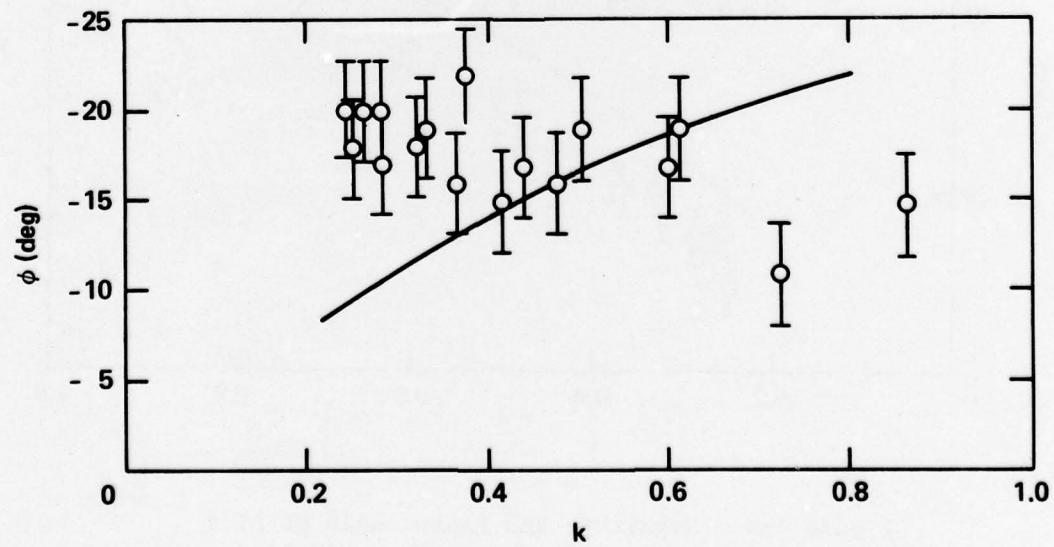
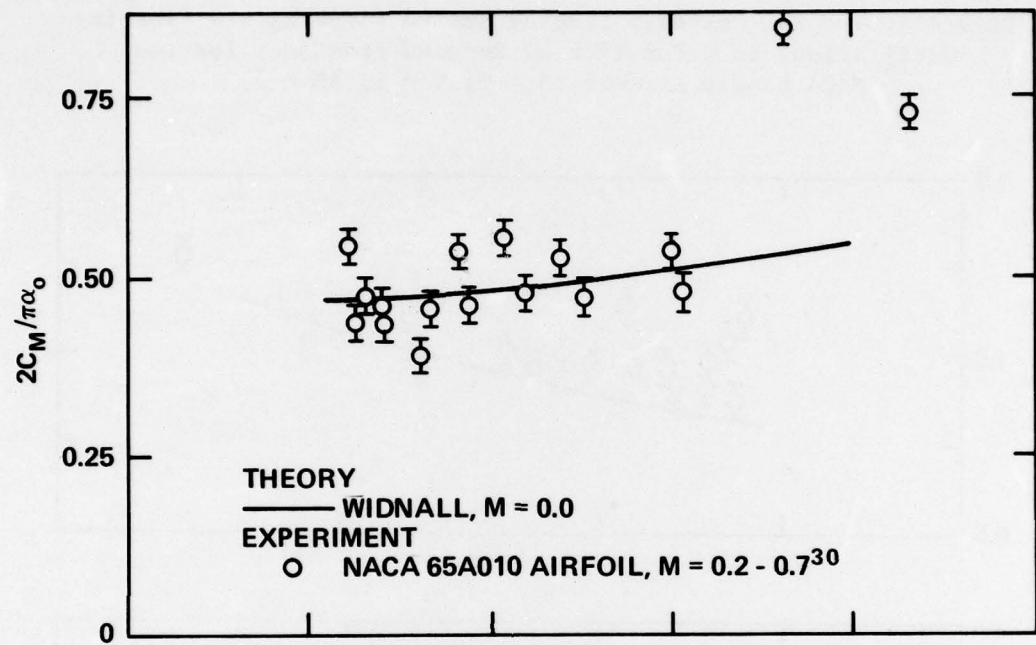


Figure 46b - Magnitude and Phase Angle of Pitching Moment Coefficient due to Pitching about Midchord

Figure 46 (Continued)

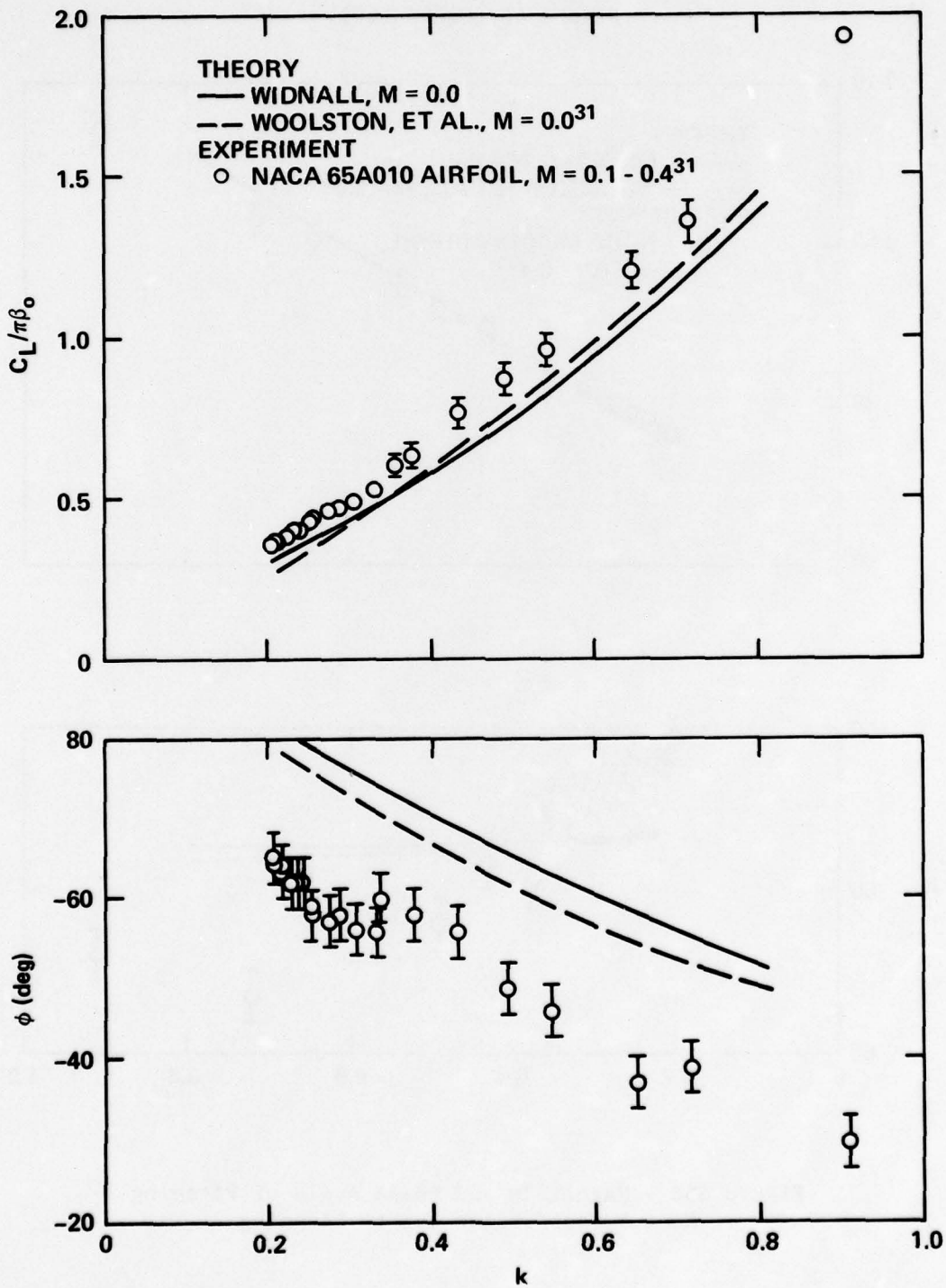


Figure 46c - Magnitude and Phase Angle of Lift Coefficient due to Flapping

Figure 46 (Continued)

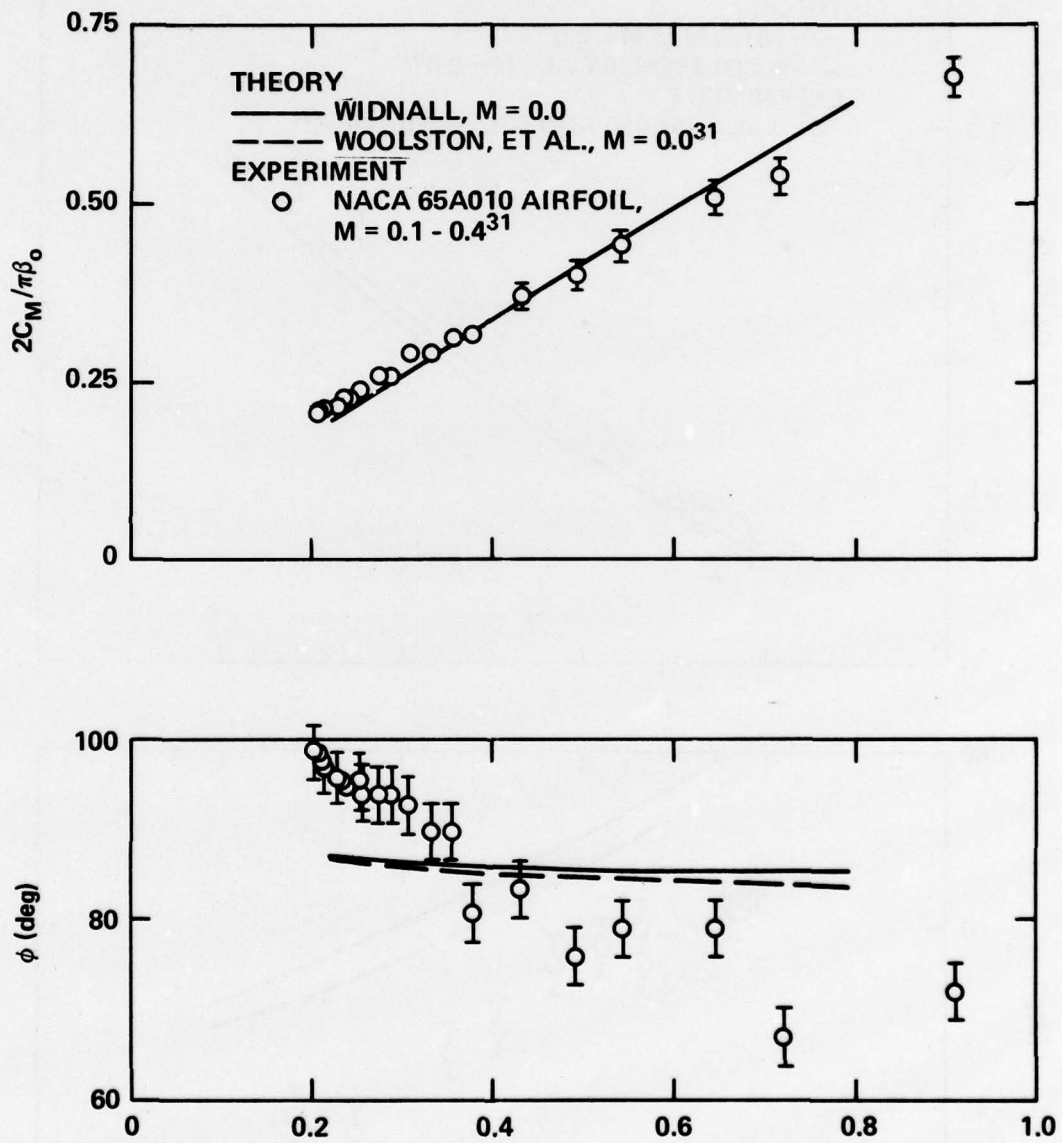


Figure 46d - Magnitude and Phase Angle of Pitching Moment Coefficient due to Flapping

Figure 46 (Continued)

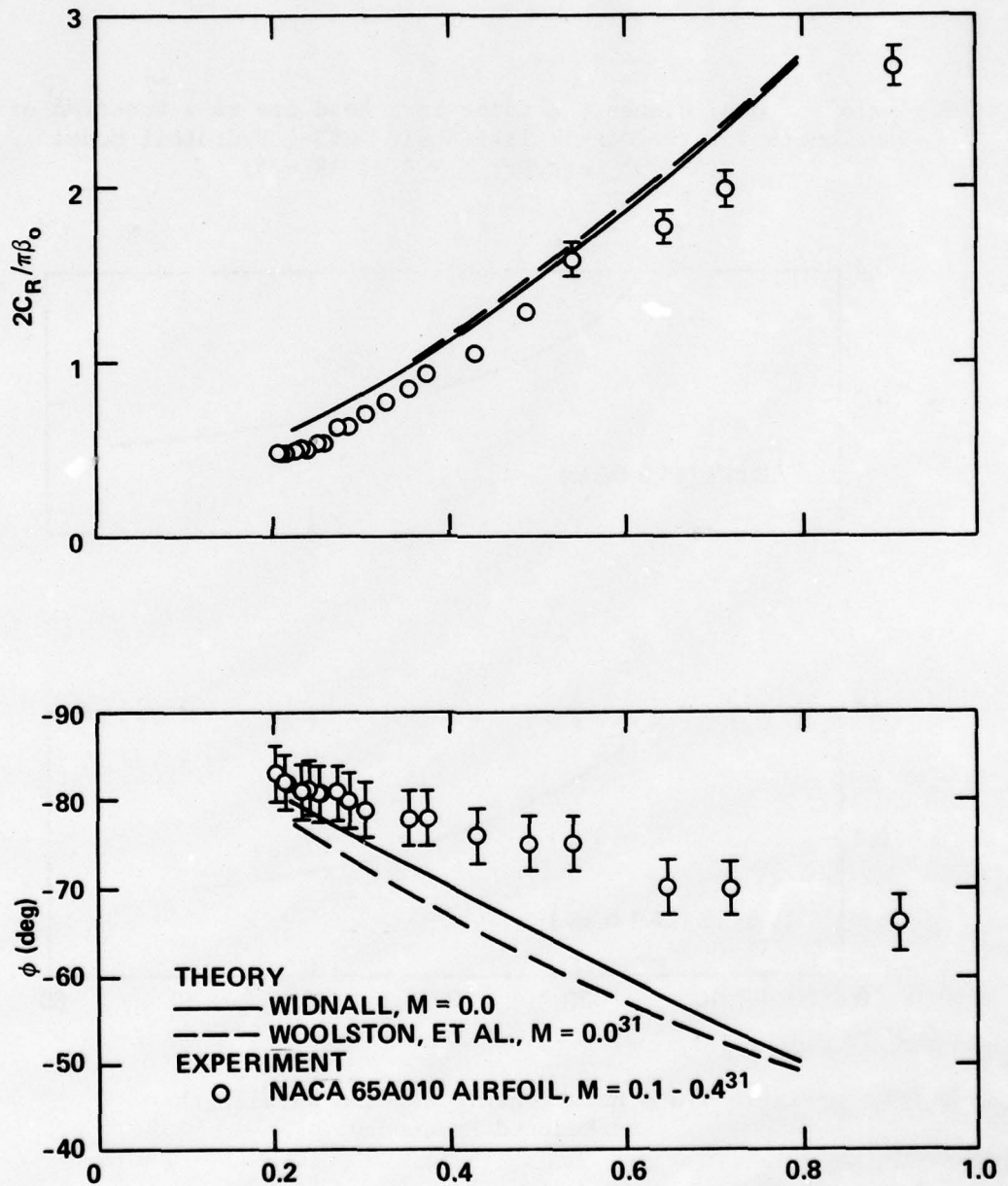


Figure 46e - Magnitude and Phase Angle of Roll Moment Coefficient due to Flapping

Figure 47 - Total Unsteady Loading in a Head Sea as a Function of Wavelength for the One-Twelfth-Scale AGEH-1 Hydrofoil Model  
( $\Lambda = 35$  Degrees;  $\tau = 0.3$ ; AR = 3)

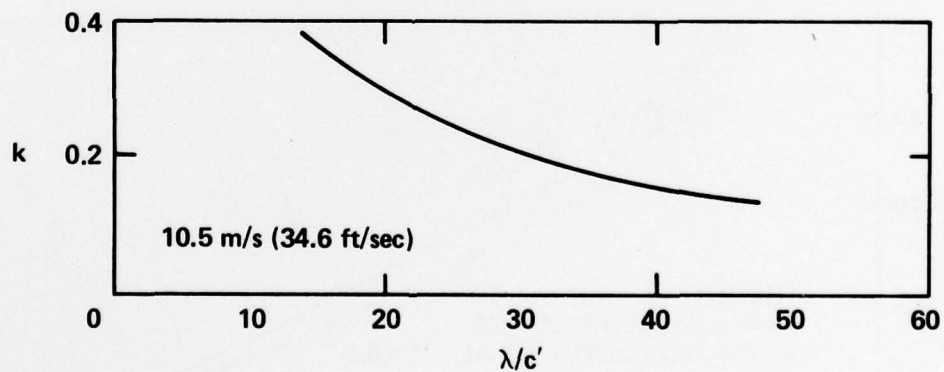
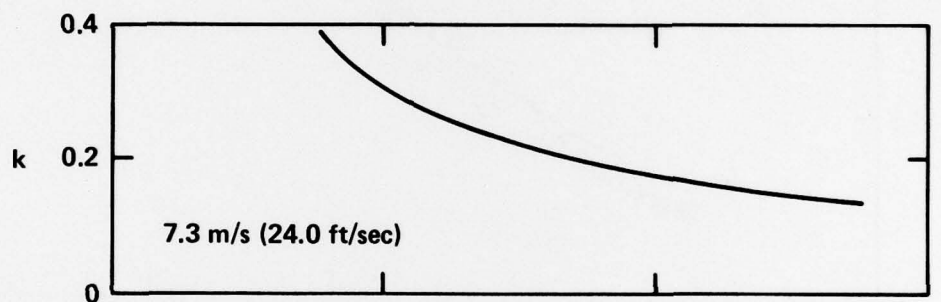


Figure 47a - Relationship between Wavelength and Reduced Frequency

Figure 47 (Continued)

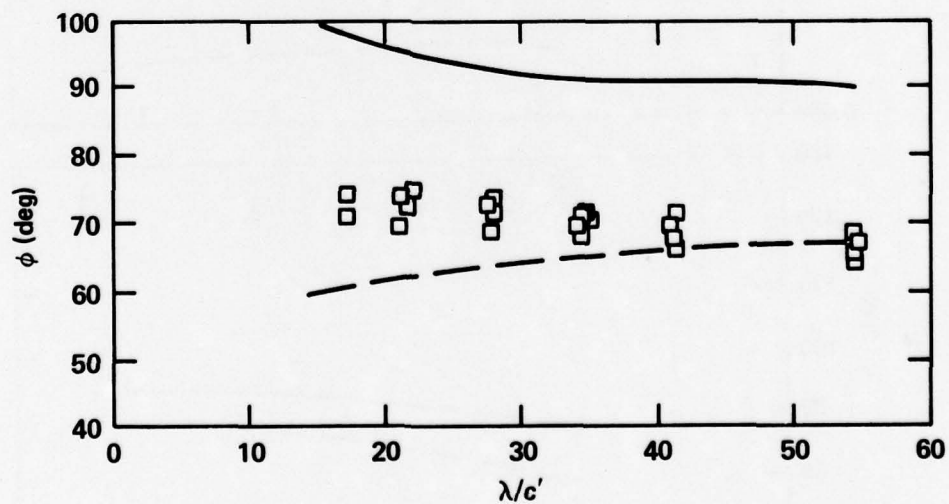
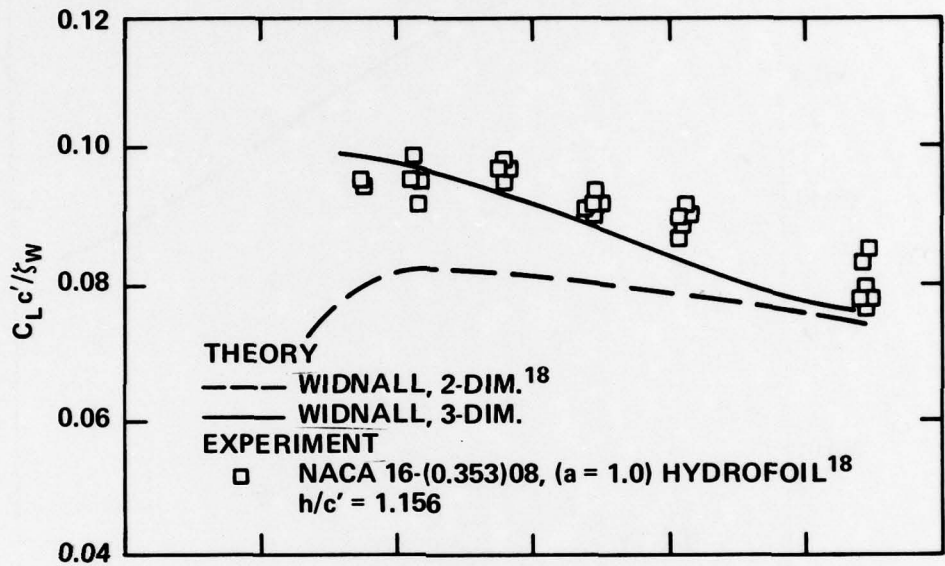


Figure 47b - Magnitude and Phase Angle of Lift Coefficient at a Speed of 7.3 m/s (24.0 ft/sec)

Figure 47 (Continued)

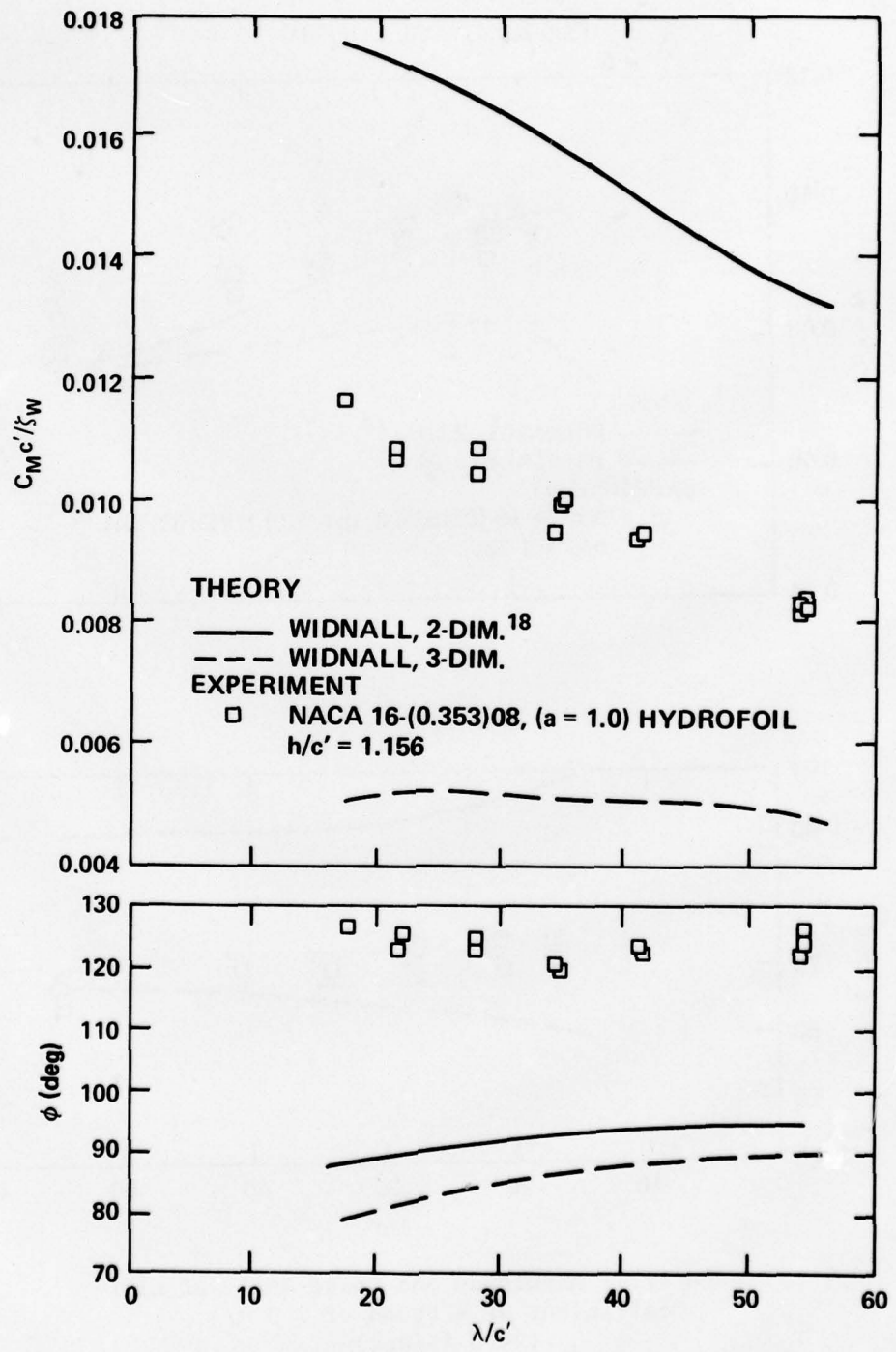


Figure 47c - Magnitude and Phase Angle of Pitching Moment Coefficient about an Axis at 32 Percent of the Mean Geometric Chord, at a Speed of 7.3 m/s (24.0 ft/sec)

Figure 47 (Continued)

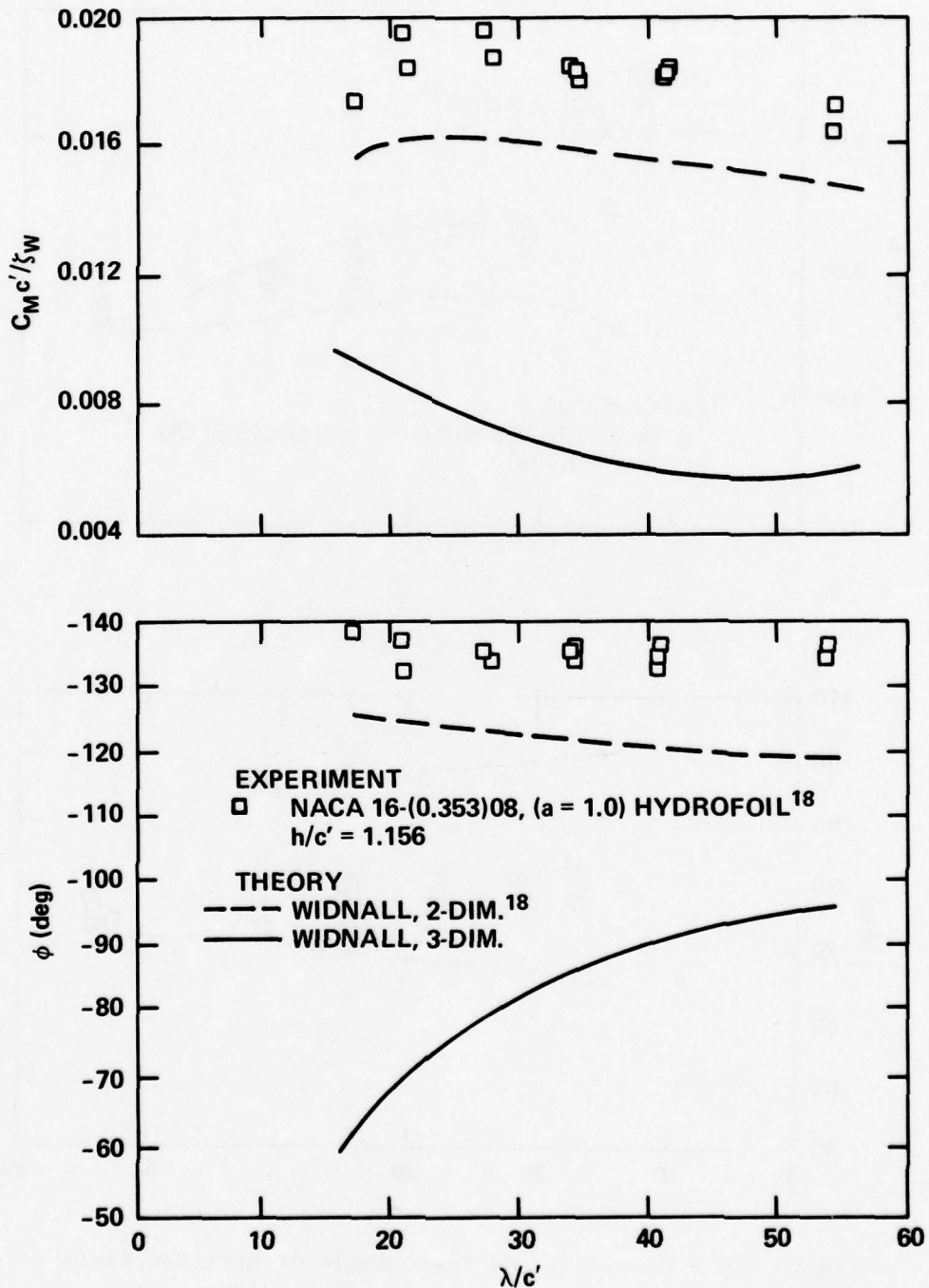


Figure 47d - Magnitude and Phase Angle of Pitching Moment Coefficient about an Axis at 6.2 Percent of the Mean Geometric Chord, at a Speed of 7.3 m/s (24.0 ft/sec)

Figure 47 (Continued)

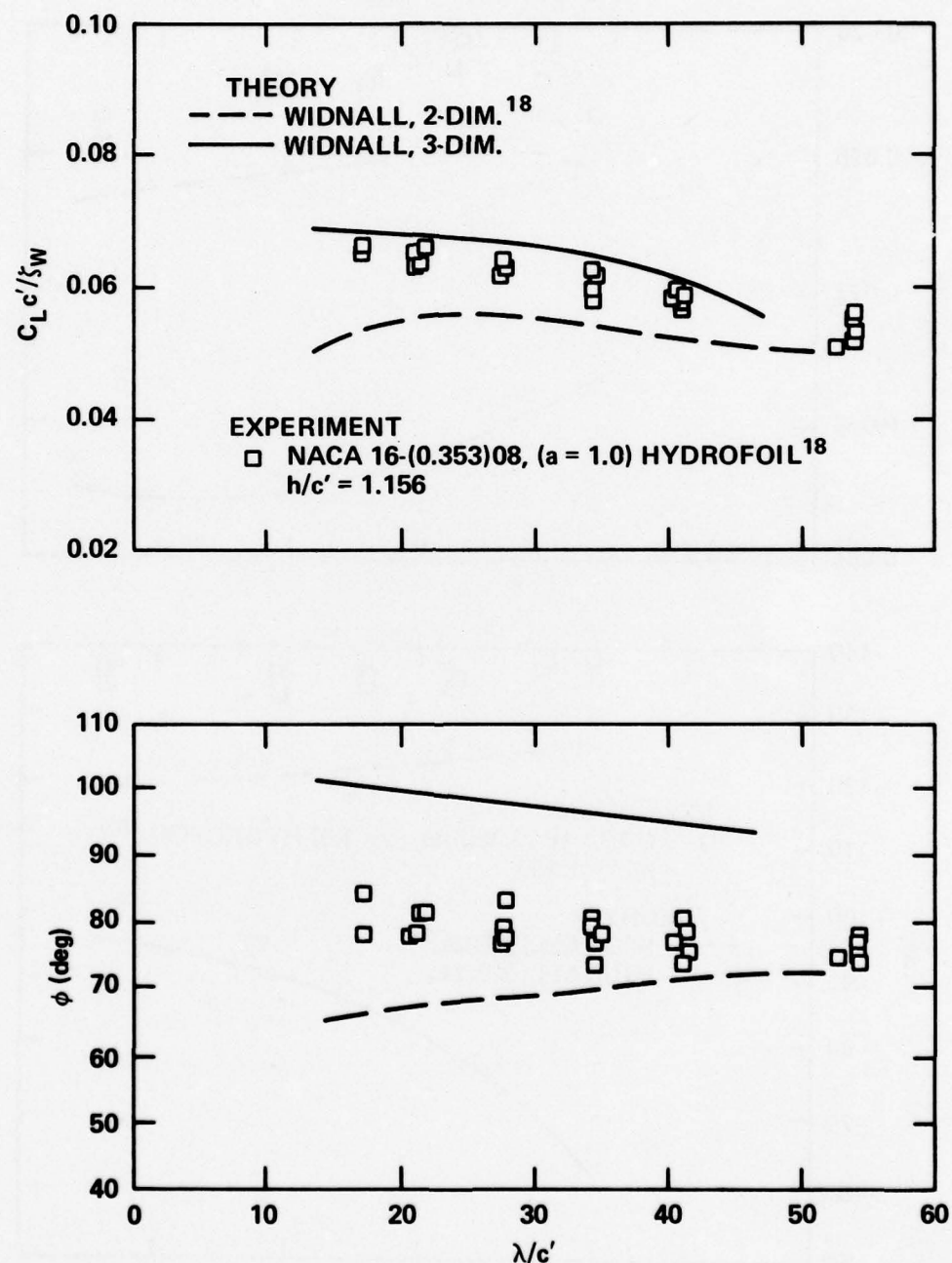


Figure 47 (Continued)

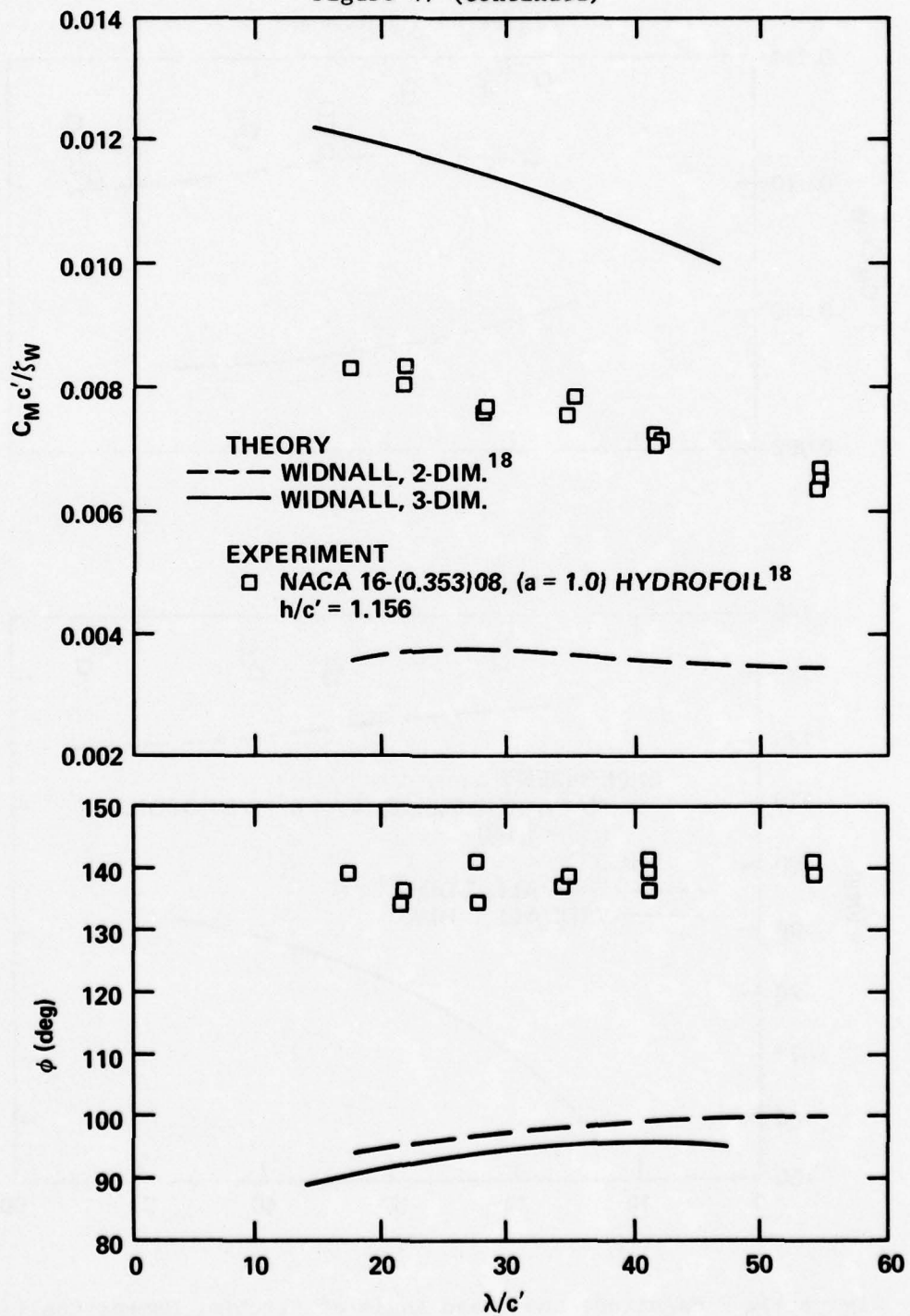


Figure 47f - Magnitude and Phase Angle of Pitching Moment Coefficient about an Axis at 32 Percent of the Mean Geometric Chord, at a Speed of 10.5 m/s (34.6 ft/sec)

Figure 47 (Continued)

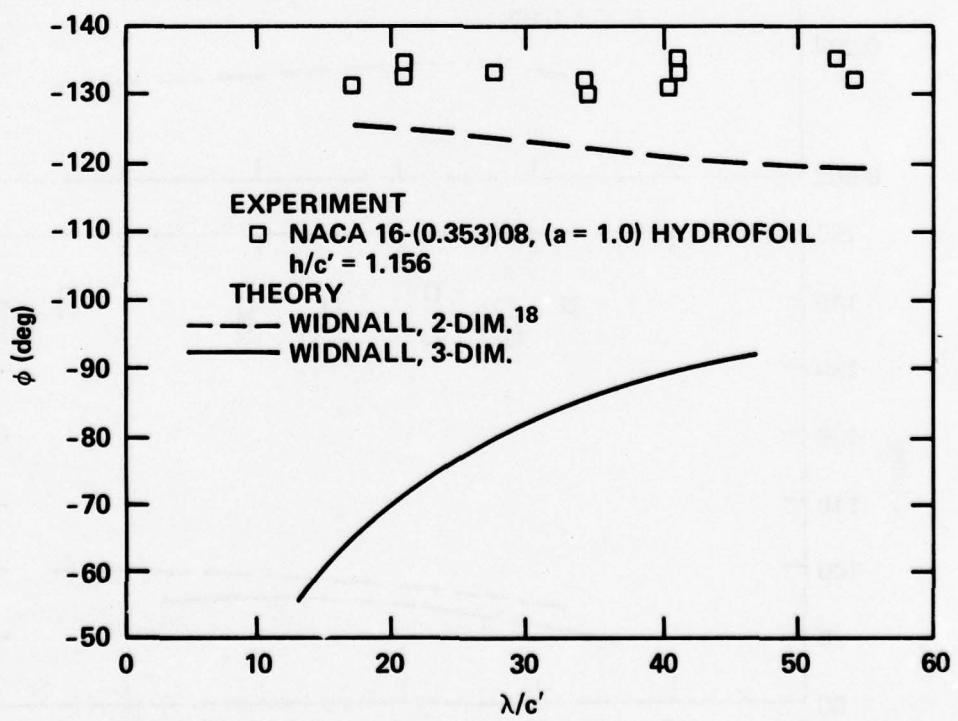
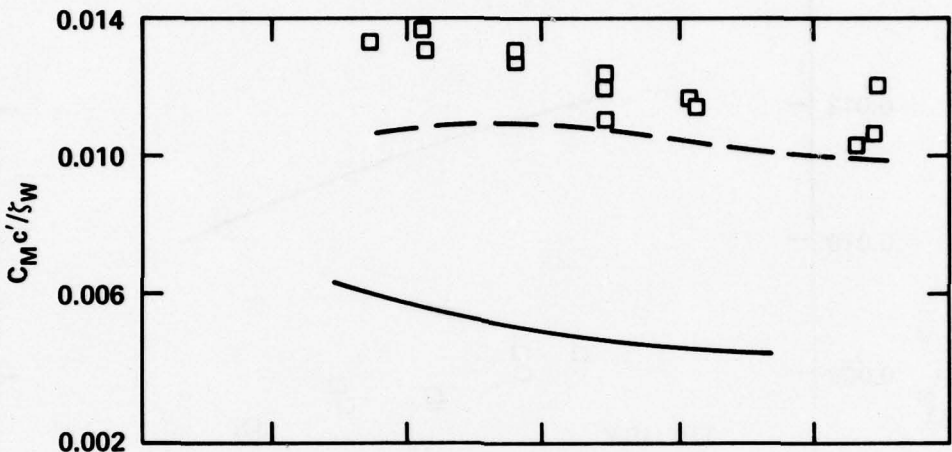


Figure 47g - Magnitude and Phase Angle of Pitching Moment Coefficient about an Axis at 6.2 Percent of the Mean Geometric Chord, at a Speed of 10.5 m/s (34.6 ft/sec)

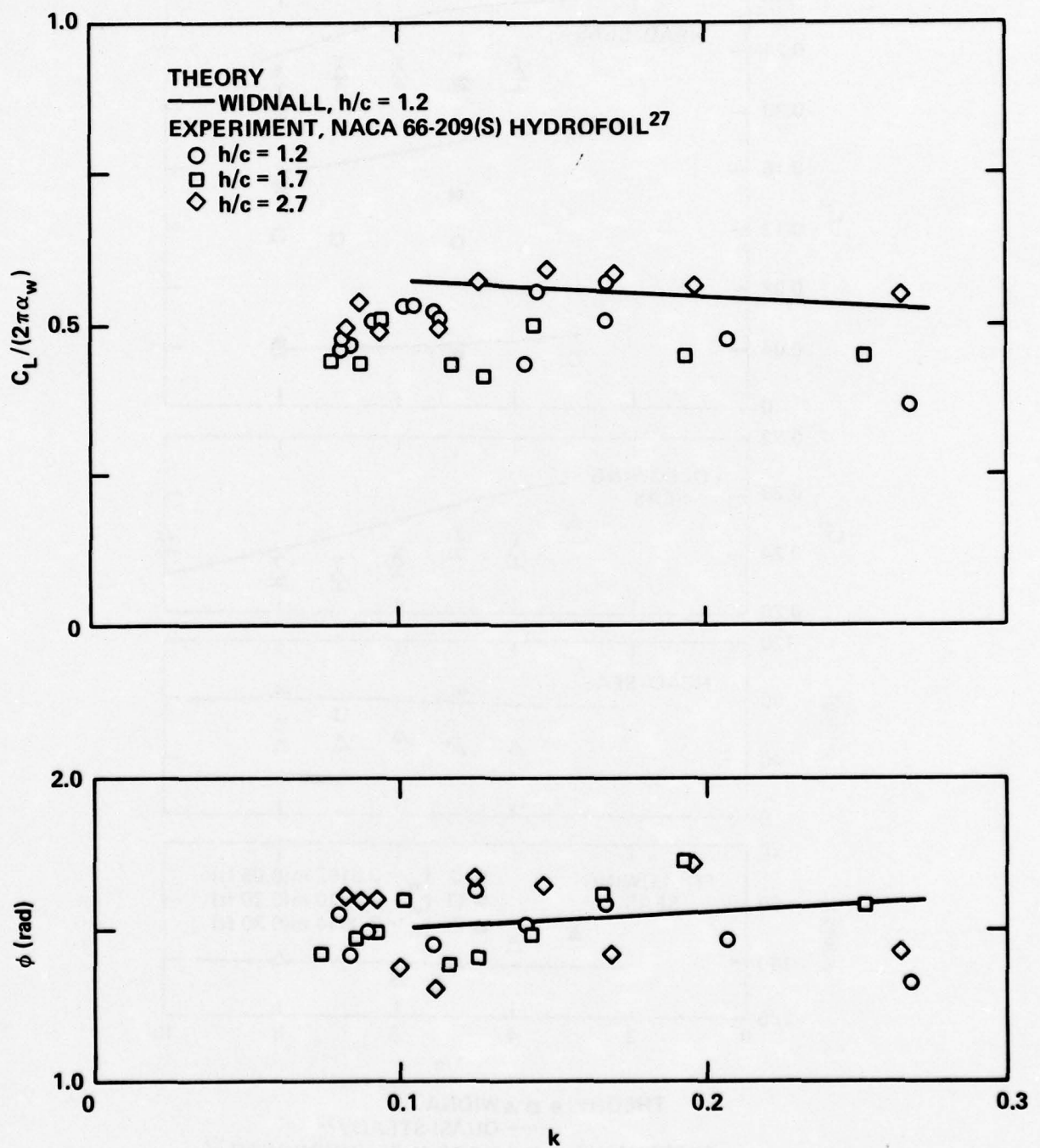


Figure 48 - Magnitude and Phase Angle of the Total Unsteady Lift  
in a Head Sea as a Function of Reduced Frequency for the  
NACA 66-209(S) Hydrofoil ( $\Lambda = 0$ ;  $\tau = 1.0$ ; AR = 5)

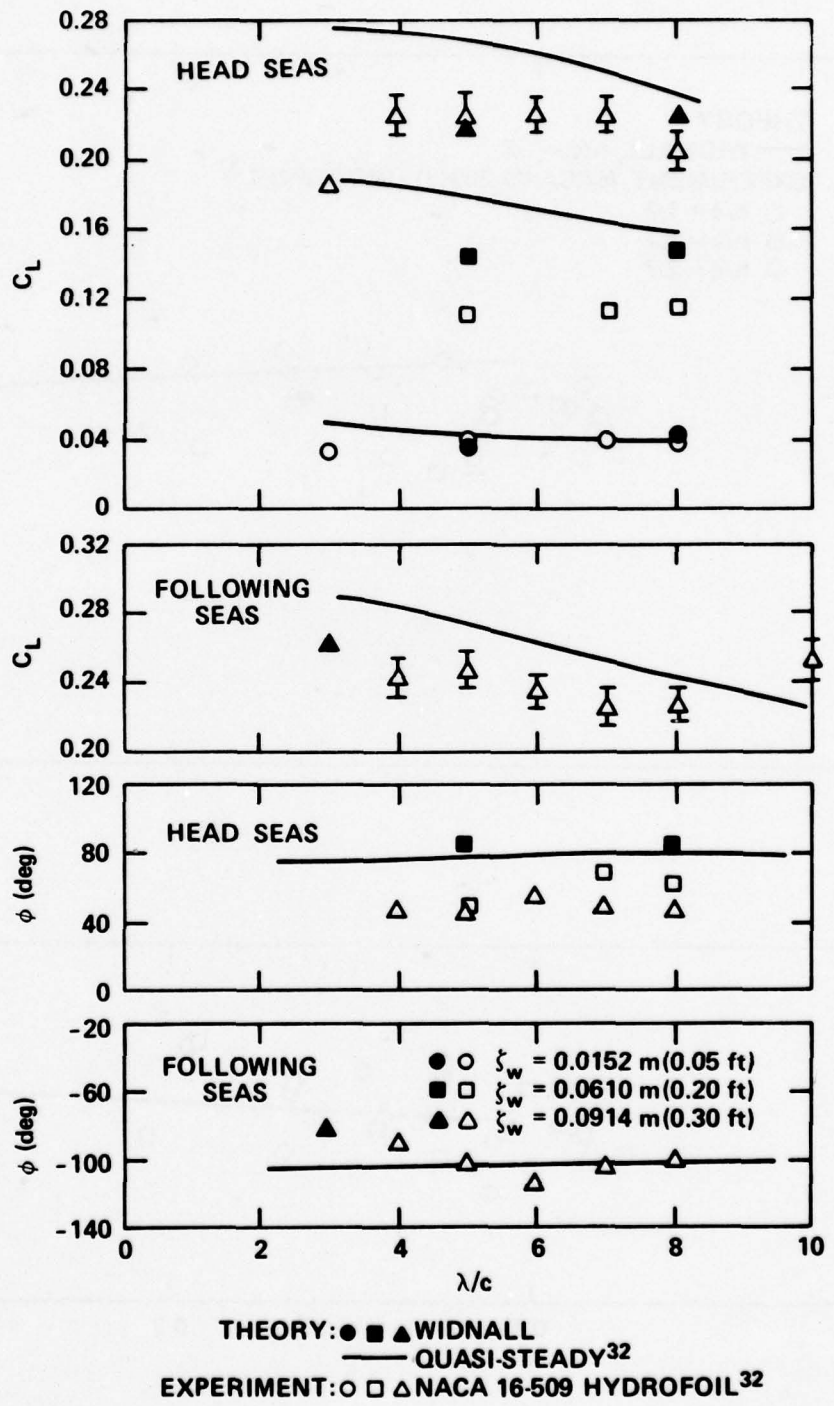


Figure 49 - Magnitude and Phase Angle of the Total Unsteady Lift in Head and Following Seas as a Function of Wavelength for the NACA 16-509 Hydrofoil ( $\Lambda = 0$ ;  $\tau = 1$ ;  $AR = 6$ )

### NACA 0010 Hydrofoil and Airfoil

These models were unusual in that structural vibration modes were simulated rather than rigid-body oscillations. At the low-to-moderate values of reduced frequency for which data are available,<sup>15,28,29</sup> predictions of lift were fair to good while moment predictions were fair to poor. Comparisons are shown in Figures 43 and 44. Calculated loading for the fully-submerged condition has been included even when no data were available.

A change from 0.1 to 0.5 in reduced frequency of airfoil oscillation had little effect on the accuracy of the loading calculation. The greatest discrepancy in calculated phase angle was a lead of up to 52 deg in pitching moment at  $k = 0.1$ . The lift magnitude ranged from 9 percent below experiment to 1 percent above experiment, while pitching moment ranged from 15 percent below experiment to 27 percent above.

In a remarkable example of experimental consistency, the fully-submerged hydrofoil data agreed fairly well with the airfoil data taken at a slightly lower reduced frequency (0.6 and 0.5, respectively). Much larger deviations characterized the comparison with the surface-piercing hydrofoil data, particularly the moment data. The lift predictions were from 27 percent below experiment to 36 percent above experiment, with phase angles up to 27 deg in error. The moment predictions ranged from 0 to 125 percent above experiment, with phase angle as much as 56 deg in error. Some of the discrepancy in the surface-piercing data due to bending was caused by a ventilated cavity which formed along the upper trailing edge of the bending model. Predictions of unsteady center of pressure  $x_{cp}$ , a quantity described in Appendix B, were from 3 percent to 16 percent of the chord aft of experimental values, as shown in Figure 44e.

### AGEH-1 One-Twelfth-Scale Hydrofoil

Predicted and experimental loading on the AGEH-1 hydrofoil<sup>18</sup> are shown in Figure 45. The loads are given both in coefficient form and as gains. The gain is a logarithmic form of load coefficient as indicated in

the figures. Because the calculated gains are given relative to calculated steady loading slopes, which did not agree with experiment, the gain does not directly indicate the accuracy of the unsteady loading predictions. In the present case, the calculated lift gain was reduced relative to experiment by this inaccuracy, while pitching moment gain was reduced for one pitching axis and increased for the other.

Lift was predicted with fair-to-good accuracy over a wide range of reduced frequency  $k$ . The prediction was 15 percent above experiment at low  $k$  and up to 33 percent below experiment for  $k$  above unity. The theory intersected the data at approximately  $k = 0.75$ . Lift phase angles were especially accurately predicted, with a deviation of only a few degrees in lag.

Pitching moment coefficients were not as well predicted. Accuracy ranged from 140 percent above experiment at low  $k$  to a large, indeterminate amount above experiment at high  $k$ . Smaller deviations of the opposite sign occurred at low  $k$  for one of the pitch axes. It should be understood that the prediction accuracy will, in general, vary markedly with axis location. Predicted phase angles led the experimental values by as much as 20 deg.

The two-dimensional version of the Widnall calculation<sup>18</sup> was much less accurate in predicting the lift gain and phase than the three-dimensional calculation. The two-dimensional calculation was also, in general, less accurate in its predictions of moment magnitude, but predicted moment phase angle more accurately. In view of its overall inaccuracy, use of the two-dimensional calculation would not be justified if the three-dimensional version was available.

#### NACA 65A010 Airfoil

This low-aspect ratio airfoil was tested both in a pitching mode<sup>30</sup> and in a flapping mode.<sup>31</sup> Comparisons between theory and experiment are shown in Figure 46.

The Widnall prediction tended to be low for lift, in good agreement with experiment for pitching moment, and high for roll moment. All calculations were within 15 percent of the average experimental values. The phase angle predictions and data varied differently with reduced frequency,

which resulted in crossover regions and in deviations as high as 17 deg. Unsteady centers of pressure were calculated within 10 percent of the chord length. The Widnall calculation was thus fairly accurate for these airfoils.

The Widnall calculations fell within a few percent of results from the Woolston lifting-surface program, and the two programs appear to be nearly equivalent.

#### WAVE-INDUCED LOADING

Unsteady lift magnitude and phase due to waves was predicted with accuracy similar to that obtained for oscillating foils. Lift magnitudes were up to 43 percent in error, while predicted phase angles deviated as much as 36 deg from experiment. Moment predictions were less accurate than lift predictions. The Widnall lifting-surface calculation was found to be more accurate than either a two-dimensional calculation or quasi-steady theory. Calculations and data from three models are presented in Figures 47 through 49, and are discussed further in the following sections.

#### AGEH-1 One-Twelfth-Scale Hydrofoil

Lift and pitching moment data were obtained for this foil in head seas over a reduced frequency range of 0.1 to 0.4.<sup>18</sup> The Widnall two- and three-dimensional predictions are compared with experiment in Figure 47.

The prediction of lift magnitude using the Widnall three-dimensional calculation was extremely accurate, while the two-dimensional version was considerably less accurate. The three-dimensional prediction of magnitude appeared to be within experimental uncertainty of the data although phase angles were consistently 20 to 30 deg in error.

Moment predictions were poor for both calculations, with accuracies ranging from 50 percent above experiment to 60 percent below experiment. Calculated phase angles were from 70 deg above experiment to 50 deg below experiment.

It is concluded that the Widnall three-dimensional calculation is significantly more accurate than the related two-dimensional calculation in predicting lift in waves at reduced frequencies between 0.1 and 0.4.

#### NACA 66-209(S) Hydrofoil

Calculated and experimental lift differed by up to 43 percent for an aspect ratio 5 rectangular hydrofoil in waves,<sup>27</sup> as shown in Figure 48. More accurate predictions occurred at deeper depths. Phase angle predictions differed from experiment by as much as 16 deg, although scatter in the data suggested that the prediction may have been within experimental uncertainty.

#### NACA 16-509 Hydrofoil

Unsteady loading in both head seas and following seas was measured on an aspect ratio 6 rectangular hydrofoil.<sup>32</sup> The results, corresponding to reduced frequencies between approximately 0.04 and 0.36, are shown in Figure 49. Theoretical results from the Widnall three-dimensional program and from quasi-steady theory are also shown.

The Widnall calculation was within 23 percent of experimental lift magnitude but as much as 36 deg different from measured phase angles. No significant difference occurred in the accuracy of predictions for head and following seas. As would be expected, the Widnall results became increasingly superior to quasi-steady theory as reduced frequency increased (corresponding to a decrease in wavelength  $\lambda$ ). It is concluded that the Widnall three-dimensional calculation should be used in preference to the quasi-steady calculation at reduced frequency greater than 0.16.

#### SUMMARY OF UNSTEADY LOADING PREDICTIONS

Just as for the steady loading calculation, the unsteady calculation showed a wide range of accuracy relative to the available data. The lift predictions ranged from about 30 percent below experiment to 40 percent above. Pitching moment predictions were substantially less accurate, up to 140 percent in error, although, generally, they were within about 60 percent of experiment. Predicted phase angles for lift were, as a rule, within 20 degrees of experiment; pitching moment phase angles varied much more widely.

Possibly due to the limited amount of data, no clear dependence of accuracy was found on the mode of unsteady loading (heave, pitch, or waves) or the foil aspect ratio. On the other hand, foil depth and reduced frequency did affect the accuracy. The largest deviations between theory and experiment occurred at shallow depth (Figures 42 and 44) and at both high and low reduced frequency. When lift predictions at deep submergence and moderate reduced frequency are considered, for example, the deviations reduce to less than 20 percent. Pitching moment deviations remain at a substantially higher level under these conditions. The effects of shallow submergence and high reduced frequency may be the reason for the generally superior agreement of the airfoil loading data with theory: the airfoil data did not include the extremely shallow submergences nor the high values of reduced frequency that the hydrofoil data did.

It is concluded that, as a rough approximation, unsteady lift predictions may be made with an accuracy of  $\pm 20$  percent for deeply submerged hydrofoils at reduced frequencies up to about 1.0. The predicted lift will probably be more than 20 percent above experiment at depths of one chord and less, and more than 20 percent below experiment at reduced frequencies above 1.0. A more detailed determination of the unsteady loading prediction accuracy of the Widnall program cannot be made in the absence of more systematic data.

Although no empirical correction to the unsteady predictions will be proposed, in view of the limited amount of data, it appears that a correction could be generated to account for effects of high reduced frequency. This correction, in conjunction with depth correction developed from both steady and unsteady loading data, would permit predictions to be extended to shallow submergences and higher reduced frequencies with no loss of accuracy.

#### DISCUSSION

The primary result of this evaluation has been to show that the Widnall program can be used to make hydrofoil lift predictions with a moderate degree of accuracy (15 to 20 percent) except at very shallow

submergences and, for unsteady loading, at very high reduced frequencies. Pitching moment predictions are much less accurate, which is not surprising in view of the dependence of pitching moment on both the magnitude and chordwise distribution of lift.

The use of an empirical correction to the steady lift predictions is of course an admission that there is some degree of inaccuracy inherent in the lifting-surface calculation. Determination of the exact amount of inaccuracy has been prevented both by residual numerical instability in the program, principally at high aspect ratio, and by a general lack of precision and scope in the body of hydrofoil data. Of particular significance for design of hydrofoil craft is the extremely limited amount of data on swept, tapered hydrofoils. For the two such planforms included in this evaluation, the predictions and the program numerical stability were both poor. This apparent deficiency must be investigated to determine whether the predictions or the model test results are in error.

Some of the findings concerning the NACA  $a = 1.0$  mean line suggest that other choices of mean line would be preferable. Experimental results show that the sectional lift on this mean line is only about three-quarters of the theoretical value, while other profiles realize approximately the full theoretical value. Furthermore, a modal approach to describing chordwise pressure distributions cannot successfully represent this type of camber lift. As a result, certain types of calculation such as estimating cavitation inception are impossible. If a camber line which produces less abrupt increases in pressure near the leading and trailing edges can meet the design requirements, more accurate predictions would probably be available from the Widnall program for optimizing other design parameters.

#### CONCLUSIONS

1. The Widnall program can be used, in conjunction with an empirical correction, to predict hydrofoil lift with a moderate degree of accuracy (15 to 20 percent) except at very shallow submergences and very high reduced frequencies. Further empirical corrections for these parameter ranges can be derived from the available data.

2. Establishment of a higher prediction accuracy may be possible but is now prevented by lack of sufficient high-quality hydrofoil loading data and by some residual numerical instability in the calculation.

3. The Widnall lifting-surface program is preferable as a design tool to the Bandler program, the Widnall two-dimensional program, and a quasi-steady theory for reasons of accuracy or numerical stability.

4. Hydrofoil model data suffer widely from unreported experimental error. The principal source of error is the angle of attack measurement. Some models may also experience a shift in transition which results in an inaccurate camber lift measurement. Model profiles may also be incorrect unless proven otherwise by measurement.

#### RECOMMENDATIONS

1. Improved-quality measurements of hydrofoil loading should be made to permit more precise determination of the accuracy of the Widnall and other calculations. Particular care should be taken to obtain accurate camber lift data, by assuring accurate measurements of angle of attack, correct model profiles, and using transition stimulation or flow visualization to avoid wrongly scaled transition behavior. Swept, tapered hydrofoils with and without pods should be emphasized.

2. The numerical aspects of the Widnall program should be investigated to eliminate numerical instabilities.

3. The Bandler lifting-surface computer program should be numerically extended to allow determination of its numerical stability and accuracy.

## APPENDIX A

### DESCRIPTION OF EXPERIMENTAL MODELS

#### HYDROFOIL AND AIRFOIL MODELS IN STEADY MOTION

Most of the steady loading data used in the present study were obtained from measurements on hydrofoils. In all, some twenty-one different model configurations were represented. The largest systematic body of data pertained to the DTMB Series HF-1 family of rectangular hydrofoils.<sup>8</sup> These foils had 0.229-m (9-in.) chords and NACA 16-309,  $a = 1.0$  profiles. Aspect ratios of 1, 2, 3, 4, 6, and 8 were investigated. The experimental data were converted from the originally published normal and longitudinal force coefficients to lift coefficients for the present comparison. Experimental uncertainty in the foil angle of attack  $\alpha$  was substantial, amounting to at least  $\pm 0.5$  deg according to internal comparisons among the data. Estimates of uncertainty in  $C_L(\alpha = 0)$  were obtained by multiplying nominal values of lift slope  $C_{L\alpha}$  by the uncertainty in  $\alpha$ . The accuracy of angle of attack changes was not reported, so that uncertainty in  $C_{L\alpha}$  could not be determined. Load measurements are plotted in Figures 34 and 35.

A second group of data pertained to three AR = 6 rectangular hydrofoils, two with NACA 16-509 and 16-1009,  $a = 1.0$  profiles and one with a NACA 23012 section.<sup>13</sup> The foils had 0.128-m (5.0-in.) chords. In the original reference, variations in lift coefficient as a function of speed were presented. Essentially constant values of lift coefficient occurred below the speeds at which cavitation appeared; these constant values were used in the present work. Uncertainty in foil angle of attack was reported as +0.2 to -0.3 deg. Error bands for  $C_L(\alpha = 0)$  were calculated using nominal values of  $C_{L\alpha}$ , but could not be calculated for  $C_{L\alpha}$  itself because the range of uncertainty for lift was not given. Data are plotted in Figures 34g and 35f.

An additional group of data included five rectangular hydrofoils of varying design. One was an uncambered plate with an elliptical nose and a bevelled trailing edge.<sup>9</sup> It had a 0.180-m (7.07-in.) chord and an aspect ratio of 1. The error in the lift slope data for this foil is indicated

in Figure 35a for a 6.10 m/s (20 ft/sec) condition; the range of experimental uncertainty in  $C_L(\alpha = 0)$  is included within the data symbol in Figure 34a. The second and third foils, of 0.204-m (8-in.) chord length, had NACA 64<sub>1</sub>A412,  $a = 1.0$  profiles and aspect ratios of 4<sup>10</sup> and 10;<sup>14</sup> see Figures 34d, 34i, 35d, and 35h. Data given in Reference 10 had been corrected for tare loading and angular deflection of the dynamometer, but the range of uncertainty was not given. The fourth and fifth foils had aspect ratios of 5.0<sup>11</sup> and 5.84;<sup>12</sup> see Figures 34e, 34f, and 35e. The AR = 5 foil had a 0.100-m (3.9-in.) chord and a NACA 66-209(S) profile. The (S) indicated a "slight" change in the lower offsets near the trailing edge. Only one value of angle of attack was used, and, consequently, no values of  $C_{La}$  were obtained. The AR = 5.84 foil had a 0.120-m (4.7-in.) chord and a circular segment profile (flat lower surface, convex upper surface) of 7.5-percent maximum thickness. No values of uncertainty were reported for the latter two foils.

Data from segmented hydrofoils with simulated bending and torsional deflections<sup>15</sup> were also used. The rectangular foils had 0.457-m (18-in.) chords and NACA 0010 profiles. An effective aspect ratio of 5 and an effectively infinite depth were produced by a large endplate, which was parallel to the free surface and perpendicular to the hydrofoil span. Dynamometers at five spanwise locations enabled spanwise distributions of loading to be measured. The two versions of the foil were mechanically deflected to produce bending and torsional deflections, respectively, in both steady and unsteady modes. Error flags shown in Figure 36 correspond to the reported  $\pm 0.2$  deg uncertainty in angle of attack.

Published loading data were available for only two swept, tapered hydrofoil models. One was a 1/12-scale model of the AGEH-1 (PLAINVIEW) main T-foil.<sup>17-20</sup> The load-bearing foil on the model had a sweep angle  $\Lambda = 35.2$  deg, a taper ratio  $\tau = 0.3$ , and a mean chord  $c = 0.220$  m (8.65 in.). Data are plotted in Figure 38. The foil had a NACA 16-(0.353)08,  $a = 1.0$  profile defined normal to the 32-percent chord line,<sup>18</sup> necessitating calculation of streamwise section characteristics for use in the computer calculations. The section offsets were inadvertently calculated

for a 25-percent chord reference line, but the difference is believed to be negligible. The relatively large model pod was not considered in the calculation. The foil was rotated in pitch about several different axes, as indicated in the figure.

The second swept, tapered foil was a 1/8-scale model of the forward T-foil on the PCH-1 (HIGH POINT) hydrofoil craft. This foil is designated as Model A in Reference 16. It had  $\Lambda = 15$  deg,  $\tau = 0.35$ , AR = 6.1, and  $c = 0.150$  m (5.9 in.). Data are shown in Figure 37. The profile was a NACA 16-309,  $a = 1.0$  section defined in the streamwise direction. No range of experimental uncertainty was reported for either of the swept, tapered models.

Four sets of measurements<sup>21,25\*</sup> on a commonly-used hydrofoil section, the NACA 16-309 ( $a = 1.0$ ) profile, in two-dimensional flow were also included to represent infinite aspect ratio. Two of the studies were done with hydrofoil models, and two with airfoil models. One hydrofoil model had a 0.15-m (6-in.) chord length and was tested in the two-dimensional test section of a water tunnel. Airfoils of 0.127-m (5-in.)<sup>25</sup> and 0.762-m (30-in.)\* chord were tested in wind tunnels. Experimental uncertainties were not given. Data for one of the airfoils and the hydrofoil are compared in Figure 39. The second hydrofoil<sup>21</sup> had a 0.15-m (6-in.) chord and was towed beneath the free surface of a towing basin; data are shown in Figure 40. Struts of 0.4-m (15.7-in.) chord were placed at each end of the foil to approximate two-dimensional flow.

#### HYDROFOIL AND AIRFOIL MODELS IN UNSTEADY MOTION

##### NACA 66-209(S) Hydrofoil

This model has been previously described in the preceding section as a source of steady loading data. It was tested<sup>27</sup> in a rigid heaving mode at a model speed of 6.1 m/s (20 ft/sec) and a fixed angle of attack of 1.8 deg. Results are shown in Figure 42. The lift coefficient used in Reference 27 was not fully defined and was here assumed to be  $C_L c' / (2\pi\delta_0)$  where  $\delta_0$  is the amplitude of the heave motion.

\*Also, informal communication (Jun 1978) with E. A. Jones of the Canadian Defence Research Establishment Atlantic.

Unsteady loading was also measured for this foil in waves,<sup>27</sup> again at a 1.8-deg angle of attack; see Figure 48. The lift data in waves were inferred to have been reported in the form  $C_L / 2\pi\alpha_w$ , where  $\alpha_w$  was the amplitude of the effective unsteady angle of attack due to the waves. No experimental uncertainty values were given.

#### NACA 0010 Hydrofoil

This category includes the two segmented models also used for steady load measurements. Foil motions were produced by oscillating the tips of the foils in translation and rotation, resulting in spanwise mode shapes approximating the first bending and first torsion modes of a cantilever beam. The axis of torsional oscillation was at the quarter-chord line. A large end plate doubled the aspect ratio when the foil was fully submerged. Pitching moments were reported about an axis at 31 percent of the chord.

The models were tested at both full submergence<sup>15,29</sup> and at 65-percent submergence.<sup>29</sup> At 65-percent submergence, the foil should be referred to as a vertical surface-piercing strut.

Although these foils were tested at several values of reduced frequency, dynamometer inaccuracy caused all data except that below  $k = 0.67$  to be unreliable. As a result, unsteady data are available only at  $k = 0.6$ ; see Figure 44. The range of uncertainty in these remaining data was not reported.

#### NACA 0010 Airfoil

Because no unsteady data were available from the flexible hydrofoil models mentioned above at low reduced frequencies, data from two very similar, uncambered NACA 0010 profile airfoils<sup>28</sup> have been included in this study. The data were obtained for both bending and torsional oscillations. Although similar in size to the hydrofoil model, the airfoil model was oscillated about the 35-percent chord line during torsional oscillations, and moments were reported about this axis. Unsteady data at the lowest reduced frequency, 0.1, and highest reduced frequency, 0.5, were

used for comparison with theory. These data are presented in Figure 43. While no range of uncertainty was given, the data are believed to be of good accuracy.

#### AGEH-1 One-Twelfth-Scale Hydrofoil

The third hydrofoil configuration was a 1/12-scale model of the AGEH-1 main strut-pod-foil system. This model was described in the preceding section on steady loading.

One type of unsteady loading was obtained<sup>18</sup> by oscillating the foil in pitch about either of two axes at reduced frequencies  $k$  up to 2. The axes were located at 5.94 and 31.94 percent of  $c'$ , measured aft of the leading edge.<sup>19</sup> These locations correspond to 47 and 64 percent of the root chord from the leading edge. In each case, the lift and the pitching moment at the axis were measured. The experimental procedure did not compensate for inertial effects of the foil and linkage. Therefore, the authors weighed and measured the model, which was available and intact, and calculated inertial corrections to the experimental data published in Reference 18. These corrections were not negligible, but did not greatly alter the published data. The corrected data, shown in Figure 45, were used in this report.

Foil loading was also measured<sup>18</sup> in head seas at a depth of 0.25 m (10 in.) for speeds of 7.3 and 10.5 m/s (24.0 and 34.6 ft/sec). The waves had 0.10-, 0.15-, and 0.25-m (4-, 6-, and 10-in.) peak-to-peak amplitudes  $\zeta_w$  and 3.8- to 12.2-m (12.5- to 40-ft) wavelengths  $\lambda$ , although not all possible combinations of amplitude and wavelength were used. The steady angle of attack was 1.4 deg at the lower speed and -1.5 deg at the higher speed. Measured loading values are given in Figure 47. The downwash used in the loading prediction included both the horizontal and the vertical components of orbital velocity.<sup>33</sup> It was assumed that the depth of the water was greater than one-half the wavelength. Since the towing basin used for the experiment was 4.9 m (16 ft) in depth, this assumption was invalid for wavelengths longer than 9.8 m (32 ft).

The experimental uncertainty in the measured loading was not given for this model.

### NACA 16-509 Hydrofoil

The remaining wave-loading data were obtained from an AR = 6 rectangular foil with a NACA 16-509,  $a = 1.0$  profile.<sup>32</sup> The foil was experimentally tested at a depth of one chord (76 mm or 0.25 ft) and an angle of attack of 4 deg in both head seas and following seas. Computer predictions for the lift were compared with experimental results for a model speed of 3.1 m/s (10 ft/sec); see Figure 49. The computer predictions were made only for  $\lambda = 1.5$  and 2.4 m (5 and 8 ft) in head seas and for  $\lambda = 0.9$  m (3 ft) in following seas. The values of  $k$  were calculated using a calculated wave propagation speed. In head seas,  $k$  varied from 0.365 to 0.161 as  $\lambda$  increased; in following seas, the variation was from 0.159 to 0.035. The plot of lift phase versus wavelength for the following seas which appears in Reference 32 is inconsistent in the labeling of the ordinate  $\phi$ . Thus the experimental phase is unknown within 40 deg. The labeling used in this report assumes that the phase due to following seas is approximately 180 deg greater than that due to head seas. Since the phase associated with head seas was correctly plotted, it was determined that the experimental phase due to following seas clustered around -100 deg and not around -60 deg. Dynamometer response limitations produced an uncertainty of  $\pm 5$  percent in lift amplitude and  $\pm 5$  deg in phase angle.

### NACA 65A010 Rectangular Airfoil

The second airfoil model had an AR = 2 rectangular planform with a NACA 65A010 profile.<sup>30,31</sup> The chord length of the foil was 0.305 m (12 in.). A rigid semispan model of the foil was oscillated in pitching<sup>30</sup> and flapping<sup>31</sup> modes at Mach numbers from 0.2 to 0.7. The axis for the flapping oscillations was a streamwise line 0.152 m (6.0 in.) behind the wall used for the image plane; the pitching axis was the midchord line. The mean angle of attack was zero. The experimental and predicted lift and pitching moment at midchord for both the pitching and flapping oscillations and the roll moment at the flapping axis for the flapping oscillation are compared from  $k = 0.2$  to  $k = 0.8$ . The exact definition of the experimental phase for the pitching oscillations could not be determined because of the

ambiguous notation used in Reference 30, but was inferred by comparison between theory and experiment. The loading was measured with an uncertainty of +4 percent in magnitude and +3 deg in phase angle.

## APPENDIX B

### COMPUTER PROGRAM USER'S MANUAL

The following material constitutes a user's instruction manual for the Widnall three-dimensional lifting-surface computer program. A complete description is given of the input and output procedures and of all output quantities. In subsequent appendices, listings of program decks and sample input and output are provided.

In order to guide a potential user, it is noted that the lengthy instructions given in this appendix might require several weeks for a person who is already familiar with FORTRAN programming to learn. The appropriate sample calculations should be run before generating any original results.

#### PROGRAM USAGE

The lifting-surface theory is contained in three computer programs: the steady loading program YKWS, the unsteady program YKWU, and the auxiliary program YKWA. The programs are related to each other as shown in Figure B.1. Both the steady (YKWS) and the unsteady (YKWU) programs calculate load coefficients and also generate, at the option of the user, punched output containing the pressure matrices which characterize the foil configurations being treated. This punched output can then be used to calculate loading for additional sets of downwash conditions in relatively short run time by using the auxiliary program (YKWA).

The three programs are each composed of a main program and several subprograms. All programming has been done in the FORTRAN Extended Language (Version 3.0). The FORTRAN names and mathematical functions of all main programs and subprograms are shown in Tables B.1 through B.3.

Listings of the FORTRAN coding for all programs are given in Appendix C.

#### PROGRAM INPUT DESCRIPTION

Input to the computer programs consists of coding in subprograms in addition to data cards. The subprograms specify the foil geometry and the spanwise pressure modes. The data cards contain foil and flow parameters,

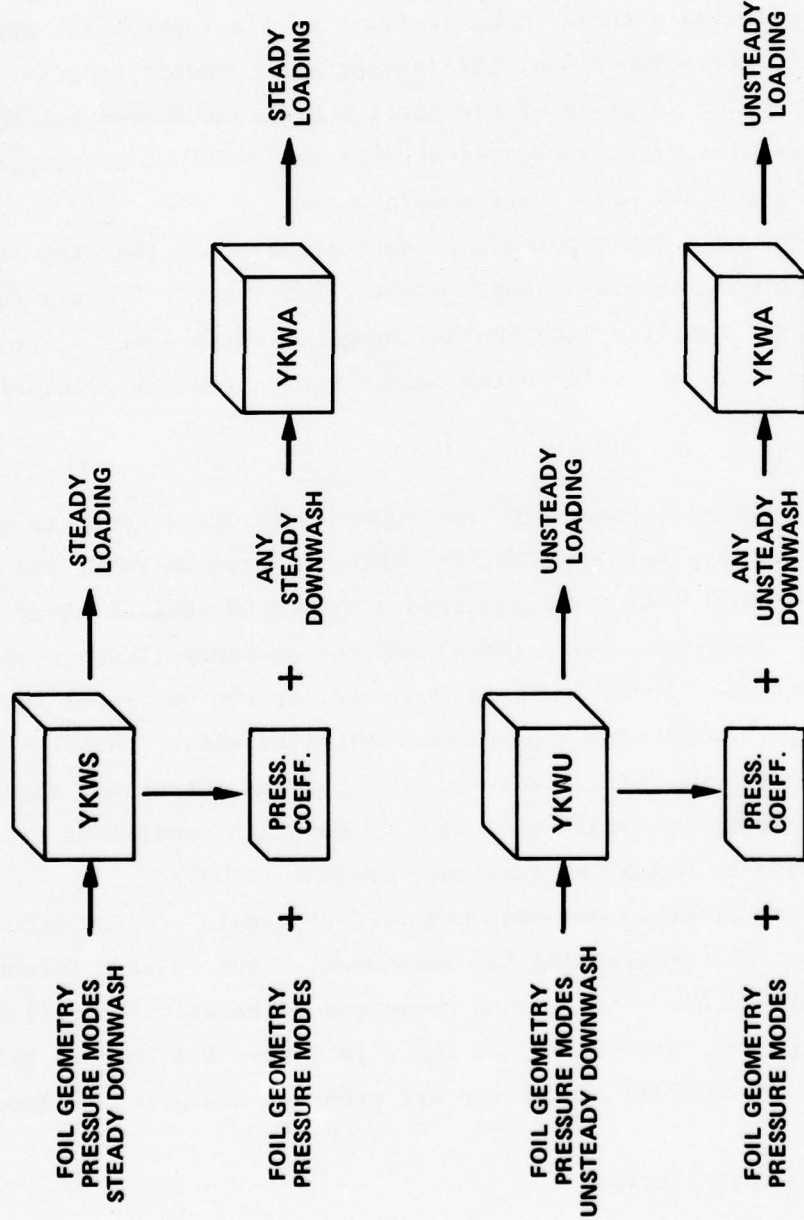


Figure B.1 - Relationship among Programs YKWS, YKU, and YKWA

TABLE B.1 - COMPOSITION OF DECK FOR PROGRAM 1 (YKWS)

Program	Function
Program YKWS	Main program (steady)
Subroutine ANSWER	Calculate steady load coefficients
Subroutine CHORD	Calculate chordwise pressure coefficient distribution
Subroutine MNGLR	Singular spanwise integration
Subroutine KERNL	Calculate steady kernel function
Subroutine MATINS	Matrix inversion
Subroutine CHDWS	Chordwise integration (steady)
Function GN	Gaussian integration intervals
Function WN	Gaussian weighting factors
Subroutine STRUCT	Foil geometry
Function XLE	Foil geometry
Function B	Foil geometry
Subroutine FUNCTN	Spanwise pressure modes

TABLE B.2 - COMPOSITION OF DECK FOR PROGRAM 2 (YKWU)

Program	Function
Program YKWU	Main program (unsteady)
Subroutine ANSWU	Calculate unsteady load coefficients
Subroutine KERNLU	Calculate unsteady kernel function
Subroutine MNGLRU	Singular spanwise integration
Subroutine CHDWU	Chordwise integration (unsteady)
Function GN	Gaussian integration intervals
Function WN	Gaussian weighting factors
Subroutine CMPINV	Complex matrix inversion
Subroutine MATINV	Matrix inversion
Subroutine HINT	Auxiliary in unsteady kernel function calculation
Subroutine WINT	Auxiliary in unsteady kernel function calculation
Subroutine BIMLI	Auxiliary in unsteady kernel function calculation
Function BIML2	Auxiliary in unsteady kernel function calculation
Subroutine BESK	Calculates K Bessel function
Subroutine STRUCT	Foil geometry
Function XLE	Foil geometry
Function B	Foil geometry
Subroutine FUNCTN	Spanwise pressure modes

TABLE B.3 - COMPOSITION OF DECK FOR  
PROGRAM 3 (YKWA)

Program	Function
Program YKWA	Main program (auxiliary)
Subroutine FUNCTN	Spanwise pressure modes
Function XLE	Foil geometry
Function B	Foil geometry

internal program constants, control point locations, and downwash values on the foil. The method of formulating the required subprograms and data values is described in the following sections.

#### Representation of Lifting Surface

Subprogram coding is used to supply most of the information about foil geometry required by the lifting-surface calculation. Any combination of foils of arbitrary planform, including both connected and unconnected lifting surfaces, can be treated by the program. However, it should be remembered that, theoretically, all foil surfaces make infinitesimally small angles with the direction of flow.

The foil being specified is located in the (x,y,z) coordinate system of Figure 1. Flow is in the positive x direction. Three user-coded subprograms are used to specify the foil coordinates in terms of two new parameters, the section number and the position along the span of the foil, given as fraction of span. Before coding for these subprograms can be written, however, integration regions on the foil and section numbers must be chosen to be consistant with each other and also with the fraction of span coordinate directions. Each of these quantities will be explained separately. Names of variables given in capital letters refer to computer input quantities which are listed in Table B.4.

Section Number, N. The foil is considered to be composed of N sections of arbitrary extent. For convenience, N should be small and the sections

TABLE B.4 - FORTRAN INPUT NOTATION

Input	Definition
AF(I)	Spanwise length of Ith section, in units of reference semichord
ARM	X-coordinate about which pitching moment is calculated (zero if left blank)
B(N,S)	Length of foil semichord at the fractional spanwise position S on foil section N (defined in FUNCTN B(N,S))
EM	Mach number; zero for hydrofoils
ETA	Half-width of the singular region (Region I); minimum of 0.1, SOS, and 1.0 - SOS
F(I)	Value of the Ith spanwise pressure mode (defined in Subroutine FUNCTN (N,S,F) for fractional spanwise position S on foil section N)
IPUNCH	Punched output indicator: IPUNCH = 0 generates no punched output; IPUNCH = 1 generates punched output required for running Program YKWA
J3	Free surface indicator: J3 = 0 signifies infinite depth; J3 = 1 signifies finite depth (a value for the finite foil depth must be given in Subroutine STRUCT)
MP	Number of chordwise integration steps in the singular region (may be 6, 8, 10, 16, or 32)
N	Section number ( $N \leq 6$ )
NCASE	Number of foil configurations
NCMBR	Number of downwash sets for each foil configuration (given once but applies to all configurations); NCMBR = 0 is valid
NCP	Number of chordwise integration steps in the nonsingular regions (may be 6, 8, 10, 16, or 32)
NI(I)	Number of spanwise integration steps in the Ith region (may be 0, 6, 8, 10, 16, or 32); zero prevents integration over regions which are not needed to represent foil
NNNN	Running index used to consecutively number the NCASE foil configurations
NOCP	Total number of control points over all sections (NOCP > NOST * NOLT; maximum values are 180 for steady loading and 90 for unsteady loading)
NOLT	Number of internally generated chordwise pressure modes ( $NOLT \leq 20$ )
NOST	Number of spanwise pressure modes ( $NOST \leq 4$ ) specified in Subroutine FUNCTN
NS	Number of foil sections ( $NS \leq 6$ )
PSI	Arc tangent of the slope $dz/dy$ of the foil surface in the y-z plane when looking upstream (see Figure B.3)
RF	Reduced frequency; $bw/U$
SF(I)	Ratio of the span of the Ith foil section to the sum of the spans of all foil sections
SOS	Spanwise location of control point on a given foil section, specified as fraction of span from the end of the section having $S = 0$
SPAN	Sum of AF values, equal to the total foil span
VR(I)	Real part of the downwash at the Ith control point
VI(I)	Imaginary part of the downwash at the Ith control point
XOC	Chordwise location of control point, specified as fraction of local chord aft of leading edge
YS	Fraction of span at which chordwise pressure jump distribution is to be calculated

should correspond to areas of simple geometry on the foil such as semispans, supporting struts, etc. When geometrical symmetry between two sections of a foil exists, however, input simplification can be achieved by extending the calculation over the similar section without giving it a section number. This procedure involves manipulation of integration regions.

Fraction of Span, S. Each numbered section of the foil must be given a signed coordinate S which specifies the fractional spanwise distance  $b'$  from one end of the section to the other. The span S may originate at either end and will range from 0 to 1 in value. The computer calculation assumes that negative values of S correspond to another, unnumbered, section which the program user may wish to have included as part of the complete foil. This unnumbered section would have a geometry describable by the coding used for the numbered section with negative S substituted for positive S.

Integration Regions. The entire foil configuration is divided into four or more regions for spanwise integration of the kernel function. The regions change in location for each control point, and, therefore, can be visualized for only one control point at a time. A narrow chordwise strip centered at the control point is called Region I. ETA is the spanwise half-width of Region I. The remainder of the foil section outboard (larger S) of Region I is Region II, while the inboard part is Region IV. Region III encompasses the unnumbered, negative-S counterpart (of the numbered wing section composed of Regions I, II, and IV). Other even-numbered regions consist of the remaining foil sections, while odd-numbered regions are the negative-S counterparts of the remaining sections. A typical set of integration regions is shown on the foil in Figure B.2.

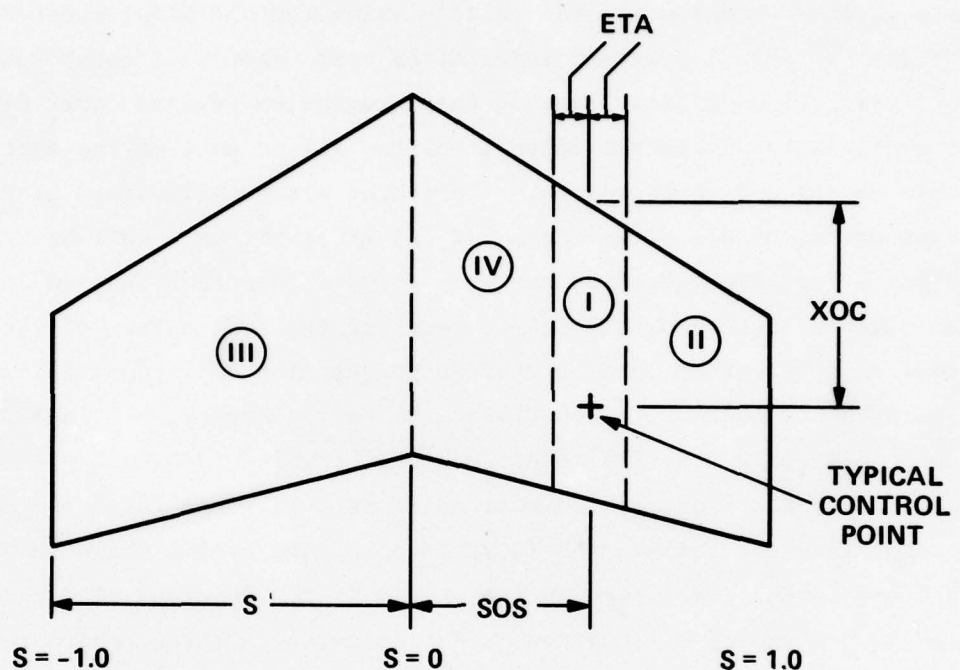
Integration regions are designed to permit special integration techniques to be used in the vicinity of each control point, where a singularity occurs in the kernel function. Because of the way in which the integration regions are chosen, the data inputs NI(J), which designate the number of spanwise integration stations in the Jth region, are also used to

indicate whether a region exists. A zero value for all  $NI(J)$  where  $J$  is odd and greater than 1 prevents integration over negative-S counterparts of specified foil sections. Because the integration regions cover different sections for different control points, all or none of the sections must have negative-S counterparts. Therefore, either all values of  $NI(J)$  must be nonzero, or all  $NI(J)$  for  $J$  odd and greater than 1 must be zero.

After a foil configuration has been divided into sections and integration regions have been selected to comprise the full extent of the foil, the required subprograms must be written to describe foil geometry and spanwise pressure modes. In describing the foil geometry, all foil dimensions are given in units of a reference length, which is usually taken as the root semichord of one of the foil sections. It, therefore, is convenient to place the foil in the  $(x, y, z)$  coordinate system shown in Figure 1 with the reference semichord on the  $x$ -axis in the interval  $-1 \leq x \leq 0$ , although such a choice of location is not necessary. Three subprograms describe the location and planform of the foil in this frame of reference. The subprograms and their variables are as follows.

Subroutine STRUCT. Subroutine STRUCT ( $N, S, Z, Y, PSI$ ) defines the  $y$  and  $z$  coordinates and the slope at each point on the foil. The parameter  $PSI$  is defined to be the arc tangent of the slope  $dz/dy$  of the foil surface in the  $y$ - $z$  plane when looking upstream as shown in Figure B.3;  $N$  denotes the foil section;  $Y$  and  $Z$  represent the  $y$  and  $z$  coordinates of the foil. The fractional distance along the span of the section,  $S$ , denoted as  $b'$  in Equation (2), can be chosen to originate at either end of the section. The fractional distance  $S$  will be set equal to  $-S$  when unnumbered counterparts to section  $N$  are being described. If more than one foil configuration is treated with a single computer run, the variable  $NNNN$ , placed in labeled common blocks CNRA, provides a running index to number the various configurations.

Foils may be treated either with or without a free surface. The  $J3$  input described below indicates whether or not a free surface is to be included. The free surface is represented by an image foil which is



NOTE: INTEGRATION REGIONS DENOTED BY ROMAN NUMERALS

Figure B.2 - Integration Regions for a Typical Control Point

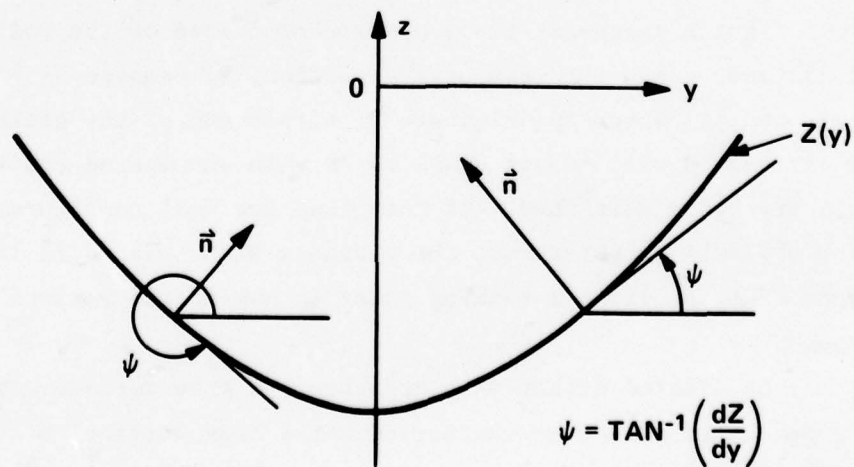


Figure B.3 - View of Nonplanar Foil Looking Upstream

generated by using the given foil geometry with z-values of opposite sign. Therefore, foils beneath a free surface must be given z-coordinates so that the plane  $z = 0$  represents the free surface. Otherwise the foil may be placed anywhere along the z-axis.

Function XLE. Function XLE( $N, S$ ) defines the x-coordinate of the leading edge of the foil. Functions  $N$  and  $S$  are the section number and fractional spanwise coordinate  $b'$ , respectively. The variable NNNN, placed in labeled common block CNRA, provides a running index corresponding to succeeding configurations treated with a single computer run.

Function B. Function  $B(N, S)$  defines the length of the semichord of the foil at the fractional spanwise position  $S$ . Function  $N$  is the number of the foil section. The variable NNNN, placed in labeled common block CNRA, provides a running index as previously described.

#### Spanwise Pressure Modes

End Conditions. As described above, the Widnall program predicts load distributions on the foil by summing several terms of a series which is used to represent the pressure jump between the upper and lower surface of the foil. Each term of the series consists of a product of a chordwise and a spanwise pressure mode. The chordwise modes are taken from two-dimensional wing theory and are built into the program. The program user must specify the spanwise pressure modes.

This set of spanwise pressure modes must be chosen to conform to physical flow conditions. In particular, each set of modes must satisfy the following boundary conditions at the ends of foil sections.

- a. Foil loading drops to zero at the end of a cantilevered foil and at the free surface on a surface-piercing foil.
- b. Foil loading is nonzero at an intersection of two or more lifting surfaces, and at an intersection of a lifting surface and a reflecting plane.
- c. Pressure jumps along a closed path around an intersection of two or more foil sections must sum to zero.

Note that the above conditions place restrictions on the magnitude of each pressure mode at the ends of foils. When zero loading is required at the end of a foil, each of the spanwise pressure modes must become zero. However, when nonzero loading contributions are required, at least one of the modes must be nonzero. Each mode must be specified on all foil sections, although the shape of the mode does not have to be the same on all the sections, and each mode must satisfy condition (c) independently of the other modes.

Certain foil configurations suggest boundary conditions on the spanwise slopes of the modes, in addition to the above conditions on the magnitudes of the modes, at the ends of the foils:

- d. Loading on submerged foil tips is approximately elliptical.
- e. Loading near the free surface on surface-piercing foils approached zero less steeply than does an elliptical distribution.
- f. The load distribution slope at foil intersections is approximately zero (an end-plate effect).

It is convenient to satisfy all of the above boundary conditions which apply to a given foil by specifying one pressure mode having all requisite end-point magnitudes and slopes. Additional modes are then formed from the first mode multiplied by integral powers of S and/or  $(1.0-S)$ . The additional modes permit refinement of the pressure distribution by the calculation process.

The pressure modes must satisfy one final condition:

- g. Both antisymmetric and symmetric pressure modes must be included on foil surfaces which do not have purely symmetric loading.
- Inclusion of both symmetric and antisymmetric modes allows the program complete flexibility in proportioning the loading among different surfaces. A commonly-encountered foil configuration requiring the use of both types of modes is the inverted-T foil at a nonzero roll angle beneath a free surface, an example of which is treated below.

Subroutine FUNCTN. The subprogram Subroutine FUNCTN (N,S,F) is used to define the pressure modes for use in the program. Function F is an array which contains the ordinates of the pressure modes as functions of section number N and fractional spanwise position S.

The direction of a pressure jump which is represented by a given mode is designated by a sign convention based on the definition of the local foil slope PSI. The positive lift direction is given by a vector  $\vec{n}$  normal to the foil and having a positive z-component, as shown in Figure B.3. This convention allows interpretation of the sign of the lift distribution output.

#### Data Card Input

Input Format. Data cards are to be punched with the input quantities shown in Table B.5 for each of the three programs. The quantities were defined in Table B.4. The required formats are shown to the right of the input quantities, and the number of the column farthest to the right in the field in which the input quantity is to be placed is shown above the quantity.

Downwash Input. The downwash is the velocity which must be added to the free stream velocity to produce the flow at the surface of the foil. The downwash on a given foil surface is normal to the foil surface and to the free stream (in accordance with the assumption of small angles of attack) and has a direction opposite to the direction of positive lift ( $\vec{n}$ ). Downwash magnitude is determined by the boundary condition that fluid cannot penetrate the surface of the foil. In the case of steady loading, the boundary condition requires tangential flow along the surface, so that the downwash to be input to the program is  $v_n/U$ , where

$$\frac{v_n}{U} = \sin \alpha \approx \alpha \text{ (Steady Downwash)} \quad (\text{B.1})$$

TABLE B.5 - DATA CARD INPUT

TABLE B.5a - PROGRAM 1  
CARD INPUT

Program 1 (YKWS) Steady Loading

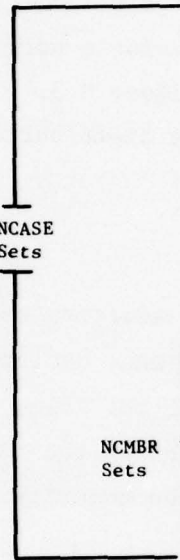
<b>NCASE Sets</b> 	Card 1:      5    10    15 NCASE/NCMBR/IPUNCH/ FORMAT(3I5)
	Card 2: Title (any 80 characters) FORMAT(1H1,80H)
	Card 3:      10   20   25   30   35   40   45   50   55   65 RF/EM/NS/NOCP/NOLT/NOST/NCP/MP/J3/ARM/ FORMAT(2F10.5,7I5,F10.5)
	Card 4:      5    10 NI(2)/NI(3)/...NI(2*NS+2)/ FORMAT(20I5)
	Card 5:      10    20 AF(1)/AF(2)/...AF(NS)/ FORMAT (10F10.5)
<b>NOCP Control Point Cards: N/XOC/SOS/ETA</b> <b>Next Card: Downwash Title (any 80 characters)</b> <b>(NOCP/3) Downwash Cards: VR(1)/VR(2)/VR(3)/</b> <b>...VR(NOCP)/</b> <b>10</b> <b>Next Card(s): YS/(one YS card for each section--NS total)</b> <b>FORMAT(15,3F10.5)</b> <b>FORMAT(1H1,80H)</b> <b>FORMAT(3(F12.3,12X))</b> <b>FORMAT(F10.5)</b>	
(begin at Card 2 again for next case)	

TABLE B.5 (Continued)

TABLE B.5b - PROGRAM  
2 CARD INPUT

Program 2 (YKWW) Unsteady Loading

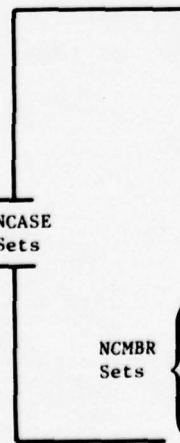
<b>NCASE Sets</b> 	Card 1:      5    10    15 NCASE/NCMBR/IPUNCH/ FORMAT(3I5)
	Card 2: Title (any 80 characters) FORMAT(1H1,80H)
	Card 3:      10   20   25   30   35   40   45   50   55   65 RF/EM/NS/NOCP/NOLT/NOST/NCP/MP/J3/ARM/ FORMAT(2F10.5,7I5,F10.5)
	Card 4:      5    10 NI(2)/NI(3)/...NI(2*NS+2)/ FORMAT(20I5)
	Card 5:      10    20 AF(1)/AF(2)/...AF(NS)/ FORMAT(10F10.5)
<b>NOCP Control Point Cards: N/XOC/SOS/ETA</b> <b>Next Card: Downwash Title (any 80 characters)</b> <b>(NOCP/3) Downwash Cards: VR(1)/VI(1)VR(2)/</b> <b>48    60    72</b> <b>VI(2)/VR(3)/VI(3)/...VR(NOCP)/VI(NOCP)/</b> <b>FORMAT(15,3F10.5)</b> <b>FORMAT(1H1,80H)</b> <b>FORMAT(6F12.3)</b>	
(begin at Card 2 again for next case)	

TABLE B.5 (Continued)

TABLE B.5c - PROGRAM  
3 CARD INPUT

Program 3 (YKWA) Auxiliary Program

Output from YKWS or YKWA	Card 1: Title (any 80 characters)	FORMAT(80H)
	Card 2: Free Surface Card	FORMAT(80H)
	10 20 25 30 35 40 45 50 60	
	Card 3: RF/SPAN/NS/NOLT/NOST/NOCP/MP/NCP/EM/ 65 70 NCMBR/ARM/	FORMAT(2F10.5,6I5, F10.5,I5,F10.5)
	10 20	
	Card 4: AF(1)/AF(2)/...AF(NS)/	FORMAT(6F10.5)
	5 10	
	Card 5: NI(2)/NI(3)/...NI(2*NS+2)/	FORMAT(14I5)
	[PR] matrix	
	[PI] matrix (if unsteady)	
NCMBR Sets	Next Card: Downwash Title (any 80 characters)	FORMAT(1H1,80H)
	12 24 36 (NOCP/3) Downwash Cards: VR(1)/VI(1)/VR(2)/ 48 60 72 VI(2)/VR(3)/VI(3)/...VR(NOCP)/VI(NOCP)/	FORMAT(6F12.3)
	if steady:	
	10	
	Next Card(s): YS/(one YS card for each section--NS total)	FORMAT(F10.5)

and  $\alpha$  is the local angle of attack. Note that downwash velocity is given in units of the free stream velocity. As indicated in this expression, the downwash input to the program is the local angle of attack (in radians), in keeping with the theoretical assumption that foil angles relative to the flow are small. Camber is thus represented by variations in  $v_n/U = \alpha$  as a function of  $x$ .

Steady downwash is input to program YKWS or YKWA using the VR array. For example, a downwash input of

$$VR(I) = 0.1, I = 1, NOCP \quad (B.2)$$

would indicate an uncambered foil at an incidence of 0.1 radian.

Unsteady loading results from either foil oscillation or from unsteady flow past the foil such as that due to the orbital velocities of waves. In the first case (foil oscillation), since the particles follow the motion of the foil, the downwash velocity is the velocity of the foil perpendicular to the mean position of the foil, which is assumed to be at zero angle of attack. Downwash input is the sinusoidal amplitude of the downwash velocity, in units of the free stream speed. If the position of the foil surface is given as

$$f(x, y, z, t) = 0 \quad (B.3)$$

then the normal velocity of the surface is

$$\frac{Df}{Dt} = \frac{\partial f}{\partial t} + \frac{\partial f}{\partial x} \frac{\partial x}{\partial t} + \frac{\partial f}{\partial y} \frac{\partial y}{\partial t} + \frac{\partial f}{\partial z} \frac{\partial z}{\partial t} \quad (B.4)$$

In this expression,  $\partial y / \partial t = \partial z / \partial t = 0$  because flow is restricted to the x-direction, while  $\partial x / \partial t = U$ , the flow speed. Since foil motion is positive upward and downwash  $v_n$  is positive downward,

$$v_n = - \frac{Df}{Dt} = - \frac{\partial f}{\partial t} - U \frac{\partial f}{\partial x} \quad (B.5)$$

The downwash may be expressed in terms of the amplitude of displacement of the foil from its mean position, which is a sinusoidally varying function

$$\delta(x, y, z, t) = \delta_0(x, y, z) e^{i\omega t} \quad (B.6)$$

where

$$f = \bar{f}(x, y, z) + \delta(x, y, z, t) \quad (B.7)$$

Using  $\delta$ , the downwash becomes

$$v_n = - \left[ i\omega \delta_o + U \frac{\partial \delta_o}{\partial x} \right] e^{i\omega t} \quad (B.8)$$

If the reduced frequency  $k$  is introduced, the downwash may be expressed as follows:

$$k = c\omega/2U \quad (B.9)$$

$$v_n = - \left[ \frac{i2kU\delta_o}{c} + U \frac{\partial \delta_o}{\partial x} \right] e^{i\omega t} \quad (B.10)$$

which is then normalized in terms of  $U$  to give

$$\frac{v_n}{U} = - \left[ i2k \frac{\delta_o}{c} + \frac{\partial \delta_o}{\partial x} \right] e^{i\omega t} \quad \begin{array}{l} \text{Unsteady Downwash} \\ \text{(Foil Oscillation)} \end{array} \quad (B.11)$$

The real component,  $-\partial \delta_o / \partial x$ , is the rate of change of the unsteady displacement amplitude in the streamwise direction, and is, therefore, nonzero for pitching motion and zero for bending motion.

The second cause of unsteady downwash is time-varying flow past the foil. An analysis is presented for the time-varying flow experienced by a foil traveling beneath waves due to a head sea in deep water. Surface waves cause the water particles beneath the surface to move in circular paths with an orbital velocity  $U'$ . The magnitude of the orbital velocity at a given depth  $h$  is given by<sup>33</sup>

$$U' = \omega' \frac{\zeta_w}{2} \exp(2\pi h/\lambda) \quad (B.12)$$

Both vertical and horizontal components of the orbital velocity contribute to the unsteady downwash, but at a relative phase difference of 90 deg. The unsteady downwash due to the orbital velocity's vertical component is

$$U' e^{i(\omega' t + \pi/2)} \quad (B.13)$$

The unsteady downwash due to the orbital velocity's horizontal component is

$$U' \alpha_o e^{i\omega' t} \quad (B.14)$$

where  $\alpha_o$  is the local slope of the foil, whether due to camber, angle of attack, or both. The total downwash due to wave motion is then

$$v_n = [U' \alpha_o + iU'] e^{i\omega' t} \quad (B.15)$$

In this expression,  $U'$  and  $\alpha_o$  are to be evaluated according to the wave characteristics and the location on the foil of each control point. The resultant downwash is similar in form to the downwash for pure pitching oscillation when  $\alpha_o$  is nonzero and is similar to the downwash for pure heaving motion when  $\alpha_o$  is zero.

The computer program requires, as input, values for the unsteady downwash seen by the foil traveling through the waves at speed  $U$ . The above expression gives the amplitude of the downwash seen by the foil, but  $\omega'$  must be replaced by  $\omega$ , the wave encounter frequency. The resulting downwash experienced by the foil is

$$\frac{v_n}{U} = \left[ \frac{U'}{U} \alpha_o + i \frac{U'}{U} \right] e^{i\omega t} \left| \begin{array}{l} \text{Unsteady Downwash} \\ \text{(Wave Motion)} \end{array} \right| \quad (B.16)$$

The downwash is input to the computer program in the form

$$\left. \begin{array}{l} VR(I) = \text{real component} \\ VI(I) = \text{imaginary component} \end{array} \right\} I = 1, NOCP$$

where the unsteady exponential  $e^{i\omega t}$  is assumed by the program and is not a direct input. The wave encounter frequency  $\omega$  is input as part of the reduced frequency RF.

Input Restrictions. Limitations on input parameter values, based on program structure or dimensioning, are indicated in Table B.4. Suggested input values are listed in Tables 2 and 6.

#### PROGRAM OUTPUT DESCRIPTION

All three programs generate printed output giving the loading on the subject foil systems and the input that was used to generate that loading. The output may be summarized as follows.

First, all input data except the downwash values are printed out. Second, Programs 1 and 2 print all matrices involved in the matrix inversion, including the resulting unit matrix. The size of the off-diagonal elements of the unit matrix indicates the quality of the inversion. Third, the resulting pressure matrix ( $[PR]+i[PI]$ ) is printed. This matrix is contained in the input for Program 3. Finally, downwash values, pressure mode coefficients, load coefficients, and center of pressure locations are printed by all programs. A chordwise pressure jump distribution is also given by Programs 1 and 3.

The pressure mode coefficients appear in the printed output as the CR and CI arrays. Array CR contains the steady loading coefficients or the real part of the unsteady coefficient, while CI contains the imaginary part of the unsteady coefficients. The matrix elements correspond to the coefficients  $a_{nm}$  found in Equation (2) in the following manner:

$$\left. \begin{array}{l} \text{Re}(a_{nm}) = CR(n+1,m+1) \\ \text{Im}(a_{nm}) = CI(n+1,m+1) \end{array} \right\} \begin{array}{l} n = 0, 1, 2, \dots, NOLT \\ m = 0, 1, 2, \dots, NOST \end{array}$$

Load coefficients\* are presented as both spanwise distributions and total loading on each foil section. The spanwise distributions consist of lift, pitching, and roll moment coefficients per unit span which are given at intervals of 5 percent of section span on each foil section. These spanwise coefficients are defined in Table B.6. The spanwise pressure modes ( $F$ ) selected by the program user are also listed at 5 percent intervals for reference. Total lift and moment coefficients are obtained by numerical integration of the spanwise distributions. Unsteady load coefficients are given in terms of both magnitude and phase angle. An example of printed output from each program is given along with the sample calculations.

Punched output can be obtained from Programs 1 and 2 and is required for running Program 3. When a value of 1 is input for IPUNCH, all necessary parameters for running Program 3 except the downwash cases are punched by having them written on the punch tape.

A center of pressure is calculated for each section whether the loading is steady or unsteady. For steady loading, the conventional center of pressure, at which the lift appears to act, is calculated and is given in terms of its  $x$ -coordinate and the fraction of the section span from the end of the section at which  $S = 0$ . For unsteady loading, the center of pressure is calculated in the following manner. Let the lift and pitching moment be given by

$$L = L_0 \cos \omega t \quad (B.17)$$

$$M = M_0 \cos (\omega t - \phi) \quad (B.18)$$

---

\*Load coefficients are only valid on sections having constant slope (PSI = constant); this restriction does not apply to pressure jump distribution coefficients CR and CI.

TABLE B.6 - OUTPUT LOAD COEFFICIENTS

CLR,CLI	Real and imaginary components of spanwise lift coefficient; (lift on a unit span)/ $qc_0$ ; positive lift opposite to positive downwash
CLMG	Magnitude of spanwise lift coefficient; $(CLR)^2 + (CLI)^2$
CLPH	Phase angle by which lift leads displacement; $\tan^{-1} (CLI/CLR)$ , deg
CPMR,CPMI	Real and imaginary components of spanwise pitching moment coefficient calculated about $x = ARM$ , positive tending to twist foil nose in direction of positive lift; (pitching moment on a unit span)/ $qc_0^2$
CPMG	Magnitude of spanwise pitching moment coefficient; $(CPMR)^2 + (CPMI)^2$
CPPH	Phase angle by which pitching moment leads displacement; $\tan^{-1} (CPMI/CPMR)$ , deg
CRMR,CRMI	Real and imaginary components of spanwise roll moment coefficient, calculated about section root chord (where $S = 0$ ); positive tending to roll foil in direction of positive lift; (roll moment due to a unit span)/ $qc_0^2$
CRMG	Magnitude of spanwise roll moment coefficient; $(CRMR)^2 + (CRMI)^2$
CRPH	Phase angle by which roll moment leads displacement; $\tan^{-1} (CRMI/CRMR)$ , deg
CP	Pressure jump coefficient (equivalent to lift per unit area in units of dynamic pressure); $2\Delta p/\rho U^2$

where the moment is calculated about an axis at  $x = a$ . By expanding the moment expression, it is possible to express the moment in terms of components which are in-phase and 90 deg out-of-phase with the lift.

$$M = M_0 \cos \phi \cos wt + M_0 \sin \phi \sin wt \quad (B.19)$$

The distance between the specified moment axis at  $x = a$  and the unsteady center of pressure,  $x = b$ , is given by the moment component in phase with the lift divided by the lift, or

$$b - a = (M_o \cos \phi) / L_o \quad (B.20)$$

The following considerations may help the reader to understand the nature of the unsteady center of pressure. If the unsteady pitching moment were calculated about an axis passing through  $x = b$ , its magnitude would be a minimum. In addition, it would have no component in-phase with the lift and would, therefore, be 90 deg out-of-phase with the lift. Measurement of either of these characteristics would permit a direct experimental determination of the unsteady center of pressure.

The program output gives the location of the unsteady center of pressure in terms of its  $x$ -coordinate,  $b$ , and the fraction of the section span from the root of the section.

#### OPERATING INSTRUCTIONS

The Widnall lifting-surface program has been adapted to run on the Control Data Corporation 6700 digital computer at DTNSRDC. All programs and subprograms are written in the FORTRAN Extended language (Version 3.0).

In its present form, the program requires about 205,000 (octal) memory locations. This amount of memory permits selection of the full range of numerical parameter values shown in Table B.5. The standard input used in the present study could be run with substantially less memory if the user reduced the appropriate array dimensions in the program. Conversely, larger arrays and increased dimensions would be required if the user desired more control points and larger numbers of integration intervals than are given in Table B.4.

Program run time varies according to the value of numerical input parameters. With the standard input, an execution time of about 35 sec was obtained, expressed in terms of the DTNSRDC convention of time required on a CDC-6400 computer. Unexpectedly and for unknown reasons, runs made

at AR = 1 required about twice as much time for execution (about 80 sec) as runs at AR = 6 and 10. Compilation of the source deck took 18 sec. It is concluded that the computer costs for using the program will normally be small compared to the cost of learning how to use the program and preparing input data.

#### SAMPLE CALCULATIONS

Sample calculations are presented to illustrate the use of each of the three programs. All data and subprogram codings corresponding to the sample calculations are included in the program listings given in Appendix C. Discussion of each case consists of description of the input data and presentation of printed output obtained from a computer run.

##### Program 1 (YKWS)

The foil configuration chosen as an example for the steady loading test case permits several aspects of program use to be illustrated. However, the calculated loading cannot be considered accurate because the numerical calculation has probably not achieved a stable condition. Considering that 60 control points were recommended on a single foil section, the sample calculation's use of only 16 on each section of a total of 48 on all three sections is probably inadequate for numerical stability. The stability of multisection foil calculations has, in fact, not been studied. Therefore, this sample calculation must be regarded as a test case only, for acquainting the user with program capabilities and providing a means of verifying other copies of the program at relatively low cost.

The subject foil is an inverted-T configuration which corresponds to a hydrofoil model for which loading has been determined experimentally.<sup>34</sup> The foil system, shown in Figure B.4, is rolled relative to the vertical and is surface-piercing. As a result, nonsymmetrical loading will occur on the foils even though the strut has zero angle of attack.

Three sections are used to represent the three foil surfaces. Values of NI(3), NI(5), and NI(7) have been set equal to zero to prevent integration over negative values of S for all sections.

Foil geometry is specified in the user-coded subprograms. Subroutine STRUCT gives the y- and z-coordinates for each section. Leading-edge

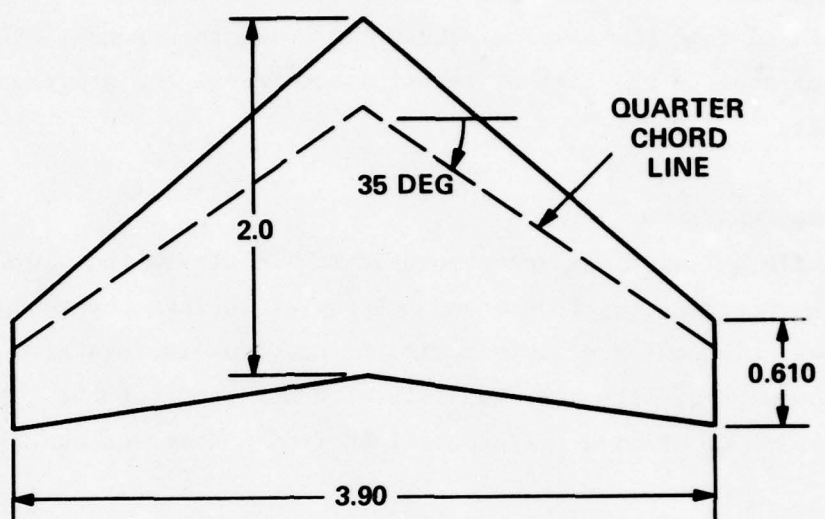


Figure B.4a - Foil Planform

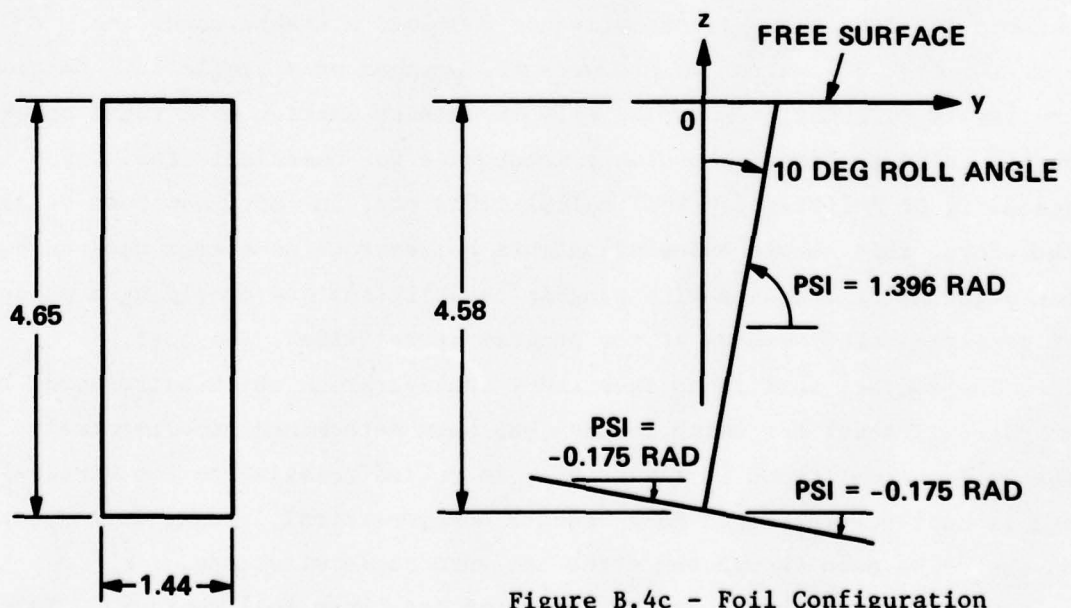


Figure B.4b - Strut Planform

Figure B.4c - Foil Configuration  
Looking Upstream

Figure B.4 - Foil Configuration for Steady Loading Test Case

x-coordinates are given in Function XLE. Local chord lengths for the tapered foils and the untapered strut appear in Function B.

Spanwise pressure modes are specified in Subroutine FUNCTN. Elliptical loading has been specified at the tips of the foils, and parabolic loading specified at the surface-piercing end of the strut. Both symmetric and antisymmetric modes are required on the foils in order to permit unequal loading. Only the minimum number of pressure modes has been specified; additional modes would allow refinement of the spanwise loading distribution shapes.

Control points were placed in networks of 4 spanwise by 4 chordwise on each section, making a total of 48 control points. Downwash values were based on the NACA 16-407,  $a = 1.0$  foil profiles, with the uncambered strut placed at zero incidence.

Printed output from the computer run is shown in Appendix D.

#### Program 2 (YKUW)

A relatively simple rectangular foil configuration<sup>15</sup> is used to illustrate an unsteady-loading calculation. The fully-wetted foil, shown in Figure B.5, undergoes forced deflection in an approximate first torsion mode.

A single section represents one half-span of the foil, while S-symmetry is invoked to represent the other half-span produced by a root reflection plate. The symmetrical half-span is included in the integration by making NI(3) nonzero. Foil geometry is specified in the subprograms listed in Appendix C. Four elliptical spanwise pressure modes were selected. Input data includes the reduced frequency value of 1.97, locations of 16 control points, and unsteady downwash values corresponding to the experimentally determined torsional mode shape at reduced frequency 1.97. Again, the use of 16 control points rather than the 60 recommended for stability is intended only to acquaint the user with the program.

Printed output is shown in Appendix E. In addition to the printed output, the PR and PI matrices, along with several auxiliary quantities, were placed on punch cards for use in Program 3. The sample calculation for Program 3 uses this punched output.

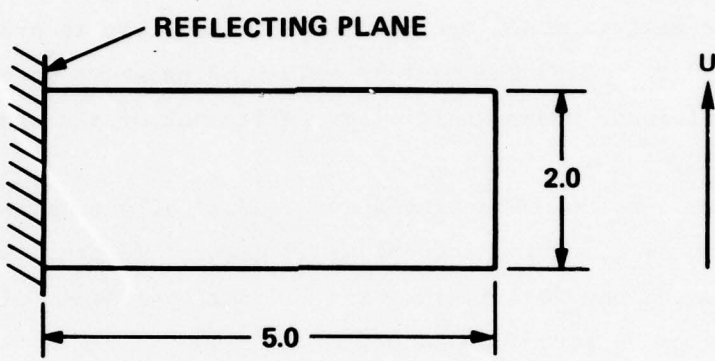


Figure B.5a - Foil Planform

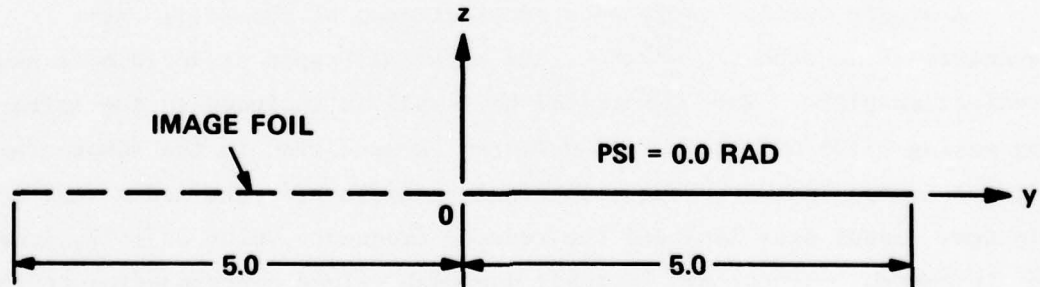


Figure B.5b - Foil Configuration  
Looking Upstream

Figure B.5 - Foil Configuration for Unsteady Loading Test Case

**Program 3 (YKWA)**

The unsteady load calculation described above is continued as the sample calculation for Program 3. The foil geometry and pressure mode subprograms are used in the same form as in Program 2. Data cards include the punched output from Program 2 and the same unsteady downwash values used for Program 2.

Printed output is shown in Appendix F.

**APPENDIX C**  
**PROGRAM LISTINGS AND INPUT FOR SAMPLE CALCULATIONS**

```

PROGRAM VNS30 INPUT,OUTPUT,PUNCH,TAPES=INPUT,TAPES=OUTPUT
C PROGRAM VNS30 COMPUTES THE STEADY STATE PRESSURE MATRIX - RF=4,0
C DIMENSIONS INVOLVING NS6=2*NS5=2*14, JS+JS15
C DIMENSION AP(16,JS+JS15),M11(16),MC(15),M15)
C DIMENSIONS INVOLVING MCP,MCP1,MCP2,MCP3,MCP4,MCP5
C DIMENSION AL15(15),AL15(15),MC11(15),MC12(15)
C DIMENSIONS INVOLVING AL15,AL15,MC11,MC12,MC13,MC14
C DIMENSIONS ALSO IN STATEMENT CALL MATRIX, CARD NUMBER
C ICR181, PUNCHES 10,11,12,13,14,15,16,17,18,19,20,21,22,23,24,25,26,27,28
C COMMON /AL15/,AL15(15),AL15(15),MC11,MC12,MC13,MC14,
C ISPLT,PSPLT,ESPLT,SPAN,PSQ1,PSQ2,EN,SPAN,ELA,MC15
C 2 /AL15/ SPAN /MC15/ MC15,MC16,MC17,MC18,MC19,MC11,MC12,MC13,MC14
C 3 MCP,MP, /CMRA/ /AMRN/
C CASEMNO = 0 IF FOIL CONFIGURATIONS, 1 FOR BLANK, 2 FOR NO PUNCHED OUTPUTS
C IPUNCH=0 IF FREQUENCIES, 1 IF BANDWIDTH NUMBER, 2 FOR NO FOIL SECTIONS
C MCPANO = 0 IF CHORDWISE PRESSURE MODES
C NOCPANO = 0 IF CHORDWISE PRESSURE MODES
C HOST=NO = 0 IF SPANNING
C MCPANO = 0 IF CHORDWISE INTEGRATION STEPS 6,8,10,16,32
C MCANO = 0 IF CHORDWISE INTEGRATION STEPS IN SINGULAR REGIONS 6,8,10,16,32
C MCANO = 0 IF CHORDWISE INTEGRATION STEPS IN J TH REGION 6,8,10,16,32
C JS=NO FOR INFINITE FROUDE NUMBER (PACE FOIL)
C JS=NO FOR INFINITE FROUDE NUMBER (INFOIL)
C 1 FOR INFINITE FROUDE NUMBER (INFOIL)
C 2 FOR INFINITE FROUDE NUMBER (INFOIL)
C 3 FOR INFINITE FROUDE NUMBER (INFOIL)
C 4 FOR INFINITE FROUDE NUMBER (INFOIL)
C 5 FOR INFINITE FROUDE NUMBER (INFOIL)
C 6 FOR INFINITE FROUDE NUMBER (INFOIL)
C 7 FOR INFINITE FROUDE NUMBER (INFOIL)
C 8 FOR INFINITE FROUDE NUMBER (INFOIL)
C 10 FOR INFINITE FROUDE NUMBER (INFOIL)
C 12 FOR INFINITE FROUDE NUMBER (INFOIL)
C 14 FOR INFINITE FROUDE NUMBER (INFOIL)
C 16 FOR INFINITE FROUDE NUMBER (INFOIL)
C 20 FOR INFINITE FROUDE NUMBER (INFOIL)
C 24 FOR INFINITE FROUDE NUMBER (INFOIL)
C 32 FOR INFINITE FROUDE NUMBER (INFOIL)
C 48 FOR INFINITE FROUDE NUMBER (INFOIL)
C 64 FOR INFINITE FROUDE NUMBER (INFOIL)
C 96 FOR INFINITE FROUDE NUMBER (INFOIL)
C 144 FOR INFINITE FROUDE NUMBER (INFOIL)
C 256 FOR INFINITE FROUDE NUMBER (INFOIL)
C 4096 FOR INFINITE FROUDE NUMBER (INFOIL)
C 65536 FOR INFINITE FROUDE NUMBER (INFOIL)
C 131072 FOR INFINITE FROUDE NUMBER (INFOIL)
C 262144 FOR INFINITE FROUDE NUMBER (INFOIL)
C 524288 FOR INFINITE FROUDE NUMBER (INFOIL)
C 1048576 FOR INFINITE FROUDE NUMBER (INFOIL)
C 2097152 FOR INFINITE FROUDE NUMBER (INFOIL)
C 4194304 FOR INFINITE FROUDE NUMBER (INFOIL)
C 8388608 FOR INFINITE FROUDE NUMBER (INFOIL)
C 16777216 FOR INFINITE FROUDE NUMBER (INFOIL)
C 33554432 FOR INFINITE FROUDE NUMBER (INFOIL)
C 67108864 FOR INFINITE FROUDE NUMBER (INFOIL)
C 134217728 FOR INFINITE FROUDE NUMBER (INFOIL)
C 268435456 FOR INFINITE FROUDE NUMBER (INFOIL)
C 536870912 FOR INFINITE FROUDE NUMBER (INFOIL)
C 107374184 FOR INFINITE FROUDE NUMBER (INFOIL)
C 214748368 FOR INFINITE FROUDE NUMBER (INFOIL)
C 429496736 FOR INFINITE FROUDE NUMBER (INFOIL)
C 858993472 FOR INFINITE FROUDE NUMBER (INFOIL)
C 1717986944 FOR INFINITE FROUDE NUMBER (INFOIL)
C 3435973888 FOR INFINITE FROUDE NUMBER (INFOIL)
C 6871947776 FOR INFINITE FROUDE NUMBER (INFOIL)
C 13743895520 FOR INFINITE FROUDE NUMBER (INFOIL)
C 27487781040 FOR INFINITE FROUDE NUMBER (INFOIL)
C 54975562080 FOR INFINITE FROUDE NUMBER (INFOIL)
C 10995112160 FOR INFINITE FROUDE NUMBER (INFOIL)
C 21990224320 FOR INFINITE FROUDE NUMBER (INFOIL)
C 43980448640 FOR INFINITE FROUDE NUMBER (INFOIL)
C 87960897280 FOR INFINITE FROUDE NUMBER (INFOIL)
C 175921794560 FOR INFINITE FROUDE NUMBER (INFOIL)
C 351843589120 FOR INFINITE FROUDE NUMBER (INFOIL)
C 703687178240 FOR INFINITE FROUDE NUMBER (INFOIL)
C 1407374356480 FOR INFINITE FROUDE NUMBER (INFOIL)
C 2814748712960 FOR INFINITE FROUDE NUMBER (INFOIL)
C 5629497425920 FOR INFINITE FROUDE NUMBER (INFOIL)
C 1125899485840 FOR INFINITE FROUDE NUMBER (INFOIL)
C 2251798971680 FOR INFINITE FROUDE NUMBER (INFOIL)
C 4503597943360 FOR INFINITE FROUDE NUMBER (INFOIL)
C 9007195886720 FOR INFINITE FROUDE NUMBER (INFOIL)
C 18014391773440 FOR INFINITE FROUDE NUMBER (INFOIL)
C 36028783546880 FOR INFINITE FROUDE NUMBER (INFOIL)
C 72057567093760 FOR INFINITE FROUDE NUMBER (INFOIL)
C 144115134187520 FOR INFINITE FROUDE NUMBER (INFOIL)
C 288230268375040 FOR INFINITE FROUDE NUMBER (INFOIL)
C 576460536750080 FOR INFINITE FROUDE NUMBER (INFOIL)
C 1152921074000160 FOR INFINITE FROUDE NUMBER (INFOIL)
C 2305842148000320 FOR INFINITE FROUDE NUMBER (INFOIL)
C 4611684296000640 FOR INFINITE FROUDE NUMBER (INFOIL)
C 9223368592001280 FOR INFINITE FROUDE NUMBER (INFOIL)
C 18446737184002560 FOR INFINITE FROUDE NUMBER (INFOIL)
C 36893474368005120 FOR INFINITE FROUDE NUMBER (INFOIL)
C 73786948736010240 FOR INFINITE FROUDE NUMBER (INFOIL)
C 147573897472020480 FOR INFINITE FROUDE NUMBER (INFOIL)
C 295147794944040960 FOR INFINITE FROUDE NUMBER (INFOIL)
C 590295589888081920 FOR INFINITE FROUDE NUMBER (INFOIL)
C 1180591177776163840 FOR INFINITE FROUDE NUMBER (INFOIL)
C 2361182355552327680 FOR INFINITE FROUDE NUMBER (INFOIL)
C 4722364711104655360 FOR INFINITE FROUDE NUMBER (INFOIL)
C 9444729422209310720 FOR INFINITE FROUDE NUMBER (INFOIL)
C 18889458844418621440 FOR INFINITE FROUDE NUMBER (INFOIL)
C 37778917688837242880 FOR INFINITE FROUDE NUMBER (INFOIL)
C 75557835377674485760 FOR INFINITE FROUDE NUMBER (INFOIL)
C 151115670755348971520 FOR INFINITE FROUDE NUMBER (INFOIL)
C 302231341510697943040 FOR INFINITE FROUDE NUMBER (INFOIL)
C 604462682221395886080 FOR INFINITE FROUDE NUMBER (INFOIL)
C 1208925364442791771520 FOR INFINITE FROUDE NUMBER (INFOIL)
C 2417850728885583543040 FOR INFINITE FROUDE NUMBER (INFOIL)
C 4835701457771167086080 FOR INFINITE FROUDE NUMBER (INFOIL)
C 9671402915542334172160 FOR INFINITE FROUDE NUMBER (INFOIL)
C 19342805830884668344320 FOR INFINITE FROUDE NUMBER (INFOIL)
C 38685611661769336688640 FOR INFINITE FROUDE NUMBER (INFOIL)
C 77371223323538673377280 FOR INFINITE FROUDE NUMBER (INFOIL)
C 154742446667177346754560 FOR INFINITE FROUDE NUMBER (INFOIL)
C 309484893334354693509120 FOR INFINITE FROUDE NUMBER (INFOIL)
C 618969786668709387018240 FOR INFINITE FROUDE NUMBER (INFOIL)
C 1237939573337418774364480 FOR INFINITE FROUDE NUMBER (INFOIL)
C 247587914667483754872960 FOR INFINITE FROUDE NUMBER (INFOIL)
C 495175829334967509745920 FOR INFINITE FROUDE NUMBER (INFOIL)
C 990351658669935019491840 FOR INFINITE FROUDE NUMBER (INFOIL)
C 198070331733987003898320 FOR INFINITE FROUDE NUMBER (INFOIL)
C 396140663467974007796640 FOR INFINITE FROUDE NUMBER (INFOIL)
C 792281326935948015593280 FOR INFINITE FROUDE NUMBER (INFOIL)
C 158456265867984031186560 FOR INFINITE FROUDE NUMBER (INFOIL)
C 316912531735968062373120 FOR INFINITE FROUDE NUMBER (INFOIL)
C 633825063471936124746240 FOR INFINITE FROUDE NUMBER (INFOIL)
C 126765012883868244949280 FOR INFINITE FROUDE NUMBER (INFOIL)
C 253530025767736489898560 FOR INFINITE FROUDE NUMBER (INFOIL)
C 507060051535472979797120 FOR INFINITE FROUDE NUMBER (INFOIL)
C 1014120103070445959594240 FOR INFINITE FROUDE NUMBER (INFOIL)
C 2028240206140891919188480 FOR INFINITE FROUDE NUMBER (INFOIL)
C 4056480412281783838376960 FOR INFINITE FROUDE NUMBER (INFOIL)
C 8112960824563567676753920 FOR INFINITE FROUDE NUMBER (INFOIL)
C 1622592169127135535351840 FOR INFINITE FROUDE NUMBER (INFOIL)
C 3245184338254271070703680 FOR INFINITE FROUDE NUMBER (INFOIL)
C 6490368676508542141407360 FOR INFINITE FROUDE NUMBER (INFOIL)
C 12980737353017084282814720 FOR INFINITE FROUDE NUMBER (INFOIL)
C 25961474706034168565629440 FOR INFINITE FROUDE NUMBER (INFOIL)
C 51922949412068337131258880 FOR INFINITE FROUDE NUMBER (INFOIL)
C 10384589882413667426251760 FOR INFINITE FROUDE NUMBER (INFOIL)
C 20769179764827334852503520 FOR INFINITE FROUDE NUMBER (INFOIL)
C 41538359529654669705007040 FOR INFINITE FROUDE NUMBER (INFOIL)
C 83076719059309339410014080 FOR INFINITE FROUDE NUMBER (INFOIL)
C 166153438118618678820028160 FOR INFINITE FROUDE NUMBER (INFOIL)
C 332306876237237357640056320 FOR INFINITE FROUDE NUMBER (INFOIL)
C 6646137524744747152800112640 FOR INFINITE FROUDE NUMBER (INFOIL)
C 13292275049489434305600225280 FOR INFINITE FROUDE NUMBER (INFOIL)
C 26584550098978868611200450560 FOR INFINITE FROUDE NUMBER (INFOIL)
C 53169100197957737222400901120 FOR INFINITE FROUDE NUMBER (INFOIL)
C 106338200395915474444801802240 FOR INFINITE FROUDE NUMBER (INFOIL)
C 212676400791830948889603604480 FOR INFINITE FROUDE NUMBER (INFOIL)
C 425352800182661897779207208960 FOR INFINITE FROUDE NUMBER (INFOIL)
C 850705600365333795558414417920 FOR INFINITE FROUDE NUMBER (INFOIL)
C 170141120070666791111682835840 FOR INFINITE FROUDE NUMBER (INFOIL)
C 340282240141333582223365671680 FOR INFINITE FROUDE NUMBER (INFOIL)
C 680564480282667164446731343360 FOR INFINITE FROUDE NUMBER (INFOIL)
C 136112896055333532889346668720 FOR INFINITE FROUDE NUMBER (INFOIL)
C 272225792110667165778693337440 FOR INFINITE FROUDE NUMBER (INFOIL)
C 544451584221333331557386674880 FOR INFINITE FROUDE NUMBER (INFOIL)
C 108890368442666666311477334960 FOR INFINITE FROUDE NUMBER (INFOIL)
C 217780736885333332622954669920 FOR INFINITE FROUDE NUMBER (INFOIL)
C 435561473770666665245909339840 FOR INFINITE FROUDE NUMBER (INFOIL)
C 871122947541333330491818679680 FOR INFINITE FROUDE NUMBER (INFOIL)
C 1742245895082666660983637359360 FOR INFINITE FROUDE NUMBER (INFOIL)
C 3484491790165333331967354718720 FOR INFINITE FROUDE NUMBER (INFOIL)
C 6968983580330666663934709437440 FOR INFINITE FROUDE NUMBER (INFOIL)
C 1393796716060333337869404874880 FOR INFINITE FROUDE NUMBER (INFOIL)
C 2787593432120666675738809749760 FOR INFINITE FROUDE NUMBER (INFOIL)
C 5575186864241333331547769599520 FOR INFINITE FROUDE NUMBER (INFOIL)
C 1115037372482666667895539119840 FOR INFINITE FROUDE NUMBER (INFOIL)
C 2230074744965333335789078239680 FOR INFINITE FROUDE NUMBER (INFOIL)
C 4460149489930666667578556479360 FOR INFINITE FROUDE NUMBER (INFOIL)
C 8920298979861333335157113148720 FOR INFINITE FROUDE NUMBER (INFOIL)
C 17840597959326666675355562295440 FOR INFINITE FROUDE NUMBER (INFOIL)
C 3568119591865333335177773458720 FOR INFINITE FROUDE NUMBER (INFOIL)
C 7136239183730666667535556417440 FOR INFINITE FROUDE NUMBER (INFOIL)
C 1427247836746133333517777383480 FOR INFINITE FROUDE NUMBER (INFOIL)
C 2854495673492266667535556766960 FOR INFINITE FROUDE NUMBER (INFOIL)
C 5708991346984533335177777333920 FOR INFINITE FROUDE NUMBER (INFOIL)
C 1141798269397066667535556766960 FOR INFINITE FROUDE NUMBER (INFOIL)
C 2283596538794133335177777333920 FOR INFINITE FROUDE NUMBER (INFOIL)
C 4567193077588266667535556766960 FOR INFINITE FROUDE NUMBER (INFOIL)
C 9134386155176533335177777333920 FOR INFINITE FROUDE NUMBER (INFOIL)
C 1826877230233133335177777333920 FOR INFINITE FROUDE NUMBER (INFOIL)
C 3653754460466266667515556766960 FOR INFINITE FROUDE NUMBER (INFOIL)
C 730750892093253333515556766960 FOR INFINITE FROUDE NUMBER (INFOIL)
C 1461501781865066667515556766960 FOR INFINITE FROUDE NUMBER (INFOIL)
C 292300356373013333515556766960 FOR INFINITE FROUDE NUMBER (INFOIL)
C 5846007127460266667515556766960 FOR INFINITE FROUDE NUMBER (INFOIL)
C 116920144593253333515556766960 FOR INFINITE FROUDE NUMBER (INFOIL)
C 2338402891865066667515556766960 FOR INFINITE FROUDE NUMBER (INFOIL)
C 467680578373013333515556766960 FOR INFINITE FROUDE NUMBER (INFOIL)
C 9353611567460266667515556766960 FOR INFINITE FROUDE NUMBER (INFOIL)
C 187072231348053333515556766960 FOR INFINITE FROUDE NUMBER (INFOIL)
C 3741444626961066667515556766960 FOR INFINITE FROUDE NUMBER (INFOIL)
C 748288925392213333515556766960 FOR INFINITE FROUDE NUMBER (INFOIL)
C 14965778507844266667515556766960 FOR INFINITE FROUDE NUMBER (INFOIL)
C 2993155701568853333515556766960 FOR INFINITE FROUDE NUMBER (INFOIL)
C 59863114031377066667515556766960 FOR INFINITE FROUDE NUMBER (INFOIL)
C 11972622806355413333515556766960 FOR INFINITE FROUDE NUMBER (INFOIL)
C 239452456127108266667515556766960 FOR INFINITE FROUDE NUMBER (INFOIL)
C 47890491225421653333515556766960 FOR INFINITE FROUDE NUMBER (INFOIL)
C 957809824508433066667515556766960 FOR INFINITE FROUDE NUMBER (INFOIL)
C 19156196490166613333515556766960 FOR INFINITE FROUDE NUMBER (INFOIL)
C 383123929803332266667515556766960 FOR INFINITE FROUDE NUMBER (INFOIL)
C 766247859606664413333515556766960 FOR INFINITE FROUDE NUMBER (INFOIL)
C 1532495719213388266667515556766960 FOR INFINITE FROUDE NUMBER (INFOIL)
C 306499143842677653333515556766960 FOR INFINITE FROUDE NUMBER (INFOIL)
C 612998287685355313333515556766960 FOR INFINITE FROUDE NUMBER (INFOIL)
C 122599657337071066667515556766960 FOR INFINITE FROUDE NUMBER (INFOIL)
C 24519931467414213333515556766960 FOR INFINITE FROUDE NUMBER (INFOIL)
C 490398629348284266667515556766960 FOR INFINITE FROUDE NUMBER (INFOIL)
C 98079725869656853333515556766960 FOR INFINITE FROUDE NUMBER (INFOIL)
C 196159451739313333515556766960 FOR INFINITE FROUDE NUMBER (INFOIL)
C 3923189034786266667515556766960 FOR INFINITE FROUDE NUMBER (INFOIL)
C 784637806957253333515556766960 FOR INFINITE FROUDE NUMBER (INFOIL)
C 156927561391451066667515556766960 FOR INFINITE FROUDE NUMBER (INFOIL)
C 31385512278290213333515556766960 FOR INFINITE FROUDE NUMBER (INFOIL)
C 627710245565804266667515556766960 FOR INFINITE FROUDE NUMBER (INFOIL)
C 125542049131160853333515556766960 FOR INFINITE FROUDE NUMBER (INFOIL)
C 2510840982623217066667515556766960 FOR INFINITE FROUDE NUMBER (INFOIL)
C 502168196524643413333515556766960 FOR INFINITE FROUDE NUMBER (INFOIL)
C 100433639104986853333515556766960 FOR INFINITE FROUDE NUMBER (INFOIL)
C 2008672782099737066667515556766960 FOR INFINITE FROUDE NUMBER (INFOIL)
C 401734556419875413333515556766960 FOR INFINITE FROUDE NUMBER (INFOIL)
C 803469112839750853333515556766960 FOR INFINITE FROUDE NUMBER (INFOIL)
C 160693822567950166667515556766960 FOR INFINITE FROUDE NUMBER (INFOIL)
C 3213876451359003266667515556766960 FOR INFINITE FROUDE NUMBER (INFOIL)
C 642775290271800653333515556766960 FOR INFINITE FROUDE NUMBER (INFOIL)
C 1285550580536013066667515556766960 FOR INFINITE FROUDE NUMBER (INFOIL)
C 257110116107202653333515556766960 FOR INFINITE FROUDE NUMBER (INFOIL)
C 514220232214405213333515556766960 FOR INFINITE FROUDE NUMBER (INFOIL)
C 1028440464428804266667515556766960 FOR INFINITE FROUDE NUMBER (INFOIL)
C 205688092885760853333515556766960 FOR INFINITE FROUDE NUMBER (INFOIL)
C 4113761857715217066667515556766960 FOR INFINITE FROUDE NUMBER (INFOIL)
C 822752371543043413333515556766960 FOR INFINITE FROUDE NUMBER (INFOIL)
C 1645504742866085266667515556766960 FOR INFINITE FROUDE NUMBER (INFOIL)
C 329100948573217053333515556766960 FOR INFINITE FROUDE NUMBER (INFOIL)
C 6582018971464341066667515556766960 FOR INFINITE FROUDE NUMBER (INFOIL)
C 1316403954288678213333515556766960 FOR INFINITE FROUDE NUMBER (INFOIL)
C 26328079085775644266667515556766960 FOR INFINITE FROUDE NUMBER (INFOIL)
C 5265615817155128853333515556766960 FOR INFINITE FROUDE NUMBER (INFOIL)
C 105312364343025777066667515556766960 FOR INFINITE FROUDE NUMBER (INFOIL)
C 21062472868605155413333515556766960 FOR INFINITE FROUDE NUMBER (INFOIL)
C 4212494573721030853333515556766960 FOR INFINITE FROUDE NUMBER (INFOIL)
C 84249891474420617066667515556766960 FOR INFINITE FROUDE NUMBER (INFOIL)
C 16849978294884123413333515556766960 FOR INFINITE FROUDE NUMBER (INFOIL)
C 33699956589768246853333515556766960 FOR INFINITE FROUDE NUMBER (INFOIL)
C 67399913179536493413333515556766960 FOR INFINITE FROUDE NUMBER (INFOIL)
C 13479926635907298653333515556766960 FOR INFINITE FROUDE NUMBER (INFOIL)
C 269598532718145973413333515556766960 FOR INFINITE FROUDE NUMBER (INFOIL)
C 53919706543629194653333515556766960 FOR INFINITE FROUDE NUMBER (INFOIL)
C 10783941308758398913333515556766960 FOR INFINITE FROUDE NUMBER (INFOIL)
C 215678826175167978266667515556766960 FOR INFINITE FROUDE NUMBER (INFOIL)
C 43135765235033595653333515556766960 FOR INFINITE FROUDE NUMBER (INFOIL)
C 862715304700671913333515556766960 FOR INFINITE FROUDE NUMBER (INFOIL)
C 17254306084013438266667515556766960 FOR INFINITE FROUDE NUMBER (INFOIL)
C 3450861216802687653333515556766960 FOR INFINITE FROUDE NUMBER (INFOIL)
C 69017224336053753413333515556766960 FOR INFINITE FROUDE NUMBER (INFOIL)
C 138034448672107506853333515556766960 FOR INFINITE FROUDE NUMBER (INFOIL)
C 276068897344215013333515556766960 FOR INFINITE FROUDE NUMBER (INFOIL)
C 5521377946884300266667515556766960 FOR INFINITE FROUDE NUMBER (INFOIL)
C 110427558937860053333515556766960 FOR INFINITE FROUDE NUMBER (INFOIL)
C 22085411787572008653333515556766960 FOR INFINITE FROUDE NUMBER (INFOIL)
C 44170823575144017066667515556766960 FOR INFINITE FROUDE NUMBER (INFOIL)
C 8834164715028803413333515556766960 FOR INFINITE FROUDE NUMBER (INFOIL)
C 17668328230557606853333515556766960 FOR INFINITE FROUDE NUMBER (INFOIL)
C 35336656461115213413333515556766960 FOR INFINITE FROUDE NUMBER (INFOIL)
C 70673312922230426853333515556766960 FOR INFINITE FROUDE NUMBER (INFOIL)
C 141346625844460853333515556766960 FOR INFINITE FROUDE NUMBER (INFOIL)
C 2826932516889217066667515556766960 FOR INFINITE FROUDE NUMBER (INFOIL)
C 565386503377843413333515556766960 FOR INFINITE FROUDE NUMBER (INFOIL)
C 113077306755686853333515556766960 FOR INFINITE FROUDE NUMBER (INFOIL)
C 2261546135113737066667515556766960 FOR INFINITE FROUDE NUMBER (INFOIL)
C 452309227022747413333515556766960 FOR INFINITE FROUDE NUMBER (INFOIL)
C 904618454045494853333515556766960 FOR INFINITE FROUDE NUMBER (INFOIL)
C 1809236908099899613333515556766960 FOR INFINITE FROUDE NUMBER (INFOIL)
C 3618473816199799266667515556766960 FOR INFINITE FROUDE NUMBER (INFOIL)
C 723694763239959853333515556766960 FOR INFINITE FROUDE NUMBER (INFOIL)
C 14473895264791981066667515556766960 FOR INFINITE FROUDE NUMBER (INFOIL)
C 2894778552958396213333515556766960 FOR INFINITE FROUDE NUMBER (INFOIL)
C 57895571059167924266667515556766960 FOR INFINITE FROUDE NUMBER (INFOIL)
C 1157811211823384853333515556766960 FOR INFINITE FROUDE NUMBER (INFOIL)
C 23156224236467797066667515556766960 FOR INFINITE FROUDE NUMBER (INFOIL)
C 4631244847293559413333515556766960 FOR INFINITE FROUDE NUMBER (INFOIL)
C 9262489694587118853333515556766960 FOR INFINITE FROUDE NUMBER (INFOIL)
C 18524979389172357653333515556766960 FOR INFINITE FROUDE NUMBER (INFOIL)
C 370499587783447153333515556766960 FOR INFINITE FROUDE NUMBER (INFOIL)
C 7409981754668943066667515556766960 FOR INFINITE FROUDE NUMBER (INFOIL)
C 148199635093378853333515556766960 FOR INFINITE FROUDE NUMBER (INFOIL)
C 2963992701867577066667515556766960 FOR INFINITE FROUDE NUMBER (INFOIL)
C 592798540371515413333515556766960 FOR INFINITE FROUDE NUMBER (INFOIL)
C 118559708068228853333515556766960 FOR INFINITE FROUDE NUMBER (INFOIL)
C 2371194161365
```

## Program 1 listing (continued)

## Program 1 Listing (continued)

Program 1 Listing (continued)

### Program 1 Listing (continued)

## Program 1 Listing (continued)

```

SUBROUTINE STRUCT(N,S,Z,Y,PSI)
C HYSTAD INVERTED T-FOIL STEADY LOADING TEST CASE
C H=DFPTH TO FOIL MIDSPAN      TH=ROLL ANGLE IN RADIANS
C NOTE THAT H DEFINED POSITIVE AS DFPTH/MN CHD
COMMON /CNRA/ NNNN
H=3.52
TH=0.17453
H=H*1.301
IF(N-2)1,2,3
1 PSI=-TH
Y=1.9495*S*COS(TH)-H*TAN(TH)
Z=-1.9495*S*SIN(TH)-H
RETURN
2 PSI=-TH
Y=-1.9495*S*COS(TH)-H*TAN(TH)
Z=1.9495*S*SIN(TH)-H
RETURN
3 PSI=(3.14159/2.0)-TH
Y=-H*TAN(TH)*(1.0-S)
Z=-H*(1.0-S)
RETURN
END
FUNCTION XLF(N,S)
C HYSTAD INVERTED T-FOIL STEADY LOADING TEST CASE
COMMON /CNRA/ NNNN
IF(N-2)1,1,3
1 XLF=-1.0+(1.9495*0.7002+0.350)*AHS(S)
RETURN
3 XLF=-0.493
RETURN
END
FUNCTION R(N,S)
C HYSTAD INVERTED T-FOIL STEADY LOADING TEST CASE
COMMON /CNRA/ NNNN
IF(N-2)1,1,3
1 R=1.0-0.695*S
RETURN
3 R=1.442
RETURN
END

```

### Program 1 User-Coded Subprograms

```
SUBROUTINE FUNCTN(N,S,F)
C HYSTAD INVERTFD T-FOIL STEADY LOADING TEST CASE
COMMON /CNRA/NNNN
DIMENSION F(6)
DO 519 J=1,6
519 F(J)=0.0
E=1.0-S**2
IF(N-2) 1,2,3
1 F(1)=SQRT(F)*(-0.05)
F(2)=SQRT(F)*(+0.05)
RETURN
2 F(1)=SQRT(F)*(+0.04)
F(2)=SQRT(F)*(+0.05)
RETURN
3 F(1)=F*0.09
RETURN
END
```

Program 1 User-Coded Subprograms (continued)

1 1 1  
 C HYSTAD INVERTED T-FOIL STEADY LOADING TEST CASE--PROGRAM CHECK ONLY  
 0.0 0.0 3 48 3 2 10 10 1  
 10 0 10 0 10 0 10  
 1.9495 1.9495 4.651

1	.1170	.9397	.0603	10	10
1	.1170	.7660	.1	10	10
1	.1170	.5000	.1	10	10
1	.1170	.1730	.1	10	10
1	.4132	.9397	.0603	10	10
1	.4132	.7660	.1	10	10
1	.4132	.5000	.1	10	10
1	.4132	.1730	.1	10	10
1	.75	.9397	.0603	10	10
1	.75	.7660	.1	10	10
1	.75	.500	.1	10	10
1	.75	.1730	.1	10	10
1	.9698	.9397	.0603	10	10
1	.9698	.7660	.1	10	10
1	.9698	.5	.1	10	10
1	.9698	.1730	.1	10	10
2	.1170	.9397	.0603	10	10
2	.1170	.7660	.1	10	10
2	.1170	.5000	.1	10	10
2	.1170	.1730	.1	10	10
2	.4132	.9397	.0603	10	10
2	.4132	.7660	.1	10	10
2	.4132	.5000	.1	10	10
2	.4132	.1730	.1	10	10
2	.75	.9397	.0603	10	10
2	.75	.7660	.1	10	10
2	.75	.500	.1	10	10
2	.75	.1730	.1	10	10
2	.9698	.9397	.0603	10	10
2	.9698	.7660	.1	10	10
2	.9698	.5	.1	10	10
2	.9698	.1730	.1	10	10
3	.1170	.9397	.0603	10	10
3	.1170	.7660	.1	10	10
3	.1170	.5000	.1	10	10
3	.1170	.1730	.1	10	10
3	.4132	.9397	.0603	10	10
3	.4132	.7660	.1	10	10
3	.4132	.5000	.1	10	10
3	.4132	.1730	.1	10	10

#### Program 1 Punch Card Input

3 .75	.9397	.0603	10	10
3 .75	.7660	.1	10	10
3 .75	.500	.1	10	10
3 .75	.1730	.1	10	10
3 .9698	.9397	.0603	10	10
3 .9698	.7660	.1	10	10
3 .9698	.5	.1	10	10
3 .9698	.1730	.1	10	10

C HYSTAD FOIL AT 4 DEG. INCIDENCE

0.022	0.022	0.022
0.022	0.062	0.062
0.062	0.062	0.096
0.096	0.096	0.096
0.153	0.153	0.153
0.153	0.022	0.022
0.022	0.022	0.062
0.062	0.062	0.062
0.096	0.096	0.096
0.096	0.153	0.153
0.153	0.153	0.000
0.000	0.000	0.000
0.000	0.000	0.000
0.000	0.000	0.000
0.000	0.000	0.000
0.0		
0.0		
0.0		

Program 1 Punch Card Input (continued)

## **Program 2 Listing**

FROM COPY OWNERSHIP TO PRACTICALITY

## Program 2 Listing (continued)

## Program 2 Listing (continued)

## **Program 2 Listing (continued)**

## **Program 2 listing (continued)**

## Program 2 Listing (continued)

## Program 2 Listing (continued)

## Program 2 Listing (continued)

**THIS PAGE IS BEST QUALITY PRATICABLY  
FROM COPY PUBLISHED 20 AGO**

```

SUBROUTINE STRUCT(N,S,Z,Y,PSI)
C UNSTEADY LOADING TEST CASE--SWRI RECTANGULAR HYDROFOIL
COMMON /CNRA/ NNNN
Y=5.0*S
Z=0.0
PSI=0.0
RETURN
END
FUNCTION XLF(N,S)
C UNSTEADY LOADING TEST CASE--SWRI RECTANGULAR HYDROFOIL
COMMON /CNRA/ NNNN
XLF=-1.0
RETURN
END
FUNCTION B(N,S)
C UNSTEADY LOADING TEST CASE--SWRI RECTANGULAR HYDROFOIL
COMMON /CNRA/ NNNN
B=1.0
RETURN
END
SUBROUTINE FUNCTN(N,S,F)
C UNSTEADY LOADING TEST CASE--SWRI RECTANGULAR HYDROFOIL
DIMENSION F(4)
R=SQRT(1.0-S**2)
F(1)=R
F(2)=R*S**2
F(3)=R*S**4
F(4)=R*S**6
RETURN
END

```

#### Program 2 User-Coded Subprograms

1 1 1  
 C UNSTEADY LOADING TEST CASE--SWRI RECTANGULAR HYDROFOIL  
 1.97 0.0 1 16 3 3 10 10 0 -0.38  
 10 10 10  
 5.0

1	.20	.20	.10
1	.40	.20	.10
1	.60	.20	.10
1	.80	.20	.10
1	.20	.40	.10
1	.40	.40	.10
1	.60	.40	.10
1	.80	.40	.10
1	.20	.60	.10
1	.40	.60	.10
1	.60	.60	.10
1	.80	.60	.10
1	.20	.80	.10
1	.40	.80	.10
1	.60	.80	.10
1	.80	.80	.10

C SWRI RECTANGULAR HYDROFOIL, TORSIONAL MODE, RF=1.97

.176	-.035	.176	.104	.176	.243
.176	.381	.363	-.072	.363	.215
.363	.501	.363	.787	.559	-.110
.559	.330	.559	.771	.559	1.211
.770	-.152	.770	.455	.770	1.062
.770	1.669				

### Program 2 Punch Card Input

### **Program 3 Listing**

### **Program 3 Listing (continued)**

```
FUNCTION XLE(N,S)
C UNSTEADY LOADING TEST CASE--SWRI RECTANGULAR HYDROFOIL--RF=1.97
XLE=-1.0
RETURN
END
FUNCTION R(N,S)
C UNSTEADY LOADING TEST CASE--SWRI RECTANGULAR HYDROFOIL--RF=1.97
B=1.0
RETURN
END
SUBROUTINE FUNCTN(N,S,F)
C UNSTEADY LOADING TEST CASE--SWRI RECTANGULAR HYDROFOIL--RF=1.97
DIMENSION F(6)
R=SQRT(1.0-S**2)
F(1)=R
F(2)=R*S**2
F(3)=R*S**4
F(4)=R*S**6
RETURN
END
```

### Program 3 User-Coded Subprograms

C UNSTEADY LOADING TEST CASE--SWRI RECTANGULAR HYDROFOIL

J3=0 INFINITE FLUID

1.97000	5.00000	1	3	3	16	10	10	0.00000	1	- .38
1.00000										
10	10									
.18477725E-01	-.30675943E-01				-.11228947E+00					
.17351283F+00	.63868057E+00				.11804733E+00					
-.75227897E+00	-.10196953E-02				-.57613615E-02					
.96467961F-02	.24478672E-01				-.57761464E+00					
-.27941997E-01	.68135495E+00				-.45963889E-02					
.10753080F+00	.28900852E-01				-.47214427E-01					
-.34580948E-01	.55652244E-01				.71269003E+00					
.22146141F-01	-.10554828E+00				-.19942488E-01					
.58583096E+00	.23218220E-01				.11458083E+00					
.33613705E-02	-.49875540F-02				-.17444346E-01					
-.70764595E-01	-.26689322E+00				-.77143908E-01					
.50662731F+00	.25138325E-03				-.16810617E-02					
-.59951081E-02	-.67279098F-02				.23824915E+00					
.15924178E-01	-.45886014F+00				-.40216593E-03					
.17135733E-01	-.13556733E-01				.19814147E-01					
.24899114F-01	-.37279304F-01				-.48520604E+00					
.60652896E-02	-.17639624F-01				.78610360E-02					
-.24092325E+00	-.15626980E-01				-.66090388E-01					
-.68822785E-02	.12109707E-01				.44706184E-01					
-.19092197F+00	-.70222948E+00				-.15152783E+00					
.96111445E+00	.70063470E-03				.14143330E-02					
-.96925924E-02	-.26115529E-01				.61912887E+00					
.36828909E-01	-.84867990E+00				.21459717E-02					
-.41516355E-01	-.32307280E-01				.54825850E-01					
.44169827E-01	-.75778312F-01				-.90181716E+00					
-.59804207E-02	.39810856F-01				.20269119E-01					
-.63497004E+00	-.27752678E-01				-.14874322E+00					
.24731548E-02	-.41605870E-02				-.16094111F-01					
.79513627E-01	.30205130F+00				.12571859E+00					
-.82448680E+00	-.22543916E-03				-.39252748E-03					
.72596514F-02	.26710346F-02				.25361066E+00					
-.21226610E-01	.72172119F+00				-.65190029E-03					
.14168333E-01	.14956353E-01				-.23406082E-01					
-.38529186E-01	.62523197E-01				.75238118E+00					
.25476870E-02	-.13568881E-01				-.62931141E-02					
.25196399E+00	.21605686F-01				.10733603E+00					
-.27842759E-02	.58649089E-02				.63458329E-01					

Program 3 Punch Card Input

THIS PAGE IS BEST QUALITY PUBLISHING CO.  
FROM GUY PUBLISHING CO.

-.22563782E-01	-.34785077E+00	.19965080E-01	.24793980E-01
.40945601E+00	-.13649903E-02	.23900082E-01	-.42646661E-02
.87299895E-02	-.11604061E+00	.18108455E-01	-.10594658E-01
.13404100E+00	-.18825516E-01	-.52204462E-02	.25314149E-01
.87475295E-02	.29726270E-01	-.12833876E+00	-.59411380E-01
-.35386527E-01	.14899775E+00	.75389699E-01	.29767810E-02
.55270247E-02	-.63546648E-01	-.20345209E-01	-.19035698E-01
.34653487E+00	.24068757E-01	.20118828E-01	-.39933747E+00
.35767808E-03	.21384147E-02	.11133602E-01	.72088548E-02
.33884298E-02	.14011575E+00	-.13517753E-01	-.10458343E-01
-.27181776E+00	-.86959528E-04	.58314003E-02	-.20342107E-02
-.44586890E-02	.38866654E-01	.27467066E-02	.81089504E-02
-.81037100E-01	-.50173060E-03	-.71530756E-03	.56772580E-02
-.10841301E-02	-.13522064E-01	.45507849E-01	.45399362E-01
.25458087E-01	-.92297972E-01	-.78216640E-01	.29677536E-03
.23677670E-02	-.13818183E-01	.80872811F-02	.38955707E-03
-.11124130E+00	-.14968275E-01	-.54109258E-02	.22329982E+00
-.12511891E-02	-.12947438E-02	-.23170867E-01	.19056987E-01
.25012401E-01	.37349280E+00	-.26126349E-01	-.35489401E-01
-.51350157E+00	.58241137E-03	-.74191113E-02	.15848975E-02
-.89090294E-02	.12583551E+00	-.26731414E-01	.12158099E-01
-.17462386E+00	.37513179E-01	.19436527E-02	-.85413046E-02
-.19626800E-02	-.30909584E-01	.14087106E+00	.34797660E-01
.42205847E-01	-.19512794E+00	-.41532819E-01	-.17780829E-02
-.10760498E-02	.27420033E-01	.25627722E-01	.21748995E-01
-.42659756E+00	-.35513202E-01	-.31330309E-01	.59336940E+00
.39935926E-03	.57127361E-03	.81346054E-02	-.86116472E-02
-.26830213E-02	-.14690516E+00	.22635650E-01	.20833747E-01
.42838977E+00	-.18732584E-03	.28652938E-02	-.73796541E-03
.43514301E-02	-.38912777E-01	.99195763E-02	-.11300588E-01
.13227360E+00	-.29624449E-01	-.68598156E-03	.31465266E-02
.11791485E-02	.12888224E-01	-.47843419E-01	-.24397777E-01
-.36321571E-01	.15188219E+00	.61592235E-01	.43786899E-03
.47716782E-03	-.94499020E-02	-.12378642E-01	.13914201E-03
.17250962E+00	.30493266E-01	.15464593E-01	-.47494711E+00

C SWRI RECTANGULAR HYDROFOIL, TORSIONAL MODE, RF=1.97

.176	-.035	.176	.104	.176	.243
.176	.381	.363	-.072	.363	.215
.363	.501	.363	.787	.559	-.110
.559	.330	.559	.771	.559	1.211
.770	-.152	.770	.455	.770	1.062
.770	1.669				

Program 3 Punch Card Input (continued)

**APPENDIX D**  
**PROGRAM 1 OUTPUT FOR SAMPLE CALCULATION**

NUMBER OF FOIL CONFIGURATIONS= 1

FOIL CONFIGURATION NUMBER 1

C MYSTAD INVERTED T-FOIL STEADY LOADING TEST CASE--PROGRAM CHECK ONLY

CHECK INPUT PARAMETERS

RF EN MS HCP MOLI HOST HCP MP J3 ARH

0.00000 0.00000 3 .44 3 2 10 10 1 -0.00000

M1(2)= 10 0 10 0 10 0 10

AP(1)= 1.94950 1.93950 4.55100

CONTROL POINT NO.	SECTION XOC	ETA	SOS	ETA
1	.978	.940	.060	
2	.978	.580	.100	
3	.978	.580	.100	
4	.978	.580	.100	
5	.978	.580	.100	
6	.978	.580	.100	
7	.978	.580	.100	
8	.978	.580	.100	
9	.978	.580	.100	
10	.978	.580	.100	
11	.978	.580	.100	
12	.978	.580	.100	
13	.978	.580	.100	
14	.978	.580	.100	
15	.978	.580	.100	
16	.978	.580	.100	
17	.978	.580	.100	
18	.978	.580	.100	
19	.978	.580	.100	
20	.978	.580	.100	
21	.978	.580	.100	
22	.978	.580	.100	
23	.978	.580	.100	
24	.978	.580	.100	
25	.978	.580	.100	
26	.978	.580	.100	
27	.978	.580	.100	
28	.978	.580	.100	
29	.978	.580	.100	

THIS PAGE IS BEST QUALITY PRAGMATIC  
FROM COPY FURNISHED TO DDC

THIS PAGE IS BEST QUALITY PRAGICABLE  
FROM COPY PUBLISHED TO DDC

.17268089E-01	.17008615E-03	.38653098E-03	.16814701E-02
.23580068E-02	.58966085E-02	.30451252E-01	.22168055E-03
.60150682E-03	.34423147E-02	.22608198E-02	.61576884E-02
.44652964E-01	.20117731E-03	.61663625E-03	.45012645E-02
.85372044E-03	.12472506E-02	.58401629E-02	.13892207E-03
.20296194E-03	.71475775E-03	.23753390E-02	.36435170E-02
.10986243E-01	.25510800E-03	.40504958E-03	.19602326E-02
.37992653E-02	.60366421E-02	.-36421278E-01	.36949784E-03
.61582092E-03	.34510280E-02	.41844280E-02	.66737208E-02
.-40704336E-01	.39635862E-03	.66626746E-03	.-40553000E-02

CAMBER CASE NUMBER= 1 OF 1 CASES

C MYSTAD FOIL AT 4 DEG. INCIDENCE

.02200	.02200	.02200
.02200	.06200	.06200
.06200	.06200	.09600
.09600	.09600	.09600
.15300	.15300	.15300
.15300	.02200	.02200
.02200	.02200	.06200
.06200	.06200	.09600
.09600	.09600	.09600
.15300	.15300	.15300
.15300	.15300	.000000
0.00000	0.00000	0.00000
0.00000	0.00000	0.00000
0.00000	0.00000	0.00000
0.00000	0.00000	0.00000
0.00000	0.00000	0.00000

REAL COEFFICIENT MATRIX CR (SPANWISE X CHRONWISE)  
-1.761E-05 1.732E-07 -2.140E-06  
1.21CE-02 1.213E-02 -1.994E-02

LOCAL COEFFICIENTS AND SPANWISE FUNCTION VALUES ON SECTION 1 AT SPANWISE POSITION S  
MOMENTS CALCULATED ABOUT X = -0.000

S	CLR	CPMR	CRMR	F(1)	F(2)	F(3)	F(4)
-	---	----	----	----	----	----	----
0.00	.306782	.040600	0.000000	-5.0E-02	5.0E-02		
.05	.306398	.031326	.014933	-5.0E-02	5.0E-02		
.10	.305244	.022021	.029754	-5.0E-02	5.0E-02		
.15	.303311	.012752	.044348	-4.9E-02	4.9E-02		
.20	.300584	.003589	.058599	-4.9E-02	4.9E-02		
.25	.297040	-.005396	.072385	-4.8E-02	4.8E-02		
.30	.292651	-.014123	.065579	-4.8E-02	4.8E-02		
.35	.287372	-.022510	.098043	-4.7E-02	4.7E-02		
.40	.281170	-.030495	.109628	-4.6E-02	4.6E-02		
.45	.273965	-.037960	.120171	-4.5E-02	4.5E-02		
.50	.265681	-.044809	.129466	-4.3E-02	4.3E-02		
.55	.256213	-.050924	.137359	-4.2E-02	4.2E-02		
.60	.245425	-.056167	.143537	-4.0E-02	4.0E-02		
.65	.233136	-.060372	.147711	-3.8E-02	3.8E-02		
.70	.219086	-.063328	.149460	-3.6E-02	3.6E-02		
.75	.202917	-.066762	.148345	-3.3E-02	3.3E-02		
.80	.184069	-.064287	.143837	-3.0E-02	3.0E-02		
.85	.161607	-.061307	.133890	-2.6E-02	2.6E-02		
.90	.133723	-.054754	.117312	-2.2E-02	2.2E-02		
.95	.0955793	-.042106	.086705	-1.6E-02	1.6E-02		
1.00	.000000	-.000000	.000000	-1.3E-08	1.3E-08		

SECTION LIFT COEFFICIENT = .240933  
SECTION PITCH MCM COEFF = -.029668  
SECTION ROLL MCM COEFF = .096666  
X-COORDINATE OF SECTION CP = .246274  
SPANWISE COORDINATE OF SECTION CP = .827335

Program 1 Output -- Steady Loading Test Case (continued)

THIS PAGE IS BEST QUALITY PROCESSED  
FROM GORY FURNISHED TO DDC

LOCAL COEFFICIENTS AND SPANWISE FUNCTION VALUES ON SECTION 2 AT SPANWISE POSITION S  
MOMENTS CALCULATED ABOUT X = 0.000

S	CLR	CPMR	CRPR	F(1)	F(2)	F(3)	F(4)
-	---	----	----	----	----	----	----
0.00	.306250	.040464	0.000000	4.0E-02	5.0E-02		
.05	.305666	.031209	.014907	4.0E-02	5.0E-02		
.10	.304714	.021922	.029702	4.0E-02	5.0E-02		
.15	.302705	.012672	.044271	4.0E-02	4.9E-02		
.20	.300862	.003528	.050497	3.9E-02	4.9E-02		
.25	.296525	-.005437	.072259	3.9E-02	4.8E-02		
.30	.292143	-.014440	.085430	3.0E-02	4.8E-02		
.35	.266679	-.022526	.097872	3.7E-02	4.7E-02		
.40	.208682	-.030466	.109438	3.7E-02	4.6E-02		
.45	.273498	-.037934	.119963	3.6E-02	4.5E-02		
.50	.265220	-.044760	.129262	3.5E-02	4.3E-02		
.55	.259769	-.050070	.137121	3.3E-02	4.2E-02		
.60	.245088	-.056100	.143288	3.2E-02	4.0E-02		
.65	.232729	-.060298	.167456	3.0E-02	3.8E-02		
.70	.218706	-.063242	.199229	2.9E-02	3.6E-02		
.75	.202565	-.066671	.160008	2.6E-02	3.3E-02		
.80	.183750	-.066193	.143288	2.4E-02	3.0E-02		
.85	.161327	-.061215	.133665	2.1E-02	2.6E-02		
.90	.133491	-.054669	.117108	1.7E-02	2.2E-02		
.95	.095626	-.042040	.088551	1.2E-02	1.6E-02		
1.00	.000000	-.000000	.000000	1.0E-08	1.3E-08		

SECTION LIFT COEFFICIENT = .240515  
SECTION PITCH MOM COEFF = -.029652  
SECTION ROLL MOM COEFF = .059443

X-COORDINATE OF SECTION CP = .246574  
SPANWISE COORDINATE OF SECTION CP = .827325

LOCAL COEFFICIENTS AND SPANWISE FUNCTION VALUES ON SECTION 3 AT SPANWISE POSITION S  
MOMENTS CALCULATED ABOUT X = 3.000

S	CLR	CPMR	CRPR	F(1)	F(2)	F(3)	F(4)
-	---	----	----	----	----	----	----
0.00	-.000369	.006027	0.000000	9.0E-02	0.		
.05	-.000368	.000027	-.000030	9.0E-02	0.		
.10	-.000365	.000027	-.000059	8.9E-02	0.		
.15	-.000361	.000027	-.000087	8.8E-02	0.		
.20	-.000354	.000026	-.000114	8.6E-02	0.		
.25	-.000346	.000026	-.000140	8.4E-02	0.		
.30	-.000336	.000025	-.000163	8.2E-02	0.		
.35	-.000324	.000024	-.000182	7.9E-02	0.		
.40	-.000310	.000023	-.000200	7.6E-02	0.		
.45	-.000294	.000022	-.000214	7.2E-02	0.		
.50	-.000277	.000020	-.000223	6.7E-02	0.		
.55	-.000257	.000019	-.000228	6.3E-02	0.		
.60	-.000236	.000017	-.000229	5.8E-02	0.		
.65	-.000213	.000016	-.000223	5.2E-02	0.		
.70	-.000186	.000014	-.000213	4.6E-02	0.		
.75	-.000161	.000012	-.000195	3.9E-02	0.		
.80	-.000132	.000010	-.000171	3.2E-02	0.		
.85	-.000102	.000008	-.000140	2.5E-02	0.		
.90	-.000078	.000005	-.000102	1.7E-02	0.		
.95	-.000036	.000003	-.000055	8.0E-03	0.		
1.00	-.000000	.000000	-.000000	5.0E-15	0.		

SECTION LIFT COEFFICIENT = -.000246  
SECTION PITCH MOM COEFF = .000018  
SECTION ROLL MOM COEFF = -.000149

X-COORDINATE OF SECTION CP = .213428  
SPANWISE COORDINATE OF SECTION CP = 1.744125

Program 1 Output -- Steady Loading Test Case (continued)

THIS PAGE IS BEST QUALITY AVAILABLE  
FROM COPY FURNISHED TO DDC

PRESSURE COEFFICIENTS		PRESSURE COEFFICIENTS						PRESSURE COEFFICIENTS							
SECTION	SPAN	SOS	MOL	MOST	SECTION	SPAN	SOS	MOL	MOST	SECTION	SPAN	SOS	MOL	MOST	
1	1.069	0.680	2	1.949	0.000	3	1.069	0.000	4	0.651	0.000	5	1.069	0.000	6
XOC	CP	XOC	CP	XOC	CP	XOC	CP	XOC	CP	XOC	CP	XOC	CP	XOC	CP
.91	.2964E+00	.91	.2957E+00	.91	.2957E+00	.91	.2957E+00	.91	.2957E+00	.91	.2957E+00	.91	.2957E+00	.91	.2957E+00
.92	.2095E+00	.92	.2090E+00	.92	.2090E+00	.92	.2090E+00	.92	.2090E+00	.92	.2090E+00	.92	.2090E+00	.92	.2090E+00
.93	.1711E+00	.93	.1708E+00	.93	.1708E+00	.93	.1708E+00	.93	.1708E+00	.93	.1708E+00	.93	.1708E+00	.93	.1708E+00
.94	.1468E+00	.94	.1478E+00	.94	.1478E+00	.94	.1478E+00	.94	.1478E+00	.94	.1478E+00	.94	.1478E+00	.94	.1478E+00
.95	.1322E+00	.95	.1324E+00	.95	.1324E+00	.95	.1324E+00	.95	.1324E+00	.95	.1324E+00	.95	.1324E+00	.95	.1324E+00
.96	.1215E+00	.96	.1211E+00	.96	.1211E+00	.96	.1211E+00	.96	.1211E+00	.96	.1211E+00	.96	.1211E+00	.96	.1211E+00
.97	.1126E+00	.97	.1123E+00	.97	.1123E+00	.97	.1123E+00	.97	.1123E+00	.97	.1123E+00	.97	.1123E+00	.97	.1123E+00
.98	.1056E+00	.98	.1054E+00	.98	.1054E+00	.98	.1054E+00	.98	.1054E+00	.98	.1054E+00	.98	.1054E+00	.98	.1054E+00
.99	.9991E-01	.99	.9986E-01	.99	.9986E-01	.99	.9986E-01	.99	.9986E-01	.99	.9986E-01	.99	.9986E-01	.99	.9986E-01
.991	.9514E-01	.991	.9490E-01	.991	.9490E-01	.991	.9490E-01	.991	.9490E-01	.991	.9490E-01	.991	.9490E-01	.991	.9490E-01
.995	.7966E-01	.995	.7927E-01	.995	.7927E-01	.995	.7927E-01	.995	.7927E-01	.995	.7927E-01	.995	.7927E-01	.995	.7927E-01
.998	.7144E-01	.998	.7124E-01	.998	.7124E-01	.998	.7124E-01	.998	.7124E-01	.998	.7124E-01	.998	.7124E-01	.998	.7124E-01
.999	.6859E-01	.999	.6642E-01	.999	.6642E-01	.999	.6642E-01	.999	.6642E-01	.999	.6642E-01	.999	.6642E-01	.999	.6642E-01
.9991	.6361E-01	.9991	.6349E-01	.9991	.6349E-01	.9991	.6349E-01	.9991	.6349E-01	.9991	.6349E-01	.9991	.6349E-01	.9991	.6349E-01
.9995	.6127E-01	.9995	.6169E-01	.9995	.6169E-01	.9995	.6169E-01	.9995	.6169E-01	.9995	.6169E-01	.9995	.6169E-01	.9995	.6169E-01
.9998	.6067E-01	.9998	.6057E-01	.9998	.6057E-01	.9998	.6057E-01	.9998	.6057E-01	.9998	.6057E-01	.9998	.6057E-01	.9998	.6057E-01
.9999	.5999E-01	.9999	.5995E-01	.9999	.5995E-01	.9999	.5995E-01	.9999	.5995E-01	.9999	.5995E-01	.9999	.5995E-01	.9999	.5995E-01
.99991	.5939E-01	.99991	.5931E-01	.99991	.5931E-01	.99991	.5931E-01	.99991	.5931E-01	.99991	.5931E-01	.99991	.5931E-01	.99991	.5931E-01
.99995	.5803E-01	.99995	.5876E-01	.99995	.5876E-01	.99995	.5876E-01	.99995	.5876E-01	.99995	.5876E-01	.99995	.5876E-01	.99995	.5876E-01
.99998	.5812E-01	.99998	.5806E-01	.99998	.5806E-01	.99998	.5806E-01	.99998	.5806E-01	.99998	.5806E-01	.99998	.5806E-01	.99998	.5806E-01
.99999	.5710E-01	.99999	.5705E-01	.99999	.5705E-01	.99999	.5705E-01	.99999	.5705E-01	.99999	.5705E-01	.99999	.5705E-01	.99999	.5705E-01
.999991	.5561E-01	.999991	.5556E-01	.999991	.5556E-01	.999991	.5556E-01	.999991	.5556E-01	.999991	.5556E-01	.999991	.5556E-01	.999991	.5556E-01
.999995	.5344E-01	.999995	.5339E-01	.999995	.5339E-01	.999995	.5339E-01	.999995	.5339E-01	.999995	.5339E-01	.999995	.5339E-01	.999995	.5339E-01
.999998	.5033E-01	.999998	.5029E-01	.999998	.5029E-01	.999998	.5029E-01	.999998	.5029E-01	.999998	.5029E-01	.999998	.5029E-01	.999998	.5029E-01
.999999	.4589E-01	.999999	.4586E-01	.999999	.4586E-01	.999999	.4586E-01	.999999	.4586E-01	.999999	.4586E-01	.999999	.4586E-01	.999999	.4586E-01
.9999991	.4191E-01	.9999991	.4191E-01	.9999991	.4191E-01	.9999991	.4191E-01	.9999991	.4191E-01	.9999991	.4191E-01	.9999991	.4191E-01	.9999991	.4191E-01
.9999995	.3642E-01	.9999995	.3642E-01	.9999995	.3642E-01	.9999995	.3642E-01	.9999995	.3642E-01	.9999995	.3642E-01	.9999995	.3642E-01	.9999995	.3642E-01

THIS PAGE IS BEST QUALITY PRODUCED  
FROM COPY FORWARDED TO DDC

Program 1 Output -- Steady Loading Test Case (continued)

**APPENDIX E**  
**PROGRAM 2 OUTPUT FOR SAMPLE CALCULATION**

NUMBER OF FOIL CONFIGURATIONS = 1

**FOIL CONFIGURATION NUMBER 1**

**C UNSTEADY LOADING TEST CASE--SWRI RECTANGULAR HYDROFOIL**

```

    CHECK INPUT PARAMETERS
      RF   EM
      1.97044  6.00000
      NITER = 10  10  10
      ATIME = 5.00000

```

卷之三

```

CONTROL POINT NO. 15
KOC SOS ETA
SECTION .60 .63 .10
1 .66 .63 .10

CONTROL POINT NO. 16
KOC SOS ETA
SECTION .45 .90 .11
1 .45 .90 .11

IF INTEST=1, MATRIX NOT SINGULAR
IF INTEST=2, MATRIX SINGULAR
IF INTEST=3,

```

THIS PAGE IS BEST QUALITY PRAGMATIC  
FROM COPY PUBLISHED BY DDO

```

-.51353157E+00 .56241137E-03 -.74191113E-02 .15848475E-02
-.89.9.29E-02 .12583551E+00 -.26731414E-01 .12158399E-01
-.17462386E+00 .37513179E-01 .19436527E-02 -.85413646E-02
-.13626800E-02 .30909594E-01 .16407166E+00 .36797664E-01
-.1376.498E-02 .27620033E-01 .25627722E-01 .21748995E-01
-.42235847E-01 -.19512794E+00 -.41532819E-01 -.17780829E-02
-.1376.498E-02 .27620033E-01 .25627722E-01 .21748995E-01
-.42659756E+00 -.35513120E-01 -.3133J3L9E-01 .59336949E+00
-.39935926E-03 .57127361E-03 .61360546E-02 -.86116472E-02
-.26933211E-02 -.14699516E+00 .22635653E-01 .26833747E-01
-.42338977E+00 .-14732594E-03 .20652938E-02 .-73796541E-03
-.43514311E-02 -.38912777E-01 .99195763E-02 .-113UJ598E-01
-.13227360E+00 .-29624493E-01 .-68598156E-03 .31465266E-02
-.11791445E-02 .12688224E-01 .-67843419E-01 .-24397777E-01
-.36321571E-01 .15108219E+00 .61592235E-01 .63786899E-03
-.47716712E-03 .-94499020E-02 .-12378642E-01 .13914201E-03
-.17250962E+00 .30493266E-01 .15464593E-01 .-47494711E+00

```

CAMBER CASE NUMBER= 1 OF 1 CASES

C SWRI RECTANGULAR HYDROFOIL, TORSIONAL MODE, RF=1.97

	.17600	-.135LJ	.17600	.114L0	.17600	.24300
	.17600	.38100	.36300	-.07200	.36300	.21500
	.16300	.56100	.38300	.78700	.55900	-.11300
	.55900	.33000	.55900	.77100	.55900	1.21100
	.77100	-.152LJ	.77300	.45500	.77000	.1.16200
	.77300	1.569LJ				

REAL COEFFICIENT MATRIX CR (SPANWISE X CHORDWISE)

```

4.090E-03 -1.078E-02 1.855E-02
2.628E-02 -9.547E-02 1.891E-01
-3.373E-03 9.373E-05 3.353E-02

```

IMAG COEFFICIENT MATRIX CI (SPANWISE X CHORDWISE)

```

1.703E-04 2.303E-02 1.751E-04
-2.696E-03 1.743E-01 2.202E-13
-4.963E-03 -7.547E-03 8.056E-03

```

S	F(1)	F(2)	F(3)	F(4)	F(5)	F(6)
-	---	---	---	---	---	---
0.00	1.0E+00	0.	0.	0.	0.	0.
.05	1.0E+00	2.5E-03	6.2E-06			
.10	9.9E-01	9.9E-03	9.9E-05			
.15	9.9E-01	2.2E-02	5.3E-04			
.20	9.9E-01	3.9E-02	1.6E-03			
.25	9.7E-01	6.1E-02	3.4E-03			
.30	9.5E-01	4.5E-02	7.7E-03			
.35	9.4E-01	1.1E-01	1.4E-02			
.40	9.2E-01	1.5E-01	2.3E-02			
.45	8.9E-01	1.9E-01	3.7E-02			
.50	8.7E-01	2.2E-01	5.4E-02			
.55	8.4E-01	2.5E-01	7.6E-02			
.60	8.1E-01	2.9E-01	1.0E-01			
.65	7.6E-01	3.2E-01	1.4E-01			
.70	7.1E-01	3.5E-01	1.7E-01			
.75	6.6E-01	3.7E-01	2.1E-01			
.80	6.0E-01	3.8E-01	2.5E-01			
.85	5.3E-01	3.9E-01	2.7E-01			
.90	4.4E-01	3.5E-01	2.9E-01			
.95	3.1E-01	2.8E-01	2.5E-01			
1.00	2.5E-07	2.5E-07	2.5E-07			

Program 2 Output -- Steady Loading Test Case (continued)

THIS PAGE IS BEST QUALITY PRACTICABLE  
FROM COPY FURNISHED TO DDC

LOCAL COEFFICIENTS ON SECTION 1 AT SPANNWISE POSITION S

MOMENTS CALCULATED ABOUT X = -.38

PHASE IS ANGLE BY WHICH QUANTITY LEADS DISPLACEMENT

S	CLR	CLI	CLMG	CLPH	CPLM	CPLM	CPLM	CPPH	CRMR	CRMI	CRMG	CRPH
-	-	-	-	-	-	-	-	-	-	-	-	-
.00	-.250866	2.307074	2.321332	96.35	.365086	-.48859	.563212	-.49.59	.004500	0.000000	0.000000	0.00
.05	-.267163	2.346108	2.361268	96.50	.372773	-.436512	.574023	-.49.5.	-.333392	.293263	.295158	96.58
.10	-.297791	2.462412	2.480354	96.98	.395721	-.459312	.606284	-.49.25	-.074468	.615603	.621188	96.98
.15	-.344496	2.653390	2.676376	97.48	.433504	-.496895	.659470	-.48.89	-.136566	.995096	1.003641	97.48
.20	-.416666	2.915618	2.945523	98.17	.465781	-.544492	.732646	-.48.47	-.209332	1.457869	1.472762	98.17
.25	.507435	3.242811	3.282272	98.89	.551471	-.613113	.824637	-.49.03	-.317147	2.026756	2.051420	98.89
.30	-.613636	3.627753	3.679245	99.60	.629534	-.689433	.933611	-.47.6.	-.460227	2.720815	2.759464	99.60
.35	-.735728	4.061211	4.127315	101.27	.710543	-.775785	1.057426	-.47.19	-.643762	3.553559	3.611431	100.27
.40	-.871731	4.531997	4.615774	101.89	.816711	-.871130	1.193374	-.46.81	-.871731	4.531997	4.615774	100.89
.45	-1.019121	5.026780	5.129047	101.46	.921927	-.970019	1.338166	-.46.46	-1.146511	5.655127	5.770178	101.46
.50	-1.174697	5.529868	5.653202	101.99	1.031179	-.1.072677	1.467796	-.46.12	-1.468372	6.912260	7.366532	101.93
.55	-1.336386	6.022500	6.168557	102.49	1.141424	-.1.173998	1.637412	-.45.81	-1.834781	8.280937	8.481765	102.49
.60	-1.492974	6.442824	6.652512	102.97	1.248410	-.1.270316	1.781076	-.45.50	-2.239661	9.724229	9.978769	102.97
.65	-1.643760	6.884297	7.777643	103.43	1.346916	-.1.356222	1.911419	-.45.20	-2.671013	11.186983	11.501431	103.43
.70	-1.777633	7.194607	7.410767	103.88	1.433222	-.1.425200	2.019091	-.44.90	-3.110858	12.590212	12.968842	103.88
.75	-1.882614	7.371707	7.618394	104.33	1.469399	-.1.468800	2.091807	-.44.6.	-3.529902	13.821950	14.265571	104.33
.80	-1.941338	7.361351	7.612067	104.78	1.511925	-.1.475463	2.112560	-.44.30	-3.882677	14.720703	15.224134	104.78
.85	-1.927322	7.078143	7.335649	105.23	1.479933	-.1.427977	2.055811	-.44.00	-4.095559	15.041053	15.588578	105.23
.90	-1.794635	6.384964	6.632391	105.70	1.357786	-.1.296832	1.077593	-.43.68	-4.037929	14.366168	14.922857	105.70
.95	-1.448351	4.963400	5.168551	106.19	1.075010	-.1.015379	1.478730	-.43.37	-3.420834	11.789029	12.275339	106.18
1.00	-.030003	4.00010	4.00010	106.13	.0000j02	-.0000j02	.000003	-.41.72	-.J00007	.000024	.000025	J06.66

REAL	IMAG	MAG	PHASE
= -1.097349	= 4.919882	= 5.040775	= 102.57
= -1.943126	= -.966195	= 1.346762	= -45.63
= -1.749937	= 7.152366	= 7.363327	= 103.75

X-COORDINATE OF SECTION CP = .076845  
SPANNWISE COORDINATE OF SECTION CP = 2.928892

Program 2 Output -- Unsteady Loading Test Case

THIS PAGE IS BEST QUALITY PRACTICABLE  
FROM COPY FURNISHED TO DDC

AD-A074 702

DAVID W TAYLOR NAVAL SHIP RESEARCH AND DEVELOPMENT CE--ETC F/G 13/10  
ACCURACY OF HYDROFOIL LOADING PREDICTIONS OBTAINED FROM A LIFTI--ETC(U)  
SEP 79 P K BESCH, E P ROOD

UNCLASSIFIED

DTNSRDC-79/039

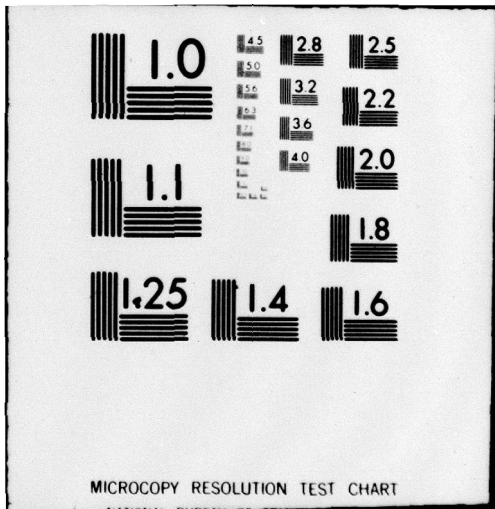
NL

3 OF 3  
ADA  
074702

FFP  
111



END  
DATE  
FILED  
11-79  
DOC



**APPENDIX F**  
**PROGRAM 3 OUTPUT FOR SAMPLE CALCULATION**

UNSTEADY LOADING TEST CASE--SWRI RECTANGULAR HYDROFOIL

CAMBER CASE NUMBER: 1 OF 1 CASES  
SWRI RECTANGULAR HYDROFOIL, TORSIONAL MODE, RF=1.97

三

### Program 3 Output -- Unsteady Loading Test Case

#### REFERENCES

1. Ashley, H. et al., "New Directions in Lifting Surface Theory," Journal of American Institute of Aeronautics and Astronautics, Vol. 3, No. 1, pp. 3-16 (Jan 1965). Also presented at the Aero Space Science Meeting, New York, N.Y. (20-22 Jan 1964).
2. Widnall, S.E., "Unsteady Loads on Supercavitating Hydrofoils of Finite Span," Journal of Ship Research, Vol. 10, No. 2, pp. 107-118 (Jun 1966).
3. Watkins, C.E. et al., "A Systematic Kernel Function Procedure for Determining Aerodynamic Forces on Oscillating or Steady Finite Wings at Subsonic Speeds," NASA Technical Report R-48 (1959).
4. Pattison, J.H., "Unsteady Hydrodynamic Loads on a Two-Dimensional Hydrofoil," NSRDC Report 3245 (Nov 1970).
5. Langan, T.J. and H.T. Wang, "Evaluation of Lifting-Surface Programs for Computing the Pressure Distribution on Planar Wings in Steady Motion," Computers and Fluids, Vol. 2, No. 1, pp. 53-78 (Mar 1974). Also NSRDC Report 4021 (May 1973).
6. Bandler, P.A., "A Program to Calculate the Pressure Distribution on a Hydrofoil of Finite Span Near the Free Surface," Engineering Research Associates Report 53/4 (Jun 1966).
7. Richardson, J.R., "Pressure Distribution on a Hydrofoil of Finite Span Near the Free Surface," Engineering Research Associates Report 53/3 (Jun 1966).
8. Feldman, J., "Experimental Investigation of Near-Surface Hydrodynamic Force Coefficients for a Series of Tee Hydrofoils, DTMB Series HF-1," David Taylor Model Basin Report 1801 (Dec 1963).
9. Wadlin, K.L. et al., "The Hydrodynamic Characteristics of Modified Rectangular Flat Plates Having Aspect Ratios of 1.00, 0.25, and 0.125 and Operating Near a Free Water Surface," NACA Report 1246 (1955).

10. Wadlin, K.L. et al., "A Theoretical and Experimental Investigation of the Lift and Drag Characteristics of Hydrofoils at Subcritical and Supercritical Speeds," NACA Report 1232 (1955).
11. Schuster, S. and H. Schwanecke, "On Hydrofoils Running Near a Free Surface," Third Symposium on Naval Hydrodynamics, edited by Stanley W. Doroff, Office of Naval Research, Department of the Navy, ACR-65 (1960).
12. Schuster, S. and H. Schwanecke, "On Oscillating Hydrofoils, Part 1," Berlin Towing Tank, ONR Contract No. N62 558-2236 (Dec 1960).
13. Ward, K.E. and N.S. Land, "Preliminary Tests in the NACA Tank to Investigate the Fundamental Characteristics of Hydrofoils," NACA WR L-766 (Sep 1940).
14. Waldin, K.L. et al., "Tank Tests at Subcavitation Speeds of an Aspect-Ratio-10 Hydrofoil with a Single Strut," NACA RM L9K14a (Jul 1950).
15. Ransleben, G.E., Jr. and H.N. Abramson, "Experimental Determination of Oscillatory Lift and Moment Distributions on Fully Submerged Flexible Hydrofoils," Journal of Ship Research, Vol. 7, No. 2, pp. 24-41 (Oct 1963).
16. Johnson, R.S., "Prediction of Lift and Cavitation Characteristics of Hydrofoil-Strut Arrays," Marine Technology, Vol. 2, No. 1, pp. 57-69 (Jan 1965).
17. Richter, J. and I. Palmer, "Hydrofoil Research Ship Hydrodynamic Report of Model Test Program," Grumman Aircraft Corporation Report M23.77 (Aug 1962).
18. O'Neill, W.C., "Unsteady Lift and Hinge Moment Characteristics of the AG(EH) Main Foil and Strut Assembly," NSRDC Report 2805 (Jul 1968).
19. Coder, D.W. et al., "Hinge Moment Reduction for the AG(EH) Main Strut-Pod-Foil Assembly by Use of Trailing Edge Tabs," DTNSRDC/SPD-332-04 (Jun 1976).
20. Coder, D.W. and D.E. Layne, "Hydrodynamic Coefficients from the 1975 Flap Incidence Control Experiment for the AGEH-1 Main Strut-Pod-Foil System," DTNSRDC/SPD-0332-05 (May 1978).

21. Robins, A.J., "A Theoretical and Experimental Study of the Lift on a NACA 16-309 Hydrofoil Section with a Sealed Flap, in Uniform Motion near a Free Surface," Admiralty Research Laboratory Report ARL/N4/G/HY/3/1, ARL/G/N63 (Oct 1977).
22. Abbott, I.H. and A.E. von Doenhoff, "Theory of Wing Sections," Dover Publications, Inc., New York (1959), p. 129.
23. Cox, G.G. and W.B. Morgan, "The Use of Theory in Propeller Design," Marine Technology, Vol. 9, No. 4, pp. 419-429 (1972).
24. Beckwith, T.G. and N.L. Buck, "Mechanical Measurements," Addison Wesley Publishing Company, Reading, Massachusetts (1969).
25. Lindsey, W.F. et al., "Aerodynamic Characteristics of 24 NACA 16-Series Airfoils at Mach Numbers between 0.3 and 0.8," NACA TN 1546 (Sep 1948).
26. Abramson, H.N. et al., "Hydroelasticity with Special Reference to Hydrofoil Craft," NSRDC Report 2557 (Sep 1967).
27. Schuster, S. and H. Schwanecke, "On Oscillating Hydrofoils, Part 11," Berlin Towing Tank, ONR Contract No. N62 558-2236 (Jun 1962).
28. Epperson, T.B. et al., "Nonstationary Airload Distributions on a Straight Flexible Wing Oscillating in a Subsonic Wind Stream," U.S. Air Force WADC Technical Report 55-323 (Jan 1956).
29. Ransleben, G.E., Jr., "Experimental Determination of Oscillatory Lift and Moment Distributions on Surface-Piercing Flexible Hydrofoils," Southwest Research Institute Technical Report 3, SWRI Project 38-1028-2 (Dec 1963).
30. Widmayer, E., Jr. et al., "Some Measurements of Aerodynamic Forces and Moments at Subsonic Speeds on a Rectangular Wing of Aspect Ratio 2 Oscillating about the Midchord," NACA Technical Note 4240 (May 1958).
31. Woolston, D.S. et al., "Analytical and Experimental Investigation of Aerodynamic Forces and Moments on Low-Aspect-Ratio Wings Undergoing Flapping Oscillations," NACA Technical Note 4302 (Aug 1958).

32. Wetzel, J.M. and W.H.C. Maxwell, "Tandem Interference Effects of Flat Noncavitating Hydrofoils," St. Anthony Falls Hydraulic Laboratory Project Report 61 (May 1962).
33. Milne-Thomson, L.M., "Theoretical Hydrodynamics," The Macmillan Company, New York (1960), p. 395.
34. Spangler, P.K., "Model Test Results for the Hystad Strut-Nacelle-Foil Combination," David Taylor Model Basin Report 2138 (Jan 1966).

INITIAL DISTRIBUTION

Copies	Copies
1 U.S. Army Waterways Experiment Station Res Center Lib	1 NAVSHIPYD PORTSMOUTH NH/Lib
1 CNR/Code 438, R. Cooper	2 NAVSHIPYD VALLEJO CA 1 Library 1 Code 250
1 USNA/P. Van Mater	1 CBC PORT HUENEME CA
1 NRL/Lib	1.2 DDC
1 NAVOCEANO/Lib	2 COGARD 1 COM (E), Sta 5-2 1 Div of Merchant Marine Safety
1 NAVPGSCOL	
1 NROTCU & NAVADMINU MIT	1 Library of Congress Sci & Tech Div
1 NAVWARCOL	
1 NAVFACENGCOM	1 MARAD/Adv Ship Prog Off
1 NAVAIRDEVVCEN	1 Merchant Marine Academy/ Tech Lib
1 NAVSWC DAHLGREN VA	
1 NUSC NEWPORT RI	2 NASA Langley Res Center 1 E. Yates 1 J. Lamar
1 NUSC NEW LONDON CT	
9 NAVSEASYSCOM 1 SEA 03 2 SEA 03D 1 SEA 05R 2 SEA 61R 1 SEA 312 1 SEA 321 1 PMS 303	1 NASA Sci & Tech Info Facility 1 National Science Foundation/ Eng Div 1 U Bridgeport/Mech Eng Dept/ E. Uram 4 U California, Berkeley/ College of Engr/Naval Arch Dept 1 Lib 1 J. Paulling 1 J. Wehausen 1 H. Schade
1 NAVSHIPYD BREMERTON WA	
1 NAVSHIPYD CHARLESTON SC/Lib	
1 NAVSHIPYD NORFOLK VA/Lib	
1 NAVSHIPYD PEARL HARBOR HI/Lib	3 Calif Inst of Tech 1 A. Acosta 1 M. Plessset 1 T. Wu
1 NAVSHIPYD PHILADELPHIA PA/Lib	

Copies	Copies
1 Colorado State U Prof M. Albertson Dept of Civil Eng	Mass Inst of Technol (Continued) Hydro Lab 1 A. Ippen
1 U of Connecticut V. Scottron Hydraulic Res Lab	Dept of Aero and Astro 3 S. Widnall
1 Cornell U W. Sears Grad School of Aero Eng	3 U of Michigan Dept of NAME 1 H. Benford 1 R. Couch 1 T. Ogilvie
1 HARVARD U G. Birkhoff Dept of Math	5 U of Minnesota St. Anthony Falls Hydr Lab 1 J. Killen 1 F. Schiebe 1 C. Song 1 J. Wetzel
1 U of Illinois College of Eng J. Robertson/Theoretical & Applied Mechanics	3 New York U 1 W. Pierson, Jr. Courant Inst of Math Sci 1 A. Peters 1 J. Stoker
3 State U of Iowa Iowa Inst of Hydraulic Res 1 J. Kennedy 1 L. Landweber 1 H. Rouse	1 U of Notre Dame A. Strandhagen
1 Kansas State U Engineering Exp Station D. Nesmith	2 Penn State U 1 Applied Res Lab 1 B. Parkin
1 Lehigh U Fritz Lab Lib	1 St. John's U Jerome Lurye Dept of Math
1 Long Island U Grad Dept of Marine Sci David Price	3 Southwest Research Inst 1 H. Abramson 1 G. Ransleben, Jr. 1 Applied Mechanics Review
1 U of Maryland P. Cunniff Dept of Mech Engr	3 Stanford U Dept of Civ Eng 1 B. Perry 1 R. Street Dept of Aero and Astro 1 H. Ashley
8 Mass Inst of Technol Dept of Ocean Eng 1 M. Abkowitz 1 J. Kerwin 1 P. Leehey 1 P. Mandel	

Copies	Copies
1    Stanford Res Inst Lib	1    Flow Research, Inc. F. Dvorak
3    Stevens Inst of Tech Davidson Lab 1 J. Breslin 1 S. Tsakonas 1 Lib	2    General Dynamics Corp 1 Electric Boat Div V. Boatwright, Jr. 1 Convair Aerospace Div A. H. Cunningham, Jr. MS 2851
1    Utah State U College of Eng R. Jeppson	1    Gibbs & Cox, Inc. Tech Info Control Section
2    Webb Institute 1 E. Lewis 1 L. Ward	2    Grumman Aircraft Eng Corp 1 W. Carl, Mgr Grumman Marine 1 J. Dulmovits
1    Worcester Polytechnic Inst Alden Res Labs	2    Hydronautics, Inc. 1 P. Eisenberg 1 M. Tulin
1    SNAME	
1    Aerojet-General W. Beckwith	4    Lockheed Missiles & Space 1 R. Kramer 1 R. Lacy 1 R. Perkins 1 R. Waid
1    Bethlehem Steel Sparrows Pt A. Haff, Tech Mgr	
12    Boeing Co. Aerospace Group 1 R. Barbar 1 H. French 1 R. Hatte 1 R. Hubbard 1 T. Marvin 1 C. Ray 1 W. Rowe 1 F. Watson Naval Sys Div 1 M. Kiehle 1 Longfelder Commercial Airplane Group 1 P. Rubbert 1 G. Saaris	1    Lockheed Missiles & Space/ Huntsville Research & Engineering Center/C. Lee
1    Cornell Aero Lab Applied Mech Dept	1    Marquardt Corporation General Applied Science Labs/F. Lane
	1    Martin Marietta Corp RIAS P. Jordan
	7    McDonnell-Douglas Corp Douglas Aircraft Co 1 J. Giesing 1 J. Hess 1 R. James 1 R. Liebeck 1 M. Lopez 1 A. Smith 1 R. Wasson

Copies		Copies	
1	Newport News Shipbuilding Tech Lib	10	5211.1 Reports Distribution
2	Northrop Corp/Aircraft Div 1 J. Gallagher 1 J. Stevens	1	522.1 (C)
1	Oceanics, Inc. P. Kaplan	1	522.2 (A)
1	Rockwell International Los Angeles Div J. Tulinius Dept 056-015		
1	Robert Taggart, Inc.		
1	TETRA-Tech/E. James		

**CENTER DISTRIBUTION**

Copies	Code	Name
3	115	R. Johnston
1	1154	HYSTU
1	15	W. Morgan (Acting)
1	1502	V. Monacella
1	1504	V. Monacella
1	1512	D. Cieslowski
1	152	
1	1524	Dr. Y. Shen
2	1532	G. Dobay
1	154	
1	1548	R. Folb
3	1552	J. McCarthy
10	1556	P. Besch
1	156	G. Hagen
1	1572	M. Ochi
1	1576	W. Smith
2	1965	Y.-N. Liu J. Casper

**DTNSRDC ISSUES THREE TYPES OF REPORTS**

- 1. DTNSRDC REPORTS, A FORMAL SERIES, CONTAIN INFORMATION OF PERMANENT TECHNICAL VALUE. THEY CARRY A CONSECUTIVE NUMERICAL IDENTIFICATION REGARDLESS OF THEIR CLASSIFICATION OR THE ORIGINATING DEPARTMENT.**
- 2. DEPARTMENTAL REPORTS, A SEMIFORMAL SERIES, CONTAIN INFORMATION OF A PRELIMINARY, TEMPORARY, OR PROPRIETARY NATURE OR OF LIMITED INTEREST OR SIGNIFICANCE. THEY CARRY A DEPARTMENTAL ALPHANUMERICAL IDENTIFICATION.**
- 3. TECHNICAL MEMORANDA, AN INFORMAL SERIES, CONTAIN TECHNICAL DOCUMENTATION OF LIMITED USE AND INTEREST. THEY ARE PRIMARILY WORKING PAPERS INTENDED FOR INTERNAL USE. THEY CARRY AN IDENTIFYING NUMBER WHICH INDICATES THEIR TYPE AND THE NUMERICAL CODE OF THE ORIGINATING DEPARTMENT. ANY DISTRIBUTION OUTSIDE DTNSRDC MUST BE APPROVED BY THE HEAD OF THE ORIGINATING DEPARTMENT ON A CASE-BY-CASE BASIS.**